

ผลของการใช้พลาสมากับไฟโบรอินไหมไทยที่มีต่อการตอบสนองของเซลล์



นายภัคดี อมรสุทธิวัฒน์

จุฬาลงกรณ์มหาวิทยาลัย

CHULALONGKORN UNIVERSITY

วิทยานิพนธ์นี้เป็นส่วนหนึ่งของการศึกษาตามหลักสูตรปริญญาวิศวกรรมศาสตรดุษฎีบัณฑิต

สาขาวิชาวิศวกรรมเคมี ภาควิชาวิศวกรรมเคมี

คณะวิศวกรรมศาสตร์ จุฬาลงกรณ์มหาวิทยาลัย

ปีการศึกษา 2556

ลิขสิทธิ์ของจุฬาลงกรณ์มหาวิทยาลัย

บทคัดย่อและแฟ้มข้อมูลฉบับเต็มของวิทยานิพนธ์ตั้งแต่ปีการศึกษา 2554 ที่ให้บริการในคลังปัญญาจุฬาฯ (CUIR)

เป็นแฟ้มข้อมูลของนิสิตเจ้าของวิทยานิพนธ์ ที่ส่งผ่านทางบัณฑิตวิทยาลัย

The abstract and full text of theses from the academic year 2011 in Chulalongkorn University Intellectual Repository (CUIR) are the thesis authors' files submitted through the University Graduate School.

EFFECTS OF PLASMA TREATMENT OF THAI SILK FIBROIN ON CELLULAR RESPONSES

Mr. Phakdee Amornsudthiwat



จุฬาลงกรณ์มหาวิทยาลัย

CHULALONGKORN UNIVERSITY

A Dissertation Submitted in Partial Fulfillment of the Requirements  
for the Degree of Doctor of Engineering Program in Chemical Engineering

Department of Chemical Engineering

Faculty of Engineering

Chulalongkorn University

Academic Year 2013

Copyright of Chulalongkorn University

Thesis Title EFFECTS OF PLASMA TREATMENT OF THAI SILK  
FIBROIN ON CELLULAR RESPONSES

By Mr. Phakdee Amornsudthiwat

Field of Study Chemical Engineering

Thesis Advisor Associate Professor Siriporn Damrongsakkul, Ph.D.

Thesis Co-Advisor Assistant Professor Rattachat Mongkolnavin, Ph.D.  
Mirko Nitschke, Ph.D.

---

Accepted by the Faculty of Engineering, Chulalongkorn University in Partial  
Fulfillment of the Requirements for the Doctoral Degree

.....Dean of the Faculty of Engineering  
(Professor Bundhit Eua-arporn, Ph.D.)

THESIS COMMITTEE

.....Chairman  
(Associate Professor Joongjai Panpranot, Ph.D.)

.....Thesis Advisor  
(Associate Professor Siriporn Damrongsakkul, Ph.D.)

.....Thesis Co-Advisor  
(Assistant Professor Rattachat Mongkolnavin, Ph.D.)

.....Thesis Co-Advisor  
(Mirko Nitschke, Ph.D.)

.....Examiner  
(Assistant Professor Sorada Kanokpanont, Ph.D.)

.....External Examiner  
(Assistant Professor Wilairat Leeanansaksiri, Ph.D.)

ภักดี อมรสุทธิวัฒน์ : ผลของการใช้พลาสมากับไฟโบรอินไหมไทยที่มีต่อการตอบสนองของเซลล์. (EFFECTS OF PLASMA TREATMENT OF THAI SILK FIBROIN ON CELLULAR RESPONSES) อ.ที่ปรึกษาวิทยานิพนธ์หลัก: รศ. ดร.ศิริพร ดำรงค์ศักดิ์กุล, อ.ที่ปรึกษาวิทยานิพนธ์ร่วม: ผศ. ดร.รัฐชาติ มงคลนาวิน, ดร.เมอโค่ นิซส์เค่อ, 225 หน้า.

งานวิจัยนี้มีวัตถุประสงค์เพื่อศึกษาอิทธิพลของการปรับปรุงพื้นผิวด้วยพลาสมาที่มีต่อสมบัติทางกายภาพและทางชีวภาพของพื้นผิวไฟโบรอินไหมไทย ช่วงแรกของงานวิจัย ได้ทำการศึกษาความเป็นไปได้ของการใช้พลาสมาในการปรับปรุงพื้นผิวไฟโบรอินไหมไทย โนโตรเจนพลาสมาซึ่งกำเนิดจากแหล่งจ่ายไฟฟ้ากระแสสลับที่ความถี่ 50 เฮิร์ตซ์ได้ถูกใช้ในการปรับปรุงพื้นผิวของไฟโบรอินไหมไทย ผลการวิจัยพบว่า โนโตรเจนพลาสมาสามารถปรับปรุงพื้นผิวให้มีความชอบน้ำมากขึ้นและทำให้เซลล์ผิวหนังของหนู (แอล929) ยึดเกาะบนพื้นผิวได้เร็วขึ้นเมื่อเทียบกับพื้นผิวที่ยังไม่ได้ปรับปรุง ข้อมูลโครงสร้างเคมีพื้นผิวพบว่าพลาสมาสร้างหมู่ฟังก์ชันที่ชอบน้ำบนพื้นผิวเท่านั้นโดยโครงสร้างทางเคมีของวัสดุทั้งหมดยังคงเหมือนเดิม ทั้งนี้สัณฐานของพื้นผิวไม่เกิดการเปลี่ยนแปลงอย่างเห็นได้ชัดหลังจากการปรับปรุงด้วยพลาสมา จากผลการทดลองเบื้องต้นนำไปสู่การศึกษาผลกระทบของพลาสมาต่อพื้นผิวไฟโบรอินไหมไทยโดยละเอียด เริ่มจากการวิเคราะห์สมบัติของพื้นผิวฟิล์มบางไฟโบรอินไหมไทย พื้นผิวไฟโบรอินไหมไทยจะถูกเตรียมเพื่อให้มีคุณภาพของพื้นผิวได้ตามข้อกำหนดของวิธีวิเคราะห์สมบัติทุกวิธีที่วางแผนไว้ จากข้อมูลของโครงสร้างเคมีพื้นผิวพบว่าพื้นผิวไฟโบรอินไหมไทยที่เตรียมด้วยวิธีนี้มีลักษณะสอดคล้องตามโครงสร้างเคมีทางทฤษฎีของไฟโบรอิน ผลการวิเคราะห์ศักย์ไฟฟ้าบนพื้นผิวพบว่าไฟโบรอินไหมไทยเป็นพื้นผิวที่มีประจุไฟฟ้าสุทธิเป็นลบ สิ่งที่พบเพิ่มเติม คือ ไฟโบรอินไหมไทยเป็นวัสดุที่บวมน้ำได้ นอกจากนั้นระดับของการบวมน้ำไฟโบรอินไหมไทยในของเหลวขึ้นอยู่กับความเข้มข้นของไอออน ในของเหลวนั้น แต่ไม่ขึ้นกับอุณหภูมิของของเหลว การปรับปรุงพื้นผิวฟิล์มบางของไฟโบรอินไหมไทยด้วยพลาสมามุ่งเน้นที่จะหาสภาวะที่สามารถสร้างหมู่ฟังก์ชันที่ต้องการได้ ผลของโครงสร้างเคมีพื้นผิวพบว่า หมู่ฟังก์ชันที่ต้องการได้ถูกเหนี่ยวนำบนพื้นผิวไฟโบรอินไหมไทย อย่างไรก็ตาม หมู่ฟังก์ชันบนพื้นผิวที่ถูกปรับปรุงด้วยพลาสมาไม่สามารถอยู่บนพื้นผิวได้ถ้าถูกชะล้างด้วยน้ำปราศจากประจุ สิ่งที่พบเพิ่มเติมคือความหนาของแผ่นฟิล์มไฟโบรอินไหมไทยลดลงหลังจากการปรับปรุงพื้นผิวด้วยพลาสมา ปรากฏการณ์เช่นนี้แสดงให้เห็นว่าพลาสมาทำให้เกิดการกัดเซาะบนพื้นผิวไฟโบรอินไหมไทยโดดเด่นกว่าการสร้างหมู่ฟังก์ชันบนพื้นผิว ถึงแม้ไม่เกิดการสร้างหมู่ฟังก์ชันบนพื้นผิว แต่ออกซิเจนพลาสมาสามารถเปลี่ยนพื้นผิวให้มีความอดูดซับของสภาพยืดหยุ่นเพิ่มขึ้นจาก 62 เป็น 500 กิโลปาสคาล โดยที่ไม่เกิดการเปลี่ยนแปลงของโครงสร้างเคมีพื้นผิว ปริมาณผลึกในโครงสร้าง ค่ามุมสัมผัสของน้ำ และ การดูดซับของโปรตีน การค้นพบนี้สามารถนำไปศึกษาอิทธิพลของความแข็งแรงของพื้นผิวต่อปฏิสัมพันธ์ระหว่างพื้นผิวกับพฤติกรรมของเซลล์ เซลล์ผิวหนังของหนู (แอล929) และเซลล์ต้นกำเนิดจากไขกระดูกของมนุษย์ได้ถูกเลือกสำหรับการศึกษา เนื่องจากเซลล์ทั้งสองประเภทอยู่บนเนื้อเยื่อที่มีความแข็งแรงแตกต่างกัน ผลการทดลองพบว่า เซลล์ผิวหนังของหนู (แอล929) สามารถยึดเกาะและแผ่ขยายพื้นที่ในการยึดเกาะได้ดีบนพื้นผิวไฟโบรอินไหมไทยที่ถูกปรับปรุงด้วยออกซิเจนพลาสมาซึ่งมีความแข็งแรงสูงกว่าพื้นผิวไฟโบรอินไหมไทยก่อนการปรับปรุง ขณะที่เซลล์ต้นกำเนิดจากไขกระดูกของมนุษย์สามารถยึดเกาะและแผ่ขยายบนพื้นผิวไฟโบรอินไหมไทยได้ดีเหมือนกันทั้งก่อนและหลังการปรับปรุงด้วยพลาสมา

ภาควิชา	วิศวกรรมเคมี	ลายมือชื่อนิสิต .....
สาขาวิชา	วิศวกรรมเคมี	ลายมือชื่อ อ.ที่ปรึกษาวิทยานิพนธ์หลัก .....
ปีการศึกษา	2556	ลายมือชื่อ อ.ที่ปรึกษาวิทยานิพนธ์ร่วม .....
		ลายมือชื่อ อ.ที่ปรึกษาวิทยานิพนธ์ร่วม .....



# # 5371813221 : MAJOR CHEMICAL ENGINEERING

KEYWORDS:

PHAKDEE AMORNSUDTHIWAT: EFFECTS OF PLASMA TREATMENT OF THAI SILK FIBROIN ON CELLULAR RESPONSES. ADVISOR: ASSOC. PROF. SIRIPORN DAMRONGSAKKUL, Ph.D., CO-ADVISOR: ASST. PROF. Rattachat Mongkolnavin, Ph.D., Mirko Nitschke, Ph.D., 225 pp.

This research aimed to study the effects of plasma treatment on the physical and biological properties of Thai silk fibroin (SF). A preliminary study was conducted to evaluate whether plasma treatment could improve the biocompatibility of silk fibroin surface. Nitrogen glow discharge plasma generated by AC 50Hz power supply was employed to treat the SF film. The results showed that N<sub>2</sub> plasma improved surface wettability and early adhesion of L929 mouse fibroblast. The XPS surface chemistry results showed that hydrophilic functional groups were induced on plasma-treated SF. The bulk chemistry of SF was unchanged after plasma treatment as confirmed by FTIR-ATR. The AFM surface topographical results indicated no significant change after plasma treatment. The encouraging results that N<sub>2</sub> plasma could improve the biocompatibility of SF led into an in-depth investigation of plasma treatment on SF. This started with the comprehensive characterization of well-defined planar SF, which was prepared as a thin film, allowing a complete assessment of all analytical techniques. XPS results showed that well-defined SF had a surface chemistry which was similar to the theoretical molecular structure of SF. Streaming potential indicated that SF was a negatively charged surface. The spectroscopic ellipsometry results revealed that SF thickness was increased in a liquid environment compared to a dry state. This observation suggested that SF was a swollen material. Moreover, SF swelling degree in liquid depended on liquid ionic concentration but not on liquid temperature. Plasma experiments were conducted to find out treatment conditions for desirable surface functionalization. The results showed that the desirable surface functional groups were successfully induced on the surface. However, the induced functional groups from plasma-treated SF could be removed by rinsing with DI. The thickness loss was also observed after plasma treatment. These findings suggested that plasma etching of SF was more prominent than plasma functionalization. The most significant plasma-treated effect was the increased elastic modulus of O<sub>2</sub> plasma-treated SF, as revealed by AFM based nano-indentation (from 62 to 500 kPa). The characterization of other related properties (e.g. XPS spectra, degree of crystallinity, surface charge, swelling degree, surface wettability, and FN adsorption) revealed that these properties were minimally affected from plasma treatment. These findings inspired the use of plasma etching of SF to alter surface stiffness for cell-substrate interaction study. L929 and hMSC were chosen for the study based on their different ECM stiffness. *In vitro* results showed that the increased stiffness of plasma-treated SF enhanced L929 adhesion and spreading, not hMSC. L929 attachment and spreading were better on stiffer O<sub>2</sub> plasma-treated SF, while hMSC spread well on all SF surfaces.

Department: Chemical Engineering Student's Signature .....

Field of Study: Chemical Engineering Advisor's Signature .....

Academic Year: 2013 Co-Advisor's Signature .....

Co-Advisor's Signature .....

## ACKNOWLEDGEMENTS

This thesis could not have been accomplished without the kind supports of countless individuals who have inspired, guided, coached, and assisted me during my study period. I wish to thank you all for your contribution to my success.

Firstly, to my advisor, Associate Professor Dr. Siriporn Damrongsakkul, thank you for giving me the freedom to pursue the research that I am interested in and offering the guidance and supports when I needed it. In addition, I am grateful with the valuable advice and insight from my co-advisor, Assistant Professor Dr. Rattachat Mongkolnavin. I sincerely thank my co-advisor, Dr. Mirko Nitschke for all the help, guidance, teaching, and friendship during my stay at Institute of Polymer Research Dresden. I would like to extend my appreciation to the staff of Leibniz Institute of Polymer Research Dresden for their analytical assistance. In addition, I would like to thank Assistant Professor Dr. Sorada Kanokpanont for her helpfulness and creative suggestions throughout my study period.

I also would like to acknowledge the financial supports from the Royal Golden Jubilee Ph.D. Program, Thailand Research Fund, Chulalongkorn University Centenary Academic Development Project, and the 90<sup>th</sup> anniversary of Chulalongkorn University Fund (Ratchadaphiseksomphot Endowment Fund).

For the supply of 'Nangnoi Srisaket I' silkworm cocoons, I am grateful for the generosity of Queen Sirikit Sericulture Center, Srisaket Province, Thailand.

I am appreciative of Associate Professor Dr. Joongjai Panpranot and Assistant Professor Dr. Wilairat Leeanansaksiri for taking the time to serve as the chairman and the thesis committee, respectively. Your comments were extremely fruitful.

I would like to recognize Dr. Dusit Ngamrungle for troubleshooting all problems related with AC50Hz plasma systems and Assistant Professor Tanom Bunaprasert, M.D. and Khun Rapeeporn Mannontarat for the use of cell culture facilities at Chulalongkorn Medical Research Center, Faculty of Medicine, Chulalongkorn University.

For all present and past members of the Biomedical Material Research Group, it was a pleasure to know you all. And I thank you for the friendship and assistance.

To all my lifelong close friends and mentors, I value your friendship, I consider myself lucky that our paths have crossed at many points in our lives.

To my aunt, I appreciate for taking good care of my parents and myself.

To my deceased parents, I am indebted to you both for your unconditional love and everything you did for me. You gave me the best possible things a child could ever hope for. I am so honored and proud to be your son. I still miss you every day.

To my only love, you have been so supportive during the best and worst times in my life. You make my life worthwhile. Thanks for loving me and I look forward for our next chapter in life together.



## CONTENTS

	Page
THAI ABSTRACT .....	iv
ENGLISH ABSTRACT .....	v
ACKNOWLEDGEMENTS .....	vi
CONTENTS .....	viii
LIST OF TABLES .....	xvi
LIST OF FIGURES .....	xix
LIST OF ABBREVIATIONS .....	xxvii
LIST OF PUBLICATIONS .....	xxxiv
CHAPTER .....	1
1.    INTRODUCTION .....	1
1.1    Background .....	1
1.2    Objectives .....	4
1.3    Scopes of Research .....	5
1.4    The publication details relating to the research objectives .....	9
2.    RELEVANT THEORY .....	11
2.1    Plasma .....	11
2.1.1    Definition .....	11
2.1.2    Particle collision .....	11
2.1.3    Motion of charges in electric and magnetic fields .....	12
2.1.4    Plasma generation methods .....	13
2.1.4.1    DC electrical discharge plasma .....	14
2.1.4.2    AC electrical discharge plasma .....	19
2.1.4.3    RF (radio frequency) power plasma .....	19

2.1.4.3.1	Inductive RF electrical discharge plasma.....	19
2.1.4.3.2	Capacitive RF electrical discharge plasma...	20
2.1.4.4	Microwave electrical discharge plasma.....	21
2.1.5	Plasma application.....	22
2.1.5.1	Plasma surface treatment.....	22
2.1.5.2	Plasma ion implantation.....	23
2.1.5.3	Plasma sputtering process for thin film deposition.....	23
2.1.5.4	Plasma Chemical Vapor Deposition (PCVD).....	24
2.1.5.5	Plasma etching.....	25
2.1.6	Plasma characteristic parameters.....	25
2.1.6.1	Number of particles ( $n_0$ ).....	25
2.1.6.2	Kinetic temperature in electron volt (T).....	26
2.1.6.3	Langmuir probe diagnostics.....	26
2.1.6.4	Langmuir probe characteristics curve.....	27
2.1.6.5	Electron kinetic temperature $T_e$ .....	29
2.1.6.6	Electron number density ( $n_e$ ).....	29
2.1.6.7	Ion kinetic temperature $T_i$ .....	30
2.1.6.8	Debye shielding length.....	31
2.2	Silk fibroin.....	32
2.2.1	Silk fiber.....	32
2.2.2	Silk fibroin structure.....	32
2.2.3	The amino acid sequence of the Bombyx mori silk fibroin heavy chain.....	33
2.2.4	Silk fibroin application in tissue engineering.....	36

2.2.5	Surface modification of silk fibroin .....	36
2.3	Tissue Engineering.....	37
2.4	Cell interaction with biomaterial surface .....	39
2.4.1	Protein adsorption on biomaterial surface .....	39
2.4.1.1	Factors controlling protein adsorption .....	40
2.4.1.2	The process of protein adsorption.....	43
2.4.1.3	The behavior of adsorbed proteins on the surface.....	44
2.4.1.3.1	The orientation of adsorbed protein: Side-on or end-on	44
2.4.1.3.2	The conformational change.....	46
2.4.1.3.3	The cooperative effect .....	47
2.4.1.3.4	Experimental precaution in protein adsorption study .....	48
2.4.2	Cell adhesion .....	49
2.4.2.1	Cell-extracellular matrix (ECM) adhesion .....	49
2.4.2.2	Cell-cell adhesion .....	51
2.4.2.3	Formation of Cell-ECM adhesions .....	52
2.4.2.4	Cytoplasmic network of adhesion molecules .....	56
2.4.3	Effect of surface chemistry on cell-substrate interaction.....	56
2.4.4	Effect of surface stiffness on cell-substrate interaction .....	65
3.	LITERATURE REVIEW .....	69
3.1	An introduction to plasma treatment as a surface modification tool .....	69
3.2	The effects of different plasma gases .....	72
3.2.1	Argon.....	72
3.2.2	Oxygen.....	73

3.2.3	Other gases used for the generation of oxygenated species.....	74
3.2.4	Nitrogen containing gases (NH <sub>3</sub> , N <sub>2</sub> and allylamine).....	76
3.2.4.1	Ammonia and nitrogen .....	76
3.2.4.2	Allylamine in Plasma polymerization .....	76
3.2.5	Hydrogen .....	77
3.3	The introduction of other molecules on surface by plasma treatment .	77
3.4	Characterization of plasma treatment .....	81
3.4.1	Plasma diagnostics .....	82
3.4.2	Surface characterization.....	82
3.4.2.1	Surface wettability .....	82
3.4.2.2	Surface chemistry.....	83
3.4.2.3	Surface topography.....	84
3.4.2.4	The effect of air exposure after plasma treatment .....	85
3.4.2.5	Stability of plasma treated surface (hydrophobic recovery).....	87
3.4.2.6	Surface charge .....	89
3.4.3	Protein adsorption.....	90
3.4.4	In vitro biological response tests of plasma treated material .....	91
3.4.4.1	Choice of cells .....	91
3.4.4.2	Cell adhesion .....	92
3.4.4.3	Cell proliferation .....	93
3.4.4.4	Cell differentiation .....	93
3.4.4.4.1	Osteogenic differentiation.....	93
4.	PRELIMINARY STUDY OF PLASMA TREATMENT ON THAI SILK FIBROIN SURFACE	95

	Page
4.1 Materials .....	95
4.2 Equipment.....	96
4.3 Experimental procedures.....	97
4.3.1 Preparation of Thai silk fibroin sample .....	99
4.3.2 Preparation of Thai silk fibroin casted films.....	99
4.3.3 AC50 Hz Glow discharge plasma experimental setup .....	99
4.3.4 Plasma diagnostics using optical emission spectroscope (OES)	100
4.3.5 Characterization of untreated and plasma-treated Thai silk fibroin films.....	101
4.3.5.1 Static water contact angle measurement.....	101
4.3.5.2 Surface chemistry.....	101
4.3.5.3 Bulk chemistry .....	101
4.3.5.4 Surface topography.....	101
4.3.6 In vitro cell culture test .....	102
4.3.6.1 Early cell adhesion test .....	102
4.3.6.2 Cell cytoskeleton staining .....	103
4.3.7 Statistical Analysis .....	103
4.4 Results and Discussion.....	103
4.4.1 Optical Emission Analysis of AC50Hz Plasma .....	103
4.4.2 Surface wettability.....	106
4.4.3 Surface chemistry .....	107
4.4.4 Bulk chemistry.....	113
4.4.5 Surface topography.....	114
4.4.6 Cell early adhesion and cell cytoskeleton .....	115



	Page
4.5 Conclusion .....	118
5. IN-DEPTH INVESTIGATION OF PLASMA TREATMENT ON THAI SILK FIBROIN SURFACE	120
5.1 Materials .....	120
5.2 Equipment.....	122
5.3 Experimental procedures.....	124
5.3.1 Preparation of Thai silk fibroin dip-coated films.....	127
5.3.2 Microwave plasma experimental setup.....	128
5.3.3 Characterization of untreated and plasma-treated Thai silk fibroin films.....	129
5.3.3.1 X ray photoelectron spectroscopy (XPS).....	129
5.3.3.2 Fourier transform infrared attenuated total reflection spectroscopy (FTIR-ATR).....	130
5.3.3.3 Electrokinetic measurements .....	131
5.3.3.4 Ellipsometry .....	132
5.3.3.5 Liquid-fluid contact angle measurements using captive air bubbles .....	133
5.3.3.6 Atomic force microscopy and nano-indentation.....	134
5.3.3.7 Fibronectin adsorption with quartz crystal microbalance (QCM)	135
5.3.4 In vitro cell cultures.....	136
5.3.4.1 Optical microscopy.....	136
5.3.4.2 Immunofluorescence microscopy .....	137
5.3.5 Statistical Analysis .....	138

5.4	Comprehensive characterization of well-defined planar silk fibroin surface.....	139
5.4.1	Results and Discussion .....	139
5.4.1.1	Surface chemistry.....	139
5.4.1.2	Surface charge .....	145
5.4.1.3	Thickness, refractive index, and swelling ratio of SF ..	146
5.4.1.4	Wetting behavior .....	153
5.4.1.5	The degree of crystallinity.....	155
5.4.1.6	Surface topography and stiffness .....	158
5.4.2	Conclusions.....	160
5.5	Finding of plasma operating conditions for surface functionalization....	161
5.5.1	Results and Discussion .....	162
5.5.1.1	Surface chemistry of oxygen plasma-treated SF.....	162
5.5.1.1.1	The effects of sample shield installation on surface functionalization by oxygen plasma.....	165
5.5.1.1.2	The trial of extremely low energy conditions for improving the surface functionalization effect by oxygen plasma.....	166
5.5.1.1.3	The effect of silk races (Thai vs. Japanese silk) on the possibility of surface functionalization by oxygen plasma.....	171
5.5.1.2	Surface chemistry of argon plasma-treated SF.....	173
5.5.1.3	Surface chemistry of argon/oxygen plasma-treated SF	176
5.5.1.4	Surface chemistry of ammonia plasma-treated SF.....	180
5.5.1.5	Surface charge .....	183
5.5.2	Conclusions.....	186

5.6	Oxygen plasma etching of silk fibroin alters surface stiffness: A cell-substrate interaction study.....	188
5.6.1	Results and Discussion .....	188
5.6.1.1	Surface chemistry.....	188
5.6.1.2	Degree of crystallinity of untreated and O <sub>2</sub> plasma-treated SF.....	189
5.6.1.3	Surface charge .....	190
5.6.1.4	Surface wettability .....	191
5.6.1.5	Surface topography.....	192
5.6.1.6	Swelling, refractive index, and surface stiffness .....	193
5.6.1.7	Adsorption of Fibronectin.....	195
5.6.1.8	L929 and hMSC adhesion.....	196
5.6.2	Conclusion .....	202
6.	CONCLUSIONS AND RECOMMENDATIONS.....	203
6.1	Conclusions.....	203
6.2	Recommendations .....	205
	REFERENCES.....	207
	APPENDIX A: MTT standard curve .....	224
	VITA.....	225

## LIST OF TABLES

	Page
Table 2-1 The list of important collisions in plasma .....	12
Table 2-2 The operating conditions of major types of plasma reactor. ....	22
Table 2-3 Surface wettability of different surface chemistry .....	58
Table 2-4 Protein adsorption capacity on different surface chemistry.....	58
Table 2-5 Protein conformation on different surface chemistry .....	60
Table 2-6 Cell attachment on different surface chemistry .....	60
Table 2-7 Cell spreading on different surface chemistry .....	61
Table 2-8 Cell integrin characteristics on different surface chemistry .....	62
Table 2-9 Cell cytoplasmic components on different surface chemistry .....	63
Table 2-10 Cell growth on different surface chemistry.....	64
Table 2-11 Cell differentiation on different surface chemistry.....	64
Table 3-1 The selected examples of materials which have been treated with various types of plasma.....	70
Table 3-2 Summary of operating power conditions of various plasma type from the selected papers.....	71
Table 3-3 Summary of the introduction of other molecules on the surface by plasma-based technique from selected papers.....	80
Table 3-4 Summary of all analytical technique performed to characterize plasma treatment from selected papers.....	81
Table 3-5 The selected examples of the change of surface topography from plasma treatment.....	85
Table 3-6 The selected examples of air exposure effect on the surface chemistry change. ....	87
Table 3-7 Isoelectric point of various material surfaces (untreated and treated surface) from the zeta potential measurement .....	89

Table 3-8 Summary of cells used for biological response test of plasma treated surface .....	92
Table 4-1 Surface atomic composition, atomic ratio, and functional groups of Thai silk fibroin surfaces before and after nitrogen plasma treatment obtained from by XPS .....	109
Table 5-1 Percent theoretical atomic composition of silk fibroin derived from the amino acid composition reported by Asakura <i>et al</i> [140].....	140
Table 5-2 Silk fibroin theoretical carbon functionality composition derived from the amino acid composition reported by Asakura <i>et al</i> [140].....	142
Table 5-3 A summary of XPS atomic composition and carbon functionalities (C <sub>1s</sub> components) results of SF surface from this work compared with previous literatures (theoretical values were % atomic composition and XPS C <sub>1s</sub> components based on the amino acid composition according to Askaura <i>et. al.</i> [140] as shown in Table 5-1 and Table 5-2, respectively).....	143
Table 5-4 Summary of water contact angle on silk fibroin surface which annealed with methanol from different literature in comparison to this work.....	155
Table 5-5 Percentage of protein secondary structure based on different Fourier self deconvolution factor (deconvolution factor 10000 and noise reduction factor 0.5).....	158
Table 5-6 Summary of primary amine of NH <sub>3</sub> plasma-treated SF and untreated SF by TFBA (4-trifluoro methyl-benzaldehyde) labelling together with nitrogen to carbon atomic ratio (N/C).....	185
Table 5-7 Advancing and receding water contact angles on untreated and O <sub>2</sub> plasma treated SF surfaces using captive air bubbles in conjunction with axisymmetric drop shape analysis (ADSA).....	192
Table 5-8 Summary of thickness, swelling ratio, refractive index and modulus of untreated and O <sub>2</sub> plasma treated SF surfaces.....	194

Table 5-9 An example of different substrate stiffness which is suitable for different cell adhesion in terms of cell spreading area or growth.....201



## LIST OF FIGURES

	PAGE
Figure 2-1 The motion of positive and negative charges in electric, magnetic, or cross fields .....	13
Figure 2-2 The configuration of DC electrical discharge plasma .....	15
Figure 2-3 Voltage-current characteristics of the DC low pressure electrical discharge plasma .....	16
Figure 2-4 Universal Paschen curve for selected gasses .....	18
Figure 2-5 The typical configuration of RF inductive coupled plasma.....	19
Figure 2-6 The typical configuration of RF capacitive coupled plasma .....	20
Figure 2-7 The most used system arrangement of microwave-generated plasma.....	21
Figure 2-8 A schematic diagram of Langmuir probe for plasma diagnostics.....	27
Figure 2-9 An example of Langmuir probe curve for plasma diagnostics .....	27
Figure 2-10 A graphical determination of plasma potentially by semi-logarithmic scale of Langmuir probe curve in the electron current region.....	30
Figure 2-11 A graphical illustration of plasma sheath at cathode.....	31
Figure 2-12 The composition of raw silk fiber .....	32
Figure 2-13 The silk fibroin structure which illustrates the linkages between H-chain & L-chain, and H-chain & P25 .....	33
Figure 2-14 The domains in the heavy chain of silk fibroin.....	33
Figure 2-15 The 3D conformation of silk fibroin heavy chain in $\beta$ -sheet structure .....	34
Figure 2-16 The amino acid sequence of silk fibroin heavy chain (5263 residues) .....	35
Figure 2-17 Schematic representation of $\beta$ -Lactoglobulin depicts the distribution of positively (red spheres) and negatively (blue spheres) charged amino acids .....	41
Figure 2-18 Vroman effect diagram for competitive protein adsorption .....	42
Figure 2-19 The protein adsorption process .....	44

Figure 2-20 The re-orientation process at high surface density of adsorbed proteins	46
Figure 2-21 Schematic of protein adsorption to hydrophobic (a) and hydrophilic (b) surface .....	47
Figure 2-22 The cooperative effect by pre-adsorbed proteins .....	48
Figure 2-23 Types of cell-ECM adhesion.....	51
Figure 2-24 The currently identified integrins presented from the combination of $\alpha$ and $\beta$ subunits .....	52
Figure 2-25 The details of domain structure of integrins (a) example of each subunit (b) one the most studied integrin ( $\alpha_v\beta_3$ ) which can bind to FN/VN and others ECM proteins .....	53
Figure 2-26 The binding mechanism of integrin with ECM ligand .....	54
Figure 2-27 Syndecan4 structure.....	54
Figure 2-28 Structure of fibronectin (FN) .....	55
Figure 2-29 The network of cytoplasmic adhesion proteins: Structural group e.g. Talin, Vinculin, $\alpha$ -actinin, F-actin (stress fiber) and signaling molecules e.g. Focal Adhesion Kinase (FAK).....	56
Figure 2-30 Location of monoclonal antibodies 3E3 and HFN7.1 probing at cell binding domain of FN.....	59
Figure 2-31 The mechanosensory model at focal adhesion through F-actin/Myosin skeleton.....	65
Figure 2-32 The effect of substrate stiffness on adhesion structures and cytoskeleton (F-actin).....	66
Figure 2-33 Tissue elasticity and differentiation of naive hMSC .....	67
Figure 3-1 The introduction of other molecules on surface by plasma-based techniques .....	79
Figure 4-1 Diagram of experimental procedures.....	98
Figure 4-2 The configuration of plasma machine using AC50Hz power supply .....	100



Figure 4-3 Voltage-current characteristics (IV chart) of nitrogen glow discharge plasma at nitrogen flowrate of 10 sccm, electrode gap of 5 cm, and supplied voltage of 40 – 220 V.....	104
Figure 4-4 Optical Emission Spectra of nitrogen glow discharge plasma at various supplied voltage of 140, 210, and 220 V with nitrogen flowrate of 10 sccm and electrode gap of 5 cm.....	105
Figure 4-5 Optical Emission Spectra of nitrogen glow discharge plasma at various nitrogen flowrate of 5, 10, and 15 sccm, with the highest supplied voltage of 220 V and electrode gap of 5 cm.....	106
Figure 4-6 The static water contact angle of nitrogen plasma-treated Thai silk fibroin films as a function of treatment time.....	107
Figure 4-7 High resolved XPS spectra of Thai silk fibroin surfaces: (1a) C <sub>1s</sub> spectra w/ peak deconvolution of untreated silk fibroin surface, (1b) ~of 10 second N <sub>2</sub> plasma-treated surface, (1c) ~of 90 second N <sub>2</sub> plasma-treated surface, (2a) N <sub>1s</sub> spectra of untreated silk fibroin surface, (2b) ~of 10 second N <sub>2</sub> plasma-treated surface, (2c) ~of 90 second N <sub>2</sub> plasma-treated surface, (3a) O <sub>1s</sub> spectra w/ peak deconvolution of untreated silk fibroin surface, (3b) ~of 10 second N <sub>2</sub> plasma-treated surface, and (3c) ~of 90 second N <sub>2</sub> plasma-treated surface.....	108
Figure 4-8 The list of all possible functional groups of silk fibroin in C <sub>1s</sub> and N <sub>1s</sub> spectra, and the illustration diagram of overlapped functional groups calculation.....	111
Figure 4-9 FTIR-ATR spectra of untreated and nitrogen plasma treated Thai silk fibroin surfaces.....	114
Figure 4-10 Surface topography of untreated and nitrogen plasma-treated Thai silk fibroin surfaces.....	115

Figure 4-11 The number of adhered L929 on tissue culture plate polystyrene (TCPS), untreated silk fibroin, 10 s nitrogen plasma-treated silk fibroin and 90 s nitrogen plasma-treated silk fibroin for 1.5, 3, 4.5 and 6 h determined by MTT assay (seeding: $8 \times 10^4$ cells/sample or $4 \times 10^4$ cells/cm <sup>2</sup> ). Each letter represents the significant difference ( $p < 0.05$ ) for all samples (the results with the same alphabet indicate that they are not significantly different)	116
Figure 4-12 F-actin cell cytoskeleton staining by Rhodamine phalloidin (R415) of L929 on untreated and plasma treated Thai silk fibroin surface after the culture period of 4 h and 1 day (the scale bar is 100 micron in length).	117
Figure 5-1 Diagram of experimental procedures (Part II)	126
Figure 5-2 Example of SF film on different substrates for all surface characterization	127
Figure 5-3 Molecular structure of amino acids and its relative abundance in silk fibroin according to Asakura et al [140].	140
Figure 5-4 XPS C 1s spectra from this work (Thai and Japanese silk fibroin) compared with those reported in the literature	144
Figure 5-5 Streaming current vs. pressure gradient and apparent zeta potential versus pH value of the silk fibroin surface for 0.1, 1 and 10 mM KCl solution. .	146
Figure 5-6 Swelling ratio in DI water and refractive index in dry and wet conditions as a function of dry film thickness	148
Figure 5-7 Swelling ratio in DI water and refractive index in dry and wet conditions of silk fibroin which had annealed with methanol for different period	149
Figure 5-8 Silk fibroin film thickness change in different media which has different ionic strength (deionized water (DI) and phosphate buffer solution (PBS)) using measurement mode of in-situ thickness monitoring at the same spot (dry film thickness of 70 nm)	150

Figure 5-9 Silk fibroin film thickness change in deionized water (DI) and phosphate buffer solution (PBS) with different strength (0.1X – 10X) using measurement mode of in-situ thickness monitoring at the same spot (dry film thickness of 70 nm).....	151
Figure 5-10 Silk fibroin film thickness in phosphate buffer solution at various temperature from 12 to 49 degree Celsius (dry film thickness of 70 nm) .....	152
Figure 5-11 Representative data sets of two water contact angle measurements on swollen SF surfaces using the captive bubble technique and ADSA (V: volume of the bubble; r: contact radius; $\theta$ : water contact angle; $\gamma$ : liquid surface tension; liquid: MilliQ water).....	153
Figure 5-12 Changes in the FTIR spectra of SF samples upon methanol treatment at amide I ( $1600 - 1705 \text{ cm}^{-1}$ ) .....	156
Figure 5-13 Fourier self deconvolution along with peak fitting of SF before $\beta$ -sheet induction with methanol (top graph) and SF after $\beta$ -sheet induction with methanol for 1 h (bottom graph) where B: $\beta$ -sheet, T: $\beta$ -turn, A: $\alpha$ -helix, R: random coil, and SC: tyrosine side chain.....	157
Figure 5-14 AFM images of silk fibroin with the scan area of $10 \times 10 \mu\text{m}^2$ in air (left) and phosphate buffer solution (PBS) (right) .....	159
Figure 5-15 Young's modulus of silk fibroin surface in phosphate buffer solution (no. of sample =3, no. of scans per sample = 50).....	159
Figure 5-16 XPS spectra together with oxygen to carbon atomic ratios (O/C) of $\text{O}_2$ plasma-treated SF before and after rinsing with DI ( $\text{O}_2$ flow 40 sccm, pressure = $7.2 \times 10^{-3}$ mbar, power 250 W, duty cycle (on/off) 1/1 ms) ...	163
Figure 5-17 An installation of the sample shield for protecting SF high energy plasma ions.....	165

- Figure 5-18 XPS spectra together with oxygen to carbon atomic ratios (O/C) of untreated SF and O<sub>2</sub> plasma-treated SF with shielding to prevent direct ion bombardment on the surface (sample was rinsed before XPS measurement)..... 166
- Figure 5-19 XPS spectra together with oxygen to carbon atomic ratios (O/C) of untreated and O<sub>2</sub> plasma-treated SF (after rinsing with DI), the plasma conditions were at highest O<sub>2</sub> flow (49 sccm), pressure =  $1.0 \times 10^{-2}$  mbar and low continuous power (65W) ..... 168
- Figure 5-20 XPS spectra together with oxygen to carbon atomic ratios (O/C) of untreated and O<sub>2</sub> plasma-treated SF, the plasma conditions were at highest O<sub>2</sub> flow (49 sccm), maximum pressure ( $1.0 \times 10^{-2}$  mbar), and extremely low power (10W) ..... 170
- Figure 5-21 XPS spectra together with oxygen to carbon atomic ratios (O/C) of both Thai silk fibroin (a, c, e) and Japanese silk fibroin (b, d, f): untreated (a & b), O<sub>2</sub> plasma-treated SF before rinsing with DI (c & d), and O<sub>2</sub> plasma-treated SF after rinsing with DI (e & f) (O<sub>2</sub> flow 40 sccm, pressure  $7.2 \times 10^{-3}$  mbar, power 250 W, duty cycle (on/off) 1/1 ms)..... 172
- Figure 5-22 XPS spectra together with oxygen to carbon atomic ratios (O/C) of untreated and Ar plasma-treated SF, plasma conditions were argon flow 40 sccm (pressure =  $6.9 \times 10^{-3}$  mbar), left panel: power 120 W, duty cycle (on/off) 1/0 ms and right bottom-three panels: power 500 W, duty cycle (on/off) 1/9 ms (Note: all plasma-treated samples were rinsed with DI before XPS measurement)..... 175
- Figure 5-23 XPS spectra together with oxygen to carbon atomic ratio (O/C) of Ar/O<sub>2</sub> plasma-treated SF (Ar flow 36 sccm, O<sub>2</sub> flow 4 sccm, pressure =  $7.2 \times 10^{-3}$  mbar, power 500 W, duty cycle (on/off) 1/9 ms (Note: all plasma-treated samples were rinsed with DI before XPS measurement) ..... 177

- Figure 5-24 XPS spectra together with oxygen to carbon atomic ratios (O/C) of Ar/O<sub>2</sub> plasma-treated SF (Ar flow 30 sccm, O<sub>2</sub> flow 49 sccm, pressure =  $3.3 \times 10^{-2}$  mbar, power 10 W, duty cycle (on/off) 1/0 ms (Note: all plasma-treated samples were rinsed with DI before XPS measurement) ..... 179
- Figure 5-25 XPS spectra together with nitrogen to carbon atomic ratio (N/C) of NH<sub>3</sub> plasma-treated SF (NH<sub>3</sub> flow 20 sccm, pressure =  $8.0 \times 10^{-3}$  mbar, power 200 W, duty cycle (on/off) 1/1 ms with the installation of sample shield to prevent direct bombardment from the high energy plasma ions ..... 182
- Figure 5-26 Streaming current to pressure gradient and apparent zeta potential of silk fibroin surface before and after plasma treatment with various plasma gases (O<sub>2</sub>, Ar/O<sub>2</sub>, and NH<sub>3</sub>) ..... 183
- Figure 5-27 a) FTIR spectra of untreated SF before/after  $\beta$ -sheet induction with methanol and 30 s O<sub>2</sub> plasma-treated SF at amide I ( $1600 - 1715 \text{ cm}^{-1}$ ) and Fourier self deconvolution along with peak fitting of b) the untreated SF before  $\beta$ -sheet induction with methanol, c) the untreated SF after  $\beta$ -sheet induction with methanol, and d) 30 s O<sub>2</sub> plasma-treated SF where B:  $\beta$ -sheet, T:  $\beta$ -turn, A:  $\alpha$ -helix, R: random coil, and SC: tyrosine side chain ..... 190
- Figure 5-28 Apparent zeta potential versus pH value of both untreated and 30 s O<sub>2</sub> plasma-treated SF surfaces for 1 mM KCl solution ..... 191
- Figure 5-29 AFM surface topography of : a) untreated SF, b) 5 s O<sub>2</sub> plasma-treated SF, c) 15 s O<sub>2</sub> plasma-treated SF, d) 30 s O<sub>2</sub> plasma-treated SF, and e) 45 s O<sub>2</sub> plasma-treated SF in 1) air and 2) in PBS..... 193
- Figure 5-30 Adsorbed fibronectin on the surfaces of untreated and O<sub>2</sub> plasma-treated SF by QCM-D (the adsorbed mass was estimated by Sauerbrey equation after the stabilization of QCM frequency change ( $\Delta f$ ) and dissipation (D)) (\*)

represents significant difference between the untreated SF and O<sub>2</sub> plasma-treated SF before and after rinsing with PBS)..... 196

Figure 5-31 L929 mouse fibroblast cultured on the surface of : a) untreated SF, b) 5 s O<sub>2</sub> plasma-treated SF, and c) 30 s O<sub>2</sub> plasma-treated SF after various cultivation time: 1) 2 h, 2) 6 h, and 3) 1 d (scale bar = 100 micron)..... 197

Figure 5-32 Human mesenchymal stem cell (hMSC) cultured on the surface of : a) untreated SF, b) 5 s O<sub>2</sub> plasma-treated SF, and c) 30 s O<sub>2</sub> plasma-treated SF after various cultivation time: 1) 2 h, 2) 6 h, and 3) 1 d (scale bar = 100 micron) ..... 198

Figure 5-33 Immunocytochemical staining of adhered cells: 1) L929 mouse fibroblast and 2) Human mesenchymal stem cell (hMSC) on the surface of: a) untreated SF, b) 5 s O<sub>2</sub> plasma-treated SF, and c) 30 s O<sub>2</sub> plasma-treated SF after 1 day of cultivation. Paxillin, one of focal adhesive proteins, is shown in green, F-actin stressed fibers are in red (Phalloidin), and the nuclei are in blue (Hoechst33342) (scale bar = 50 micron)..... 199

## LIST OF ABBREVIATIONS

$A_0$	The surface area of the Langmuir probe
AA	Acrylic acid
AC	Alternating current
AC 50 Hz	Alternating current power supply at 50 Hz frequency
ADSA	Axisymmetric drop shape analysis
AFM	Atomic force microscopy
AJs	Adherens junctions
Ala	Alanine
ALP	Alkaline phosphatase enzyme
APTES	Amino-propyltriethoxysilane
Arg	Arginine
Asn	Asparagine
Asp	D-aspartic acid
ATR	Attenuated total reflection
ATM	Atmospheric pressure
bFGF	Basic fibroblast growth factor
BOPP	Biaxially oriented polypropylene
BSA	Bovine Serum Albumin
BSP	Bone siloprotein
CBD	Cell binding domain
CCD	Charge couple device
Cys	Cysteine
d	Day
DARCE <sup>TM</sup>	Diode Array Rotating Compensator Ellipsometer
DC	Direct current

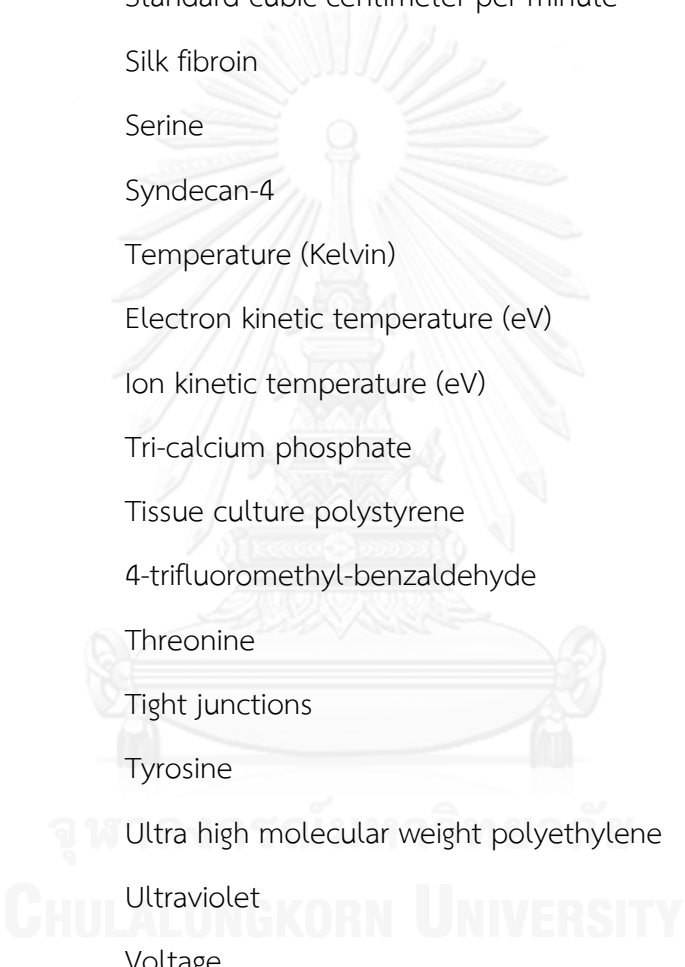
DI	Deionized water
DMEM	Dulbecco's modified eagle medium
DMSO	Dimethylsulfoxide
e	Electron charge
ECM	Extra-cellular matrix
ECR	Electron cyclotron resonance
EDC	1-Ethyl-3-(3-dimethylaminopropyl)carbodiimide
EDTA	Ethylene diamine tetraacetic acid
eV	Electron volt
FA	Focal Adhesion
FAK	Focal adhesion kinase
FB	Fibrillar Adhesion
FBS	Fetal bovine serum
FCX	Focal Complex
FEP	poly(tetrafluoroethylene-co-hexafluoropropylene)
FN	Fibronectin
FSD	Fourier self-deconvolution
FTIR	Fourier transform infrared spectroscopy
FTIR-ATR	Fourier transform infrared attenuated total reflection spectroscopy
FWHM	Full width at half maximum
Gly	Glycine
Glu	Glutamic acid
GPa	Giga-Pascal
GSA	Goat serum albumin
h	Hour
HA	Hydroxyapatite



HBD	Heparin binding domain
H-chain	Heavy chain of silk fibroin
HEMA	(2) 2-hydroxyethyl methacrylate
HFIP	Hexafluoroisopropanol
hFOB	Immortalized human fetal osteoblastic cell line
His	Histidine
HSA	Human serum albumin
hMSC	Human bone marrow derived stem cell
HUVEC	Human umbilical vein endothelial cell
$I_{es}$	Electron saturation current
$I_{is}$	Ion saturation current
IEP	Isoelectric point
IgG	Immunoglobulin G
IPA	isopropyl alcohol
IPF	Institute of Polymer Research Dresden, Germany
IRE	Internal reflection element
$I_r$	Background spectrum
$I_s$	Sample spectrum
Ile	Iso leucine
I-V charge	Voltage-current characteristics
K	Boltzmann constant (J/K)
L02	L02 human hepatocyte
L929	L929 mouse fibroblast cell line
L-chain	Light chain of silk fibroin
Leu	Leucine
Lys	Lysine
M	Ion mass

MCT	Mercury cadmium telluride
MeOH	Methanol
Met	Methionine
MG-63	MG-63osteosarcoma cell line
min	Minute
MMP	Matrix metalloproteinase
MSC	Mesenchymal stem cell
MTT	3-(4,5-dimethylthiazol-2-yl)-2,5-diphenyltetrazolium bromide
$n_0$	Number of particles (molecules/m <sup>3</sup> )
$n_e$	Electron number density (electrons/m <sup>3</sup> )
N/C	Atomic nitrogen to carbon ratio
NHS	N-Hydroxysuccinimide
O/C	Atomic ratio of oxygen to carbon
OC	Osteocalcin
OCT-1	OCT-1 osteoblast-like cell
OES	Optical emission spectroscopy
OCN	Osteocalcin
ON	Osteonectin
OP	Osteopontin
P	Pressure (Pa)
Pa	Pascal
PA	polyacrylamide
PAAc	poly(acrylic acid)
PBS	Phosphate buffer solution
PCVD	Plasma chemical vapor deposition
PDMS	Polydimethylsiloxane
PE	Polyethylene

PEEK-WC-PU	Modified polyether-ether-ketone with cardo group
PEG	Polyethylene glycol
PEI	poly(ethylene imine)
PEMAc	poly(ethylene-alt-maleic acid)
PEO	poly(ethylene oxide)
PET	Polyethylene terephthalate
PFA	Paraformaldehyde
PHB	Poly(hydroxybutyrate)
Phe	Phenyl allanine
pI	Isoelectric point
PGA	Polyglycolic acid
PLGA	Poly-d,l-lactic-co-glycolic acid
PLLA	Poly-l-lactic acid
poly(HEMA)	poly(2-hydroxyethyl methacrylate)
polyMPTS	Poly methacryloxypropyl trimethoxysilane
PP	Polypropylene
Pro	Proline
PS	Polystyrene
PSS	anionic poly (sodium 4-styrene sulfonate)
PTFE	Polytetrafluoroethylene
PU	Polyurethane
PVMEMAc	poly(vinyl methyl ether-alt-maleic acid)
QCM	Quartz crystal microbalance
QCM-D	Quartz crystal microbalance with dissipation monitoring
RF	Radio frequency
R.I.	refractive index
RLC-18	Rat embryonic liver (E-17) cell line



RMS	Root mean square
RPMI 1640	Roswell Park Memorial Institute 1640 Medium
RT	Room temperature
s	second
SBB	Corn starch-based biomaterial
sccm	Standard cubic centimeter per minute
SF	Silk fibroin
Ser	Serine
Syn4	Syndecan-4
T	Temperature (Kelvin)
T <sub>e</sub>	Electron kinetic temperature (eV)
T <sub>v</sub>	Ion kinetic temperature (eV)
TCP	Tri-calcium phosphate
TCPS	Tissue culture polystyrene
TFBA	4-trifluoromethyl-benzaldehyde
Thr	Threonine
TJs	Tight junctions
Tyr	Tyrosine
UHWPE	Ultra high molecular weight polyethylene
UV	Ultraviolet
V	Voltage
V <sub>B</sub>	Break-down voltage
Val	Valine
VN	Vitronectin
V <sub>p</sub>	Plasma potential
VP	1-vinyl-2-pyrrolidone
W	Watt

XPS

X-ray photoelectron spectroscopy

 $\lambda_d$ 

Debye shielding length



จุฬาลงกรณ์มหาวิทยาลัย  
CHULALONGKORN UNIVERSITY

## LIST OF PUBLICATIONS

The following is a list of published, accepted, or submitted manuscripts which have been incorporated into this thesis.

- Colloids and Surfaces B: Biointerfaces [IF(2012)=3.554]: published, 2013; 111: 579-86.
- Plasma Processes and Polymers [IF(2012)=3.730]: accepted (Apr13, 2014)

Also, some parts of this work were accepted for oral and poster presentations as follows:

- German-Thai Symposium on Nanoscience and Nanotechnology 2011 (GTSNN2011), Synchrotron Light Research Institute, Nakorn Ratchasima, Thailand, 13-16 September 2011
- 9th World Biomaterials Congress, Chengdu, People republic of China, 1-5 June 2012
- 8th Asia-Oceania Top University League on Engineering (AOTULE) meeting and conference, Bangkok, Thailand, 17-19 October 2013

## CHAPTER

### 1. INTRODUCTION

#### 1.1 Background

The multidisciplinary science of tissue engineering has been developed to address the issues of transplanted organ shortage and growing demand for tissue repair or replacement. Tissue engineering principles are based on three key components: the use of proper cell types, the use of a scaffold for homing cells to attach and grow, and the use of signaling molecules, such as growth factors, for the induction of cells to differentiate to desirable tissues [1-3]. Material engineering has a great role to play in tissue engineering field especially in the scaffold part. The focus of material scientists could be scaffold material, fabrication technique, or surface modification. However, it is difficult to deliver the material which has combined excellent physical and biological properties. The surface modification addresses this issue by improving the biological properties on the surface of materials which have superb physical properties but poor biocompatibility.

Silk fibroin (SF), a promising material for tissue engineering scaffolds, is biocompatible, biodegradable and mechanically strong. These favorable properties allow researchers to explore SF application in biomedical fields, such as a scaffold for bone tissue engineering [4-9], a carrier for controlled drug release [10, 11], and wound healing mat [12, 13]. SF properties could be enhanced by blending or using with other materials such as gelatin [4-6, 8-12], chitosan/chito-oligosaccharide [5, 7, 9], hydroxyapatite [6], human bone [8], or bee/shellac/carnauba waxes [13]. These material systems could be achieved with chemical crosslinking with either EDC/NHS

[6-8, 10, 11, 14] or glutaraldehyde [5, 9, 12, 14], electrostatic blending [4], or simple coating[13]. However, chemical crosslinking also raises the issue of toxicity, i.e. glutaraldehyde could induce crosslinking between DNA and protein, resulting in genotoxic and mutagenic threat [15, 16].

Plasma surface functionalization could be an alternative to chemical crosslinking. Plasma treatment offers highly energetic active species which are ready for surface reaction. This reaction is very quick, and leaves no trace chemicals. This process also does not alter the mechanical properties of material, because it reacts only with the surface layers of the material. Plasma treatment has been used to modify surface of various materials in biomedical applications. The treatment induces the change of surface wettability, introduces selective functional groups, and changes electrostatic charges of the surface. The treated surface could be ready for use or further treated to immobilize other bioactive molecules such as basic fibroblast growth factor [17], collagen [18], cationized gelatin [19], heparin [20], *etc.*

Beside plasma surface functionalization, plasma treatment could be used to etch the surface. Plasma etching could provide a similar surface chemistry if oxygen plasma is employed with hydrocarbon surface and the treatment conditions are optimized to achieve the perfect oxidation reaction [21]. Other properties related to surface chemistry such as surface charge, and surface wettability would be affected minimally. Moreover, plasma treatment affects only few nanometers depth from the surface [22]. This means the bulk properties (e.g. degree of crystallinity, swelling ratio, optical properties, etc.) should be similar to the untreated surface. In addition, plasma etching could alter surface stiffness through crosslinking process by UV radiation, a common side effect from plasma etching [21].

Few investigators have explored the plasma treatment on silk fibroin surface. There have been two reports of using microwave argon plasma to treat silk fibroin surfaces in Biomaterials in the past 10 years. Both reports aimed to enhance



biocompatibility and chondrogenic responses of articular chondrocytes on silk fibroin surface [23, 24]. Regarding plasma power supplies, radio frequency source at the frequency of 13.56 MHz has been employed for generating plasma treatment by many investigators [17, 19, 20, 25-40] whereas the AC power supply have less frequently been explored [41-43]. In our group, we have successfully used it for treating crosslinked gelatin surface [42, 43].

Many researchers have been trying to explain the role of surface properties in improving the biological responses on the plasma-treated surface. The investigations have focused on surface wettability [17, 19, 20, 22, 24, 27, 30-34, 38, 40, 42-48], surface chemistry [17, 19, 20, 26, 27, 34-38, 40, 42, 45-49] and surface topography [17, 24, 31, 35, 37, 42-47]. However, a few important properties of plasma-treated materials had not been thoroughly investigated, especially swelling properties, protein adsorption, and surface stiffness. These properties play important role in cell-substrate interaction. The swelling measurement of material could be used as an indicator of how well hydrated the material is once it was brought to contact with fluid. Hydration process is a truly first step and happens before any other processes in cell-substrate interaction [50, 51]. Protein adsorption happens right after the material hydration process and has biological effects on cell-substrate interaction [50, 52, 53]. However few researchers have paid attentions to study protein adsorption on plasma-treated materials [17, 31, 47, 54]. Surface stiffness plays an important role in cell fate such as adhesion [55] or phenotype expression in case of mesenchymal stem cell (MSC) [56]. Cells sense the surface stiffness through adhesion sites; this mechanosensation gives a signal for reinforcement adhesion and growth, or disassembly of focal adhesion if the surface is either too soft or too stiff [55].

In this study, the preliminary investigations were conducted to evaluate whether plasma treatment could improve the biocompatibility of silk fibroin surface. The glow discharge plasma was generated by an in-house AC 50Hz power supply.

Nitrogen was used as a plasma gas because it could induce nitrogen species such as amine on surfaces. Amine has been reported to improve cell adhesion on material surfaces [48, 57]. The plasma operating conditions were optimized by maximizing nitrogen active species. Both untreated and plasma-treated surfaces were characterized in terms of wettability by water contact angle, surface chemistry, bulk chemistry, and surface topography. L929 mouse fibroblast was employed in cell culture tests. Early cell adhesion was evaluated by MTT assay along with F-actin cytoskeleton development.

An in-depth investigation was conducted later to gain a better understanding of the plasma treated effects on silk fibroin properties. A well-defined planar surface was prepared as a thin film to meet the requirements of all analytical techniques. This enables a consistent result interpretation. The characterization of untreated and plasma-treated materials covered surface chemistry, degree of crystallization, surface charge, swelling ratio together with optical properties, surface wettability, surface modulus, and protein adsorption. The effect of surface stiffness on cell-substrate interaction was then explored using two different cell types: L929 mouse fibroblast and human mesenchymal stem cell (hMSC), based on their residing on different microenvironment, which differs in matrix stiffness. The cell studies focused on cell adhesion behaviors by evaluating stress fiber and focal adhesion formation.

## 1.2 Objectives

1. To evaluate the biocompatibility of plasma-treated Thai silk fibroin surfaces using relevant biological response tests such as cell adhesion and cytoskeleton development.

2. To gain a comprehensive understanding of silk fibroin properties such as surface chemistry, degree of crystallinity, surface charge, swelling degree, optical property, surface wettability, surface modulus and surface topography before and after plasma treatment using a well-defined planar silk fibroin surface.
3. To investigate the effect of different surface stiffness of silk fibroin on cell-substrate interaction.

### **1.3 Scopes of Research**

Part I – A preliminary study of plasma treatment on Thai silk fibroin surface (Chapter 5)

1. The setup of plasma machine using AC50Hz power supply for treating Thai silk fibroin surfaces.
  - 1.1. Nitrogen was used mainly to generate reactive species for plasma treatment.
  - 1.2. The plasma-generated reactive species were measured by optical emission spectroscopy (OES) for selecting the suitable plasma operating conditions such as plasma pressure, input power, electrode gap, etc.
2. The untreated and plasma-treated Thai silk fibroin surfaces were characterized as follows:
  - 2.1. Surface wettability by static water contact angle measurement
  - 2.2. Surface chemistry by X-ray photoelectron spectroscopy (XPS)

2.3. Bulk chemistry by Fourier transform infrared attenuated total reflection spectroscopy (FTIR-ATR)<sup>1</sup>

2.4. Surface topography by atomic force microscopy (AFM)

3. *In vitro* biological response tests of plasma treated Thai silk fibroin surfaces using L929 mouse fibroblast.

3.1. Cell early adhesion and proliferation by MTT assays

3.2. The cytoskeleton development study by F-actin staining



---

<sup>1</sup> FTIR-ATR could be used to detect the change of bulk chemistry of silk fibroin after plasma treatment because it could go down to several microns of sample depth [22], while plasma treatment affects only few nanometer scales of outermost layer [23, 126].

## Part II – An in-depth investigation of plasma treatment on Thai silk fibroin surface (Chapter 6)

1. Comprehensive characterization of untreated Thai silk fibroin surfaces was conducted as follows:
  - 1.1. Surface chemistry by X-ray photoelectron spectroscopy (XPS)
  - 1.2. Degree of crystallinity by Fourier transform infrared attenuated total reflection spectroscopy (FTIR-ATR) together with Fourier self-deconvolution (FSD) along with peak fitting of amide I region
  - 1.3. Surface charge by streaming potential
  - 1.4. Swelling ratio and optical property (i.e. refractive index) by spectroscopic ellipsometry
  - 1.5. Surface topography by atomic force microscopy (AFM)
  - 1.6. Surface elastic modulus by atomic force microscopy (AFM) based nano-indentation.
2. The setup of plasma machine using microwave power supply for treating Thai silk fibroin surfaces.
  - 2.1. Oxygen, argon, carbon dioxide, and ammonia were used to generate reactive species for plasma treatment.
  - 2.2. The plasma operating conditions were optimized for the induction of desirable functional groups on plasma-treated silk fibroin surface by using X-ray photoelectron spectroscopy (XPS).

3. The effect of surface stiffness on cell-substrate interaction was studied by using oxygen plasma etching.
  - 3.1. Both untreated and plasma-treated silk fibroin films were characterized by following techniques.
    - 3.1.1. Surface chemistry by X-ray photoelectron spectroscopy (XPS)
    - 3.1.2. Surface wettability by dynamic water contact angle using captive air bubbles in conjunction with axisymmetric drop shape analysis (ADSA)
    - 3.1.3. Degree of crystallinity by Fourier transform infrared attenuated total reflection spectroscopy (FTIR-ATR) together with Fourier self-deconvolution (FSD) along with peak fitting of amide I region
    - 3.1.4. Surface topography by atomic force microscopy (AFM)
    - 3.1.5. Surface elastic modulus by atomic force microscopy (AFM) based nano-indentation.
    - 3.1.6. Fibronectin adsorption by quartz crystal microbalance (QCM)
  - 3.2. *In vitro* cell culture tests were conducted using two different cell types: L929 mouse fibroblasts and human mesenchymal stem cells (hMSC). The cell studies focused on cell adhesion behaviors by using following techniques
    - 3.2.1. Adhesion study by using optical microscopy
    - 3.2.2. Cytoskeleton development by evaluating stress fiber and focal adhesion formation using confocal laser scanning microscopy.

#### 1.4 The publication details relating to the research objectives

##### 1. The biocompatibility of plasma-treated Thai silk fibroin surfaces

The outcome from the first objective was published as a research paper entitled “Improvement of early cell adhesion on Thai silk fibroin surface by low energy plasma” in *Colloids and Surfaces B: Biointerfaces* journal and was described in the chapter 4 of this thesis.

The study was conducted to investigate whether plasma treatment could improve the biocompatibility of silk fibroin surface. Low energy plasma in this article was generated by AC50Hz power supply.

##### 2. An comprehensive understanding of silk fibroin properties

This outcome of the second objective was summarized as a research paper entitled “A comprehensive characterization of silk fibroin – Towards multi-technique studies of surface modification effects” planned for submission to the journal and was described in the chapter 5 (section 5.3 and 5.4) of this thesis.

The study was conducted after the successful proving that plasma could improve the biocompatibility of Thai silk fibroin. The study began with developing a well-defined planar silk fibroin surface, prepared as a thin film which met all analytical requirements and had a similar surface chemistry to the theoretical molecular structure of silk fibroin. This approach allowed a consistent interpretation of all characterization results and enabled to gain a better understanding of plasma-treated effects.

3. The effect of silk fibroin surface stiffness on cell-substrate interaction.

This outcome of the third objective was summarized as a research paper entitled “Oxygen plasma etching of silk fibroin alters surface stiffness: A cell-substrate interaction study” which was accepted for publication in Plasma Processes and Polymers journal and was described in the chapter 5 (section 5.3 and 5.6) of this thesis.

This study highlighted the important plasma-treated effect on silk fibroin surface. An in-depth investigation revealed that plasma etching was more prominent than plasma surface functionalization on silk fibroin surface. Plasma etching of silk fibroin increased elastic modulus on silk fibroin surfaces, while other properties of plasma-treated surface were similar to the untreated surface properties. This finding provided a perfect foundation for studying the effects of surface stiffness on cell-substrate interaction.



## CHAPTER

### 2. RELEVANT THEORY

#### 2.1 Plasma

##### 2.1.1 *Definition*

In a nutshell, plasma is ionized gas. It was also defined as the fourth state of matter by Sir William Crooks in 1879, but this fourth state of matter was named “plasma” later by Irving Langmuir in 1928. When the energy keeps adding into gas (the third state of matter), the gas atoms start to collide with each other and eventually break apart into electrons and charged ions. The transition from weakly ionized gas into the plasma state happens when the ionized gas develops unique properties, such as when it is electrically quasi-neutral, and capable of responding to electric and magnetic fields [58, 59].

##### 2.1.2 *Particle collision*

In plasma, there are many collisions which involve electrons, ions and neutral atoms. The interactions are not only between these particles but also involving other things which surround the plasma, such as electrodes and plasma chambers. All important collisions are listed in Table 2.1 [60].

Table 2-1 The list of important collisions in plasma

Reaction	Collision type
<i>Electron</i>	
$e + A \rightarrow e + A$	Elastic scattering
$e + A \rightarrow e + A^* \rightarrow e + A + h\nu$	Excitation
$e + A \rightarrow A^+ + 2e$	Ionization
$e + A^* + B \rightarrow 2e + A + B^+$	Penning ionization
$e + AB \rightarrow 2e + A^+ + B$	Dissociative ionization
$e + AB \rightarrow A^- + B$	Dissociative Attachment
$e + A^+ + B \rightarrow A + B$	Recombination
<i>Ions</i>	
$A^+ + B \rightarrow A + B^+$	Charge exchange
$A^+ + B \rightarrow A^+ + B$	Elastic scattering
$A^+ + B \rightarrow A^+ + B^* \rightarrow A^+ + B + h\nu$	Excitation
$A^+ + B \rightarrow A^+ + B^+ + e$	Ionization
$A^+ + BC \rightarrow A^+ + B + C$	Dissociative ionization
$e + A^+ + B \rightarrow A + B$	Recombination
$A + BC \rightarrow C + AB$	Chemical reaction

### 2.1.3 Motion of charges in electric and magnetic fields

One of the unique aspects of plasma is its response to electric and magnetic fields. In electric fields, electrons will move towards positive polarity, and conversely, positive charged ions towards negative polarity. In magnetic fields, electrons will spin counter-clockwise perpendicular to the direction of the magnetic field while the positive charged ions clockwise [61]. Both electric and magnetic fields are used to manipulate charged particle movement in plasma.

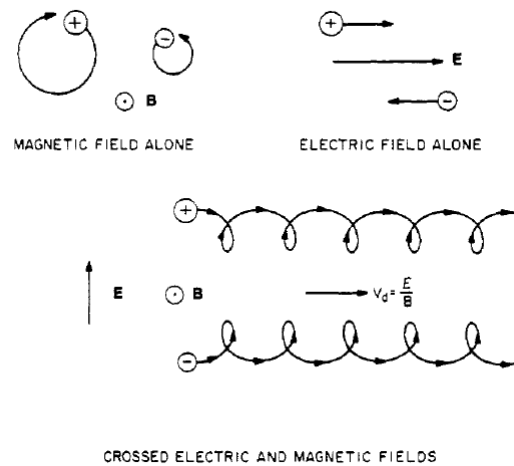


Figure 2-1 The motion of positive and negative charges in electric, magnetic, or cross fields

The top two diagrams illustrate the motion of positive and negative charges in electric and magnetic fields. The lower diagram shows crossed electric and magnetic fields. The magnetic induction points out of the plane of the diagram. The electric field points vertically upwards (reproduced from [61])

#### 2.1.4 Plasma generation methods

[58, 59, 62-67]

Plasma is typically generated by imposing electric fields on gas or applying high frequency waves to the gas. Electric fields or high frequency waves will knock off electrons from the plasma gas. The knocked off electrons will participate in electron-atom collision. This cascading process will generate more electrons and charged ions. However, these generated electrons could be consumed by the charged ions. The consequence of this recombination process will release the excess energy as photons. Both electron generation and the ion recombination process will continue until an equilibrium between charged ions and electrons is reached.

There are many types of reactors which are used to generate plasma. Most of them could be grouped by their power sources; direct current (DC), alternating current (AC), radio frequency (RF), and microwave (MW). The power frequency starts from power line frequencies (50/60 Hz) to the whole

of the electromagnetic spectrum (1 kHz - 10 GHz). In summary, plasma reactors could fall into these following categories.

- 1) DC electrical discharge plasma
- 2) AC electrical discharge plasma
- 3) RF (radio frequency) electrical discharge plasma
  - a. Inductive RF electrical discharge plasma
  - b. Capacitive RF electrical discharge plasma
- 4) Microwave electrical discharge plasma

Each type of plasma reactor has different advantages. The DC and AC power systems offer the cheapest power supply costs, but they could not generate high energy plasma. The RF power sources are much more expensive and complex. However, they deliver higher plasma energy and efficiency. The distinct advantage of RF power is that it generates plasma by displacement currents, not real currents. Hence, RF electrodes could be designed outside of the plasma chamber. The important consequence is the elimination of potentially serious contamination from electrodes in certain applications. The plasma chamber could also operate with lower vacuum conditions, because there are no electrodes penetrating into the plasma chamber.

#### ***2.1.4.1 DC electrical discharge plasma***

The DC electrical discharge plasma is generated by applying electric fields inside the gas chamber. The electrons from the cathode will be accelerated by electric fields and collide with atoms, resulting in electrons and charged particles. The knocked off electrons further participate in electron-atom collision since they still have enough energy from the electric field acceleration. This cascading process increases the amount of electrons in the

gap between the cathode and the anode [62-64]. The configuration of the DC electrical discharge plasma is illustrated in Figure 2.2

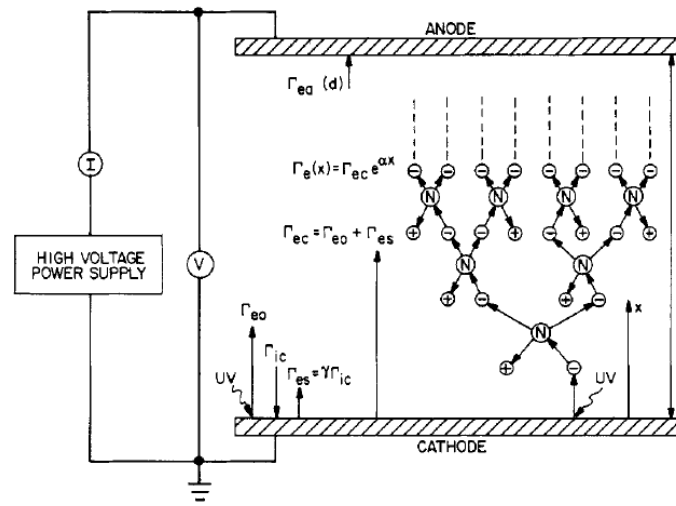


Figure 2-2 The configuration of DC electrical discharge plasma  
(reproduced from [63])

To better understand the DC electrical discharge plasma, voltage-current characteristics (I-V chart) and break-down voltage ( $V_B$ ) need to be discussed.

### Voltage-Current Characteristic

According to the voltage-current chart of a DC low pressure electrical discharge, shown in Figure 2.3, the DC electrical discharge is divided into three regions; dark discharge, glow discharge, and arc discharge.

#### Dark discharge regions (A-E) [62, 63]

##### *Background ionization (A-B):*

At very low voltage, ions and electrons are generated by background radiation, not from tiny electric fields. Examples of surrounding radiation are cosmic rays, radioactive minerals, etc.

##### *Saturation regime (B-C):*

If the voltage between the electrodes is increased far enough, eventually all the available ions and electrons produced from the

background ionization will be collected at the electrodes. At this stage, the electrons do not have sufficient energy to create additional ionization, so the current remains constant even with an increase of voltage. This is called 'current saturation regime'.

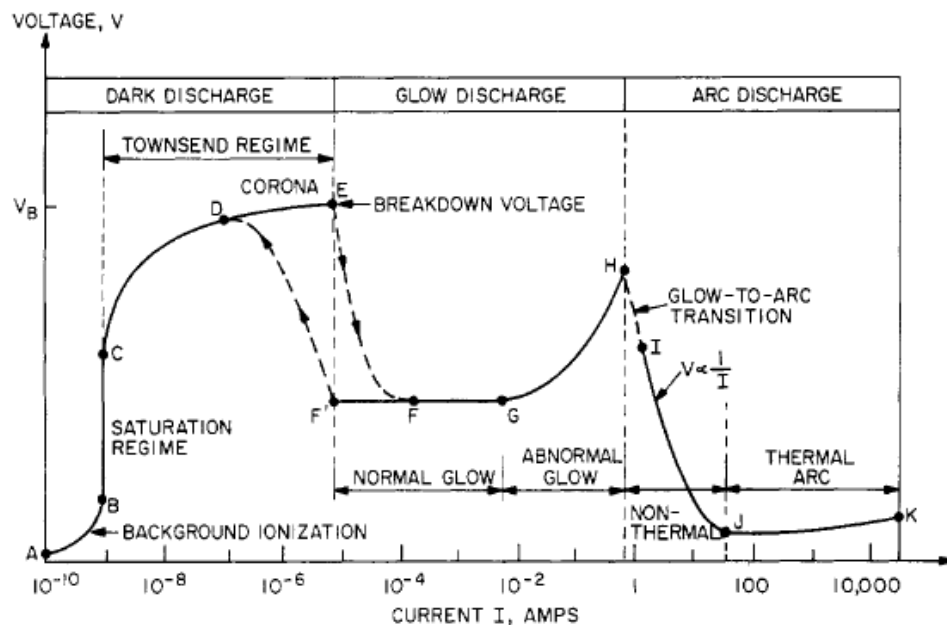


Figure 2-3 Voltage-current characteristics of the DC low pressure electrical discharge plasma (reproduced from [62])

#### *Townsend regime (C-E):*

In the Townsend regime, the electrons have sufficient energy from the increased electric field to participate in electron-atom collision, resulting in much higher number of electrons. This results in a very rapid, exponentially increased current as a function of the voltage.

#### *Corona discharge (D-E):*

At this stage, there are accumulations of locally strong electric fields at sharp points or edges on the surface of the electrodes. These electric fields exceed the breakdown strength of the surrounding neutral gas. This point signifies the corona discharge and it is visible to the naked eye. When

the voltage is increased to the breakdown voltage ( $V_B$ ), electrical breakdown will occur.

#### Glow discharge regions (E-H) [62, 64]

##### *Normal glow discharge (E-G):*

When electrical breakdown happens at point E (as illustrated above), the discharge has high enough current and neutral background gas excitation to make the plasma visible to the naked eye. This regime is called 'glow discharge'. After the transition to point F, the voltage remains constant despite an increase in current. This makes the plasma covered the whole cathode surface at point G.

If the current is reversed at point F, the process retracts to point F', instead of moving to point E. It then makes the transition back to the Townsend regime, without passing to the corona discharge.

##### *Abnormal glow discharge (G-H):*

At point G, the voltage increases again as a function of the current.

#### Arc discharge regions (H-K) [62]

##### *Non-thermal arc discharge (H-I):*

At point H, the current density of the cathode is high enough to heat it and emit visible light. It causes a disruptive glow-to-arc transition at point I. The voltage drops while the current increases. This voltage drop is called 'non-thermal arc discharge'.

##### *Thermal arc discharge (J-K):*

Thereafter, thermal arc discharge occurs when the voltage increases as a function of the current.

### Electrical breakdown [63]

This electrical breakdown is an important parameter which needs an awareness of all plasma operations, both to achieve it, or not to reach it, depending on applications. In DC direct discharge as in parallel plate plasma reactor, the breakdown voltage depends only on the product of pressure and electrode gap ( $pd$ ) (a discovery by Friedrich Paschen (1865-1947)). The breakdown voltage ( $V_b$ ) is estimated by following equation used to develop the universal Paschen curve.

$$V_b = V_{b,min} * \frac{\frac{pd}{pd_{min}}}{1 + \ln\left(\frac{pd}{pd_{min}}\right)} \quad (2.1)$$

Where  $V_{b,min}$  is the minimal breakdown voltage constant in volt (Nitrogen: 275 volt, Dry air: 360 volt, Oxygen: 450 volt)

and  $pd_{min}$  is the minimal  $pd$  in torr.cm

(Nitrogen: 0.75 torr.cm, Dry air: 0.57 torr.cm, Oxygen: 0.7 torr.cm)

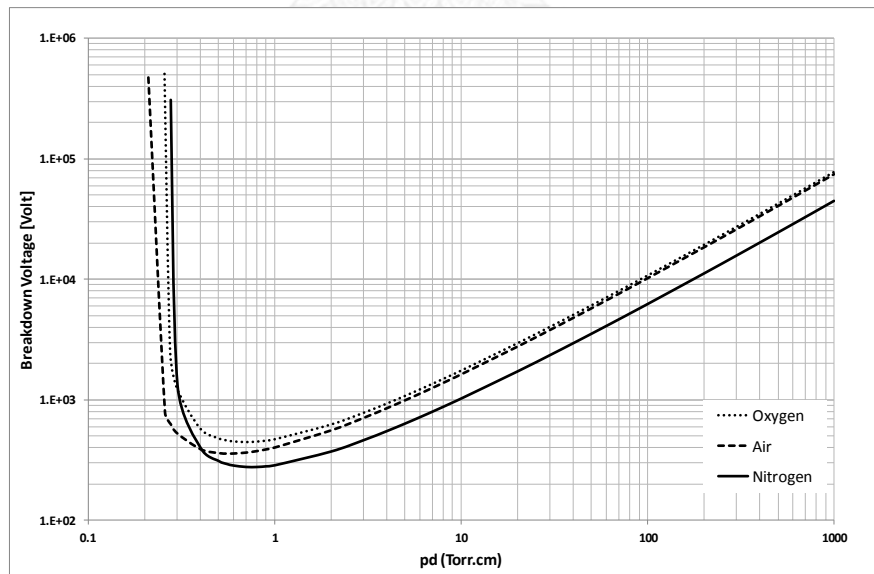


Figure 2-4 Universal Paschen curve for selected gasses



### 2.1.4.2 AC electrical discharge plasma

This low frequency AC electrical discharge (50/60Hz) does not behave differently from the DC electrical discharge, in term of plasma phenomena and theories. The timescale of power frequency change is much longer than any in the physical plasma process. The only difference from DC electrical discharge is that AC anode and cathode will alternate with the power frequency [65].

### 2.1.4.3 RF (radio frequency) power plasma

[65-67]

Radio frequency power generates plasma from an oscillating magnetic field by inductive coupling, an oscillating electric field by capacitive coupling. The high frequency RF waves induce displacement current, rather than real current, so electrodes could be placed outside of the plasma chamber.

#### 2.1.4.3.1 Inductive RF electrical discharge plasma

The principle of inductive RF electrical discharge plasma is an induction coil which wraps around or is above the plasma chamber and has running RF power. The typical configuration is illustrated in Figure 2.5 [65].

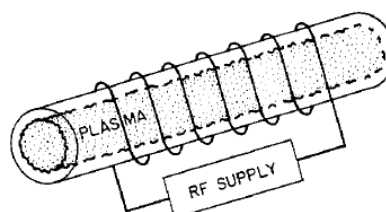


Figure 2-5 The typical configuration of RF inductive coupled plasma  
(reproduced from [65])

The applied inductive couple RF frequencies are ranged from around 10 kHz to 30 MHz. The plasma chamber is operated normally between a few torr to

a few hundred torr<sup>2</sup>. However, there might be other applications which operate outside the above conditions e.g. operating near atmospheric pressure or higher frequency. The use of inductive couple RF plasma is less frequent than other types of plasma, but it plays an important role for certain applications, such as plasma torch.

#### 2.1.4.3.2 Capacitive RF electrical discharge plasma

Capacitive coupled RF plasma is generated by imposing high frequency oscillating electric fields into a neutral gas. The frequency in typical applications is from 1 to 100 MHz. The configuration is normally parallel plates, which have a grounded electrode to achieve a steady state operation. The contact electrode might have real current but it has little effect on energy transfer to the plasma. In essence, most capacitive RF plasma reactors are not modified by magnetic fields. The configuration of RF coupled plasma reactors is shown in Figure 2.6 [66].

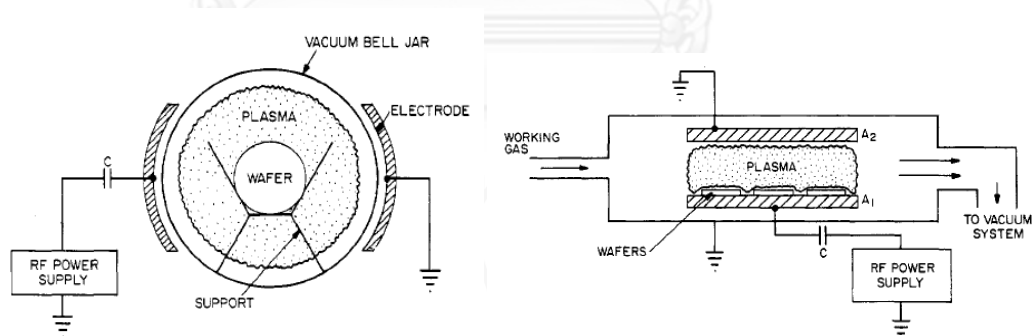


Figure 2-6 The typical configuration of RF capacitive coupled plasma

The left illustrates the non-contact electrode set up, and the right, the contact electrode setup (adapted from [66])

The capacitive RF plasma is widely used in industry. The application could apply to surface treatment, thin film deposition, etching, etc.

<sup>2</sup> 1 torr = 133.332 Pa or 1.33332 mbar

#### 2.1.4.4 Microwave electrical discharge plasma

Microwave frequency (0.3 – 30 GHz) power induces both electric and magnetic fields in plasma gas, resulting in the gas breakdown. Microwave RF power supplies typically deliver higher energy plasma than DC, AC, or low frequency RF power supplies (the electron kinetic temperature is the range of 5 to 15 eV, compared to 1 to 8 eV). The microwave-generated plasma could be operated under stable conditions in the wide range of gas pressure from 10 mTorr to 1 atm. The higher energy microwave-generated plasma, supplies a higher fraction of ionization and dissociation than DC or low frequency RF generated plasma. This provides a significant advantage in chemical surface treatments. The best utilized system of microwave-generated plasma is pictured in Figure 2.7 [67].

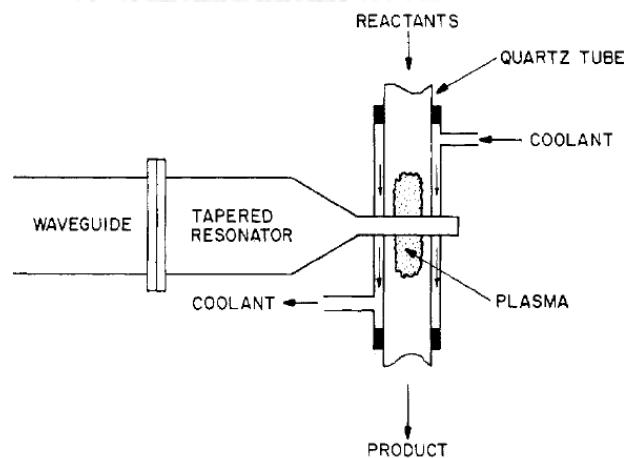


Figure 2-7 The most used system arrangement of microwave-generated plasma  
(reproduced from [67])

The operating conditions of major plasma reactor types are demonstrated in Table 2.2.

Table 2-2 The operating conditions of major types of plasma reactor.

[64, 66, 67]

Parameter	DC glow discharge			Capacitive RF			Microwave		
	Low	Typical	High	Low	Typical	High	Low	Typical	High
Frequency	Not applicable			1kHz	13.56MHz	100MHz	0.3GHz	2.45GHz	30GHz
Gas pressure (Torr)	$10^{-6}$	0.5	760	$10^{-3}$	0.3	5	$2 \times 10^{-5}$		760
Power (W)	$10^{-2}$	200	250,000	50	200	500	200	500	50,000
Electrode voltage (V)	100	1,000	50,000	100	300	1,000		No data	
Number density (electron/m <sup>3</sup> )		No data		$10^{15}$	$5 \times 10^{15}$	$3 \times 10^{17}$	$10^{16}$	$10^{17}$	$5 \times 10^{18}$
Electron kinetic temperature (eV)	1	2	5	3	5	8	5	10	15
Ion energy (eV)		No data		5	50	500	10	30	50

### 2.1.5 Plasma application

[68-73]

Plasma can be used in various applications. It can add or remove adsorbed layers on material surface (surface treatment); it can add thin layers on the surface (thin film deposition); it can inject ions or atoms beneath the surface (ion implantation); and it can partially remove bulk materials (etching).

#### 2.1.5.1 Plasma surface treatment

Plasma can be used to modify surface properties of solid materials by its active species. The interaction might be from chemical reaction, or physical action or surface charge change. Plasma surface treatment only affects the surface properties such as, surface energy, wettability, charge, printability, adhesion, etc. The treatment could also be used for surface cleaning and grafting chemical functional groups on the surface. Normally, low energy plasma is suitable for this application. For DC direct discharge, it operates in

the abnormal glow region. The ion energy could be approaching 1 eV, if the pressure is above 10 torr [69].

#### ***2.1.5.2 Plasma ion implantation***

Ion implantation is the process which injects high energy ions through the atomic structure of material. The ions then place themselves several atomic layers beneath the surface. The ion energy for the implantation process needs to be very high (10-300 keV). The depth of implantation is marginally less than a micron. The applications of ion implantation are in the fields of corrosion, wear resistance, surface electrical, and optical properties. The ion implantation process is complex and involves many types of equipment such as plasma generator, ion extractors, focus lens, accelerator, deflection plates, etc. [70].

#### ***2.1.5.3 Plasma sputtering process for thin film deposition***

Thin film deposition could be done by either plasma sputtering process or plasma chemical vapor deposition (PCVD). Examples of the applications are microelectronic circuit fabrication, optical coatings, recording media, ornamental brightwork, protective coatings, oxygen barrier coated food packaging etc. The film thickness is usually from 0.2 to 10 micron. In this section, only plasma sputtering process will be discussed. The key sputtering parameter is very low vacuum (1 - 50 mTorr), so that sputtered atoms could be delivered to the target with almost no collisions. There are two major types of plasma-assisted sputter deposition; plasma-assisted ion-beam sputter deposition, and plasma/cathode sputter deposition.

For plasma-assisted ion-beam sputter deposition, the ion beam is delivered to the target by external ion source. The collisionless ion beam will

hit the target to generate sputtered atoms for deposition on the work piece. The glow discharge plasma might be present either around the target and/or the work piece. The plasma helps to decontaminate the surface or increase surface energy of the work piece. In the plasma/cathode sputter deposition, the ions are accelerated to sputter the cathode to generate sputtered atoms for deposition. The work piece could be either mounted on the anode, or reside in the plasma [68, 71].

#### **2.1.5.4 Plasma Chemical Vapor Deposition (PCVD)**

[68, 72]

The plasma chemical vapor deposition (PCVD) is heterogeneous chemical reaction which involves working gas, plasma active species, and the surface of work piece. This chemical reaction in PCVD differentiates itself from the purely physical sputter deposition processes. The thin film deposited by PCVD can be divided into polymeric and non-polymeric deposition. The non-polymeric PCVD coatings are normally oxides which could be used as insulating layers, optical coatings, and oxygen barriers for food packaging. The polymeric PCVD thin films are made by the polymerization of monomers which are the plasma-generated active species. The polymeric thin films are normally used as insulating layers in microelectronic chips, as protective coatings, and as reflective or anti-reflective optical coatings. The typical plasma reactors are either an electron cyclotron resonance (ECR), or 13.56 MHz RF capacitive plasma. The pressure is not as low as the sputtering process. It is usually in the range from 100 mTorr to 1 Torr [68, 72].

### 2.1.5.5 Plasma etching

[73]

Plasma etching is a technology essential to microelectronic circuit fabrication. The plasma reactors used in etching are normally RF or microwave glow discharge plasma. It provides the active species necessary for etching such as ions, electrons, free radicals, excited states, molecular fragments, atomic species, and photons. The most active ones are ions. The etched pattern is generated by a mask which has high resistance of etching. The etched layer is typically from one-half to a few microns. The operating vacuum is from 50 mTorr to 1 torr.

### 2.1.6 Plasma characteristic parameters

[60, 62, 74]

The important parameters in plasma characteristics are number of particles ( $n_0$  – molecules/m<sup>3</sup>), plasma potential ( $V_p$ ), electron kinetic temperature ( $T_e'$  – eV), electron number density ( $n_e$  – electrons/m<sup>3</sup>), ion kinetic temperature ( $T_i'$  – eV), and Debye shielding length ( $\lambda_d$ ). From Langmuir probe,  $V_p$ ,  $T_e'$ ,  $T_i'$ , and  $n_e$  could be obtained. Debye shielding length can be calculated from electron kinetics temperature ( $T_e'$ ) and electron number density ( $n_e$ ).

#### 2.1.6.1 Number of particles ( $n_0$ )

The number density in particles per cubic meter ( $n_0$ ) could be calculated by the perfect gas law.

$$p = n_0 k T \quad (2.2)$$

where  $p$  – pressure in pascal (Pa)

$k$  – Boltzman constant =  $1.3806488 \times 10^{-23}$  J/K

$T$  – temperature in Kelvin

### 2.1.6.2 Kinetic temperature in electron volt (T')

An electronvolt (eV) is the kinetic energy that an electron (or a singly-charged ion) which has charge ( $e$ ) of  $1.602 \times 10^{-19}$  C, gains when it is accelerated by electric fields of one volt. The relationship between temperature (K) and the kinetic temperature (T') in electronvolt units (eV) is shown in equation (2.3).

$$kT = eT' \quad (2.3)$$

where

$k$  is Boltzmann's constant =  $1.3806488 \times 10^{-23}$  J/K

$T$  is the temperature in degrees Kelvin

$e$  is the electron charge =  $1.602 \times 10^{-19}$  C

Note: The degree kelvin (K) unit is too small to measure kinetic temperatures in plasmas i.e.1 eV is equivalent to 11,604 K.

### 2.1.6.3 Langmuir probe diagnostics

The Langmuir probe is used for measuring plasma potential ( $V_p$ ), electron kinetics temperature ( $T'_e$ -eV), electron number density ( $n_e$  – electrons/m<sup>3</sup>), and ion kinetics temperature ( $T'_i$ -eV) in DC and RF glow discharge plasmas at intermediate and low pressures. The Langmuir probe consists of a bare wire, connected to the DC power system which supplies bias voltage from negative to positive values. The current is also measured along with the voltage. The schematic diagram is illustrated in Figure 2.8 [74].

For accurate reading, the electrons must not have collisions in the sheath between the plasma and the probe surface. To achieve that condition, the electron mean free path must be greater than the sheath thickness (Debye length). For a low pressure plasma process, the electron mean free path is ranged from a millimeter to centimeters. The sheath



thickness is in millimeter scale for typical industrial plasma. In short, the lower vacuum condition, the more accurate reading from Langmuir probes.

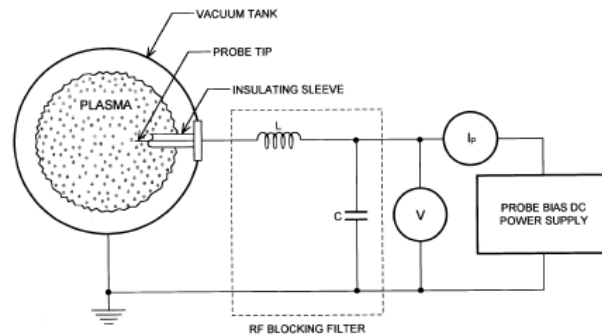


Figure 2-8 A schematic diagram of Langmuir probe for plasma diagnostics (reproduced from [74])

#### 2.1.6.4 Langmuir probe characteristics curve

When the probe bias voltage ( $V$ ) is applied to the Langmuir probe in the range which cover the plasma potential ( $V_p$ ), together with the measured current flow. It generates a Langmuir probe curve, which is shown in Figure 2.9 [74].

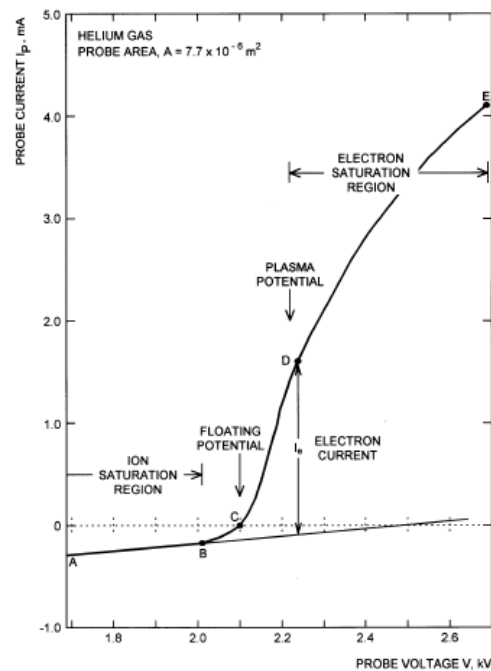


Figure 2-9 An example of Langmuir probe curve for plasma diagnostics (reproduced from [74])

### **Ion saturation current**

In the ion saturation current region (A- B) in Figure 2.9, the probe potential is negative, compared to the plasma potential. In this region, only ions are collected by the probe. However, the ion current is not constant because the sheath boundary moves away from the probe surface at the increase of negative potential. Hence, there is more effective surface area of the probe which draws more positive ions, resulting in higher current at the higher negative potential. If the voltage is increased and becoming more positive, the sheath boundary will be closer to the probe which reduces the ion current. The least ion current at point B is defined as ion saturation current (0.15 mA in figure 2.9)

### **Floating potential**

If the potential is more positive than point B, the bias potential is now positive compared to plasma potential. It pushes all ions back to the plasma and starts to collect more electrons. The potential at point C where there is no current, is called the floating potential of the plasma. In this region, the electron current increases exponentially.

### **Plasma potential**

The plasma potential is defined where all plasma available electrons are collected at the probe (point D). After point D, the system reaches the electron saturation region.

Like in the ion saturation region, the current is also increased as the potential. The more positive potential pushes the sheath away from the probe, thus the probe effective areas are increased, yielding the increased current. To better determine the plasma potential, the Langmuir curve is

plotted on the semi-logarithmic scale of the electron current portion. The plasma potential is defined at the intersection of the electron current exponential rising and the electron saturation line. This process is graphically shown in Figure 2.10[74]. The plasma potential ( $V_p$ ) is 2,220 V and the electron saturation current ( $I_{se}$ ) = 2.35 mA for the electron saturation current.

#### 2.1.6.5 Electron kinetic temperature $T'_e$

The electron kinetic temperature could be determined from the slope of electron current rising region (before electron saturation region).

$$T'_e = \frac{V - V_p}{\ln(I_e/I_{es})} \quad (2.4)$$

For the data of Figure 2.10, the electron kinetic temperature ( $T'_e$ ) is 42 eV.

#### 2.1.6.6 Electron number density ( $n_e$ )

Since the Langmuir probe in electron saturation collects the entire electrons incident on the plasma-sheath boundary, one may write the total electron current collected by the probe as

$$n_e = \frac{4I_{es}}{eA_0} \sqrt{\frac{\pi m_e}{8eT'_e}} \quad (2.5)$$

Where  $A_0$  is the surface area of the probe,  $m_e$  is the electron mass and ( $T'_e$ ) is the electron kinetics temperature. The number of electrons ( $n_e$ ) is equal to  $1.75 \times 10^{15}$  electrons/m<sup>3</sup> if the electron kinetic temperature ( $T'_e$ ) of 42 eV and the electron saturation current ( $I_{es}$ ) of 2.35mA are substituted into equation (2.5).

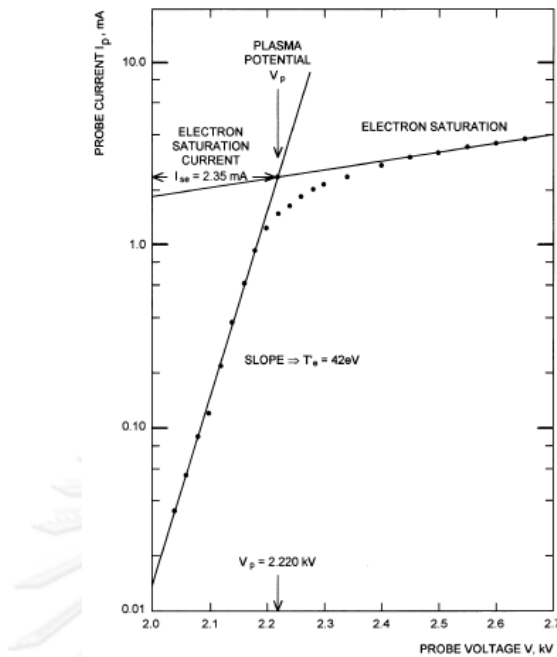


Figure 2-10 A graphical determination of plasma potential by semi-logarithmic scale of Langmuir probe curve in the electron current region (reproduced from [74])

### 2.1.6.7 Ion kinetic temperature $T'_i$

[74]

The ion kinetic temperature from the ion saturation current of equation (2.6),

$$T'_i = \left( \frac{4I_{is}}{eA_0n_i} \right)^2 \frac{\pi M}{8e} \quad (2.6)$$

Where  $I_{is}$  is ion saturation current,  $M$  is ion mass,  $A_0$  is the surface area of the probe,  $n_i$  is the number of ion which can be estimated as same amount of number of electron ( $n_e$ ) for quasi-neutral plasma. If ion saturation current ( $I_{is}$ ) of 0.15 mA is substituted with others previous calculated parameters into (2.6), the effective ion kinetic temperature for this singly ionized helium plasma is 1,270 eV.

### 2.1.6.8 Debye shielding length

[62]

When electrode or wall or anything in contact with plasma, there will be a surface sheath formed between plasma and the surrounding which shields plasma itself from applied electric fields. The Debye shielding distance is the characteristic thickness which describes this phenomenon. It is graphically described in Figure 2.11 [62].

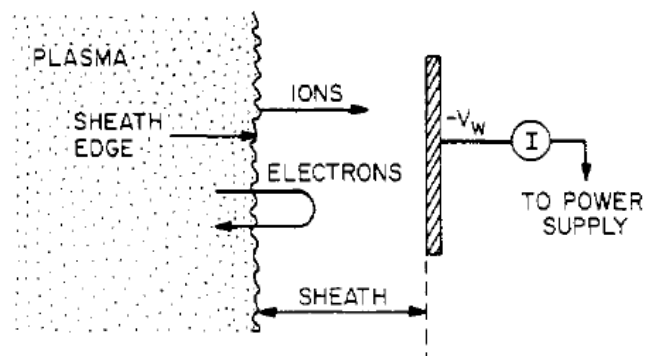


Figure 2-11 A graphical illustration of plasma sheath at cathode  
(reproduced from [62])

The Debye shielding distance ( $\lambda_d$ ) could be estimated from equation 2.7

$$\lambda_d \approx 7434 \left( \frac{T_e'}{n_e} \right) \quad (2.7)$$

Where  $n_e$  is number of electron and  $T_e'$  is the electron kinetics temperature. For typical industrial plasma conditions,  $T_e'$  of 5 eV and  $n_e$  of  $10^{16}$  electrons/m<sup>3</sup>, the Debye shielding distance will be approximately 0.17 mm.

## 2.2 Silk fibroin

### 2.2.1 *Silk fiber*

Silk fiber was first used to produce a fabric in ancient China[75]. In medical applications, it has been used as a suture material over centuries[76]. Silk fiber is normally extracted from the cocoons of domesticated silkworms, *Bombyx mori*. The raw silk fiber is composed of two parts; fibroin and sericin. Fibroin is a natural polymer which has a highly repetitive amino acid sequence. Sericin is an adhesive protein which binds fibroin strands together. Primarily, fibroin is used more than sericin as a biomaterial. To obtain pure silk fibroin, the cocoons are boiled in an alkaline solution. The amount of sericin is approximately twenty-five to thirty percent of the total cocoon mass [76].

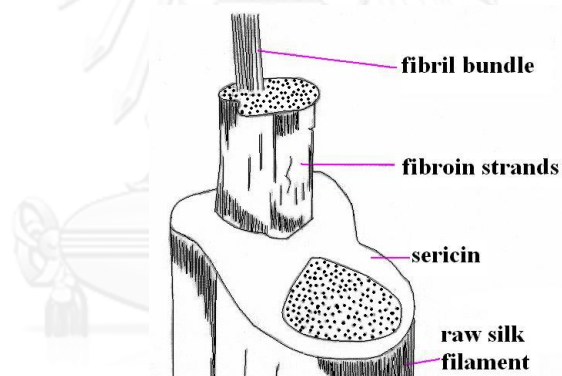


Figure 2-12 The composition of raw silk fiber

(reproduced from [77])

### 2.2.2 *Silk fibroin structure*

Silk fibroin consists of three parts of protein: the heavy chain (390 kDa) [78], the light chain (L-chain : 25 kDa), and P25 (30 kDa) [79]. The heavy chain (H-chain) is the crystalline portion of the silk fibroin. The amino acid sequence is repetitive, a Glycine (gly) rich protein. It forms a tertiary structure of  $\beta$ -sheet. The light chain (L-chain) has standard amino acids with a non-repetitive

sequence. It contributes to fiber properties. The heavy chain is linked to the light chain with a single disulfide bond [78]. P25 is a glycoprotein containing Asparagine (Asn)-linked oligosaccharide chains. The hydrophobic part of P25 is connected to the hydrophobic portion of the heavy chain. This linkage is called a ‘hydrophobic interaction’; not a covalent bond [79].

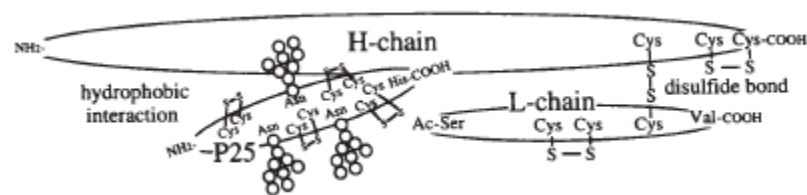


Figure 2-13 The silk fibroin structure which illustrates the linkages between H-chain & L-chain, and H-chain & P25 (reproduced from [79])

### 2.2.3 The amino acid sequence of the *Bombyx mori* silk fibroin heavy chain

The heavy chain (5,263 residues or 390 kDa) has twelve crystalline domains which has a majority of glycine-others (Gly-X) dipeptides (94%). X is either Alanine (Ala:64%), Serine (Ser:22%), Tyrosine (Tyr:10%), Valine (Val:3%), or Threonine (Thr:1.3%). Besides the crystalline domains, the remaining 6% are non-repetitive, amorphous regions: N-terminal header (151 residues), eleven almost identical linkers (43 residues), and C-terminal (58 residues).

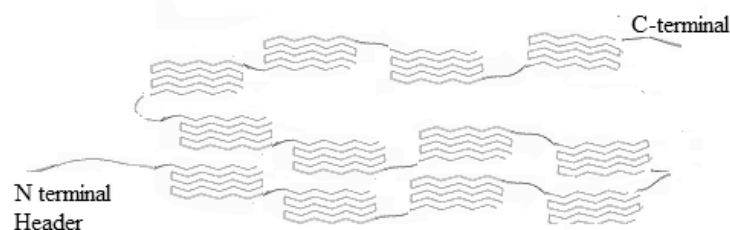


Figure 2-14 The domains in the heavy chain of silk fibroin (The heavy chain composes of the N-terminal header, 12 crystalline domains, 11 linkers, and the C-terminal.)

In each crystalline domain, the sub-domains of seventy residues are observed. The sub-domains generally begin with a hexapeptide sequence of GAGAGS and end with a GAAS tetrapeptide. In the sub-domains, the peptide sequence strictly follows the pattern of Gly-X. This pattern leads to a  $\beta$ -sheet formation where the  $\beta$ -sheets pack on each other in alternating layers of Gly/Gly and X/X contacts.

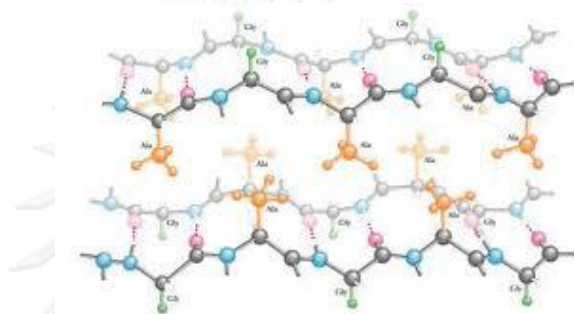


Figure 2-15 The 3D conformation of silk fibroin heavy chain in  $\beta$ -sheet structure (reproduced from [80])

Zhou *et. al.* [78] suggested that each sub-domain formed a  $\beta$ -strand. The sub-domain  $\beta$ -strand, packed with another  $\beta$ -strand, formed a  $\beta$ -sheet. The folding of each  $\beta$ -strand could have been caused by a GAAS tetrapeptide at the end of a strand. The strict Gly-X pattern was, therefore, disrupted. Instead of continuing the zigzag  $\beta$ -strand, it caused  $\beta$ -turn to a neighboring sub-domain. N-terminal header, eleven linkers, and C-terminal are the amorphous regions of fibroin heavy chain. The eleven linkers connect twelve crystalline domains together. It almost has an identical sequence and contains twenty-five residues, non-repetitive peptide (boldface character in Figure 2.16). This is also present in the N-terminal header. This twenty-five residue peptide contains Proline and charged residues which are not present in the crystalline domains. In the C-terminal, there are three Cysteines (Cys), one of which forms disulfide linkage with the light chain, and the rests form



internal linkage. C-terminal is arginine/lysine-rich and has no hydrophobic residues.

```

Header (1,1=151)
MRVKTFVILCCALQYVAYTNANINDPDEDVYFGSDVTVQSSNTTDEIIRDASGAVIEEQIT
TKMKQRKNKNHGILGKNEKMIKTFVITTDSDGNESIVEEDVLMKTLSDGTVAQSYVAADA
GAYSQSGPYVNSCYSTRQGYTSDFSSTAAV
GX1 (152,1=511)
1.1 GAAAGSGAYGAAS
1.2 GAAYGTGAGAYAYAYAYAYGAAS
1.3 GAYCQGVGSGAAS
1.4 GAGAsAAGSAGTYAYGAAS
1.5 GTuyGGASaayCTuGAayGAYGAGYGVVYAGYsGAAS
1.6 GAGSssssssGTGAGSsYGAysGAAS
1.7 ssssyGAYGAYGAGAGVGYsGAAS
1.8 sssssssGAGVGYGAGVAGYUysGAAS
Linker 1 (1=44)
GAGAGAGAGAGTGSSGFGPYVANGGYSRSDCYEYAWSSDFGTGS
GX2 (706,1=511)
2.1 ssssyGAGVGVGYUysGAAS
2.2 sssssssGAGVGSsGAGAGVGYGAGACVGYsGAAS
2.3 sssssssGAGVGYGAGVAGYUysGAAS
2.4 ssssssssyGAYUysGAAS
2.5 GAGSsGAsssssyGAGVAGYUysGAAS
2.6 sssssGAGVGYUysGAAS
Linker 2 (1=43)
GAGAGAGAGAGTGSSGFGPYVAHGGYSGYEYAWSSDFGTGS
GX3 (1259,1=361)
3.1 ssssuGVGAGYUysGAGS
3.2 sssssssyUysGAGS
3.3 ssssssyGAGVAGYUysGAGS
3.4 sssGAGVGSsSyUysGAGS
3.5 sssssGAGVGYGAGVAGYUysGAAS
Linker 3 (1=43)
GAGAGAGAGAGTGSSGFGPYVANGGYSGYEYAWSSDFGTGS
GX4 (1662,1=147)
4.1 sssyUysGAGS
4.2 sssssGAGSGSsSyGAGVAGYGVGYAysGAAS
Linker 4 (1=43)
GAGAGAGAGAGTGSSGFGPYVAHGGYSGYEYAWSSDFGTGS
GX5 (1853,1=428)
5.1 sssssyGAGVuAYGAysGAAS
5.2 sssssssyGAYsGAGS
5.3 sssssGAGSGSsSyGAGVAGYUysGAGS
5.4 syGAYuyGAGAGTGAGS
5.5 sssssGAGSGSsSyGAYUysGAGS
5.6 sssyGAGYsGAAS
Linker 5 (1=43)
GAGAGAGAGAGTGSSGFGPYVAHGGYSGYEYAWSSDFGTGS
GX6 (2124,1=275)
6.1 sasyGAGVAGYUysGTGS
6.2 syGAGVAGYsGAAF
6.3 GAGAsssssyUCVAGYsGAAS
6.4 ssssyGAGVAGYUysGAAS
6.5 sGAsssGAGSsSyGAAS
Linker 6 (1=43)
GAGAGAGAGAGTGSSGFGPYVANGGYSGYEYAWSSDFGTGS
GX7 (2643,1=596)
7.1 ssssyGAGVAGYUysGAGS
7.2 sssssyGAAS
7.3 sssssyGAGVAGYGVGYAysGAGS
7.4 sssGAGSsGAGSsYGVGYAysGAGS
7.5 sssGAGSsSyGAGVAGYGVGYAysGAGS
7.6 sssssGAGSsGAGSsSyGAGVAGYGVGYAysGAGS
7.7 sGAsssssyGVuGAGVGYAysGAAS
7.8 GAsGAGACTysGAAS
Linker 7 (1=43)
GAGAGAGAGAGTGSSGFGPYVANGGYSGYEYAWSSDFGTGS
GX8 (3283,1=494)
8.1 sssyGAGVAGYsGAGS
8.2 sssyGTGS
8.3 sssssGAGVAGYGVGYAysGTGS
8.4 ssssyGAGVAGYGVGYAysGAGS
8.5 sssGAGSsGAGSsYGVGYAysGAGS
8.6 sssGAGSsSyGAGVAGYGVGYAysGAGS
8.7 sssssGAGSsSyGAGVAGYGVGYAysGAAS
Linker 8 (1=43)
GAGAGAGAGAGTGSSGFGPYVANGGYSGYEYAWSSDFGTGS
GX9 (3821,1=348)
9.1 sSyuGVuGAGVGYAysGAAS
9.2 assGAyGAGYGIcVUCAGVGYAysGAAS
9.3 sssssyGVuGAGVGYAysGAAS
9.4 GAAssssssyGAGVuCYOysGAAS
9.5 ssssyGAAS
Linker 9 (1=42)
GAGAGAGAGAGTGSSGFGPYVANGGYSGYEYAWSSDFGTGS
GX10 (4212,1=302)
10.1 sSyGAGVAGYUysGAAS
10.2 sssGAGSsSyGAGVAGYUysGAAS
10.3 sGAsssssGAGSsYGVuGAGVGYAysGAAS
10.4 sGCAGSsGAsssyGAGYsGAAS
Linker 10 (1=43)
GAGAGAGAGAGTGSSGFGPYVANGGYSGYEYAWSSDFGTGS
GX11 (4558,1=566)
11.1 sSyGAGVAGYUysGAGS
11.2 sssssyuyGAGAGVGYAysGAGS
11.3 sGSsGSGAGSsSyGAGYGIcVUCAGVGYAysGAAS
11.4 ssssssyGAGAGVGYsGAAS
11.5 sssssGAGSsYUCVAGYyGAGYVysGAGS
11.6 sssGAGSsYGAysGAAS
11.7 GAGAsssGAGSsYGAAS
11.8 sGAsssyGAAS
Linker 11 (1=44)
GAGAGAGAGAGTGSSGFGPYVANGGYSRRGEYAWSSKSDFGTGS
GX12 (5169,1=36)
12.1 GAASGAsssss
C-ter (5206,1=58)
VSYGAGRGYQGAGSAASSVSSAGSRsYDYSRRNVRKNCGIPRRQLVVXFRALPCVNC

```

Figure 2-16 The amino acid sequence of silk fibroin heavy chain (5263 residues)

The sequence is broken into: N-terminal header, domains, sub-domains and C-terminal. The position number of the first residue and the length of that domain is shown in brackets. The 25-residue repeats, found in the header and the linkers, are in boldface characters. The lowercase letters s, y, a, and u, are commonly found hexapeptides. The number of repeats is shown in brackets after the hexapeptide sequence. s GAGAGS (433) y GAGAGY (120) a GAGAGA (27) u GAGYGA (39) (reproduced from [78])

#### **2.2.4 *Silk fibroin application in tissue engineering***

Silk fibroin is biocompatible, biodegradable and mechanically strong. Its modulus (15-17 GPa) is much higher than crosslinked collagen (0.4-0.8 GPa) or polylactic acid (1.2-3 GPa). It could fabricate in different forms such as fibers, non-woven mats, films, hydrogels, and porous sponges, depending on its application in tissue engineering. The examples of silk fibroin applications are: film/sponge for wound dressings, sponge/hydrogel/non-woven mats for bone tissue engineering, sponge for cartilage tissue engineering, fiber for ligament/tendon tissue engineering, film for antithrombogenesis/ hepatic tissue engineering, non-woven mats for connective tissue/endothelial and blood vessel tissue engineering, etc [76].

#### **2.2.5 *Surface modification of silk fibroin***

Silk fibroin surface could be modified with either physical adsorption or chemical immobilization. The surface is hydrophobic. It could either draw or repel proteins, depending on protein hydrophobicity. The chemical method in immobilizing functional groups, generally employs amino acid side chain chemistry. This could be done by glutaraldehyde or carbodiimide chemistry. Glutaraldehyde chemistry connects the amine group with other amine, while carbodiimide connects the carboxyl group with the amine group. The limitation of carbodiimide chemistry for modifying silk fibroin surface is, that silk fibroin has less available carboxyl side groups (3.3%) than other biomaterials such as bovine collagen (9.5%). The silk surface could also form a covalent bond with inorganic materials such as Hydroxyapatite. This is achieved by using 2-methacryloxyethyl isocyanate to generate vinyl groups to graft with poly methacryloxypropyl trimethoxysilane (polyMPTS).

Hydroxyapatite particles then could be bonded with alkoxy-silyl groups of MPTS to form siloxane bonds [76].

The alternative to treating the silk fibroin surface is plasma surface treatment. Plasma offers highly energetic active species which are capable for surface reaction. This reaction is very quick, and leaves almost no trace chemicals. This process also does not alter the mechanical properties of silk fibroin because, it reacts only with the surface layers of the material [69].

### 2.3 Tissue Engineering

Tissue engineering field has been developed to address the issues of transplanted organ shortage and growing demand for tissue repair or replacement. To engineer new tissues, three major components are required: the right types of cells, a scaffold for cells to attach and grow, and signaling molecules, such as growth factors, for cells to differentiate to the desirable tissue. Scaffold plays a major role in tissue engineering since it is involved in every step of tissue formation. Initially, it needs to be biocompatible and has acceptable foreign body reaction from the body's immune system. Structural-wise, it is required to have a high surface area and interconnected pores for cells to grow in large amounts. These interconnected pores allow nutrient diffusion to the scaffold core and removal of waste from the scaffold. For example, woven meshes, hydrogels or sponges could be used to serve this purpose. Meanwhile, the scaffold should be strong enough for handling during the implantation process and has the mechanical strength comparable with implant site. Furthermore, the surface of scaffold needs to enhance cell attachment. The extra-cellular matrix (ECM) has been imitated in scaffold design to enhance cell attachment. Finally, the scaffold is preferred to be

biodegradable when engineered tissue is functional, so it could not potentially develop unwanted side effects in the long term [1-3].

Materials used in scaffold fabrication fall into three groups: ceramics, synthetic polymers and natural polymers. Ceramics are used in the majority for hard tissue regeneration, such as bone because of their high mechanical strength. Hydroxyapatite (HA) and tri-calcium phosphate (TCP) are commonly used for bone scaffolds. However, they do not attract cell adhesion. The second group is synthetic polymers such as polystyrene, poly-L-lactic acid (PLLA), polyglycolic acid (PGA) and poly-D,L-lactic-co-glycolic acid (PLGA). They are produced with consistent properties and desirable degrading time. Similar to ceramics, the drawback is cell compatibility. Another issue is the toxicity of degraded products. For example, lactic acid, the degraded product of PLA, can cause muscle fatigue. The last group is natural polymers, such as protein (collagen, gelatin, silk fibroin, etc.), proteoglycans, glycosaminoglycan, and carbohydrates (chitosan, alginate, etc.). This group has excellent biological properties such as biocompatibility and biodegradability. Some natural polymers could promote cell attachment and proliferation. In addition, its biodegradable products are nontoxic since they are basic amino acids and sugars. The common major drawback is its weak mechanical strength, which limits load bearing applications [3]. In addition, some materials are not very bioactive so their surfaces need to be modified to enhance cell adhesion.

Since this research focuses only on material side, the rest of relevant theories will be reviewed mainly on cell-surface interaction field such as protein adsorption, cell adhesion and the effect of surface chemistry.

## 2.4 Cell interaction with biomaterial surface

The surface properties of biomaterial have major impacts to the cell fate. The cell-material interaction starts with protein adsorption on the surface and subsequently follows by cell adhesion [50, 52]. The quality of adhesion contributes to later stages of cell life such as spreading, migration, proliferation and eventually differentiation [50, 52, 81-83]. Thus the knowledge of cell interaction on material surface is crucial for designing the suitable scaffolds or implants in tissue engineering. In this section, the protein adsorption on biomaterial surface will be firstly discussed because it is the first step of cell interaction with the surface. Then, the topic of cell adhesion will be reviewed, and followed by the surface chemistry.

### 2.4.1 *Protein adsorption on biomaterial surface*

Cells do not interact directly with material surface. The materials are always covered by either body fluid or culture medium. Protein adsorption is suspected to happen on surface before any cell interaction [50, 52, 53]. For implanting material, proteins such as immunoglobulins, vitronectin, fibrinogen, and fibronectin (FN), adsorb onto the surfaces immediately once contact with body fluid and activate the inflammatory responses such as facilitating the attachment and the activation of inflammatory cells e.g. neutrophils, macrophages, etc. For culture applications, cell adhesion is facilitated by the proteins from serum-containing media. The attachment is a starting point for various cell fates such as proliferation and differentiation [84]. Logically, the protein adsorption plays its connecting roles between surface and cell interaction. Consequently, the protein adsorption should be studied in order to fully understand cell-material interaction.

### **2.4.1.1 Factors controlling protein adsorption**

The factors which control protein adsorption are temperature, pH, the ionic composition and strength of solution, protein properties, and surface properties.

#### **Influence of external parameters on protein adsorption**

Temperature, pH and ionic strength are controlled in physiological condition. Manipulating these parameters is not the option for the implant material. However, it is still worth to understand how these parameters have effects on protein adsorption. Temperature affects protein adsorption in term of equilibrium and kinetics. The adsorption rate is increased with the elevated temperature. The equilibrium is shifted toward the adsorption. Higher temperature also drives the adsorbed water out of the surface which enhances protein adsorption. In general, protein can be adsorbed more on the surface at higher temperature [53].

The pH dictates the electrostatic state of proteins. Proteins are in neutral state when pH equals  $pI$  (isoelectric point). When pH is higher than  $pI$ , proteins will have net negative charges. On the other hand, proteins will have net positive charges if pH is lower than  $pI$ . The adsorption rate is high when there are electrostatic attraction forces of the opposite charge between proteins and surface. However, there will be the repulsion force between proteins due to their same charge. The highest protein packing density is generally at the isoelectric point where there is no electrostatic repulsion force between proteins [53].

The amount of dissolved ions, ionic strength, plays the role of dampening the electrostatic interaction among charged particles. It minimizes both the attraction force between the opposite charges and repulsion force

from the same charge. In general, higher ionic strength allows higher packed density of proteins. Apart of damping electrostatic interaction, certain types of salt ions also have impact on protein precipitation. The ions which cause protein to precipitate are named kosmotropes (e.g.  $\text{SO}_4^{2-}$ ,  $\text{F}^-$ ,  $\text{Mg}^{2+}$  and  $\text{Ca}^{2+}$ ) while chaotropes are the ions which prevent protein to precipitate (e.g.  $\text{ClO}_4^-$ ,  $\text{SCN}^-$ , and  $\text{NH}_4^+$ ). The relationship between salt ion type and protein adsorption is still inconclusive [53].

### Influence of protein properties on protein adsorption [51, 53, 85]

Proteins are very complex biopolymers generated from the combination of 20 amino acids with the additional of side chains such as phosphates, oligosaccharides, or lipids from the translation process. This unique combination of the protein building blocks is leading to the large variety of size, shape, structural arrangement, and functionality which adds complexity to the protein adsorption study. An interesting protein property is its amphiphilicity. Proteins typically contain both hydrophobic and hydrophilic regions depending on the local composition of amino acid residues. To visualize proteins structure, it is needed to segment protein into different patches of hydrophobic, hydrophilic, positively, or negatively charged nature as illustrated in Figure 2.17.

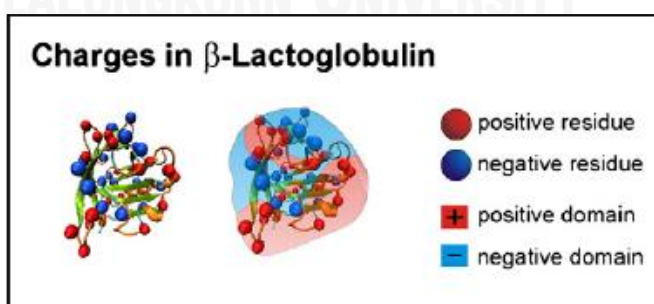


Figure 2-17 Schematic representation of  $\beta$ -Lactoglobulin depicts the distribution of positively (red spheres) and negatively (blue spheres) charged amino acids (reproduced from [53])

In respect to protein size, small and rigid proteins like lysozyme,  $\beta$ -lactoglobulin, or  $\alpha$ -chymotrypsin are considered as 'hard' proteins because they are unlikely to change their structures once they adsorb on the surface. In contrast, the intermediate size proteins such as albumin, transferrin, immunoglobulins, etc., could reorient their conformation upon contacting certain surface. For the high molecular weight proteins such as lipoproteins and glycoprotein, the adsorption behavior is usually dominated by the contents of lipids or glycans. Lipoproteins show a strong affinity to hydrophobic surface and will undergo significant conformational reorientation. On the other hand, glycoprotein could not be adsorbed on hydrophobic surface effectively because of its high content of hydrophilic glycans.

In protein mixture, the adsorption process is the series of protein transportation from bulk, adsorption and desorption. Initially, small and abundant proteins will be the first ones to diffuse and deposit on surface since they could diffuse faster. Later on, they will be replaced with larger proteins which have higher affinity to the surface of material due to their larger contact areas. The larger ones could even repel the smaller ones during spreading process. This phenomenon is called competitive protein adsorption or Vroman effect, as pictured in Figure 2.18.

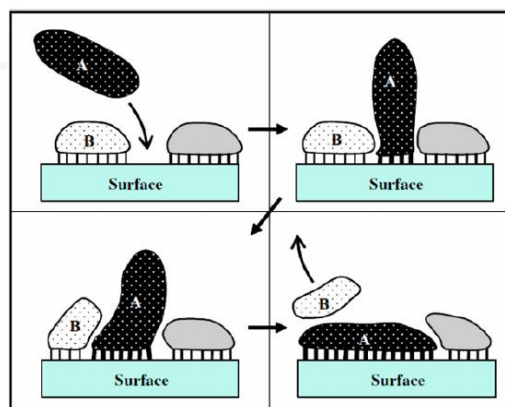


Figure 2-18 Vroman effect diagram for competitive protein adsorption  
(reproduced from [85])



### Influence of surface properties on protein adsorption

In general, proteins have tendency to adsorb on hydrophobic than hydrophilic surface, on high surface tension than low surface tension surface and on charged than uncharged surface. The hydrophobic surface has interaction with the protein hydrophobic core which results in denaturing protein conformation. The denatured proteins have more surface area to anchor on the surface which will lead into stronger protein-surface interaction. However, the only exception to this rule of thumb is glycoprotein. It could adsorb on to the hydrophilic surface better than the hydrophobic one [51, 53, 85].

#### **2.4.1.2**      *The process of protein adsorption*

The adsorption process starts with the hydration of the surface which happens almost immediately once there is a contact between surface and protein solution. The water-surface interface is then formed. Proteins diffuse, inflate, and fill the interphase to its capacity within milliseconds. After that, the proteins will remove either the surface-bound water (surface dehydration process) or pre-adsorbed protein (competitive protein adsorption). This process takes much longer time than the interphase inflation. The timescale is minutes to hours. The strength of the bonding between water and surface depends on surface wettability. Proteins require more energy to displace water bound on hydrophilic surface than hydrophobic surface. That is why hydrophobic surface could adsorb more protein than hydrophilic one. Vogler [51] defined hydrophilic surface with the advancing water contact angle  $\Theta < 65^\circ$  and hydrophobic surface  $\Theta > 65^\circ$ . His conclusion was made after the extensive review of literature which showed the pivotal change of the biological response at the advancing water contact angle  $\Theta = 65^\circ$ . In the last

step of protein adsorption, the interphase will have a stable layer after the equilibrium is reached. The protein adsorption process is illustrated in Figure 2-19.

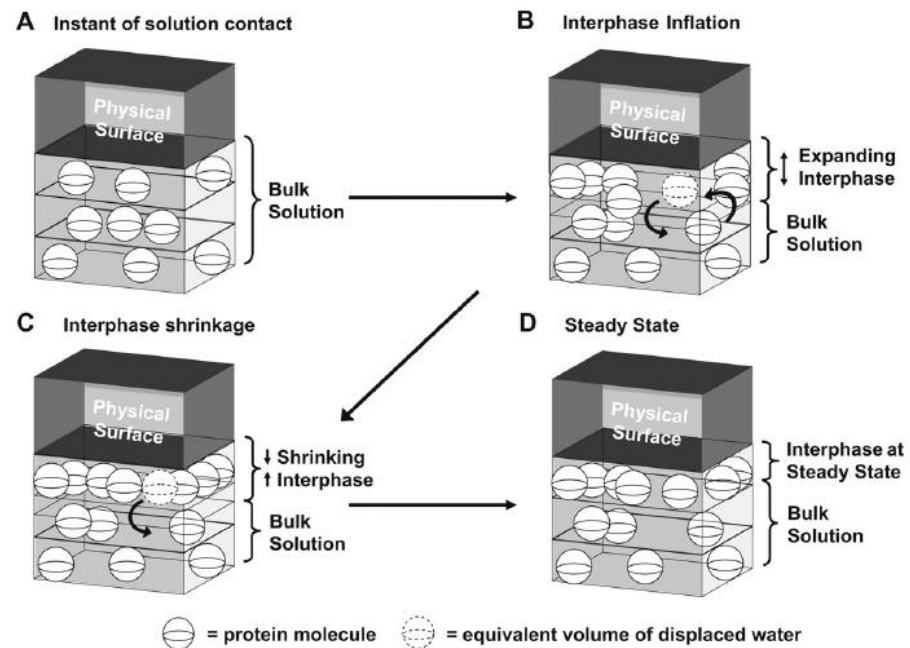


Figure 2-19 The protein adsorption process  
(reproduced from [51])

### 2.4.1.3 The behavior of adsorbed proteins on the surface

On the surface, the adsorbed proteins undergo several processes start from the orientation of the initial contacted protein, the conformational change, the co-operative effect from the already adsorbed proteins, the aggregation of protein, and the desorption of proteins.

#### 2.4.1.3.1 *The orientation of adsorbed protein: Side-on or end-on*

[53]

In most cases, the shapes of proteins are asymmetric and usually in elliptical form. Some have sophisticated shapes such as heart-like (BSA: Bovine Serum

Albumin), or Y shaped (IgG: Immunoglobulin G), etc. The orientation of adsorbed protein is an important issue if adsorbed proteins are designed for enzymatic reaction, or attracting the cell receptors, or any specific biological activity. The orientation is determined by the part of protein that interacts with the surface and the part that is exposed to the bulk solution. The preferred orientation of a protein is resulted from the minimum free energy from attractive coulomb and van-der-Waal interactions, and hydrogen bonds. Net positively or negatively charged protein could also adsorb on a like-charged surface because it will expose oppositely charged region to the surface.

If protein structure is not changed from its original shape, the orientation on the surface could be defined as either 'side-on' or 'end-on'. The 'end-on' orientation normally yields higher packed density of protein. The orientation of already adsorbed protein could be changed due to the increasing protein density on the surface. The repulsion force between neighboring adsorbed proteins, could be increasingly unfavorable for original orientation if the like charged patches are next to each other. Proteins will re-orient themselves to reach the optimal free energy; however, this process will go along with desorption process. This re-orientation process is illustrated in Figure 2-20.

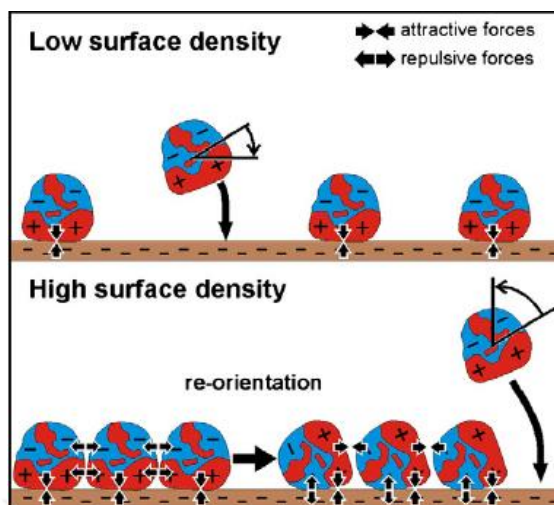


Figure 2-20 The re-orientation process at high surface density of adsorbed proteins  
(reproduced from [53])

#### 2.4.1.3.2 The conformational change

[51, 53, 85, 86]

Proteins could change their conformations upon adsorption to a solid interface especially hydrophobic surface. The minimum free energy concept is still applied for explaining this conformational change. The protein conformation which yields minimum free energy in solution will not be same as the protein conformation on the surface. The structural flexibility of protein ('hard' and 'soft') allows the extent of the reorganization of protein on the surface.

The inner hydrophobic core of a protein plays very active role in structural rearrangement for stronger interaction with a hydrophobic surface. This will result in a denaturing protein from its native structure. Proteins are usually bound strongly with the hydrophobic surface. The denatured protein could have lower biological activity than its native stage.

In case of the hydrophilic surface, the water is bound favorably with the surface which is creating a barrier for proteins. They need to penetrate through the hydration layer before adsorbing on the surface. The

hydrophobic core of protein does not react with the hydrophilic surface, thus the tertiary structure is still maintained. The protein is generally adsorbed weakly and reversibly on the hydrophilic surface.

Browne, *et al.* [86] have illustrated protein adsorption on different surfaces as shown in Figure 2-21.

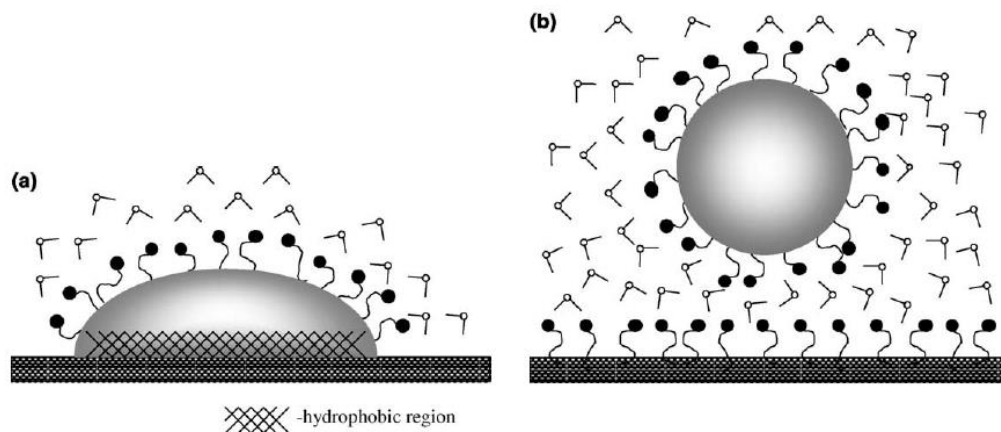


Figure 2-21 Schematic of protein adsorption to hydrophobic (a) and hydrophilic (b) surface (reproduced from [86])

#### 2.4.1.3.3 The cooperative effect

The pre-adsorbed protein on the surface could influence the protein adsorption from the bulk content. If the adsorption is increased by pre-adsorbed proteins, it is called positive cooperative adsorption. On the other hand, if the adsorption rate is hindered by the pre-adsorbed proteins, it is called the negative cooperative adsorption. If there is no effect from the adsorbed protein, it is non-cooperative adsorption [53]. The cooperative effect is illustrated in Figure 2-22.

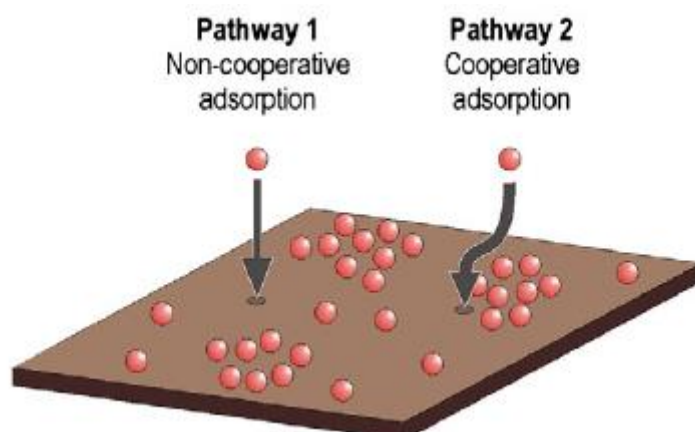


Figure 2-22 The cooperative effect by pre-adsorbed proteins  
(reproduced from [53])

#### 2.4.1.3.4 *Experimental precaution in protein adsorption study*

In his leading opinions paper, Vogler [51] cautioned the researchers about the total different experimental approaches about surface rinsing and labeling protein in the protein adsorption studies.

Researchers believe that strong bound proteins are important for any biological response, will employ the surface rinsing which eliminates all loosely bound proteins. However, there are another group of researchers who insist that all proteins must be taken into account for protein studying.

Labeled protein is not exactly the same as the protein without label. The label such as dye or fluorescent could change the structure and amphiphilicity of proteins which will affect the adsorption process. At least, it adds more weight to the original protein. Care must be taken when applying the results from the labeling protein researches to the studied models.

There are some analytical techniques which have less protrusion into the protein interphase such as the modern in-situ ellipsometry (adsorbed thickness in contact with solution), the solution depletion method (mass balance before-and-after contact with adsorbate), interfacial tensiometry

(contact angle and wetting techniques), quartz crystal microbalance (QCM), and various types of spectroscopy (especially including attenuated total reflection ATR and surface plasmon resonance SPR) [51].

## **2.4.2 Cell adhesion**

Cell adhesion is a foundation step of anchorage dependent cells before any cell activities such as survival, differentiation and migration. The adhesion process is highly ordered, dynamic with spatial structure, controlled at the subcellular level, and responsive to extracellular environment. There are two types of cell adhesions: cell-extracellular matrix (ECM) adhesion, and cell-cell adhesion [87, 88].

### **2.4.2.1 Cell-extracellular matrix (ECM) adhesion**

Cell-ECM adhesion is critical for cell survival and growth. It also has impacts on cell shape (morphology) and migration. ECM adhesion could be categorized into five types: Focal Complex (FCX), Focal Adhesion (FA), Fibrillar Adhesion (FB), Podosome, and Invadopodia.

#### **A. Focal Complex (FCX)**

Focal complex adhesion or close contact [89] is a weak and not stable. The adhesion is formed around cell periphery without stress fibers. This type of adhesion could be mature and developed into stronger adhesion like focal adhesion (FA). The separation distance of the plasma membrane is 30 nanometers (nm) from the surface [88].

#### **B. Focal Adhesion (FA)**

The term of focal adhesion (FA) is now commonly used to describe the strong adhesion to ECM instead of adhesion plaque and focal

contact. FA is larger and more stable than FC. The stress fibers are present in the adhesion structure, enabled strong cell anchoring on the ECM. The adhesions involve many proteins which have roles for adhesion stability and transmission of traction force from the ECM. The separation distance of the plasmic membrane is 10-15 nanometers (nm) from the surface [88].

C. Fibrillar Adhesion (FB)

The distinguish difference between fibrillar adhesions (FBA) and focal adhesion (FA) is that FB relates with fibronectin (FN), the ECM protein. The adhesion structures are longitudinal and parallel to fibrillar bundles of fibronectin. The adhesion sites are also the location of the matrix deposition.

D. Podosome & E. Invadopodia

Podosome and Invadopodia are the only adhesions which could degrade ECM by initiating matrix metalloproteinase (MMP) secretion process. Podosomes are most commonly found in monocytic originated cells such as macrophages, or osteoclasts while invadopodia are apparent in malignant cells. In term of shape, invadopodia looks like finger protruding into ECM [87, 88]. All types of cell-ECM adhesions are shown in Figure 2-23.



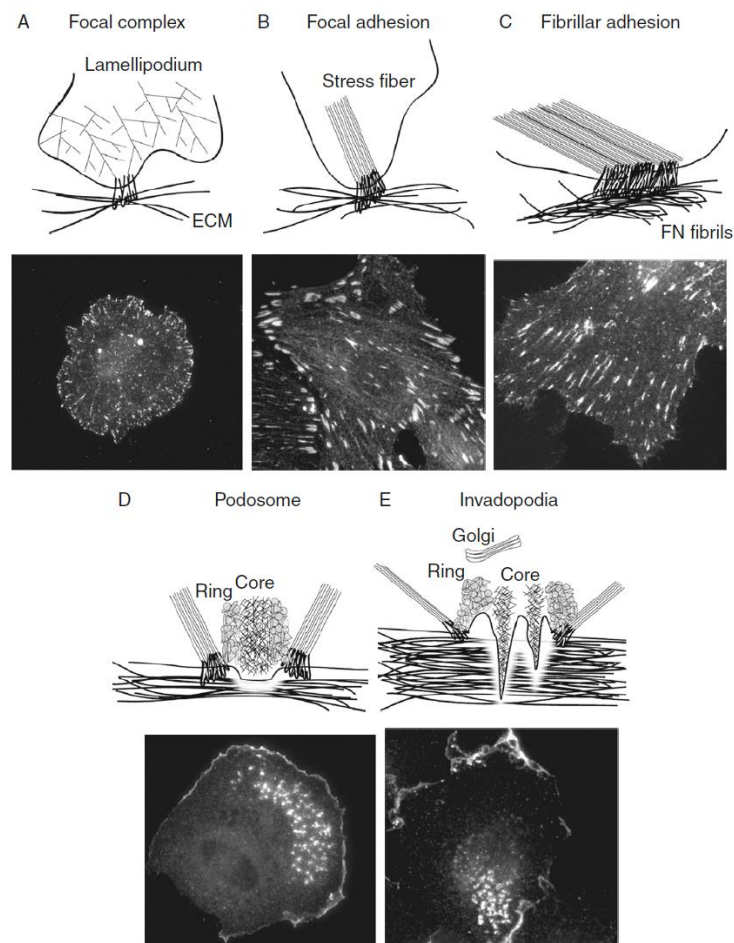


Figure 2-23 Types of cell-ECM adhesion  
(reproduced from [88])

#### 2.4.2.2 Cell-cell adhesion

Many cell types also adhere with adjacent cells such as epithelial and endothelial cells. Cell-cell adhesion is fundamental to tissue structure. The adhesion is facilitated by junctional complexes such as tight junctions (TJs), adherens junctions (AJs), gap junctions, and desmosomes. These junctions enable cells to communicate and interact via the signaling molecules and cytoskeletal proteins [87].

### 2.4.2.3 Formation of Cell-ECM adhesions

Cell-ECM adhesion is formed by bonding between cell adhesion receptors and ligands or cell binding domain (CBD) of ECM components. The cell adhesion receptors could be categorized into two groups; integrins and syndecan-4 (syn4).

#### Integrin

The majority of cell-ECM adhesion is facilitated by the integrin family of cell-surface receptors. Integrins do not have their roles only on cell attachment responses but also serving as a signaling trigger which regulate various cellular activities such as survival, proliferation, and differentiation [84]. Integrins are the cell receptors that bind to various ECM ligands. The adhesion receptors are transmembrane and made up with two different protein chains, heterodimeric. The two chains are noncovalently linked, and named  $\alpha$  and  $\beta$  subunits. The combinations of 18  $\alpha$  subunits and 8  $\beta$  subunits, yield 24 different integrins which bind to specific ECM proteins as illustrated in Figure 2-24 [88, 90].

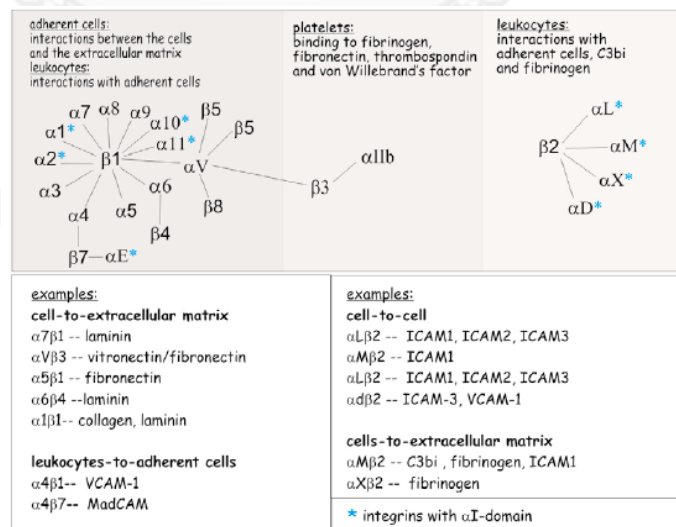


Figure 2-24 The currently identified integrins presented from the combination of  $\alpha$  and  $\beta$  subunits (reproduced from [90])

Majority portions of integrins are outside of cell membrane which enables ECM binding. The cytoplasmic portions are lack of enzymatic activity and relatively short except  $\beta_4$  subunit. The most studied integrins are  $\alpha_5\beta_1$  and  $\alpha_v\beta_3$  because of their binding to FN and VN. For comparison of their binding specificity,  $\alpha_5\beta_1$  almost binds only to FN, while  $\alpha_v\beta_3$  could bind to FN, VN, and other ECM proteins [88]. The structure of integrin is shown in Figure 2-25.

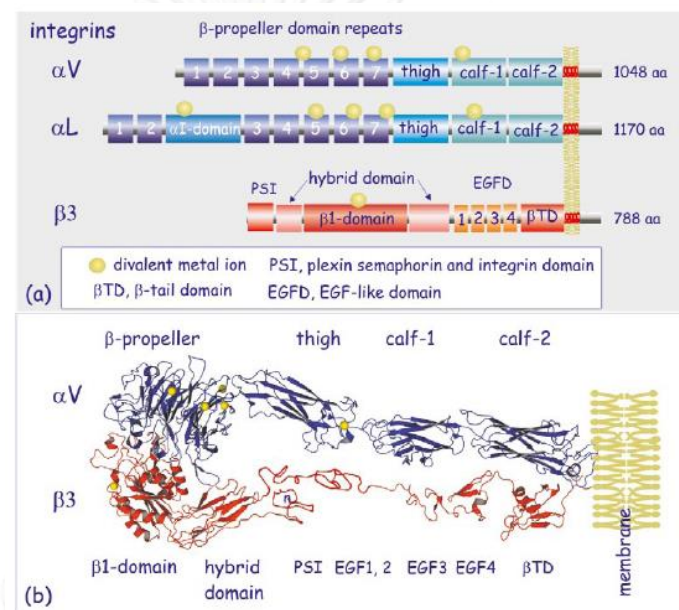


Figure 2-25 The details of domain structure of integrins (a) example of each subunit (b) one the most studied integrin ( $\alpha_v\beta_3$ ) which can bind to FN/VN and others ECM proteins (reproduced from [90])

The integrin binding is a three-step process. Initially, integrins are folded and inactive. Then, the separation of two subunits ( $\alpha$  and  $\beta$ )  $\beta$  pushes the extension of integrin domains especially the rotation of the hybrid section of  $\beta$  subunit to outside. This movement enables integrins to the primed stage ready for binding ligand (RGD in case of fibronectin). For the integrin which contains  $\alpha$ -I domain, the activation mechanism is slightly different. The intrinsic ligand of  $\alpha$  subunit will bind with the  $\beta_1$  section of  $\beta$  subunit which

will leave room available for ligand bind site. Both binding mechanisms are illustrated in Figure 2-26 [90].

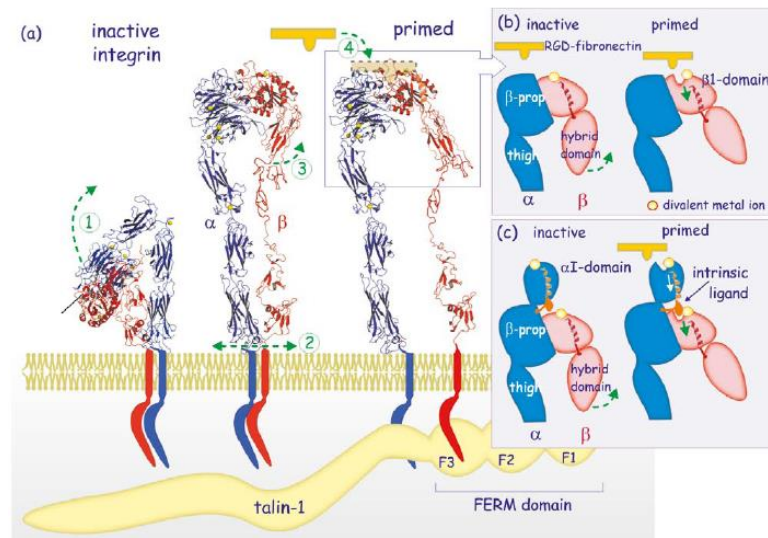


Figure 2-26 The binding mechanism of integrin with ECM ligand (reproduced from [90])

### Syndecan-4 (syn4)

Syndecan-4 (syn4) is the second type of cell adhesion receptor. It is an important for the development of mature focal adhesion. Syndecan-4 has a lot of heparin sulfate proteoglycan in its structure which allows binding several different ECM proteins. The structure of syn4 is pictured in Figure 2-27.

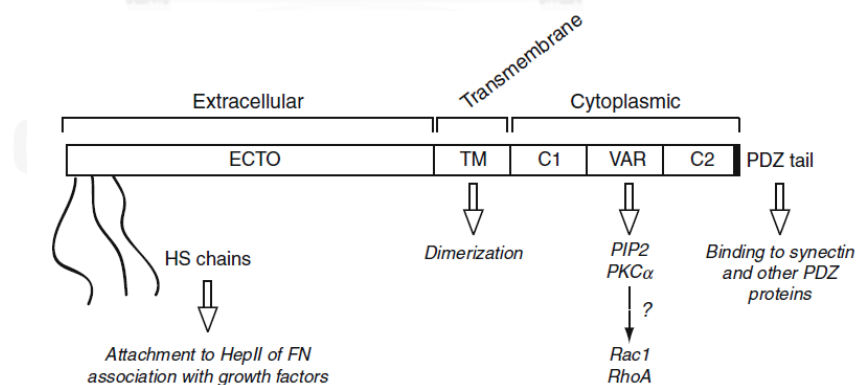


Figure 2-27 Syndecan4 structure (reproduced from [88])

In fibronectin (FN) molecules, there are different regions which could serve as ligands for binding cell integrins or syndecan-4. The cell binding domain (CBD)

which has tripeptide RGD sequence is the universal recognition site for integrin binding. The specific region for binding syndecan-4 is called heparin binding site (HBD or HepII) [88].

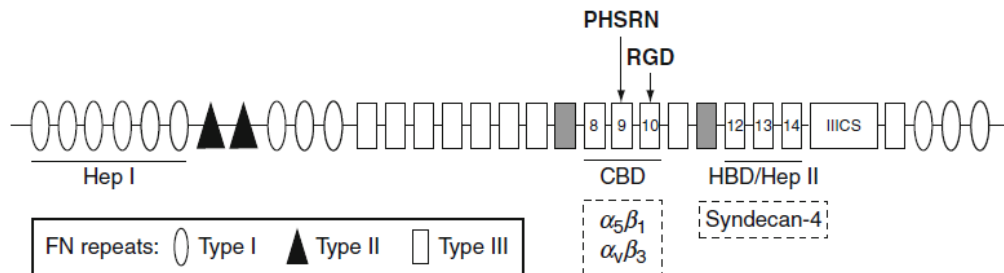


Figure 2-28 Structure of fibronectin (FN)  
(reproduced from [88])

Fibronectins (FN), cell-adhesive glycoproteins, could be found as both soluble (body fluids) and insoluble forms (fibrils in extracellular matrices) [91]. The FN molecule is composed of three different types of repeating domains, type I, II, and III. The integrin binding site is type III repeats 9–10 (CBD) also called cell binding domain (CBD). The location of syn4 adhesion is at type III repeats 12–14 or heparin binding domain (HBD/HepII) [88]. It is worth to mention that  $\alpha_5\beta_1$  integrin binding with fibronectin requires both the PHSRN sequence in the 9th type III repeat and the RGD in the 10th type III repeat of the molecule. On its own, both sequences could not yield strong binding, but collectively both sequences enhance binding with excellent adhesion strength [84]. Besides fibronectin role for facilitating cell adhesion, the fibronectin matrix is also important for regulating the composition and stability of the extracellular matrix. Collagen and thrombospondin proteins are only deposited into fibronectin fibrillar matrix [92].

#### 2.4.2.4 Cytoplasmic network of adhesion molecules

Focal adhesion structures are made of many cytoplasmic proteins. These proteins could be probed with fluorescent label for studying cell adhesions. The first protein recruited at the adhesion site is talin connected to the  $\alpha$ -integrin subunit, before the recruitment of additional proteins in the complex network such as vinculin,  $\alpha$ -actinin, and focal adhesion kinase (FAK). The vinculin serves as the adaptor between integrin and the actin cytoskeleton. While FAK is a part of cell signaling pathway [87, 90].

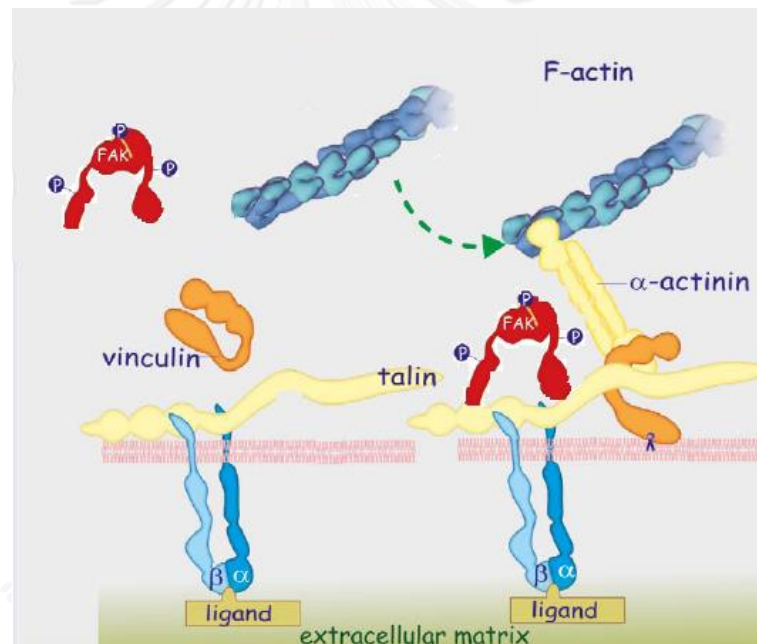


Figure 2-29 The network of cytoplasmic adhesion proteins: Structural group e.g. Talin, Vinculin,  $\alpha$ -actinin, F-actin (stress fiber) and signaling molecules e.g. Focal Adhesion Kinase (FAK) (reproduced from [90])

#### 2.4.3 *Effect of surface chemistry on cell-substrate interaction*

Surface chemistry plays the crucial roles for cell interaction on biomaterials. First, it has direct impact on surface wettability which controls protein adsorption capability and could alter protein conformation. The protein

conformation is critical for activating many biological activities such as attachment, proliferation and differentiation [53, 84, 85]. The surface chemistry also has effect on cell adhesion integrins, which cells use to connect to the surface [87, 88], and cytoplasmic components, which control cell cytoskeleton and signaling pathway [87]. Here are the summaries of findings from different investigators about the effects of surface chemistry on cell interaction. All of them used self-assembled monolayer as a model for different surface chemistries. Self-assemble monolayer could be either alkane thiols with thin layer gold coating or organosilane with thin silica coating. Even the self-assembled monolayer could not be applied directly for *in vivo* application. It still provides a good starting point for surface modification with different surface chemistries.

#### A. Surface wettability

Surface wettability is an indication of effective bonding between water and surface. The surface functional groups play the key role of manifesting surface wettability through developing hydrogen bonding with water. Hydrophobic functional groups such as  $\text{CH}_3$  do not effectively bind with water, resulting in high water contact angle ( $>90^\circ$ ) of the surface. On the other hand, hydrophilic functional groups such as  $\text{OH}$ ,  $\text{NH}_2$ ,  $\text{COOH}$ , etc., could form hydrogen bonding with water, leading to lower water contact angle ( $< 90^\circ$ ) of the surface. The water bonding is developed by Lewis acid/base mechanism. Stronger Lewis acid/base with higher affinity with water, could lower contact angle more than the weaker one [51].

Keselowsky *et al* [84], Faucheux *et al* [92], and Curran J *et al* [93] reported similar findings about the decreasing order of water



contact angle by different surface function groups *i.e.* CH<sub>3</sub> >NH<sub>2</sub> >COOH > OH as summarized in Table 2-3.

Table 2-3 Surface wettability of different surface chemistry

Investigator	Self-assembled monolayer	Contact angle (°)			
		CH <sub>3</sub>	OH	NH <sub>2</sub>	COOH
Keselowsky B [84]	Alkanethiol	107	25	43	28
Faucheux N [92]	Silane	90	20	62	48
Curran J [93]	Silane	90	60	80	70

#### B. Protein adsorption capacity

The contribution of surface chemistry to protein adsorption is from its role of manipulating the surface wettability and surface charge. As previously mentioned in section 2.4.1.3, the hydrophobic surface could adsorb more proteins than the hydrophilic one, and the charged surface adsorbs proteins more than the uncharged surface.

Table 2-4 Protein adsorption capacity on different surface chemistry

Investigator	Self- assembled monolayer	Pre- adsorbed protein	Media	Investigated items	Protein adsorption			
					CH <sub>3</sub>	OH	NH <sub>2</sub>	COOH
Keselowsky B [84]	Alkanethiol	Fibronectin	2mM dextrose in PBS (serum free)	FN adsorption at sat (ng/cm <sup>2</sup> )	360	110	410	280
Faucheux N [92]	Silane	None	DMEM, 10%FBS 1%antibiotic	protein adsorption from culture media in relative to CH <sub>3</sub>	100%	50%	110%	90%

The findings from both Keselowsky *et al* [84], and Faucheux *et al* [92], support the theory that the hydrophobic surface (CH<sub>3</sub>) adsorbed more protein than the hydrophilic surface (OH). The positively charged surface (NH<sub>2</sub>) and the negatively charged surface (COOH) adsorbed more protein than the neutral surface (OH). Fibronectin, net negative charged protein, adsorbed more on the positively charged surface



than the hydrophobic and negatively charged surface. The summary of findings is in the above Table 2-4.

### C. Protein conformation

The protein conformation could be evaluated by using monoclonal antibodies to probe at the cell binding domain of studied protein. Keselowsky *et al* [84] used the antibodies 3E3 and HFN7.1 of cell binding domain of fibronectin.

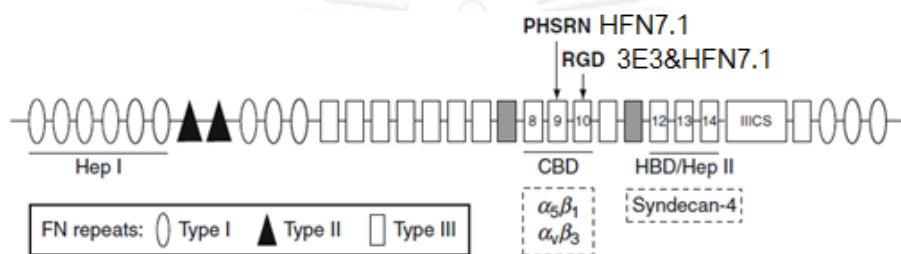


Figure 2-30 Location of monoclonal antibodies 3E3 and HFN7.1 probing at cell binding domain of FN  
(reproduced from [88])

The results showed that the hydrophobic surface required higher protein concentration to reach the level of protein binding affinity at the half of maximum binding. In contrary to the hydrophilic one, they require less protein concentration. As stated in section 2.4.1.3, the hydrophobic surface denatures protein conformation; as a result, it loss the binding affinity [51, 53, 85]. However, at very high density of protein, the hydrophobic surface could not effectively denature protein due to protein-protein interaction [53]. The order of the loss of protein conformation is as same as surface hydrophobicity, *i.e.*  $\text{CH}_3 > \text{NH}_2 > \text{COOH} > \text{OH}$  as shown in Table 2-5.

Table 2-5 Protein conformation on different surface chemistry

Investigator	Self-assembled monolayer	Pre-adsorbed protein	Media	Investigated items	Protein conformation			
					CH <sub>3</sub>	OH	NH <sub>2</sub>	COOH
Keselowsky B [84]	Alkanethiol	Fibronectin	2mM dextrose in PBS (serum free)	FN density at half of maximal HFN7.1 antibody binding affinity (ng/cm <sup>2</sup> )	210	32	180	150
				FN density at half of maximal 3E3 antibody binding affinity (ng/cm <sup>2</sup> )	160	24	110	170

#### D. Cell attachment and cell spreading

The effect of surface chemistry on cell attachment could not be concluded clearly in comparison with that on hydrophilicity, protein adsorption and protein conformation. The cells, media, culture time were totally different. The only thing in agreement is that hydrophobic surface does not support cell attachment. The summary is shown in Table 2-6.

Table 2-6 Cell attachment on different surface chemistry

Investigator	Pre-adsorbed protein	Media	Cell	Investigated items	Cell attachment			
					CH <sub>3</sub>	OH	NH <sub>2</sub>	COOH
Keselowsky B [84]	Fibronectin	2mM dextrose in PBS (serum free)	MC3T3-E1	Effective cell adherent strength (cm <sup>2</sup> /ng)	+	+++	+	++
Faucheux N [92]	None	DMEM, 10%FBS, 1%antibiotic	human fibroblast	% cell attachment at 2 h	30%	30%	70%	60%
Curran J [93]	None	MSC basal growth medium	Human MSC	% cell attachment at 1 day	20%	60%	40%	60%

In term of cell spreading as it demonstrated in Table 2-7, the conclusion couldn't be drawn from 2 groups of investigators: Faucheux *et al* [92], and Curran J *et al* [93].

Table 2-7 Cell spreading on different surface chemistry

Investigator	Pre-adsorbed protein	Media	Cell	Investigated items	Cell spreading			
					CH <sub>3</sub>	OH	NH <sub>2</sub>	COOH
Faucheux [92]	N	DMEM, 10%FBS, 1%antibiotic	human fibroblast	spreading area at 2 h (μm <sup>2</sup> )	4,000	5,000	10,000	9,000
Curran J [93]	None	MSC basal growth medium	Human MSC	Cell morphology at day1	round	round	round	Mixed between round & spread

#### E. Cell integrins and cytoplasmic components.

Keselowsky *et al* [84, 94] studied cell attachment in details by looking closer at cell integrins and cell cytoplasmic components. His findings were in agreement with the cell attachment data. OH functional group enhanced  $\alpha 5$  cell integrin binding affinity. It also enabled the highest recruitment of talin (the first protein to be recruited at adhesion site [87]), and  $\alpha$ -actinin (the linkage to stress fiber [87]). The data was aligned with Curran *et al* [93] but conflicting with Faucheux *et al* [92]. The other similar findings between Keselowsky *et al* [84, 94] and Curran *et al* [93] were that NH<sub>2</sub> surface enhance the highest recruitment of vinculin (adaptors between integrin and the actin cytoskeleton [87]). The effects of surface chemistry on cell integrin characteristics are summarized in Table 2-8, while Table 2-9 shows the effects of surface chemistry on cell cytoplasmic components.

Table 2-8 Cell integrin characteristics on different surface chemistry

Investigator	Pre-adsorbed protein	Media	Cell	Investigated items	Cell integrins			
					CH <sub>3</sub>	OH	NH <sub>2</sub>	COOH
Keselowsky B [84]	Fibronectin	2mM dextrose in PBS (serum free)	MC3T3	FN density at half of maximal $\alpha_5$ integrin binding affinity (ng/cm <sup>2</sup> )	150	15	86	84
				Location of $\alpha_5$ integrin	very little	fewer at center but intense at periphery	only at periphery area	entire spread area
				Location of $\alpha_v$ integrin	very little	very little	very little	entire spread area
Keselowsky B [94]	Fibronectin	2mM dextrose in PBS (serum free)	MC3T3	Effective $\alpha_5$ integrin binding affinity (cm <sup>2</sup> /ng)	+	+++	++	++

Table 2-9 Cell cytoplasmic components on different surface chemistry

Investigator	Pre-adsorbed protein	Media	Cell	Investigated items	Cell cytoplasmic components			
					CH <sub>3</sub>	OH	NH <sub>2</sub>	COOH
KeselowskyB [94]	Fibronectin	2mM dextrose in PBS	MC3T3	Talin recruitment	+	+++	+	++
				Vinculin recruitment	+	++	+++	+++
Curran J [93]	None	MSC basal growth medium	Human MSC	Vinculin at day1	almost none	minimal formation	well developed	minimal formation
				Vinculin at day7	increased coverage	minimal formation	well developed	minimal formation
KeselowskyB [94]	Fibronectin	2mM dextrose in PBS	MC3T3	$\alpha$ -actinin recruitment	+	+++	++	+++
Curran J [93]	None	MSC basal growth medium	Human MSC	Stress fiber (F-actin) at day1	not well defined, cluster in a round shape	spread but lack of organization of fibers	well define cytoskeleton	well define cytoskeleton
				Stress fiber (F-actin) at day7	well define cytoskeleton	spread but lack of organization of fibers	well define cytoskeleton	well define cytoskeleton
KeselowskyB [94]	Fibronectin	2mM dextrose in PBS	MC3T3	paxillin recruitment	+	+++	++	++
				tyrosine-phosphorylated protein recruitment	+	+++	++	++
				Focal adhesion kinase (FAK)	+	++	+++	++

#### F. Cell growth

Faucheux *et al* [92] and Curran J *et al* [93] reported similar findings that NH<sub>2</sub> functional group enhance cell growth when it was compared with others. However, there was no explanation why it could do so. The summary of cell growth on various surface chemistries is demonstrated in Table 2–10.

Table 2-10 Cell growth on different surface chemistry

Investigator	Pre-adsorbed protein	Media	Cell	Investigated items	Cell growth				
					CH <sub>3</sub>	OH	NH <sub>2</sub>	COOH	
Faucheux [92]	N	None	DMEM, 10%FBS, 1%antibiotic	human fibroblast	Growth index at 2 days (no. of folds compare with seeding)	1	1	2.2	2
					% cell viability (% living cells/total cells)	80%	80%	100%	100%
Curran J [93]	None	MSC basal growth medium	Human MSC		Growth index at 7 days (no. of folds compare with seeding)	1.9	1.9	2.5	1.7

### G. Cell differentiation

Both Keselowsky *et al* [94] and Curran *et al* [93] reported similar finding that NH<sub>2</sub> surface enhanced osteogenic differentiation even they used different cells. The summary of cell differentiation on different surface chemistry is shown in Table 2-11.

Table 2-11 Cell differentiation on different surface chemistry

Investigator	Pre-adsorbed protein	Media	Cell	Investigated items	Cell differentiation			
					CH <sub>3</sub>	OH	NH <sub>2</sub>	COOH
KeselowskyB [94]	Fibronectin	α-MEM, FBS, Vit C, β-glycerol phosphate	MC3T3	% mineralized area	1.0%	12.0%	12.1%	0.4%
Curran J [93]	None	MSC basal growth medium	Human MSC	ODC at day7 - proliferation	not increase	increase	not increase	not increase
				CBFA1 at day7- osteogenic differentiation	not increase	not increase	5.8 fold increase from day1	decrease
				Collagen1 at day7	not increase	not increase	decrease	increase
				Collagen2 at day7 - chondrogenic differentiation	not increase	not increase	decrease	increase

#### 2.4.4 Effect of surface stiffness on cell-substrate interaction

Surface stiffness is an important substrate property which affects the fate of all anchorage dependent cells since they need to adhere on the surface for survival. Cells interact with the substrate through their adhesion complexes and actin-myosin skeletons as shown in Figure 2.31 [56, 88, 95, 96].

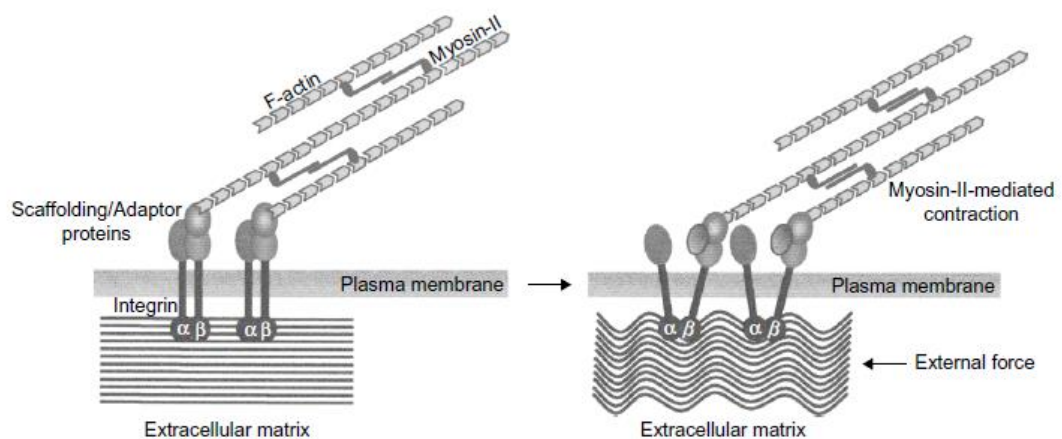


Figure 2-31 The mechanosensory model at focal adhesion through F-actin/Myosin skeleton (reproduced from [97])

It is also important to note that cells not only adhere to the surface but also exert a force through the substrate or pull their microenvironment; this phenomenon was easily observed by the wrinkles caused by cells on a soft substrate. The resistance of the substrate to the cellular force causes the reorganization of the adhesion sites, cytoskeleton, and overall cell states. For example, as pictured in Figure 2.32, the cell adhesion sites are dynamic on the soft substrate, while the adhesion sites on the stiff substrate are static [95].

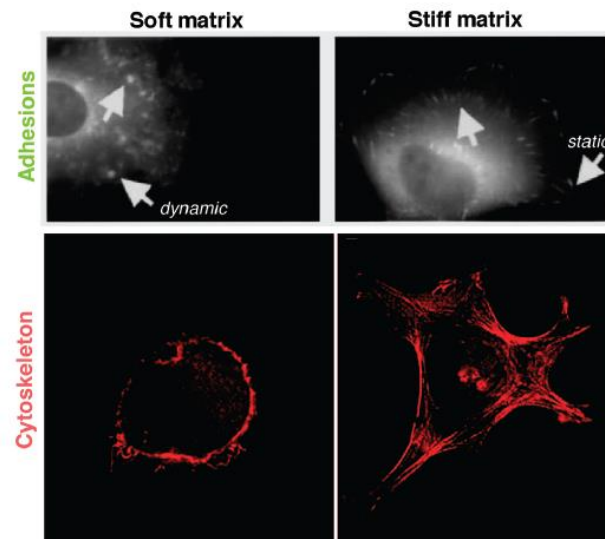


Figure 2-32 The effect of substrate stiffness on adhesion structures and cytoskeleton (F-actin)

(Top) The arrows point to dynamic adhesions on soft gels and static, focal adhesions on stiff gels.

(Bottom) F- actin cytoskeleton. (reproduced from [95])

Figure 2.33 illustrates that the surface stiffness could influence the uncommitted human mesenchymal stem cells (hMSC) to differentiate to the phenotype of which tissue elasticity is in the same range of the adhered surface. Engler *et al* [56] reported that human mesenchymal stem cells (hMSC) adhered to a very soft matrix (0.1 – 1 kPa), which mimics the brain tissue, differentiated to the neuron cells. Their stiffer surface matched the elasticity of muscle tissue (8 – 17 kPa), induced myogenic differentiation on the adhered hMSC and the rigid surface, of which elasticity is in the same range of osteoid matrix (25 – 40 kPa), enabled hMSC to transition to osteoblast. On the other hand, if the surface elasticity is far greater than any of the tissue elasticity (i.e. glass surface - 80 GPa), it would enable the development of well distributed adhesion sites and F-actin cytoskeleton throughout the cell spreading area.



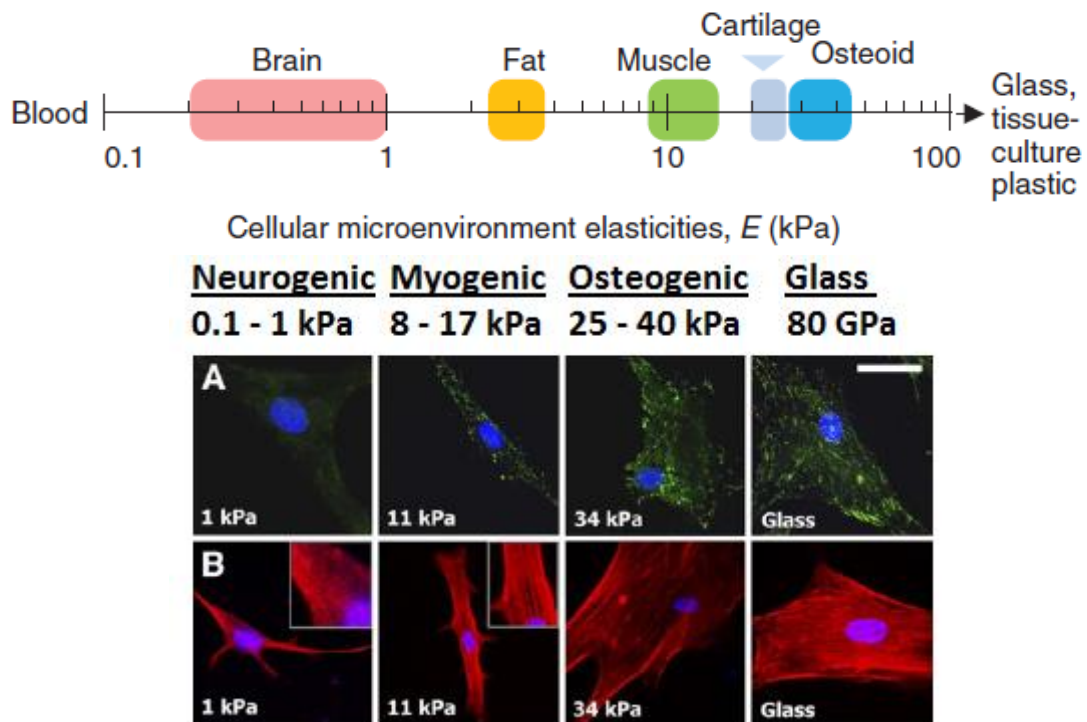


Figure 2-33 Tissue elasticity and differentiation of naive hMSC

(Top panel) the range of tissue stiffness, as measured in the elastic modulus –  $E$ , (Bottom panel) the cytoskeletal organization of hMSC on different surface with different substrate stiffness (A) Paxillin-labeled adhesion sites and (B) F-actin cytoskeleton development (adapted from [56, 96])

In the field of surface stiffness study for cell-substrate interaction, the most studied substrates are polyacrylamide (PA) gel, of which the flexibility could be manipulated by adjusting bis-acrylamide components. However, the modulus of this PA gel was rather low, ranging from 0.002 to about 50 kPa [56, 98-101]. Another stiffer material is poly(dimethyl siloxane) silicone (modulus:1.5–2,000 kPa) [102-104]. Its stiffness could be manipulated by adjusting curing agent ratio and baking time [102, 103], using photolithography to generate a micro-pillar pattern surface [104], or photo-crosslinking with light sensitive chemicals [105]. Hydrogel systems could be used to study surface stiffness by manipulating crosslinking degree such as poly(HEMA) (poly(2-hydroxyethyl methacrylate)) [106] and hyaluronic acid (HA)/poly(ethylene glycol) di-acrylate (PEGDA) [107]. However, the crosslinked hydrogel has side effects. For example, the swelling ratio of HA/PEGDA was

decreased, while the modulus was increased when decreasing HA content [107]. Besides hydrogel system, polyelectrolyte multilayer (PEM) could also be used to study surface stiffness. The stiffness is adjusted either by crosslinking [108] or changing pH to manipulate the tightness of polyelectrolyte-layer packing during the assembly [109]. Examples of PEM systems are poly(L-lysine)/ hyaluronan [108] and poly(acrylic acid) /poly(acrylamide) [109].

The use of plasma to increase surface stiffness has been explored by Bartalena *et al.* using air plasma as an intermediate to hydrophilize PDMS surface before submersing the surface in amino-propyltriethoxysilane (APTES), then UV-crosslinking with sulfo-SAN-PAH [105]. Their procedure generated a thin and stiff plasma-assisted-oxidized layer (296 nm thickness and 3.66 MPa elastic modulus) on a thick PDMS (10 mm thickness and 10.5 kPa elastic modulus). Both unmodified and plasma-assisted-oxidized PDMS were later used to measure cell stiffness on the surface based on their own developed method [105]. The increased stiffness in Bartalena and co-workers report was not totally attributed to the plasma effect since it involved the crosslinking with other chemicals. Plasma only improved surface wettability before silanization with APTES.

## CHAPTER

### 3. LITERATURE REVIEW

#### 3.1 An introduction to plasma treatment as a surface modification tool

Plasma treatment is an effective tool to modify surface of various materials used in the biomedical applications. The treatment induces the change of surface wettability, introduces the selective functional groups, and changes electrostatic charges on the surface. The treated surface could be ready for use or further treated with other techniques. Plasma gas is chosen based on the desired surface functionality. The plasma is usually generated by radio frequency power supply at frequency of 13.56 MHz. The AC power supply is less frequently used. However, in our laboratory, we have successfully used it for plasma treatment [42, 43]. Apart from our laboratory, there was only one report published in Biomaterials during the past 10 years. Anderson *et al* [41] used phase shifted AC100Hz power supply to generate argon plasma for the polymerization of 1-vinyl-2-pyrrolidone (VP) on the silicon rubber surface to reduce the activation of blood coagulation.

The range of investigated materials in plasma treatment covers from metal, glass, synthetic polymer, biodegradable polymer, and natural polymer. Most researchers put their efforts to study plasma treatment effects on synthetic polymers and metals [17-20, 22, 25-27, 30-34, 36, 39-41, 45-49, 52, 54, 86, 87, 93, 110-113]. There were a few reports of using plasma to treat natural polymers [23, 24, 37, 38, 42-44]. Our laboratory is exploring the use of plasma to improve biocompatibility of natural polymer [42-44]. There have

been two reports of using plasma to treat silk fibroin materials in Biomaterials in the past 10 years. Both reports used microwave argon plasma to treat silk fibroin surface to improve biocompatibility and chondrogenic responses of articular chondrocytes on silk fibroin surface [23, 24].

Table 3-1 The selected examples of materials which have been treated with various types of plasma

Type of material	Material	Plasma gas	No. of reports	Plasma generator type				
				AC	DC	Conventional RF	Microwave RF	Unidentified
Synthetic	Nafion	Ar	1			1 [25]		
Polymers (non-degradable)	Nylon-6	NH <sub>3</sub>	1			1 [26]		
	PDMS	O <sub>2</sub> , Ar, N <sub>2</sub> , NH <sub>3</sub>	1			1 [27]		
	PE	O <sub>2</sub> , N <sub>2</sub> , CF <sub>4</sub> , Ar, NH <sub>3</sub>	3			3 [27-29]		
	PEEK-WC-PU <sup>3</sup>	H <sub>2</sub> , NH <sub>3</sub>	1			1 [30]		
	PET	O <sub>2</sub> , NH <sub>3</sub>	3			1 [31]		2 [48, 111]
	PHB	NH <sub>3</sub> , H <sub>2</sub> O	1				1 [47]	
	PP	O <sub>2</sub> , NH <sub>3</sub>	2			2 [26, 31]		
	PS	O <sub>2</sub> , N <sub>2</sub> , CF <sub>4</sub> , Ar, NH <sub>3</sub> , (CH <sub>3</sub> ) <sub>2</sub> CO, (CH <sub>3</sub> ) <sub>2</sub> CHOH	6			2 [28, 29]	4 [45, 46, 49, 54]	
	PTFE	O <sub>2</sub> , Ar, N <sub>2</sub> , NH <sub>3</sub> , CO <sub>2</sub> , H <sub>2</sub> O, H <sub>2</sub>	7			4 [27, 32-34]	2 [22, 112]	1 [48]
	PU silicone rubber	O <sub>2</sub> , Ar, N <sub>2</sub> , NH <sub>3</sub> Ar	1 1	1 [41]		1 [27]		
<b>Total</b>			<b>28</b>	<b>1</b>		<b>17</b>	<b>7</b>	<b>3</b>
Biodegradable	PLGA	O <sub>2</sub> , CO <sub>2</sub>	3			3 [17, 19, 35]		
synthetic polymers	PLLA	Ar, NH <sub>3</sub>	2			1 [36]		1 [113]
<b>Total</b>			<b>5</b>			<b>4</b>		<b>1</b>
Natural	Chitosan	Ar	1			1 [37]		
Polymers	corn starch-based biomaterials (SBB) blend	O <sub>2</sub>	1			1 [38]		
	Gelatin	O <sub>2</sub> , Air, N <sub>2</sub>	3	2 [42, 43]	1 [44]			
	Silk fibroin	Ar	2				2 [23, 24]	
<b>Total</b>			<b>7</b>	<b>2</b>	<b>1</b>	<b>2</b>	<b>2</b>	
Others	316L SS	NH <sub>3</sub> , Ar	1			1 [20]		
	Titania nanotube	Allylamine	1			1 [39]		
	Titanium	NH <sub>3</sub> , Ar, Allylamine	2				1 [18]	1 [110]
	glass slip	Allylamine & Hexane	1			1 [40]		
<b>Total</b>			<b>4</b>			<b>3</b>	<b>1</b>	<b>1</b>
<b>Grand total</b>			<b>45</b>	<b>3</b>	<b>1</b>	<b>26</b>	<b>10</b>	<b>5</b>

The selected examples of selected plasma treatment papers which were published for the past ten years are shown in Table 3-1. Regards to the type of plasma generators, microwave plasma could generally provide higher

<sup>3</sup> PEEK-WC-PU modified polyether-ether-ketone with cardo group (PEEK-WC) and polyurethane (PU)

plasma power in the scale of hundreds of watts, while the AC plasma provides the lowest plasma power in the single digit of watt. The summary of plasma power from the selected papers is shown in Table 3-2.

Table 3-2 Summary of operating power conditions of various plasma type from the selected papers

Plasma type	Plasma operating power (w)		
	Minimum	Typical	Maximum
AC [41-43]	2	4	12
Conventional RF [17, 19, 20, 25-40]	10	30	2,000
Microwave RF [18, 22-24, 45-47, 49, 54, 112]	120	400	1,000

Besides plasma generator type and operating power, it is worth to mention base pressure because it could indicate the level of contamination in the system. Base pressure is the pressure of plasma chamber before the introduction of plasma gas. Plasma chamber needs to be evacuated to minimize unwanted gaseous species such as air and moisture. The lower base pressure gives higher effect from the studied plasma gas. The lowest base pressure has been reported at  $1 \times 10^{-8}$  mbarA [29], while the highest was at  $1 \times 10^{-1}$  mbarA [19]. Most researchers reported the base pressure below  $1 \times 10^{-3}$  mbarA [22, 26, 29, 30, 37, 44-47, 49, 54, 112].

Even though the results from different plasma machines could not be compared due to the different setup and operating conditions, but the intent of the following discussion was to present a broad overview of plasma treatment.

## 3.2 The effects of different plasma gases

### 3.2.1 Argon

The intention of argon plasma is to create the free radicals on the surface. If the treated surface is exposed to the air after treatment, it will react with oxygen and nitrogen. Wu *et al* [37] reported that the increase of oxygen and nitrogen atoms, after the argon plasma treatment on the chitosan film. The results of high-resolution XPS spectra for the C1s region, showed that amine (C-NH<sub>2</sub>), alcohol (C-OH), and carbonyl (-C=O) groups were increased from the untreated value of 7.3, 21.6, 9.7 to 10.5, 25.6, 21.7% respectively after 20 minutes of argon plasma treatment. Their findings confirmed their hypothesis about the post-plasma reaction between the surface activated sites and air. Ding *et al* [36] also reported an increase of the ratio of oxygen to carbon (O/C) on PLLA from 0.64 to 0.83 after a 30 second of argon plasma treatment. They did not notice an increase of nitrogen content after argon plasma treatment. The differences between Ding *et al* [36] and Wu *et al* [37] were the treatment time and RF frequency. Wu *et al* used higher RF frequency 13.56 MHz and treatment time of 20 minutes, while Ding *et al* used 20 kHz and 30 seconds treatment time. Rhodes *et al* [27] noted an interesting point that if the argon plasma treated samples were stored in phosphate buffer solution (PBS) immediately after treatment, there would only be oxygen species without any nitrogen species on the samples after air exposure.

Argon plasma is usually employed as a pre-treatment to generate free radicals for subsequent treatment such as plasma polymerization. Anderson *et al* [41] pre-treated silicon rubber with argon plasma for 2 minutes to activate free radicals, before subsequently 20 minutes treatment with plasma polymerization of 1-vinyl-2-pyrrolidone (VP) which is a non-toxic compound

used in polymer blends to increase blood compatibility of dialysis membranes. Valdes *et al* [25] pretreated Nafion, a membrane material in biosensors, with argon plasma for 2 minutes before plasma polymerization of tetraethylene glycol dimethyl ether (for enhancement of non-fouling properties) for 18 minutes, and (2) 2-hydroxyethyl methacrylate (HEMA, for biocompatibility and addition of hydroxyl group content) for 20 minutes. Argon is also used as a carrier gas in plasma polymerization [18, 20]. The other use of argon plasma is for covalent fixation of coating material on the surface. Nitschke *et al* [49] used argon plasma to covalently fix poly(vinyl methyl ether-alt-maleic acid) (PVMEMAc) on the polystyrene surface.

In summary, argon plasma generates free radicals on surface without conjugating itself on the surface. The change of surface chemistry of argon treated surface is caused by either air exposure or subsequent treatment.

### 3.2.2 Oxygen

Oxygen plasma has received much attention from researchers [19, 27-29, 31, 34, 35, 38, 42, 43, 111, 112]. Oxygen plasma creates oxygenated species on the surface such as hydroxyl (-C-OH), carbonyl (-CR=O), and carboxyl (-COOH) [35, 38]. The same oxygenated species are also on the surface of tissue culture polystyrene (TCPS) which has approximately 7.4% hydroxyl, 1.8% carbonyl, and 2.5% carboxyl with the total oxygen content of 11.8% [46].

The oxygen plasma treatment produces a negatively charged surface. Prasertsung *et al* [42] demonstrated that the isoelectric point (IEP) of gelatin was decreased from 8 to 7 after a 30 second treatment of oxygen plasma. The lower IEP indicated the introduction of negatively charged species on the surface [112]. Shen *et al* [19] treated PLGA with oxygen plasma to generate negatively charged surface before conjugating with cationized gelatin. The XPS

results showed that the combining oxygen treatment with cationized gelatin increased the gelatin anchorage on the PLGA surface. The XPS spectra before and after washing were not greatly different. Qu *et al* [35] also treated PLGA with oxygen plasma and then incubated it in a modified simulated body fluid to prepare a bone-like apatite layer. They expected the negative charge would draw the positive calcium ions and deposit them on the PLGA. Both calcium and phosphate depositions were enhanced tremendously compared with the untreated ones. The calcium content was increased from 3.84 to 15.1% after a 30 minute treatment of oxygen plasma. However, Ca/P ratio was still much lower than the hydroxy apatite stoichiometric ratio.

### **3.2.3 Other gases used for the generation of oxygenated species**

#### **A. Carbon dioxide**

Shen *et al* [17] used carbon dioxide as plasma gas because they expected more carboxylic groups on the surface. The carboxylic content was increased from 30.2 to 41.0% after a 30 minute treatment of carbon dioxide plasma on PLGA surface (20W, RF13.56 MHz). They also performed the oxygen plasma treatment on their PLGA [19] but they did not report the carboxylic content from XPS. Qu *et al* [35] also used PLGA but they treated it with an oxygen plasma. They reported the carboxylic content was increased from 35.6 to 39.7% after a 30 minute treatment of oxygen plasma on PLGA surface (20W, RF13.56 MHz). The comparison of two papers on same material (PLGA) with different plasma gases (CO<sub>2</sub> vs. O<sub>2</sub>), suggested that carbon dioxide might be better to enhance carboxylic content. However, the experiment needs to be set up to verify that carbon dioxide could provide more carboxylic groups than other gases.



### B. Isopropyl alcohol and Acetone

Mitchell *et al* [46] used isopropyl alcohol (IPA) plasma to generate only hydroxyl and carbonyl on the surface of polystyrene. The carboxylic groups were not introduced on the surface by this IPA plasma. The cell attachment and proliferation on IPA plasma treated surface was comparable with tissue culture PS plate. Mitchell *et al* [45] also proved that acetone plasma could also be used to generate oxygenated compounds such as hydroxyl, carbonyl and carboxyl on PS surface.

### C. Water vapor

Water vapor plasma could be used to generate oxygenated species on surfaces. The most significant point about this plasma is its long sustaining effect on plasma treatment. König *et al* [22] reported that the effect from H<sub>2</sub>O plasma treatment still existed after 6 months. Nitschke *et al* [112] also reported that no hydrophobic recovery from H<sub>2</sub>O plasma treated PTFE was observed in several weeks later.

### 3.2.4 *Nitrogen containing gases (NH<sub>3</sub>, N<sub>2</sub> and allylamine)*

#### 3.2.4.1 *Ammonia and nitrogen*

Both ammonia and nitrogen plasmas are designed to implant nitrogen species such as amine on surfaces [26, 30, 49, 54]. Amine was reported to improve cell adhesion on material surfaces [48].

Ammonia plasma could be used to create positively charged surface for subsequent conjugation with negatively charged molecules. Nitschke *et al* [112] used ammonia plasma treatment on poly(tetrafluoroethylene-co-hexafluoropropylene) (FEP) to create a positively charged surface, and then added anionic poly (sodium 4-styrene sulfonate) (PSS). The attachment between FEP and PSS was electrostatic interaction.

The free amino from ammonia plasma could also be used to react with other reactive molecules such as maleic acid to form anhydride. The anhydride moieties are powerful for covalent bonding with other bioactive molecules without a crosslinking agent. Nitschke *et al* [49] used ammonia plasma to treat polystyrene. The induced free amine on PS surface, then reacted with poly(ethylene-alt-maleic acid) (PEMAC) to form anhydride functionality on the surface.

#### 3.2.4.2 *Allylamine in Plasma polymerization*

Allylamine is used as monomer in plasma polymerization process. Plasma reaction initiates free radicals in allylamine molecules for polymerization process. The amine-rich polymer layers will be coated on the treated surface. The additional amine could be further used to increase the conjugation amount with other bioactive molecules. Plasma polymerization of allylamine has been investigated by many researchers [18, 20, 39, 40]. Ammonia plasma

treatment could not alter negatively charged surface to positively charged surface because  $\text{NH}_3$  plasma treatment could not induce sufficient positive ions to dampen the negatively charged surface. Plasma polymerization of allylamine addresses this issue. The thickness could be controlled to ensure that the outermost layer expresses positive amine species [18].

### 3.2.5 Hydrogen

Pavlica *et al* [30] used hydrogen plasma as a pre-treatment to crosslink and stabilize PEEK-WC-PU<sup>4</sup> membranes before ammonia plasma treatment. They believed that the pre-treatment could reduce the hydrophobic recovery of the final treated sample surface. They reported the stability of water contact angle for the period of 8 days. The membrane without hydrogen plasma pre-treatment, returned to its original contact angle within 8 days.

## 3.3 The introduction of other molecules on surface by plasma treatment

Plasma treatment could be employed to introduce others molecules on the surface. The plasma generates either reactive species for the surface reaction or charged molecules for electrostatic adsorption. There are several methods to introduce other molecules on the surface such as grafting polymerization (grafting from), surface reaction (grafting to), plasma immobilization, and electrostatic adsorption [49, 112].

#### A. Grafting polymerization (grafting from)

Surface functional groups could be used as initiators for the polymerization of desired monomer, such as acrylic acid to form

---

<sup>4</sup> PEEK-WC-PU modified polyether-ether-ketone with cardo group (PEEK-WC) and polyurethane (PU)

polyacrylic acid [111, 112]. This grafting polymerization takes place outside the plasma chamber, whereas plasma polymerization is inside at the vapor-solid interphase. The thickness of grafted layers could produce thick layers ranged from a few nanometers up to a few microns. This process usually generates the swellable and soft surface [112]. The grafting is graphically shown in Figure 3-1 (a).

B. surface reaction (Grafting to)

In this “grafting to” technique [Figure 3-1 (b)], the immobilized molecules will react with functional groups on the surface. The reaction could be either with or without crosslinking agents depend on surface functional groups. For example, Yang *et al* [20] used carbodiimide chemistry to crosslink amine, generated by plasma polymerization of allylamine on 316SS, with heparin. Finke *et al* [18] also used carbodiimide chemistry to crosslink amine, generated by plasma polymerization of allylamine on titanium, with collagen. Alternatively, the reaction between maleic anhydride and amine/hydroxyl moieties could be done without using crosslinking agents [49, 54, 112]. The limitation of this technique is the low amount of immobilized molecules on the surface due to the diffusion limitations of immobilized molecules into the grafted layers [112].

C. Plasma immobilization

Argon plasma could be used to crosslink the pre-adsorbed film of immobilized molecules with the surface. The thickness of pre-adsorbed film could be up to few tens of nanometers [112]. The plasma immobilization is pictured in Figure 3-1 (c).

#### D. Electrostatic adsorption

Plasma treatment also generates a charged surface [112]. The charged surface could form electrostatic bonding with oppositely charged molecules, especially polyelectrolytes or proteins because of its amphiphilicity [51, 53, 85]. Nitrogen containing gases such as ammonia, generate a positively charged surface [39, 47, 112]. In contrast, oxygen containing gases such as oxygen, water vapor, carbon dioxide, etc., generate a negatively charged surface [17, 19, 35, 47]. The electrostatic adsorption is graphically shown in Figure 3-1 (d).

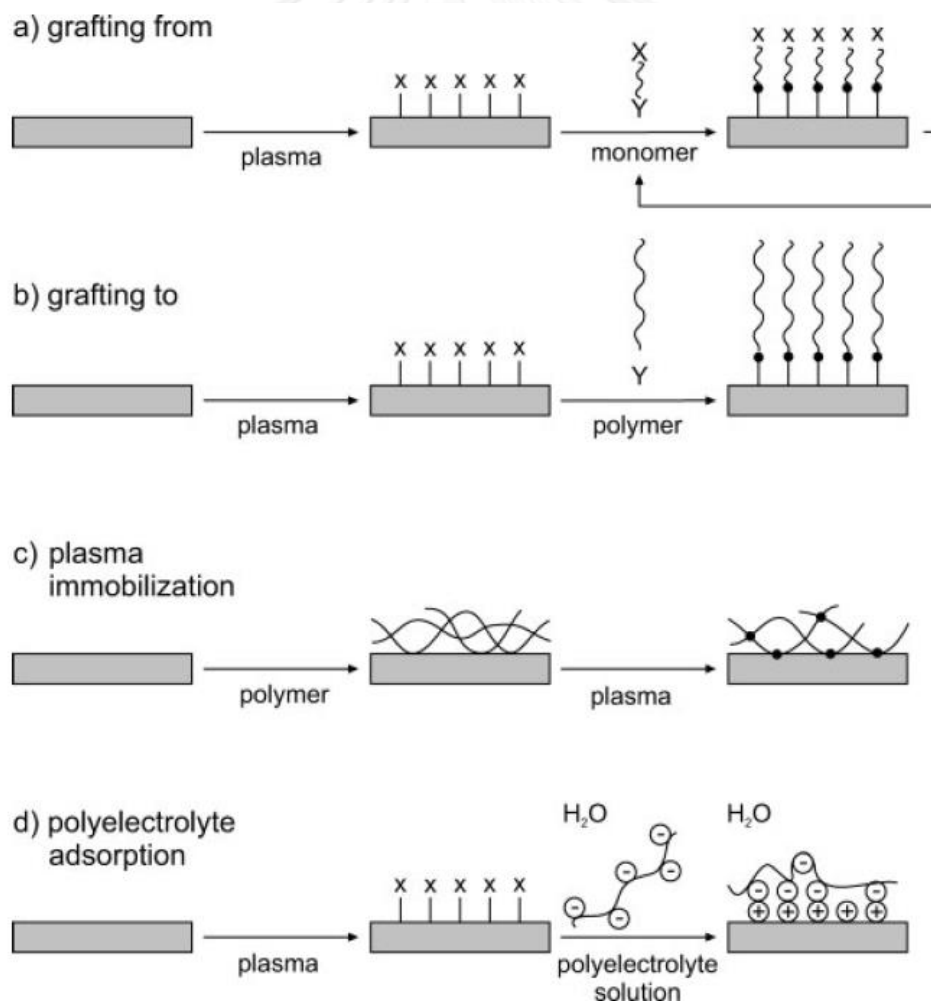


Figure 3-1 The introduction of other molecules on surface by plasma-based techniques

(reproduced from [112])

Many varieties of bioactive molecules could be immobilized on various surfaces with different combinations between plasma surface treatment and other techniques. The summary is in Table 3-3.

**Table 3-3 Summary of the introduction of other molecules on the surface by plasma-based technique from selected papers**

Material	Bonding type	Plasma gas	Introduced molecules	Purpose of further treatment
PLGA	Electrostatic	O <sub>2</sub>	cationized gelatin	To improve cell adhesion [19]
		CO <sub>2</sub>	basic fibroblast growth factor (bFGF)	to control deliver of Basic fibroblast growth factor (bFGF) for enhancing cell adhesion and growth [17]
		O <sub>2</sub>	Ca <sup>2+</sup> , PO <sub>4</sub> <sup>2-</sup>	To induce bone-like apatite layer for enhancing the growth of osteoblast-like cells [35]
PLLA	Immobilization	Ar	Chitosan	Not clear [36]
316L SS	EDC crosslinking	PPAm <sup>5</sup>	Heparin	Prevent blood clotting [20]
Titanium	CDI crosslinking	PPAm	Collagen	Enhance cell growth [18]
Titania nanotube	Grafting to	PPAm	polyethylene glycol (PEG)	Protein resistant surface [39]
	electrostatic	PPAm	polystyrene sulphonate (PSS).	antithrombogenic properties [39]
Nafion <sup>6</sup>	Grafting from	Ar	tetraethylene glycol dimethyl ether 2-hydroxyethyl methacrylate	Enhancing non-fouling characteristics
				Enhancing biocompatibility and increasing OH content. [25]
PET	Grafting from	O <sub>2</sub>	acrylic acid (AA)	generate spacer of polyacrylic acid [111]
	Grafting to	O <sub>2</sub>	poly(ethylene oxide) (PEO), Insulin,& heparin	to produce blood and tissue compatible material [111]
PHB	Electrostatic	NH <sub>3</sub> / H <sub>2</sub> O	Fibronectin	enhance cell matrix adhesion [47]
PS	Grafting to	NH <sub>3</sub>	maleic acid	To create maleic anhydride platform that could conjugate with amine or hydroxyl moieties of various biomolecules without using crosslinking agents. [54]
	Grafting to	NH <sub>3</sub>	poly(vinyl-methyl-ether-alt-maleic acid) (PVMEMAc)	Same as above [49]
	Plasma immobilization	Ar	PVMEMAc	Same as above [49]
PTFE	Grafting to	N <sub>2</sub>	Transpoelastin	Control cell adhesion with cell adhesive protein [32, 33]
	Grafting from	H <sub>2</sub> O	acrylic acid	To generate polyacrylic acid surface [112]
	Grafting to	NH <sub>3</sub>	poly(styrene-co-2,3,4,5,6-pentafluorostyrene) PSF-COOH, poly(2-vinylpyridine) PVP-COOH	To create the chemical responsive surface. Upon treatment with selective solvents (toluene for PSF and acidic water for PVP), the surface wetting behavior can be reversibly switched from ultra-hydrophobic to hydrophilic.[112]
	Plasma immobilization	Ar	poly(acrylic acid) - PAAc poly(ethylene imine) - PEI	PAAc- to induce negatively charged surface PEI - to induce positively charged surface [112]
	Electrostatic	NH <sub>3</sub>	anionic poly (sodium 4-styrenesulfonate) (PSS)	To induce negatively charged surface [112]

<sup>5</sup> PPA-m-plasma polymerization of allylamine

<sup>6</sup> membrane material

### 3.4 Characterization of plasma treatment

The characterization of plasma treatment can be divided into three groups: plasma diagnostics, surface characterization and biological response test of plasma treated surface. Most researchers focused on surface characterization and biological response test of plasma treated surface.

Table 3-4 Summary of all analytical technique performed to characterize plasma treatment from selected papers

Characterization of plasma treatment	References
<b>Plasma diagnostics</b>	
Langmuir probe – - plasma potential ( $V_p$ ), - electron kinetics temperature ( $T_e$ ), - electron number density ( $n_e$ ), - ion kinetics temperature ( $T_i$ )	[29]
Optical Emission Spectroscopy (OES) - Optical emission from plasma excited species	[22, 29, 42]
<b>Surface characterization</b>	
Water contact angle	[17, 19, 20, 22, 24, 27, 30-34, 38, 40, 42-48]
Surface chemistry by X-ray photoelectron spectroscopy (XPS)	[17, 19, 20, 26, 27, 34-38, 40, 42, 45-49]
Surface chemistry by Fourier transform infrared spectroscopy (FTIR)	[20, 22, 24, 28, 29, 31, 33, 37, 38, 43]
Surface topography by atomic force microscopy (AFM)	[17, 24, 31, 35, 37, 42-47]
Storage effect – hydrophobic recovery	[20, 22, 30, 31, 43, 112]
Surface charge	[18, 22, 42, 47, 112]
Film thickness	[18, 20, 22, 28]
Protein adsorption	[17, 31, 47, 54]
<b>Biological response test of plasma treated surface</b>	
Cells	25 different cell types [17-20, 23, 24, 26, 30, 32-38, 40, 42, 43, 45, 46, 48, 54, 110]
Cell adhesion	[17-20, 23, 32, 33, 35, 37, 38, 42-44, 46-48, 110]
Cell proliferation	[19, 20, 23, 24, 34, 36, 38, 44-46, 48, 110]
Cell differentiation	[23, 24, 26, 30, 34, 110]

### 3.4.1 *Plasma diagnostics*

Generated plasma could be characterized in order to determine type, quantity, and energy of plasma active species. The Langmuir probe could be used to measure plasma potential ( $V_p$ ), electron kinetics temperature ( $T_e$ ), electron number density ( $n_e$ ), and total ion kinetics temperature ( $T_i$ ). Optical emission spectroscopy identifies the optical emission from plasma excited species. These plasma diagnostics were hardly performed in plasma treated biomaterial researches [22, 29, 42]. Most researchers omit the plasma diagnostics and only pay attention to the surface chemistries of the treated samples. However, plasma diagnostics are powerful tools which could be used to understand and manipulate the plasma conditions for treatments e.g. plasma input power, operating pressure, etc., that yield the highest density of plasma ions. The Langmuir probe could be used to identify the highest plasma ions density location in the plasma chamber [29].

### 3.4.2 *Surface characterization*

#### 3.4.2.1 *Surface wettability*

Many researchers performed the contact angle measurement [17, 19, 20, 22, 24, 27, 30-34, 38, 40, 42-48]. Most reported the increased hydrophilicity, except one, Wang *et al* [34]. They reported the increase of the water contact angles on PTFE from 107.5° to 127.5 - 153.9° after a 30 minute treatment with O<sub>2</sub> plasma even the hydrophilic groups such as hydroxyl and carbonyl were introduced on the surface. They explained that an increase of surface roughness contributed to the increase of contact angles, when the contact angle of the untreated substrate was above 90°. The finding contradicted with Rhoads *et al* [27] who also used O<sub>2</sub> plasma to treat PTFE. The contact



angle was decreased from 93° to 62° after 1 minute treatment with O<sub>2</sub> plasma. The surface roughness probably was not significantly increased.

Some researchers compared which plasma gases were effective for wettability improvement. König *et al* [22] reported that the hydrophilicity of PTFE was improved in the following order: H<sub>2</sub>O > H<sub>2</sub>/H<sub>2</sub>O (2%) > CO<sub>2</sub> plasma. The water contact angle was reduced from 124° to 84°, 83° and 106° after treatment with H<sub>2</sub>O plasma for 60 seconds, H<sub>2</sub>/H<sub>2</sub>O (2%) plasma for 240 seconds, and CO<sub>2</sub> plasma for 240 seconds, respectively.

Pompe *et al* [47] found that H<sub>2</sub>O plasma could better improve the hydrophilicity of poly(hydroxybutyrate), PHB, than NH<sub>3</sub> plasma. The water contact angle of PHB was reduced from 80.9° to 60.3° and 71.2° after a 60 second treatment of H<sub>2</sub>O plasma and a 300 second treatment of NH<sub>3</sub> plasma, respectively.

#### **3.4.2.2 Surface chemistry**

X-ray photoelectron spectroscopy (XPS) and Fourier transform infrared spectroscopy (FTIR) are common tools for investigating surface chemistry of material. The difference between these two is the depth of analysis. XPS reveals approximately 5 nm of the outermost layer, while FTIR picks up several microns [22]. XPS [49, 55-57, 59, 61-65, 69-72, 75, 78, 81] is more popular for measuring the change of surface chemistry than FTIR [20, 22, 24, 28, 29, 31, 33, 37, 38, 43]. If the intended surface chemistries are similar to the bulk chemistries, FTIR could not be used to detect a change of surface chemistry. Alves *et al* [38] reported that no difference of FTIR spectra was found between untreated and O<sub>2</sub> plasma treated samples. The samples were corn starch blend with cellulose acetate, ethylene vinyl alcohol and polycaprolactone. All samples had carbon-oxygen bonds. The change of

surface oxygen containing moieties was minimal when they were combined with bulk chemistry. On the other hand, if the bulk chemistry is totally different from surface chemistry, FTIR will be an effective tool for detecting change in plasma treatment. Meichsner *et al* [29] noticed the difference of treated polyethylene (PE) with O<sub>2</sub> plasma using FTIR. PE does not have carbon to oxygen bond, so oxygen implanted species could be detected on O<sub>2</sub> plasma treated PE using FTIR.

There is currently no report to compare which oxygen containing gases (O<sub>2</sub>, CO<sub>2</sub>, H<sub>2</sub>O, alcohol and acetone) are effective to generate hydroxyl, carbonyl and carboxyl bonds. Only Mitchell *et al* [46] reported that isopropyl alcohol (IPA) plasma could be used to generate only hydroxyl and carbonyl, without carboxylic group on the surface of polystyrene. However for nitrogen containing gases (N<sub>2</sub>, NH<sub>3</sub>), Meyer-Plath reported that ammonia is more effective for generating amine on the surface than nitrogen or the mixture between N<sub>2</sub> and NH<sub>3</sub> [57].

### **3.4.2.3 Surface topography**

In most cases, plasma treatment could increase surface roughness less than 10 nanometers. In some cases, there was no difference in surface roughness before and after treatment [42, 45-47]. Mitchell *et al* [46] reported that the change of surface roughness from 3.5 to 9.5 nm was not significant to influence cellular attachment or proliferation. The summary of plasma effect on surface topography is shown in Table 3-5.

Table 3-5 The selected examples of the change of surface topography from plasma treatment

Material	Plasma type	Power (W)	Plasma gas	Treatment time	Ref	Surface roughness (nm)		
						Surface Parameter	Before treatment	After treatment
Chitosan	RF	40	Ar	20 min	[37]	Ra <sup>7</sup>	1.98±0.7	5.47 ± 0.9
Gelatin	AC50Hz	12	O <sub>2</sub>	15 sec	[43]	RMS <sup>8</sup>	0.5	4.5
		4	Air, O <sub>2</sub> , N <sub>2</sub>	30 sec	[42]	RMS	0.48	not change
	PICP	-	N <sub>2</sub>	1 pulse	[44]	RMS	0.488 ± 0.033	1.075 ± .087
PET,PP	RF	80	O <sub>2</sub>	120 sec	[31]	RMS	3.84 ± 0.63	9.59 ± 1.06
PHB	MW	400	NH <sub>3</sub> /H <sub>2</sub> O	300 sec	[47]	RMS	not change	
PLGA	RF	20	O <sub>2</sub>	30 min	[35]	Ra	0.406	4.937
		20	CO <sub>2</sub>	20 min	[17]	Ra	0.4	16.8
PS	RF	10	isopropyl alcohol	3600 s	[46]	RMS	not change	
		10	Acetone	600 s	[45]	RMS	not change	

#### 3.4.2.4 The effect of air exposure after plasma treatment

Some researchers reported the presence of nitrogen (N) or oxygen (O) atoms which were not supposed to be on the surface because these atoms were not contained in the plasma gas [26, 27, 37, 38, 42, 48]. The introduction of these atoms might be either inside or outside plasma chamber. Air remaining inside plasma chamber could induce N and O atoms on the treated surface during plasma treatment. On the other hand, the plasma reactive species might react with air outside plasma chamber after the treatment.

Only Pompe *et al* [47] did not find the surface moieties which were not generated from plasma gas. They evacuated the plasma chamber to the very low vacuum pressure of  $1 \times 10^{-7}$  mbar. Their findings supported that the source of the unintended moieties were from the air remaining inside plasma chamber and there would be no surface reaction after plasma treatment if the base pressure was at  $1 \times 10^{-7}$  mbar before the introduction of plasma gas.

<sup>7</sup> Ra – arithmetic mean of surface roughness

<sup>8</sup> RMS – root mean square of surface roughness

Other researchers, who either operated at higher base pressure than  $1 \times 10^{-7}$  mbar or did not reported base pressure, found the unintended O and N atoms [26, 27, 36-38, 42, 48]. For example, Mwale *et al* [26] found oxygen atoms on  $\text{NH}_3$  treated BOPP and Nylon-6, even though they operated at a very low base pressure of  $1 \times 10^{-6}$  mbar.

Regarding surface reaction after plasma treatment, König *et al* [22] found that there was surface reaction, even though the base pressure was at  $1 \times 10^{-7}$  mbar before the introduction of plasma gas. They introduced nitric oxide (NO) on  $\text{H}_2\text{O}$  plasma treated samples that still were inside plasma chamber without breaking vacuum. The samples before and after NO introduction were analyzed with XPS without breaking vacuum. They found that nitrogen atoms were introduced on the surface. They suspected that the free radicals from plasma treatment still remained and reacted with NO.

Another notable point from Rhodes *et al* [27] was that the storage conditions of the plasma treated samples might contribute to the presence or absence of air contaminated species. They detected only oxygen atoms but did not find any nitrogen atom on the  $\text{O}_2$  and Ar plasma treated UHWPE. They had submersed plasma treated samples in distilled water right away after plasma treated for 24 hours. The storage in water could not really confirm the absence of nitrogen atom from the air contamination in plasma chamber since they might be dissolved during water storage. Meanwhile, the presence of oxygen atoms might be generated from the reaction between plasma treated surface and water.

From the currently available reports, it was suggested that there is the surface reaction after plasma treatment. However, it needs further investigation of this assumption. The air exposure effect on plasma treated surface is summarized in Table 3-6.

Table 3-6 The selected examples of air exposure effect on the surface chemistry change.

Material	Plasma type	Plasma Power (watt)	Treatment time (sec)	Base pressure (mbar)	Operating pressure (mbar)	Plasma gas	Nitrogen content (% or N/C)		Oxygen content (% or O/C)	
							Before	After	Before	After
Gelatin [42]	AC50Hz	4	30	0.3	1	N <sub>2</sub>	9.5%	15.8%	20.4%	21.4%
						O <sub>2</sub>	9.5%	9.7%	20.4%	30.6%
PET	-	-	-	-	-	NH <sub>3</sub>	-	-	0.267	0.354
PTFE [48]						NH <sub>3</sub>	0	0.109	0	0.138
PLLA [36]	RF	32	30	-	7.7 × 10 <sup>-1</sup>	Ar	-	-	0.64	0.83
UHWPE <sup>9</sup> [27]	RF	-	60	-	8 × 10 <sup>-2</sup>	O <sub>2</sub>	0	0	0.02	0.18
						Ar	0	0	0.02	0.18
						N <sub>2</sub>	0	0.12	0.02	0.15
						NH <sub>3</sub>	0	0.07	0.02	0.21
SBB <sup>10</sup> [38]	RF	100	180	2.67 × 10 <sup>-1</sup>	-	O <sub>2</sub>	0.07%	1.05%	35.19%	41.37%
Chitosan [37]	RF	40	1,200	1 × 10 <sup>-3</sup>	4 × 10 <sup>-1</sup>	Ar	3.52%	7.11%	15.12%	25.31%
BOPP <sup>11</sup>	RF	20	30	1 × 10 <sup>-6</sup>	4 × 10 <sup>-1</sup>	NH <sub>3</sub>	0	14%	0	5%
Nylon-6 [26]						NH <sub>3</sub>	9%	17%	15%	20%
PHB <sup>12</sup> [47]	MW	400	60	1 × 10 <sup>-7</sup>	7 × 10 <sup>-3</sup>	H <sub>2</sub> O	0	0	0.4	0.45
			300			NH <sub>3</sub>	0	0.04	0.4	0.32

### 3.4.2.5 Stability of plasma treated surface (hydrophobic recovery)

The stability of plasma treatment effects depends on the storage ambient conditions. Both König *et al* [22] and Chen *et al* [31] investigated the increase of water contact angle (hydrophobic recovery) of plasma treated surface in different storage mediums (air and water). König *et al* [22] stored CO<sub>2</sub> plasma treated PTFE in both air and water. After 2 weeks, there was complete hydrophobic recovery of PTFE stored in air. However, if the samples were stored in water, the water contact angle was reduced from 106° to 77° within 10 days and leveled off afterward.

<sup>9</sup> The samples were immediately put in distilled water after plasma treatment for 24 hrs.

<sup>10</sup> SBB - corn starch-based biomaterials (SBB) blend

<sup>11</sup> BOPP - Biaxially oriented Polypropylene

<sup>12</sup> PHB - poly(hydroxybutyrate)

Chen *et al* [31] found the contrary results that the storage in water caused faster hydrophobic recovery than in air. They investigated the stability of O<sub>2</sub> plasma treated PET and PP. After storage in water for a short time (24 hrs), the water contact angle of plasma treated PET was increased from  $36.63 \pm 1.59^\circ$  to  $49.42 \pm 0.87^\circ$  and that plasma treated PP was increased from  $55.63 \pm 1.05^\circ$  to  $73.21 \pm 1.67^\circ$ . They explained that water might dissolve the O<sub>2</sub> plasma-implanted species on the surface, so the remaining species on the surface were less than the air storage surface. After 90 days of storage, the surface of both PET and PP were still more hydrophilic than the untreated ones. The water contact angles of plasma treated PET were  $59.14 \pm 2.33^\circ$  (in water) and  $48.43 \pm 2.58^\circ$  (in dry air), while those of plasma treated PP were  $81.72 \pm 2.15^\circ$  (in water) and  $71.20 \pm 3.49^\circ$  (in dry air). In comparison to the untreated PET and PP, the water contact angles were  $85.93 \pm 2.11^\circ$  and  $103.22 \pm 3.46^\circ$ , respectively.

Presertsung *et al* [43] investigated the storage temperature effect (5°, 20°, 50° C) on the hydrophobic recovery of O<sub>2</sub> plasma treated gelatin films. After 7 days storage in air, they found that the higher storage temperature condition yielded a higher water contact angle.

Another interesting point which König *et al* [22] discovered, is that H<sub>2</sub>O plasma preserved the treatment effect for over 6 months. Pavlica *et al* [30] also reported that pre-treatment hydrogen plasma reduced the hydrophobic recovery of the ammonia plasma treated PEEK-WC-PU<sup>13</sup> membranes. They reported the stability of water contact angle for a period of 8 days.

Nitschke *et al* [112] found that electrostatic coating of the polyelectrolyte helped to reduce the hydrophobic recovery. Poly(sodium

---

<sup>13</sup> PEEK-WC-PU modified polyether-ether-ketone with cardo group (PEEK-WC) and polyurethane (PU)

4-styrene- sulfonate) was coated on the ammonia plasma treated poly (tetrafluoro- ethylene-co-hexafluoropropylene) surface. The water contact angle of the surface was increased less than 10° in a period of 30 days, compared with 20° increase for the non-coated ammonia plasma treated surface.

### 3.4.2.6 Surface charge

Surface zeta potential is a tool to investigate the surface charge, little used by few researchers [18, 22, 47, 112]. As previously mentioned in section 3.2, oxygen containing gases (H<sub>2</sub>O, O<sub>2</sub>, CO<sub>2</sub>, etc.) could generate a negatively charged surface, whereas nitrogen containing gases (N<sub>2</sub>, NH<sub>3</sub>) generate a positively charged surface. An example of surface charge (zeta potential) changes from the untreated surface by plasma treatment or surface coating, is summarized in Table 3-7.

Table 3-7 Isoelectric point of various material surfaces (untreated and treated surface) from the zeta potential measurement

Material	Negatively charged induction				Untreated	Positively charged induction	
	PSS <sup>14</sup> coating	PAAc <sup>15</sup> coating	H <sub>2</sub> O plasma	CO <sub>2</sub> plasma		PEI <sup>16</sup> coating	NH <sub>3</sub> plasma
PTFE [22]			<3	3.5	4		
PTFE [112]		<3			3.5	5.6	
PHB <sup>17</sup> [47]			<3		3.5		6.7
FEP <sup>18</sup> [112]	<3				4		6.8

<sup>14</sup> anionic poly (sodium 4-styrene sulfonate) – PSS

<sup>15</sup> poly(acrylic acid) – PAAc

<sup>16</sup> poly(ethylene imine) - PEI

<sup>17</sup> poly(3-hydroxybutyrate) – PHB

<sup>18</sup> poly(tetrafluoroethyleneco-hexafluoropropylene) – FEP

### 3.4.3 Protein adsorption

Only few researchers [17, 31, 47] included the protein adsorption study on the plasma treated surface even though the protein adsorption is the first step of the cell-material interaction process [50, 52, 53]. The protein adsorption studies could be performed by different methods such as ATR-FTIR spectra for polymers containing no amide bonds [31], fluorescent labeling of interested protein [47], or protein immune assay kit [17].

Both Pompe *et al* [47] and Chen *et al* [31] reported that untreated hydrophobic polymer adsorbed more proteins than plasma treated polymers. Pompe *et al* [47] used fibronectin as a model protein on H<sub>2</sub>O and NH<sub>3</sub> plasma treated poly(hydroxy-butyrate) surfaces. While Chen *et al* [48] used fibrinogen and human serum albumin on O<sub>2</sub> plasma treated PET and PP surfaces. Both reports are not surprising and agree with protein adsorption theory, that proteins have a tendency to adsorb on a hydrophobic rather than a hydrophilic surface. The hydrophobic surface has an interaction with the protein hydrophobic core, which results in denaturing protein conformation. The denatured proteins have more surface area to anchor onto the material surface, which leads to stronger protein-surface interaction [51, 53, 85].

Shen *et al* [17] found that CO<sub>2</sub> plasma treatment led to an increase of basic fibroblast growth factor (bFGF) adsorption on PLGA than the untreated ones. They explained that the net positive-charge bFGF (pI=10) might form electrostatic interaction with the negatively charged PLGA induced by CO<sub>2</sub> plasma treatment. The CO<sub>2</sub> plasma treated PLGA could adsorb up to 66.3% bFGF from 200  $\mu$ l of 500 ng/ml bFGF solution, while the untreated one could only achieve 16.1% of bFGF. They explained that the negatively



charged surface of CO<sub>2</sub> plasma treated PLGA formed electrostatic interaction with the positively charged bFGF (Isoelectric point = 10.0). Pompe *et al* [47] also reported the effect of charged surface on the displacement of adsorbed fibronectin. The negatively charged fibronectin (Isoelectric point = 5) was more difficult to replace on positively charged NH<sub>3</sub> plasma treated PHB surface than the negatively charged H<sub>2</sub>O plasma treated PHB surface. The untreated PHB still had the strongest affinity with fibronectin. Their results showed that hydrophobic surface still adsorb more proteins than the charged surface.

Another important aspect of protein adsorption is protein conformation on the plasma treated surface. The adsorbed proteins might lose their biological activities due to the change of the conformation or orientation. The protein biological activities could be evaluated by using monoclonal antibodies to probe at the active site of protein. For example, Keselowsky *et al* [33] used the antibodies 3E3 and HFN7.1 to probe cell binding domain of fibronectin for studying of the protein conformation change. If the protein conformation was changed, the antibodies could not probe into the cell binding domain. However, this study has not been performed on plasma treated surface.

### ***3.4.4 In vitro biological response tests of plasma treated material***

#### ***3.4.4.1 Choice of cells***

Many types of cells have been employed to study biological responses of plasma treated surface. The summary is shown in Table 3-8.

Table 3-8 Summary of cells used for biological response test of plasma treated surface

Cell	References
Mouse 3T3 fibroblasts	[17, 19, 40]
L929 (mouse fibroblasts)	[36, 44]
Human dermal fibroblast	[32, 33]
Transformed human fibroblast cells (1BR.3N)	[45, 46]
Human umbilical vein endothelial cells (HUVECs)	[20, 47, 48, 54]
Mouse bone marrow cell	[110]
Rat bone marrow derived stem cell	[42]
Human mesenchymal stem cells	[26]
MG-63 osteoblastic cells (osteosarcoma cell line)	[18, 38]
OCT-1 osteoblast-like cells	[35]
Primary Rat calvaria osteoblasts	[34]
Immortalized human fetal osteoblastic cell line (hFOB)	[37]
Neonatal human knee articular chondrocytes	[23, 24]
Rat embryonic liver (E-17) cell line (RLC-18)	[30]
L02 (human hepatocytes)	[36]

#### 3.4.4.2 Cell adhesion

Cell adhesion on plasma treated surface is usually studied within the first 24 hours after cell seeding. Most researchers measured the number of cells adhered on the surface. They all reported the improvement of cell adhesion on the plasma treated surfaces [19, 20, 23, 33, 35, 37, 38, 42, 44, 46, 48, 110]. Some researchers investigated the details of cytoskeleton proteins formation such as focal adhesion kinase, paxillin, vinculin, and actin [18, 47]. The good development of cell cytoskeleton on the plasma treated surface was suggested.

Apart from other researchers who studied only cell adhesion in static conditions, Shen *et al* [17] investigated the different aspect of cell adhesion under dynamic condition, by flowing culture medium through the seeded surface. They reported CO<sub>2</sub> plasma treatment with the immobilization of bFGF enhanced 3T3 fibroblasts cell adhesion under these dynamic conditions.

The general explanation for the improvement of cell adhesion is that plasma treatment increases surface wettability or is able to couple bioactive molecules which have cell adhesive properties.

#### **3.4.4.3 Cell proliferation**

All proliferation studies were performed by determining numbers of cell growth on the surface. Most researchers reported the improvement of cell proliferation [17, 20, 24, 34, 44-46, 48, 113] except Kawai *et al* [110]. They reported that the amount of osteoclasts on argon plasma-treated titanium plates was not increased after 1 week of culture.

#### **3.4.4.4 Cell differentiation**

There are a few reports of cell differentiation on plasma treated surfaces, including osteogenic differentiation [26, 34, 35, 110], chondrogenic differentiation [23, 24], and liver cell differentiation [30].

##### **3.4.4.4.1 Osteogenic differentiation**

According to the reports by Curan *et al* [93] and Keselowsky *et al* [94], amine functional group enhanced osteogenic differentiation. The preferred choice of plasma gas should be nitrogen containing gases such as  $N_2$  or  $NH_3$ . However, some researchers have investigated oxygen plasma for enhancing osteogenic differentiation [34, 35].

Qu *et al* [35] used oxygen plasma to create negatively charged PLGA to draw positive calcium ions. They created apatite layers on the surface. Even though they could attract lots of calcium deposited on the surface, but Ca/P ratio was still much lower than hydroxy apatite stoichiometric ratio. Furthermore, the level of alkaline phosphatase

(ALP) enzyme, which represents the early marker of osteogenic differentiation, was not enhanced after 7 days of OCT-1 osteoblast-like cell culture.

Wang *et al* [34] used oxygen plasma to treat PTFE. They found the up-regulate of ALP, osteopontin (OP), osteonectin (ON), osteocalcin (OCN) after 12 days of culture of primary rat calvaria osteoblast cells on the O<sub>2</sub> plasma treated PTFE, compared with the untreated one.

Mwale *et al* [26] used ammonia plasma to treat biaxially oriented polypropylene (BOPP) and Nylon-6. They found that NH<sub>3</sub> treated BOPP suppressed osteogenic differentiation of human mesenchymal stem cells (hMSC). While NH<sub>3</sub> treated Nylon-6 was not conclusive for supporting osteogenic differentiation of hMSC. ALP was up-regulated on day 3, down-regulated on day 7 and back up-regulated on day 14 of culture. For osteogenic differentiation, the ALP level needed to be down-regulated at the later stage of differentiation. The level of osteopontin (BSP) was cyclically up-regulated on the treated surface, as same as ALP. Lastly, there was a slight increase in osteocalcin (OC) expression.

CHULALONGKORN UNIVERSITY

## CHAPTER

### 4. PRELIMINARY STUDY OF PLASMA TREATMENT ON THAI SILK FIBROIN SURFACE

#### 4.1 Materials

1. *Bombyx mori* silkworm cocoon (Nangnoi Srisaket1, Queen Sirikit Sericulture Center, Thailand)
2. Sodium carbonate ( $\text{Na}_2\text{CO}_3$ , Ajax Finechem, Australia)
3. Lithium bromide (LiBr, Sigma-Aldrich, Germany)
4. Dialysis tube (cellulose membrane in 0.1% sodium azide, MWCO 12,000 – 14,000 Da, Viskase, Japan)
5. Glass slip (15/20 mm in diameter, (Menzel Gläser, Germany)
6. Nitrogen gas ( $\text{N}_2$ , 99.99 %, MW 28.01 g/mol, Thai Industrial Gas, Thailand)
7. Untreated and treated tissue culture plates (Corning, USA)
8. Ethanol ( $\text{C}_2\text{H}_5\text{OH}$ , MW 46.04 g/mol)
9. Phosphate buffer saline (PBS, pH 7.4, Bio Basic Inc., Canada)
10. Centrifugal tubes (Corning, USA)
11. Nonpyrogenic serological pipet (Costar®, Corning, U.S.A)
12. Dulbecco's modified eagle medium (DMEM, 10%medium + L-glutamine + AB, Hyclone, Thermo Scientific, USA)

13. Fetal bovine serum (FBS, Hyclone, Thermo Scientific, USA)
14. Penicillin/streptomycin antibiotic (100 U/ml, Hyclone, Thermo Scientific, USA)
15. Trypsin-EDTA (0.25% trypsin with EDTA·Na, Gibco BRL, Canada)
16. 3-(4,5-dimethylthiazol-2-yl)-2,5-diphenyltetrazolium bromide (MTT, Sigma-Aldrich, USA)
17. Dimethylsulfoxide (DMSO,  $(\text{CH}_3)_2\text{SO}$ , MW 78.13 g/mol, Sigma-Aldrich, USA)
18. Glutaraldehyde solution ( $\text{CH}_2(\text{CH}_2\text{CHO})_2$ , 25% v/v, MW 100.12 g/mol, Sigma-Aldrich, USA)
19. Rhodamine phalloidin R415 (Invitrogen, USA)
20. Methanol ( $\text{CH}_3\text{OH}$ , 99.99%, MW: 32.04 g/mol, Acros, Belgium)
21. L929 mouse fibroblast (faculty of dentistry, Chulalongkorn university, Thailand)

#### 4.2 Equipment

1. Digital balance (AL204, Mettler Toledo, USA)
2. Heating oven (ED23, Binder GmbH, Germany)
3. Magnetic stirrer / Hot plate (RCT Basic, Ika labortechnik, Germany)
4. Centrifuge (Universal 320R, Hettich, Germany)
5. Freezer (-20 °C) (Sandenintercool, Thailand)
6. Freezer (-40 °C) (Haier, China)

7. Lyophilizer (CHRIST®, Germany)
8. Autopipette (Eppendorf , Germany)
9. AC 50Hz plasma apparatus
10. Optical Emission spectroscope (OceanOptics, USB4000 charge couple device (CCD) spectrometer
11. Water contact angle and video contact analyzer (Camplus Micro, Tantec Inc, USA)
12. X-ray photoelectron spectroscope (XPS) (ESCALAB 250, VG Scientific, USA)
13. Fourier transform infrared spectroscope (FT-IR, Spectrum GX, Perkin Elmer, UK)
14. Atomic force microscope (MFP-3D Asylum Research, USA)
15. Water bath (1235 PC, Shel-Lab, Sheldon Manufacturing, Inc., USA)
16. Laminar Flow (Thermo scientific, USA)
17. Hematocytometer (Boeco, Germany)
18. CO<sub>2</sub> Incubator (HEPA class 100, Steri-Cycle, Thermo scientific, USA)
19. Micro plate reader (UVM 340, ASYS, Australia)
20. Digital microscope (Eclipse 80i , Nikon Instruments, USA)

### 4.3 Experimental procedures

The experiments in this chapter were set up to evaluate whether plasma surface treatment could improve the biocompatibility of Thai silk fibroin (SF) surfaces. SF surface was a film casted from the SF solution which was prepared from the

cocoon of Nangnoi Srisaket 1 silkworm. An in-house AC 50 Hz power supply was used to generate nitrogen plasma. Nitrogen ( $N_2$ ) was selected for a plasma gas because it could induce nitrogen species such as amine on surfaces. Amine was reported to improve cell adhesion on material surfaces [48, 57]. The plasma operating conditions were optimized by maximizing nitrogen active species using optical emission spectroscopy. The surface characterization included static water contact angle, surface chemistry by XPS, bulk chemistry by FTIR-ATR, and surface topography by AFM. Mouse fibroblast L929 cell line was employed in *in vitro* tests. Early cell adhesion will be evaluated by MTT assay along with F-actin cytoskeleton. The experimental setup was illustrated as a diagram in Figure 4-1.

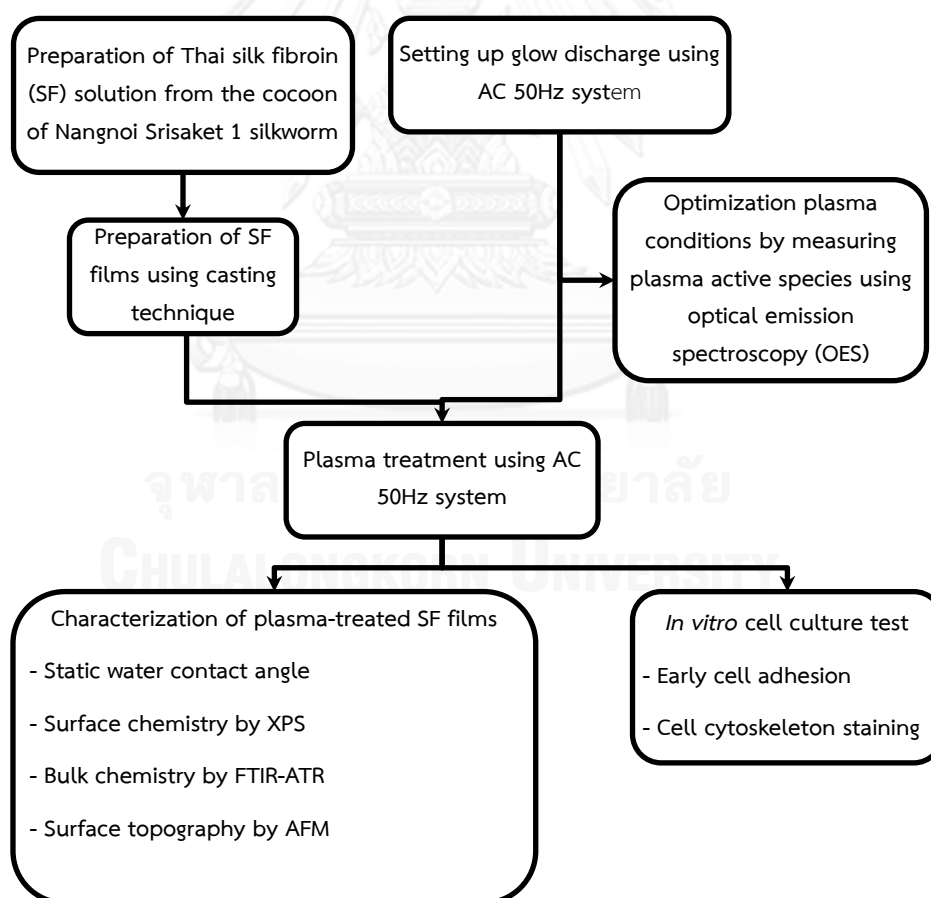


Figure 4-1 Diagram of experimental procedures



#### **4.3.1 Preparation of Thai silk fibroin sample**

Thai silk fibroin solution was prepared according to the method previously described by Kim *et al* [114]. In brief, cocoons were boiled in an aqueous solution of 0.02 M Na<sub>2</sub>CO<sub>3</sub> and then rinsed thoroughly with deionized water to remove sericin or silk gum. The degummed Thai silk fibroin was mixed with 9.3 M LiBr solution with the ratio of 1:3 (by weight). The mixture was stirred occasionally at 60°C until silk fibroin was completely dissolved. The solution was dialyzed in deionized water for 2 days. The dialyzed water was changed regularly until its conductivity was the same as that of the deionized water. The final concentration of Thai silk fibroin aqueous solution was about 6–6.5 wt%.

#### **4.3.2 Preparation of Thai silk fibroin casted films**

Thai silk fibroin film was prepared by solution casting technique using 0.5 wt% solution. The solution (100 µl) was dropped onto a glass cover, and air-dried in clean conditions. After solvent evaporation, methanol was used to induce the beta-sheet formation of silk fibroin structure for 30 minutes [115]. The films were then left air-dried overnight prior to use.

#### **4.3.3 AC50 Hz Glow discharge plasma experimental setup**

The plasma treatment was performed in an in-house built plasma machine using an alternating-current (AC) 50Hz power supply [43]. The configuration of this system is demonstrated in Figure 4-2. The plasma chamber was made of cylindrical glass with two inside circular parallel plate electrodes of 10 cm in diameter. The electrode gap was set at 5 cm. The maximum power is less than 12 watts. Before plasma treatment, Thai silk fibroin films were placed inside the plasma apparatus. Then the chamber was

evacuated to less than 0.1 mbar before the nitrogen was flowed at 5-10 sccm (standard cubic centimeter per minute). Finally, the glow discharged plasma was generated. The treatment times were varied from 5 to 160 seconds.

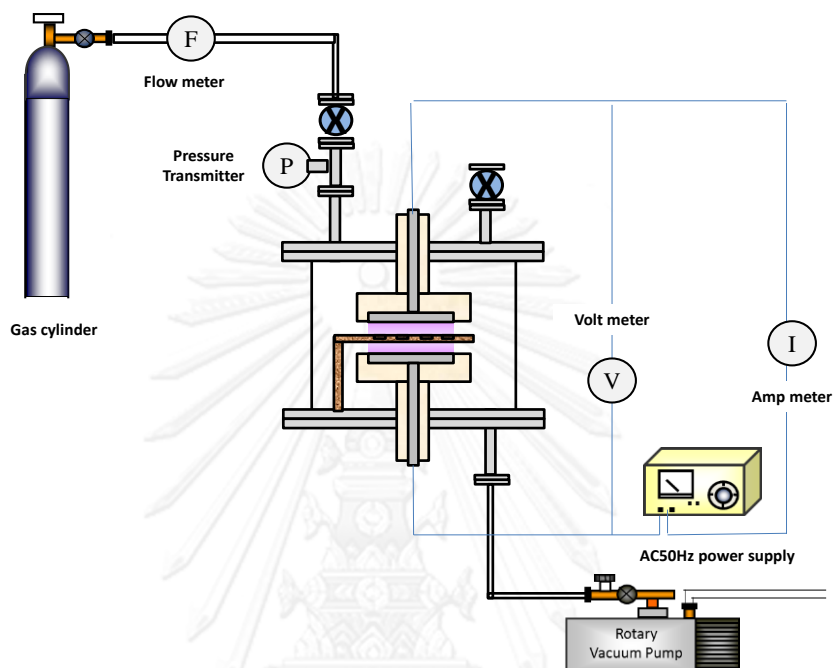


Figure 4-2 The configuration of plasma machine using AC50Hz power supply

#### 4.3.4 Plasma diagnostics using optical emission spectroscopy (OES)

A charge couple device (CCD) spectrometer USB4000 (Ocean Optics, USA) was used to monitor plasma reactive species of nitrogen glow discharge plasma in the wavelength range of 200–1000 nm. The optical emissions were collected using an optical fiber placed in front of the glass chamber. The fiber was connected to the spectrometer through a 10  $\mu\text{m}$  entrance slit. The data were acquired with the Ocean Optics' Spectra Suite software.

#### **4.3.5**      *Characterization of untreated and plasma-treated Thai silk fibroin films*

##### **4.3.5.1**      *Static water contact angle measurement*

Static water contact angle was measured using sessile drooping technique by a contact angle meter Cam-Plus Micro (Tantec, USA). The medium is deionized water at room temperature. The contact angles of the sample were averaged from 3 measurements at 30 seconds dropped.

##### **4.3.5.2**      *Surface chemistry*

The surface chemistry was examined by X-ray photoelectron spectroscopy ESCA LAB250 (VG Scientific, USA) using an Al-K $\alpha$  (1486.6 eV) X-ray source. The pressure in the sample chamber was controlled at  $10^{-8}$ – $10^{-9}$  Torr. The photo-emitted electrons were collected perpendicular to the sample surface. The C1s/N1s XPS spectra were deconvoluted by using OriginPro8.1 SR3 software (OriginLab Corporation, MA, USA).

##### **4.3.5.3**      *Bulk chemistry*

To determine bulk chemistry, Fourier transform infrared attenuated total reflection spectroscopy (FTIR-ATR) spectra were collected by spectrum GX spectrometer (Perkin Elmer, USA). Each spectrum represents the ratio against a reference spectrum obtained by recording scans of an empty ATR cell with uncoated glass cover slip.

##### **4.3.5.4**      *Surface topography*

Surface topography of the plasma-treated and untreated samples was evaluated using MFP-3D atomic force microscope (Asylum Research, USA) in

a tapping mode. The surface topography parameter data were calculated by Gwyddion2.22 software (Czech metrology institute, Czech republic) while three dimensional images were acquired using Asylum Research ARgyle software (USA). The surface parameters were averaged from 4 areas of each sample and expressed as the mean  $\pm$  SD.

#### 4.3.6 *In vitro cell culture test*

##### 4.3.6.1 Early cell adhesion test

The films were placed into 24-well untreated cell-culture plates and sterilized in 70 vol% ethanol for 30 min. Then the films were extensively rinsed with phosphate-buffered saline (PBS). The control surface was a treated-tissue-culture-polystyrene (TCPS). Mouse fibroblast (L929) cell line was used as *in vitro* cell culture model. Cells were seeded onto the films at  $8 \times 10^4$  cells/film ( $417.5 \text{ cells/mm}^2$ ). The cells were incubated at  $37^\circ\text{C}$  in 5%  $\text{CO}_2$  condition using Dulbecco's Modified Eagle Medium (DMEM) containing 15 vol% of fetal bovine serum (FBS) and 100 U/ml penicillin/ streptomycin as culture media. After cell culture for 1.5, 3, 4.5 and 6 h, the films were transferred to a new plate and rinsed with PBS. The adhered cells on surface were evaluated by using MTT assay [116]. In addition, the percentage of adhered cells was calculated according to the following equation:

$$\% \text{ adhered cell} = \left[ \frac{n_1}{n_0} \right] \times 100 \quad (4.1)$$

where  $n_1$  and  $n_0$  are the number of attached cells at a specific culture time and seeded cells, respectively.

#### **4.3.6.2 Cell cytoskeleton staining**

After 4 h and 1 day of culture, attached L929 on the films were fixed in 3 vol% glutaraldehyde solution at 4°C for 30 min. For actin staining, cells were stained with Rhodamine phalloidin R415 (Invitrogen, USA) according to supplier staining protocol which was originally developed for use with NBD phalloidin [117]. The pictures were taken with digital microscope Eclipse 80 i (Nikon Instruments, USA).

#### **4.3.7 Statistical Analysis**

All statistical calculations were performed using MINITAB release 14.12.0 software (Minitab, USA). Statistically significant levels were confirmed by the paired t-test at  $p < 0.05$  ( $n = 3$ ).

### **4.4 Results and Discussion**

#### **4.4.1 Optical Emission Analysis of AC50Hz Plasma**

OES was used to determine the plasma operating condition which provided the highest nitrogen active species. The nitrogen flowrate and the supplied voltage were varied from 5 to 40 sccm and from 40 to 220 V respectively, while electrode gap was controlled at 5 cm.

Before OES measurement, the current and voltage across electrodes were recorded for each nitrogen flowrate during the variation of supplied voltage (40 – 220V) to develop the voltage-current characteristics of nitrogen glow discharge plasma (IV chart). Figure 4-3 illustrates IV chart of one flowrate condition (10 sccm). In this diagram, the supplied voltage was classified

according to plasma appearance which was labelled with three different colors: red labels (40 – 100 V) represented the conditions which plasma was invisible, yellow labels (120 – 140 V) represented the conditions which plasma was visible but not stable across the whole electrode gaps, and green labels (160 – 220 V) represented the conditions which plasma was both visible and stable across the electrode gaps. The data from IV chart provided the plasma power, i.e. the plasma power generated from the supplied voltage of 220V was 11.6W.

$$[\text{plasma power} = 614V * 27mA * 0.7 \text{ power factor} = 11.6 W]^{19}$$

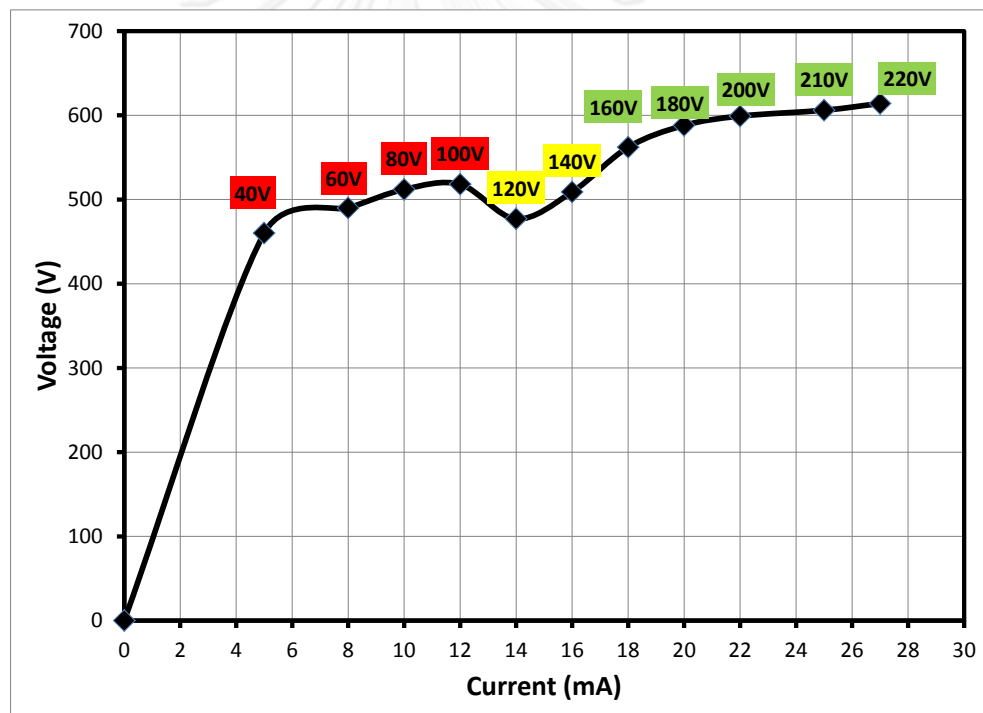


Figure 4-3 Voltage-current characteristics (IV chart) of nitrogen glow discharge plasma at nitrogen flowrate of 10 sccm, electrode gap of 5 cm, and supplied voltage of 40 – 220 V.

<sup>19</sup> Power formula is derived from the dot product of vector current and vector voltage. Power factor is the phase shift between current and power. The data reading from voltmeter and ammeter are in RMS value, not the amplitude.

$$\text{So } P = I_{\text{rms}} * V_{\text{rms}} * \text{Power factor}$$

After IV chart data were collected, OES spectra of each supplied voltage (40 – 220 V) were captured. The active nitrogen species were compared among all supplied voltage conditions. Figure 4-4 exemplified the comparison of nitrogen active species generated from different supplied voltage with the fixed nitrogen flowrate of 10 sccm and electrode gap of 5 cm. Only 3 supplied voltage conditions were shown for clear illustration purpose (if all conditions were shown, the graph would not be readable). It could be observed that 220 V supplied voltage generated the highest nitrogen active species: nitrogen molecule ions ( $N_2^+$ , 391.44 nm) [118], excited nitrogen molecule ( $N_2^*$ , 337.13 nm) [118], excited nitrogen atom ( $N^*$ , 427.33 nm) [119], and nitrogen atom ions ( $N^+$ , 470.42 nm) [119]. Oxygen atom ions ( $O^+$ , 357.38 nm) were also observed in this nitrogen glow discharge plasma. The source of oxygen species could be from slight system leakage.

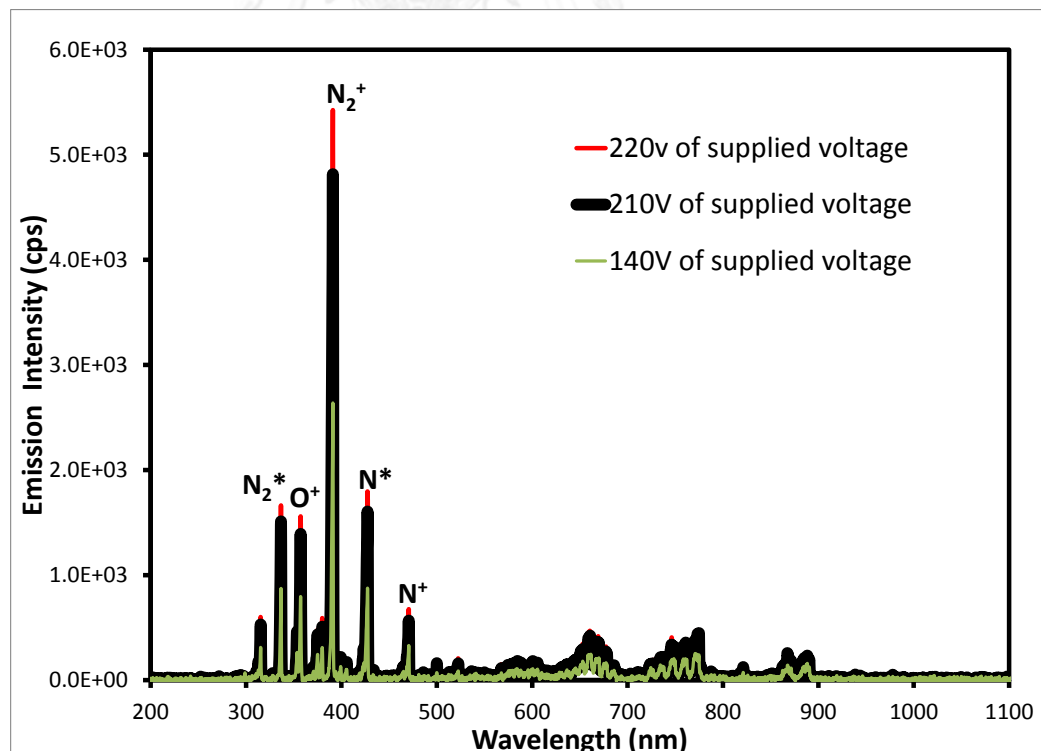


Figure 4-4 Optical Emission Spectra of nitrogen glow discharge plasma at various supplied voltage of 140, 210, and 220 V with nitrogen flowrate of 10 sccm and electrode gap of 5 cm

The last step of finding which plasma conditions generated the highest nitrogen active species was to compare the OES spectra generated from different nitrogen flowrate (5 – 40 sccm at the highest supplied power of 220 V. Figure 4-5 illustrates only three voltage for clear illustration. The optimum nitrogen was 10 sccm at the supplied voltage of 220V and electrode gap of 5 cm. When the nitrogen flowrate was increased to 15 sccm, the number of nitrogen active species was lower. At the higher nitrogen flow (> 15 sccm), the supplied power might not be able to generate plasma species effectively due to the higher amount of nitrogen molecules.

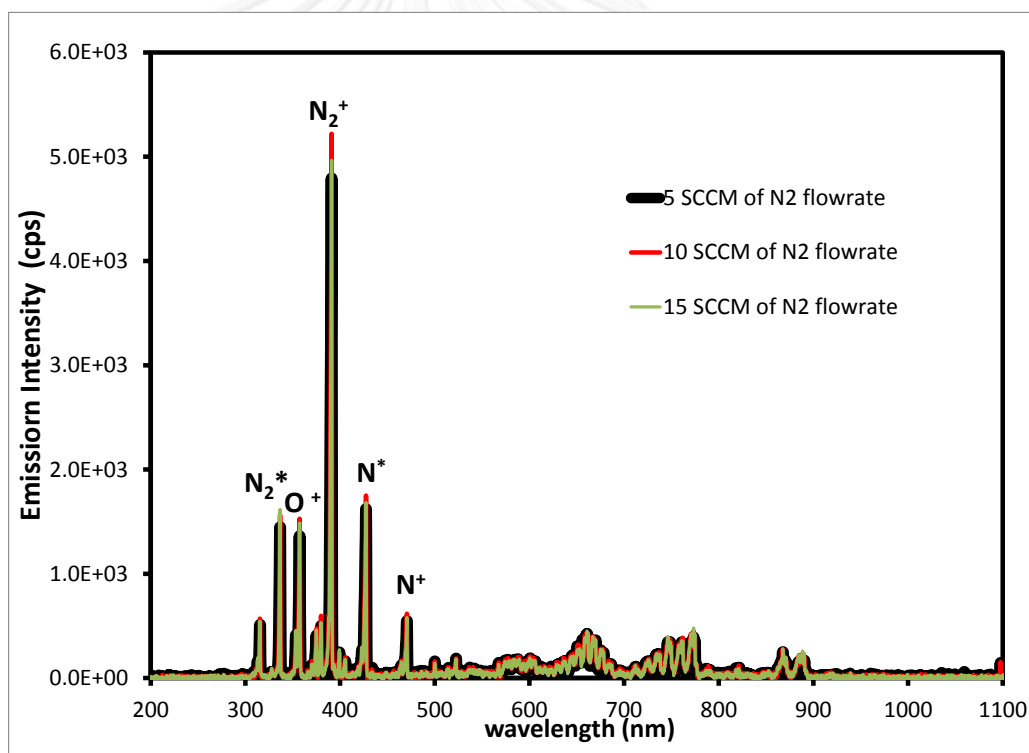


Figure 4-5 Optical Emission Spectra of nitrogen glow discharge plasma at various nitrogen flowrate of 5, 10, and 15 sccm, with the highest supplied voltage of 220 V and electrode gap of 5 cm

#### 4.4.2 Surface wettability

Figure 4-6 shows the water contact angle of untreated and nitrogen plasma-treated silk fibroin surface. Nitrogen plasma improved the wettability



of Thai silk fibroin surface as seen in the reduction of water contact angle from  $70^\circ$  on untreated surface. In Figure 4-6, it could be noticed that the contact angles of plasma-treated surface were in 2 ranges: one was in the range of  $40^\circ$  (treatment time of 5 – 40 s) and the other was in the range of  $20^\circ$  (treatment time of 80 – 160 s). The treatment time of 10 and 90 second were chosen for the rest of experiments to represent two different regions of contact angle.

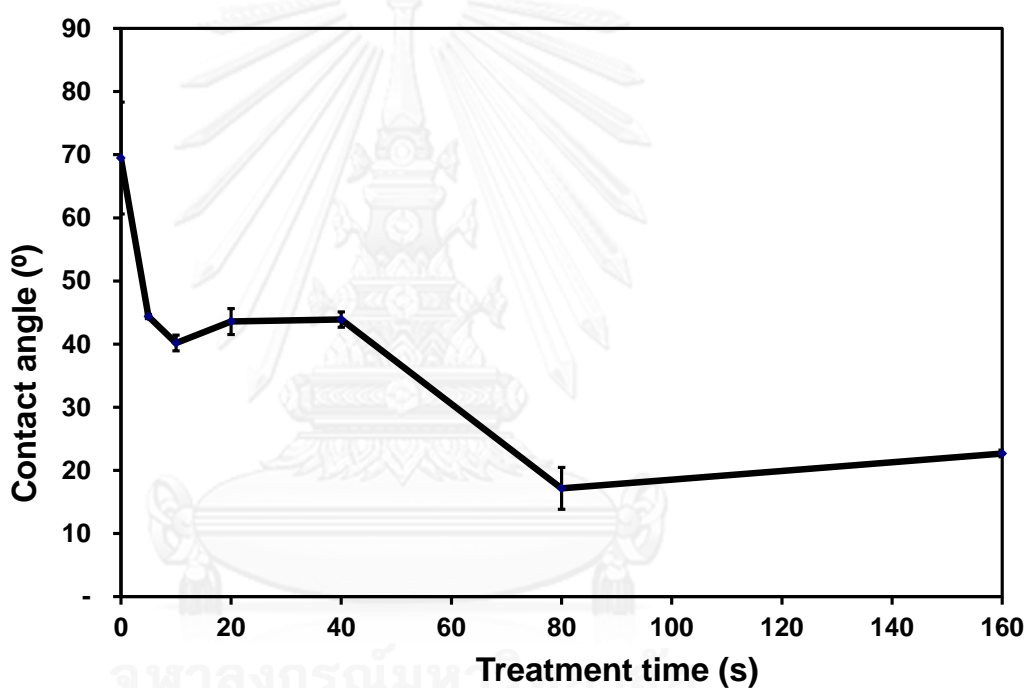


Figure 4-6 The static water contact angle of nitrogen plasma-treated Thai silk fibroin films as a function of treatment time

#### 4.4.3 Surface chemistry

The high-resolved XPS element spectra of  $C_{1s}$ ,  $N_{1s}$ , and  $O_{1s}$ , and peak deconvolution of  $C_{1s}$  and  $N_{1s}$  of Thai silk fibroin surfaces (untreated, 10 second  $N_2$  plasma-treated surface, and 90 second  $N_2$  plasma-treated surface) are shown in Figure 4-7.

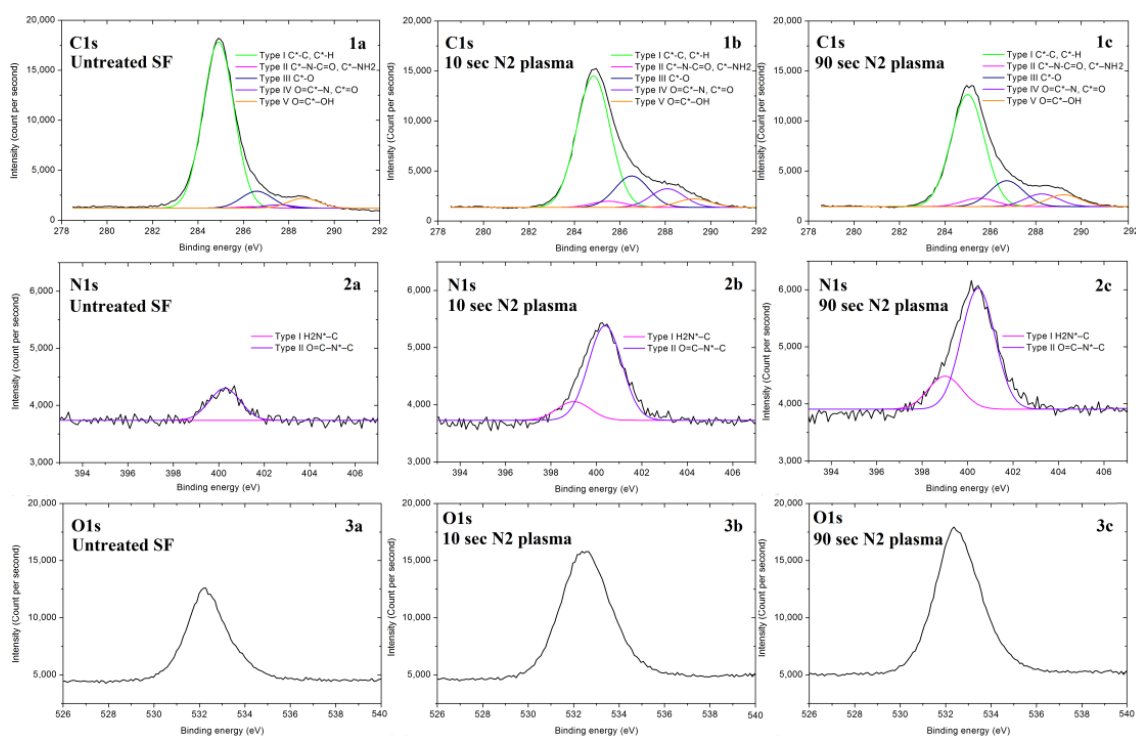


Figure 4-7 High resolved XPS spectra of Thai silk fibroin surfaces: (1a)  $C_{1s}$  spectra w/ peak deconvolution of untreated silk fibroin surface, (1b) ~of 10 second  $N_2$  plasma-treated surface, (1c) ~of 90 second  $N_2$  plasma-treated surface, (2a)  $N_{1s}$  spectra of untreated silk fibroin surface, (2b) ~of 10 second  $N_2$  plasma-treated surface, (2c) ~of 90 second  $N_2$  plasma-treated surface, (3a)  $O_{1s}$  spectra w/ peak deconvolution of untreated silk fibroin surface, (3b) ~of 10 second  $N_2$  plasma-treated surface, and (3c) ~of 90 second  $N_2$  plasma-treated surface

It could be noticed that nitrogen plasma induced functional groups on the surface of silk fibroin as observed by the shift of  $C_{1s}$  peak to higher binding energy peak after plasma treatment. The nitrogen and oxygen contents on silk fibroin surface were increased as noticed by the higher intensity of  $N_{1s}$  and  $O_{1s}$  peaks with increasing treatment time. N atoms were increased from 1.2% to 4.0% and 5.8%, while the O atoms were increased from 15.7%, to 21.2% and 24.7% after plasma treatment for 10 and 90 seconds, respectively as shown in Table 4-1. In addition, both N/C and O/C ratios were also increased in the same direction as %N and %O atoms were increased. N/C was increased from 0.01 to 0.05 and 0.08 and O/C was

increased from 0.19 to 0.28 and 0.35 after plasma treatment for 10 and 90 seconds, respectively (Table 4-1).

Table 4-1 Surface atomic composition, atomic ratio, and functional groups of Thai silk fibroin surfaces before and after nitrogen plasma treatment obtained from by XPS

	Untreated SF	10 s of N <sub>2</sub> plasma	90 s of N <sub>2</sub> plasma
<b>% atomic composition</b>			
% carbon atom	83.1%	74.8%	69.5%
% nitrogen atom	1.2%	4.0%	5.8%
% oxygen atom	15.7%	21.2%	24.7%
<b>atomic ratio</b>			
N/C	0.01	0.05	0.08
O/C	0.19	0.28	0.35
<b>Functional group</b>			
Type I <sub>C1s</sub> : C*-C or C*-H	84.0%	67.0%	65.7%
Type II <sub>C1s</sub> :	0.7%	3.1%	4.9%
<i>Free amine (C*-NH<sub>2</sub>)</i>	0.0%	0.5%	1.0%
<i>Amide (C*-N-C=O)</i>	0.7%	2.6%	3.9%
Type III <sub>C1s</sub> : C*-O	8.6%	16.0%	15.1%
Type IV <sub>C1s</sub> :	1.7%	9.5%	7.4%
<i>Amide (O=C*-N)</i>	0.7%	2.6%	3.9%
<i>Ether (C*=O)</i>	1.0%	6.9%	3.5%
Type V <sub>C1s</sub> : O=C*-OH	5.0%	4.4%	6.9%

The source of increased oxygen atoms could be either inside or outside plasma chamber. Air remaining inside the plasma chamber could induce O atoms on the treated surface during plasma treatment. On the other hand, the generated plasma reactive species might react with air outside plasma chamber after treatment. This phenomena is common, as other researchers also reported the increase of oxygen atom, even they used

nitrogen containing plasma gas [17, 18, 27-29, 33, 40]. For example, Mwale *et al* [26] found increased oxygen atoms on ammonia treated biaxially-oriented polypropylene or BOPP (0 to 5%), even though the plasma chamber was evacuated to the very low base pressure of  $1 \times 10^{-6}$  mbar before the introduction of ammonia as a plasma gas.

To understand which functional groups were generated on the plasma-treated surface, the curve fittings of  $C_{1s}$ , and  $N_{1s}$  were performed. The basis of surface functional group deconvolution was based on silk protein backbone structure. Silk fibroin molecules consist of carbon, oxygen, and nitrogen. All functional groups could be found in  $C_{1s}$  spectra, while the types of nitrogenated carbon functional groups could be found in  $N_{1s}$  spectra. In  $C_{1s}$ , there were 5 possible carbon components on silk fibroin surface. The first carbon group (type  $I_{C_{1s}}$ ) was a carbon atom bonded only to carbon or hydrogen ( $C^*-C$  or  $C^*-H$ ). The second one (type  $II_{C_{1s}}$ ) was a carbon atom bonded with one nitrogen atom along with carbon or hydrogen atoms ( $C^*-N-C=O$  or  $C^*-NH_2$ ). The third one (type  $III_{C_{1s}}$ ) was a carbon atom with a single bond to oxygen atom ( $C^*-O$ ) as in a hydroxyl group. The fourth one (type  $IV_{C_{1s}}$ ) was a carbon from an amide ( $C-N-C^*=O$ ) or ether ( $C^*=O$ ) groups. The fifth one (type  $V_{C_{1s}}$ ) was a carbon atom from a carboxyl group ( $O=C^*-OH$ ). The electron binding energy of these five types could be found at following positions: type  $I_{C_{1s}}$  284.6–285 eV, type  $II_{C_{1s}}$  285.5–286.5 eV, type  $III_{C_{1s}}$  286.4–287 eV, type  $IV_{C_{1s}}$  287.4–288.4 eV, and type  $V_{C_{1s}}$  288.5–289.6 eV [120, 121].

In  $N_{1s}$  spectra, there were two types of nitrogenated carbon functional groups: free amine (type  $I_{N_{1s}}$   $H_2N^*-C$ ) and amide (type  $II_{N_{1s}}$   $O=C-N^*-C$ ). The electron binding energy of these two functional groups could be found at following peaks: type  $I_{N_{1s}}$  at 398–398.9 eV [122, 123], and type  $II_{N_{1s}}$  at 399.6–400 eV [122-124]. Both type  $I_{N_{1s}}$  and type  $II_{N_{1s}}$  contributed to

type II<sub>C1s</sub>, while type II<sub>N1s</sub> only contributed to type IV<sub>C1s</sub>. O<sub>1s</sub> is typically a featureless peak [120], so the peak deconvolution was not relevant in this case. However, the peak height could be used as an indicator of oxygenated carbon content.

For the deconvolution process, the fitting parameter of full width at half maximum (FWHM) was set with the same value for all peaks because all photoelectrons were passing through the same components in the spectrometer, so the shape of the peak caused by the spectrometer must be the same, regardless of the origin electron species [125]. In addition, % atomic of C, N, and O from the deconvoluted C<sub>1s</sub> needs to be similar to % atomic of C, N, and O from XPS wide scan data.

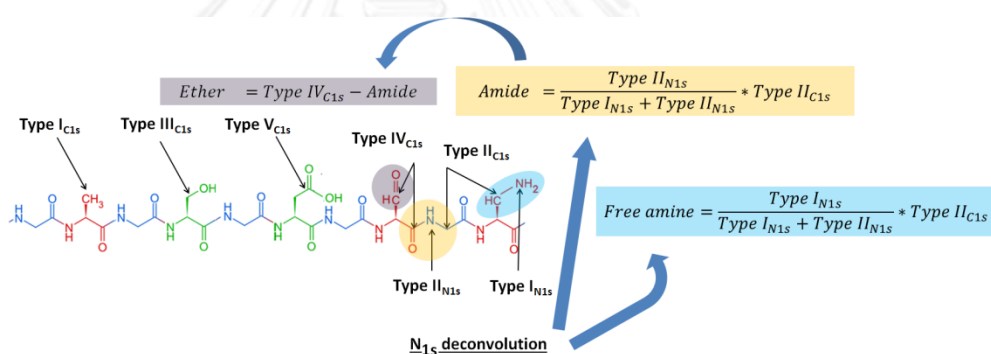


Figure 4-8 The list of all possible functional groups of silk fibroin in C<sub>1s</sub> and N<sub>1s</sub> spectra, and the illustration diagram of overlapped functional groups calculation

In addition, we proposed a methodology to reveal all functional groups including the overlapped functional groups at the same C<sub>1s</sub> peaks as illustrated in Figure 4-8. As previously mentioned, type II<sub>C1s</sub> represents both free amine (C\*-NH<sub>2</sub>) and amide (C\*-N-C=O), however, the N<sub>1s</sub> deconvolution could distinguish these 2 types of nitrogenated carbons: free amine (type I<sub>N1s</sub>) and amide (type II<sub>N1s</sub>). The amount of these carbons from N<sub>1s</sub> deconvolution could be used to determine free amine (C\*-NH<sub>2</sub>) and amide (C\*-N-C=O) in type II<sub>C1s</sub> as shown in equation (4.2) and (4.3).

$$\text{Free amine} = \frac{\text{Type } I_{N1s}}{\text{Type } I_{N1s} + \text{Type } II_{N1s}} * \text{Type } II_{C1s} \quad (4.2)$$

$$\text{Amide} = \frac{\text{Type } II_{N1s}}{\text{Type } I_{N1s} + \text{Type } II_{N1s}} * \text{Type } II_{C1s} \quad (4.3)$$

Since the amount of amide in type II<sub>C1s</sub> is exactly the same in type IV<sub>C1s</sub>, it could be used to calculate ether amount in type IV<sub>C1s</sub>, which represents both amide (C–N–C\*=O) and ether (C=O) as shown in equation (4.4).

$$\text{Ether} = \text{Type } IV_{C1s} - \text{Amide} \quad (4.4)$$

The deconvolution results of XPS high resolution spectra C1s and N1s of Thai silk fibroin surfaces before and after nitrogen plasma treatment are summarized in Table 4-1. It was noticed that all samples had very high aliphatic hydrocarbon (type I<sub>C1s</sub>). The major contribution could be from residual hydrocarbon which appeared during sample storage and transfer. These phenomena have been witnessed in other reports [120, 123]. The type II<sub>C1s</sub> nitrogenated compounds were increased by nitrogen plasma treatment. A small amount of free amine was observed (0.5% and 1%) when silk fibroin films were treated for 10 and 90 seconds, respectively. The type of oxygenated compounds introduced by nitrogen plasma or subsequent reaction with air were hydroxyl (type III<sub>C1s</sub>), ether (type IV<sub>C1s</sub>), and carboxyl (type V<sub>C1s</sub>) groups. The short treatment time of 10 seconds increased both hydroxyl (from 8.6% to 16.0%) and ether groups (from 1.0% to 6.9%) on the surface. However, the increased treatment time to 90 seconds dropped the increased level to 15.1% for hydroxyl and 3.5% for ether groups. Nevertheless, the longer treatment time still induce higher level of both compounds than untreated surface. The carboxylic groups showed a reversed pattern. The shorter treatment time of 10 seconds reduced the carboxylic

content from 5.0% to 4.4%, while the longer treatment time of 90 second increased the content to 6.9%.

The XPS results indicated that hydrophilic functional groups such as amine, hydroxyl, ether, and carboxyl groups were induced on Thai silk fibroin surface through nitrogen plasma treatment. This could improve the surface wettability as seen in the reduction of water contact angle.

#### **4.4.4 Bulk chemistry**

FTIR-ATR could be used to detect the change of bulk chemistry of silk fibroin after plasma treatment because it could go down to several microns of sample depth [22], while plasma treatment affects only few nanometer scales of outermost layer [23, 126]. Figure 4-9 shows FTIR spectra of untreated SF, 10 s N<sub>2</sub> plasma-treated SF, 90 s N<sub>2</sub> plasma-treated SF, and 160 s N<sub>2</sub> plasma-treated SF. The spectra revealed that there was no change of bulk chemistry of silk fibroin caused by nitrogen plasma treatment as observed from the unaltered shape and peak positions. FTIR could not normally detect the change of surface chemistry when the intended surface chemistry is similar to the bulk chemistry. Alves *et al* [38] reported that no difference of FTIR spectra was found between untreated and O<sub>2</sub> plasma treated samples. The samples were corn starch blended with cellulose acetate, ethylene vinyl alcohol and polycaprolactone. All samples had carbon-oxygen bonds. The change of surface oxygen containing moieties induced by plasma was minimal when they were combined with bulk chemistry.

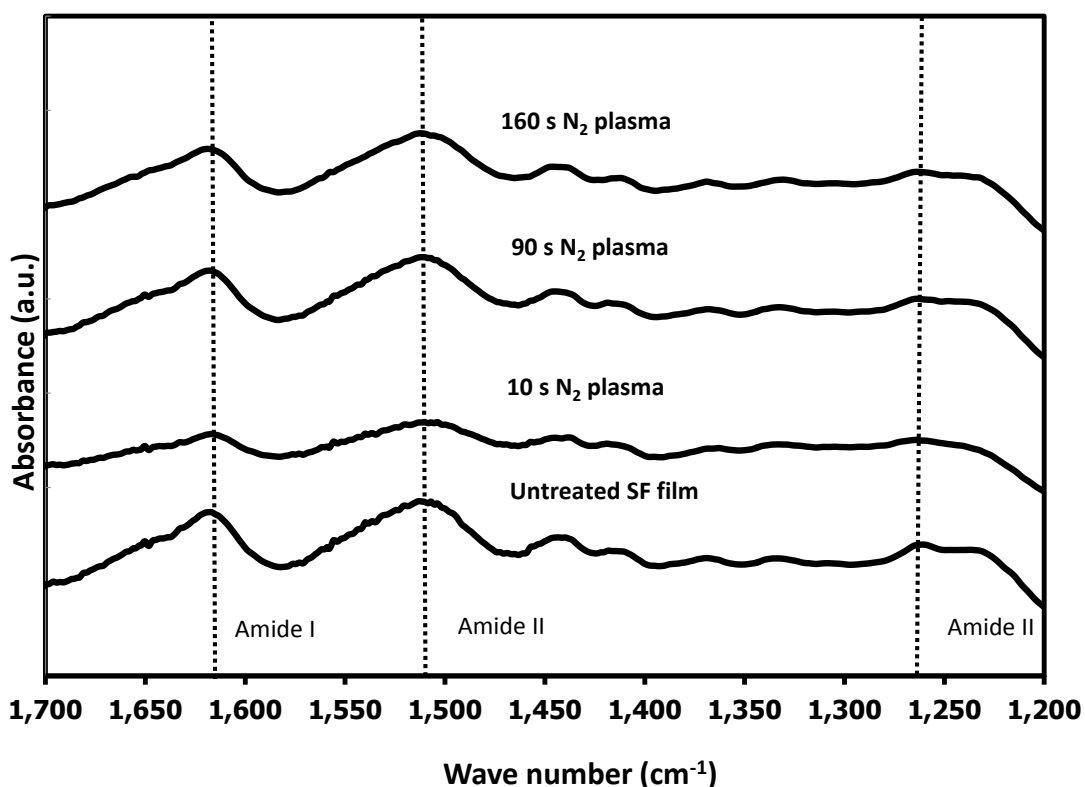


Figure 4-9 FTIR-ATR spectra of untreated and nitrogen plasma treated Thai silk fibroin surfaces

#### 4.4.5 *Surface topography*

The surface topography of silk fibroin surfaces before and after the nitrogen plasma treatment was investigated by AFM as shown in Figure 4-10. Nitrogen plasma slightly increased the root mean square (RMS) roughness of untreated silk fibroin surface from  $7.1 \pm 1.7$  nm to  $8.9 \pm 3.7$  nm when the surface had been treated for 90 seconds. On the other hand, plasma treatment for 10 seconds could result in a decrease in RMS roughness to  $6.2 \pm 0.7$ . However, there was no significant difference among all samples. This implied that a low energy nitrogen glow discharge plasma did not change the surface topography of silk fibroin surface.



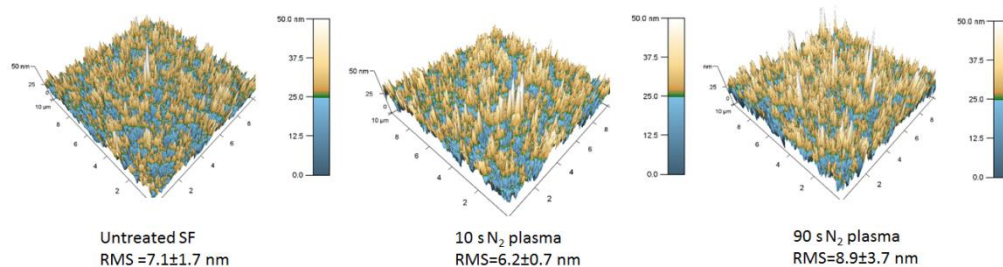


Figure 4-10 Surface topography of untreated and nitrogen plasma-treated Thai silk fibroin surfaces

#### 4.4.6 *Cell early adhesion and cell cytoskeleton*

Figure 4-11 shows the number of L929s cell adhered on untreated and nitrogen plasma treated silk fibroin surface, compared to control surface of tissue culture polystyrene (TCPS). The N<sub>2</sub> plasma treatment time of 90 seconds, enabled L929 to adhere on silk fibroin surface earlier than 10 second N<sub>2</sub> plasma-treated surface and untreated surface. At 3 h after seeding, cell population on 90 second N<sub>2</sub> plasma-treated surface reached the seeding level of 80,000 cells, while it took longer for L929 on 10 second N<sub>2</sub> plasma-treated surface to reach the seeding level. For untreated surface, the number of adhered L929 was still much lower than the seeding level. For TCPS, L929 could adhere on this surface as well as 90 second N<sub>2</sub> plasma-treated surface.

CHULALONGKORN UNIVERSITY

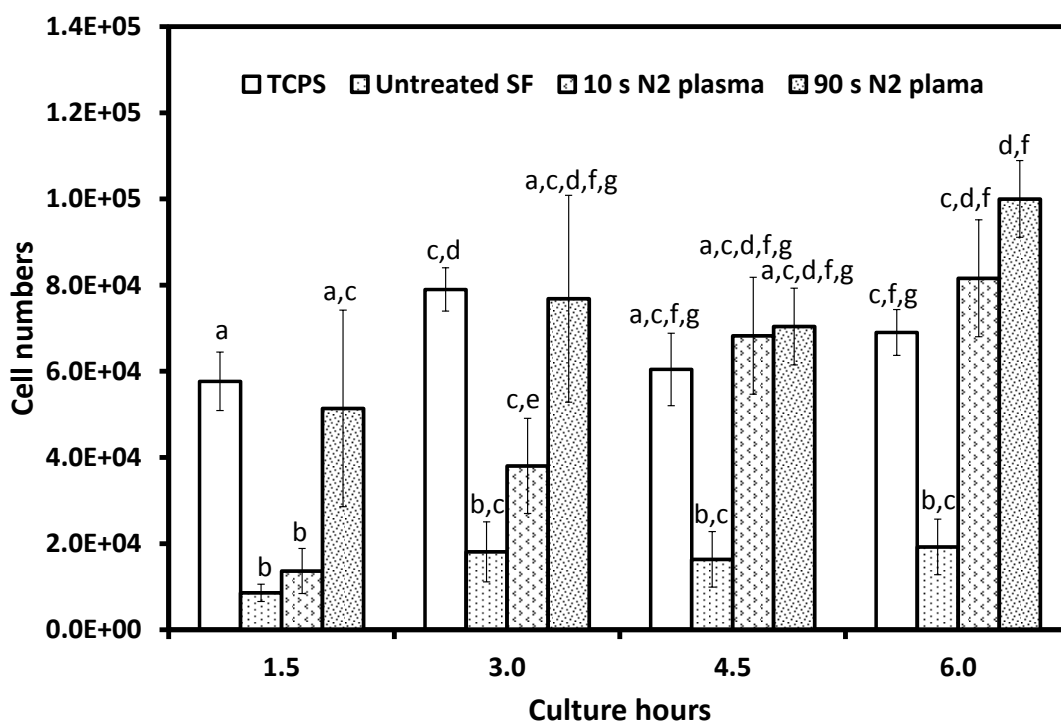


Figure 4-11 The number of adhered L929 on tissue culture plate polystyrene (TCPS), untreated silk fibroin, 10 s nitrogen plasma-treated silk fibroin and 90 s nitrogen plasma-treated silk fibroin for 1.5, 3, 4.5 and 6 h determined by MTT assay (seeding:  $8 \times 10^4$  cells/sample or  $4 \times 10^4$  cells/cm<sup>2</sup>). Each letter represents the significant difference ( $p < 0.05$ ) for all samples (the results with the same alphabet indicate that they are not significantly different)

The reason that cell adhered well on 90 second N<sub>2</sub> plasma-treated surface compared to on the others could be the improved surface wettability and the higher amount of free amine and carboxylic groups of 90 second N<sub>2</sub> plasma-treated surface. It is widely known that the hydrophobic surface does not support cell attachment because it changes the conformation of adhesive proteins [51, 53, 85, 86]; and untreated silk fibroin surface is a hydrophobic surface [76]. Amine and carboxyl groups have been reported that they enabled cell spreading [84, 92, 93]. Fauchaux *et al* [92], reported that human fibroblast could adhere better on amine (70% cell adhesion) and carboxylic (60% cell adhesion) surfaces

than hydroxyl (30% cell adhesion) and hydrophobic methyl (30% cell adhesion) surfaces after 2 h of seeding. Curran J *et al* [93], reported that human MSC could adhere better on carboxylic (60% cell adhesion), hydroxyl (60% cell adhesion), and amine (40% cell adhesion) surfaces than on hydrophobic methyl (20% cell adhesion) surface after 1 day of seeding. Keselowsky B *et al* [84] reported that MC3T3-E1 adhered on the surface in following preferential order of hydroxyl > carboxyl > amine > hydrophobic methyl.

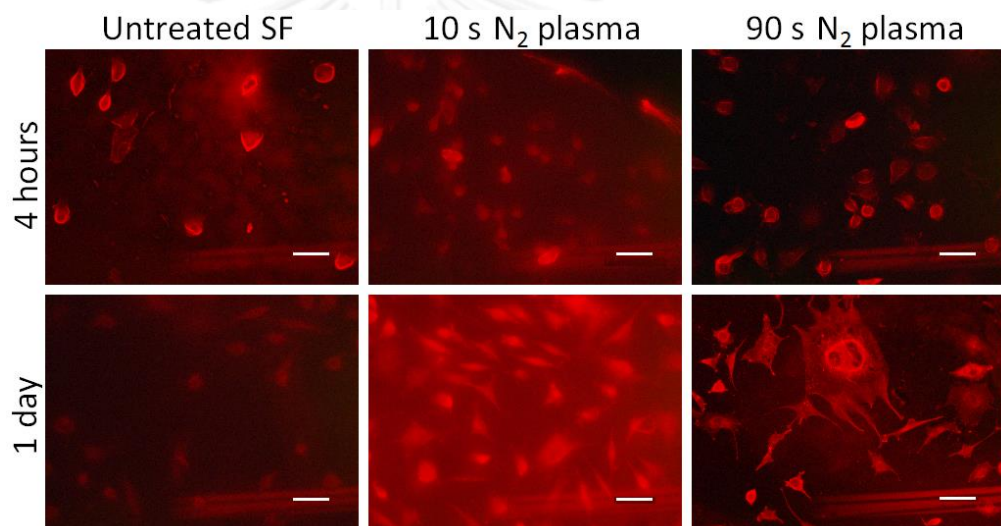


Figure 4-12 F-actin cell cytoskeleton staining by Rhodamine phalloidin (R415) of L929 on untreated and plasma treated Thai silk fibroin surface after the culture period of 4 h and 1 day (the scale bar is 100 micron in length).

Figure 4-12 illustrates the F-actin cytoskeleton of L929 cell adhered on untreated and nitrogen plasma treated silk fibroin surface at the culture time of 4 h and 1 day. After 4 h of cell culture, there was no difference in cell spreading among all surfaces. However, after 1 day of cell culture, the actin cytoskeleton developed more prominently on 90 second N<sub>2</sub> plasma-treated surface than on 10 second N<sub>2</sub> plasma-treated surface and untreated surface. The enhancement of F-actin cytoskeleton development could contribute

from the higher amount of free amine and carboxylic on 90 second N<sub>2</sub> plasma-treated surface. Keselowsky *et al* [84, 94] and Curran *et al* [93] found that amine surface enhanced the highest recruitment of vinculin, the adaptors between integrin and the F-actin cell cytoskeleton [87]. Curran *et al* [93] also reported that F-actin cell cytoskeleton was well developed on amine and carboxylic surface after 1 day of culture. However, cells were lack of organization on hydroxyl surface.

It could be concluded that nitrogen glow discharged plasma induced surface hydrophilic functionalities such as amine and carboxylic groups which improved surface wettability, accelerated early cell adhesion, and promoted cell spreading.

#### 4.5 Conclusion

The low energy nitrogen plasma generated by AC50Hz power supply was introduced to modify Thai silk fibroin surface. Nitrogen plasma treatment improved silk fibroin surface wettability as witnessed by the reduction of water contact angle because it induced the hydrophilic functional groups such as free amine, hydroxyl, ether, and carboxylic groups on the modified silk fibroin surface as revealed by XPS. The treatment did not significantly change bulk chemistry and surface topography as observed by FTIR and AFM, respectively. The higher amounts of free amine and carboxylic groups, induced on 90 s N<sub>2</sub> plasma-treated silk fibroin surface, accelerated early cell adhesion on the surface. On 90 s N<sub>2</sub> plasma-treated silk fibroin surface, L929 took 3 h to reach 100% cell adhesion which was comparable to L929 on tissue culture plate, but earlier than on other Thai silk fibroin surfaces (10 s N<sub>2</sub> plasma-treated and untreated silk fibroin surface). The cell adhesion results

were in agreement with the cytoskeleton development. L929 F-actin was more evident on 90 s N<sub>2</sub> plasma-treated surface than the others. The results suggested that the low energy AC50Hz plasma system could be effectively used to enhance L929 mouse fibroblast early adhesion on Thai silk fibroin surface without any significant change to surface topography and bulk chemistry.



## CHAPTER

5. IN-DEPTH INVESTIGATION OF PLASMA TREATMENT ON THAI  
SILK FIBROIN SURFACE5.1 Materials

1. *Bombyx mori* silkworm cocoon (Nangnoi Srisaket1, Queen Sirikit Sericulture Center, Thailand)
2. Tissue culture plates (Corning, USA)
3. Ethanol (C<sub>2</sub>H<sub>5</sub>OH, MW 46.04 g/mol)
4. Hexafluoroisopropanol (HFIP, C<sub>3</sub>H<sub>2</sub>F<sub>6</sub>O, 99%, MW: 168.05 g/mol, Aldrich)
5. PTFE syringe filter with 0.2 µm pore size (Carl Roth GmbH, Germany)
6. Silicon wafer precuts with 30 nm oxide thickness: 15x20 mm<sup>2</sup> for ellipsometry, 7x7 mm<sup>2</sup> for XPS, and 20x20 mm<sup>2</sup> for contact angle measurements (Technical University of Dresden, Germany)
7. Methanol (CH<sub>3</sub>OH, 99.99%, MW: 32.04 g/mol, Acros, Belgium)
8. Oxygen (O<sub>2</sub>, 99.99 %, MW 32.00 g/mol, Air Liquide, Germany)
9. Carbon dioxide (CO<sub>2</sub>, 99.99 %, MW 44.01 g/mol, Air Liquide, Germany)
10. Argon (Ar, 99.99 %, MW 39.95 g/mol, Air Liquide, Germany)
11. Ammonia (NH<sub>3</sub>, 99.99 %, MW 17.03 g/mol, Air Liquide, Germany)
12. 4-trifluoromethyl-benzaldehyde (TFBA, C<sub>8</sub>H<sub>5</sub>F<sub>3</sub>O, 98%, MW 174.12 g/mol, Aldrich, Germany)

13. Human fibronectin (FN, Roche, Switzerland)
14. Nonpyrogenic serological pipet (Costar®, Corning, U.S.A)
15. Roswell Park Memorial Institute 1640 Medium (RPMI 1640 Medium, stable glutamine, PAN-Biotech GmbH, Germany),
16. Dulbecco's Modified Eagle Medium (Gibco® DMEM, High Glucose, GlutaMAX™, Life Technology corp., USA)
17. Phosphate-buffered saline (PBS; Biochrom AG, Germany)
18. Phosphate buffer solution with  $100 \text{ mg.l}^{-1} \text{ MgCl}_2 \cdot 6\text{H}_2\text{O}$  and  $100 \text{ mg.l}^{-1} \text{ CaCl}_2$  (PBS w/  $\text{Mg}^{2+}/\text{Ca}^{2+}$ ; Biochrom AG, Germany)
19. Fetal bovine serum (FBS, Hyclone, Thermo Scientific, USA)
20. Penicillin/streptomycin antibiotic (100 U/ml, Hyclone, Thermo Scientific, USA)
21. Trypsin-EDTA (0.25% trypsin with EDTA•Na, Gibco BRL, Canada)
22. Paraformaldehyde (PFA,  $\text{OH}(\text{CH}_2\text{O})_n\text{H}$  ( $n=8-100$ ), Sigma-Aldrich, USA)
23. TritonX-100 (Sigma-Aldrich, USA)
24. Hoechst 33342 (Life Technologies, USA)
25. Goat serum albumin (GSA;  $60 \text{ mg.ml}^{-1}$ ; Dianova GmbH, Germany)
26. Monoclonal mouse anti-human/mouse paxillin antibody (clone 349/Paxillin; BD Transduction Laboratories, Germany)
27. Polyclonal rabbit anti-human/mouse fibronectin antibody (Fibronectin (H-300) sc-9068; Santa Cruz Biotechnology, Inc, USA.)

28. Alexa Fluor®488 goat anti-mouse IgG (Life Technologies, USA)
29. Alexa Fluor®488 goat anti-rabbit IgG (Life Technologies, USA)
30. Alexa Fluor® 633 phalloidin (Life Technologies, USA)
31. Anti-fading mounting medium (O. Kindler GmbH, Germany)
32. L929 mouse fibroblast (Catalog number 85011425, European collection of cell cultures (ECACC), UK)
33. Human mesenchymal stem cells (University Clinic, Technical University of Dresden, Germany)

## 5.2 Equipment

1. Digital balance (AL204, Mettler Toledo, USA)
2. Autopipette (Eppendorf , Germany)
3. Water bath (1235 PC, Shel-Lab, Sheldon Manufacturing, Inc., USA)
4. Laminar Flow box (Thermo scientific, USA)
5. CO<sub>2</sub> Incubator (HEPA class 100, Steri-Cycle, Thermo scientific, USA)
6. Micro plate reader (UVM 340, ASYS, Australia)
7. Microwave plasma apparatus (MicroSys, Roth&Rau, Germany)
8. Dip coater model KSVDC (KSV instruments Ltd., Helsinki, Finland)
9. Research grade X-ray photoelectron spectrometer (Axis Ultra, Kratos Analytical, UK) with a monochromatic Al K<sub>α</sub> X-ray source (operated at 300 W and 15 kV)



10. General X-ray photoelectron spectrometer using for routine measurement  
(Amicus, Kratos Analytical, UK) with a monochromatic Mg  $K_{\alpha}$  X-ray source  
(operated at 240 W and 8 kV).
11. Equinox 55 FTIR spectrometer (Bruker, Germany)
12. IPF in-house developed electrokinetic set up for streaming potential  
(Institute for Polymer Research Dresden-IPF, Germany)
13. A variable angle spectroscopic ellipsometer M-2000V (J.A. Woollam Co.,  
USA).
14. IPF in-house developed set-up for measuring water contact angle using  
captive air bubbles in conjunction with axisymmetric drop shape analysis  
(ADSA)
15. Atomic force microscope (AFM, NanoWizard II, JPK Instruments, Germany)
16. Quartz crystal microbalance with dissipation monitoring (QCM-D, Q-Sense,  
Sweden)
17. Optical microscope (Olympus IX 50, Olympus GmbH, Hamburg, Germany)  
with Hoffman modulation contrast objective HMC10 LWDLCA 0.25 na,
18. Digital camera AxioCam HR and image analysis software AxioVision 4.7 (Carl  
Zeiss MicroImaging GmbH, Göttingen, Germany).
19. Confocal laser scanning microscopy with a Leica TCS SP5, objective HCX PL  
APO Lbd. Bl 63x/1.40-0.60 oil, UV-diode (405 nm), argon laser (488 nm) and  
helium-neon laser (633 nm) (Leica Microsystems GmbH, Germany)

### 5.3 Experimental procedures

Figure 5-1 summarized the experiments in this chapter. In brief, the experiments were setup to gain a comprehensive understanding of silk fibroin (SF) properties and the effects from plasma treatment on the surface. All experiments were conducted at Institute of Polymer Research (IPF) Dresden, Germany. The surface model was a well-defined thin film which allows taking an advantage of advanced surface characterization techniques such as protein adsorption from quartz crystal microbalance (QCM). The thin film preparation process started from lyophilisation of SF aqueous solution. Then, the freeze-dried SF was dissolved in hexafluoroisopropanol (HFIP), a volatile solvent. The thin SF film (70 nm thickness) was prepared by dip coating substrates.

The comprehensive characterization of untreated SF ensured that SF thin film was prepared with consistent properties. X-ray photoelectron spectroscopy (XPS) was used to determine that the surface chemistry of prepared SF film had similar chemical components as the theoretical values of SF and to evaluate the contamination from the solvent. Fourier transform infrared attenuated total reflection spectroscopy (FTIR-ATR) was employed to ensure that the SF crystallinity was induced consistently. Spectroscopic ellipsometry was utilized for evaluating the thickness of thin film and the swelling ratio in various liquids. The other properties (surface charge, optical property, surface wettability, surface modulus and surface topography) were also characterized and compared to the literature reports if there were available.

The plasma conditions suitable for surface functionalization were investigated by using XPS for desirable surface chemistry and streaming potential for intended surface charge. Plasma gases ( $O_2$ , Ar, Ar/ $O_2$ ,  $NH_3$ ) were varied to evaluate their effects on the surface chemistry of SF surface. Gas flow, plasma

generating power, and treatment time were the main parameters. In addition, the sample shield was also installed in some cases to minimize the etching effects from the high energetic plasma-generated species. During the survey of plasma conditions, oxygen plasma was found that it could etch SF surface without the significant change of surface chemistry. This finding led to the study of O<sub>2</sub> plasma etching to alter SF surface stiffness for a cell-substrate interaction study.

The study of O<sub>2</sub> plasma etching to alter SF surface stiffness was divided into two parts: physico-chemical characterization and *in vitro* cell cultures. The characterizations were intended to confirm that surface stiffness was a prominent effect from O<sub>2</sub> plasma etching, while other properties e.g. surface chemistry, dynamic water contact angle, degree of crystallinity, and protein adsorption (FN) were minimally affected. *In vitro* cell cultures focused on evaluating cytoskeleton of two different cells, L929 mouse fibroblast and human mesenchymal stem cell (hMSC), of which their matrixes were different in stiffness.

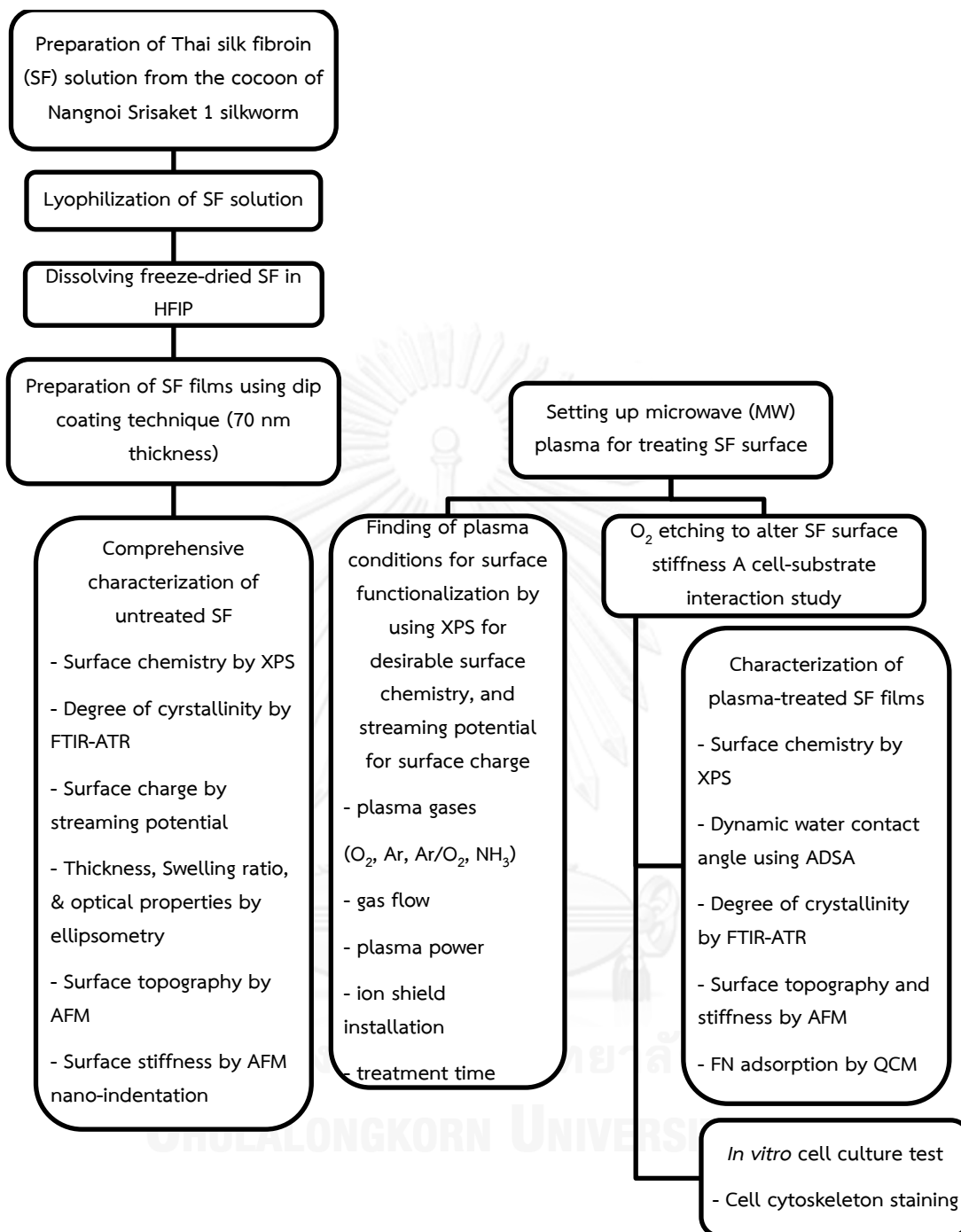


Figure 5-1 Diagram of experimental procedures (Part II)

### 5.3.1 Preparation of Thai silk fibroin dip-coated films

Thai silk fibroin was extracted by the same method described in 4.3.1. Freeze-dried SF was obtained from the regenerated aqueous SF solution by lyophilization. Freeze-dried SF was dissolved in hexafluoroisopropanol (HFIP, 99% Aldrich) to form 1% wt solution. The solution was filtered using a PTFE syringe filter with 0.2  $\mu\text{m}$  pore size (Carl Roth GmbH, Karlsruhe, Germany). SF thin films were prepared by dip coating on different planar substrates using a dip coater model KSVDC (KSV instruments Ltd., Helsinki, Finland).

Substrates included silicon wafer precuts with 30 nm oxide thickness (15x20  $\text{mm}^2$  for ellipsometry, 7x7  $\text{mm}^2$  for XPS, and 20x20  $\text{mm}^2$  for contact angle measurements), glass cover slips 20 mm diameter (Menzel Gläser, Braunschweig, Germany) for cell culture tests, internal reflection elements (IRE, silicon, 52x20x2  $\text{mm}^3$ , incident angle 45°) for infrared spectroscopy, special silicon carriers (20x30  $\text{mm}^2$ ) for streaming potential measurements, and QCM gold electrode.

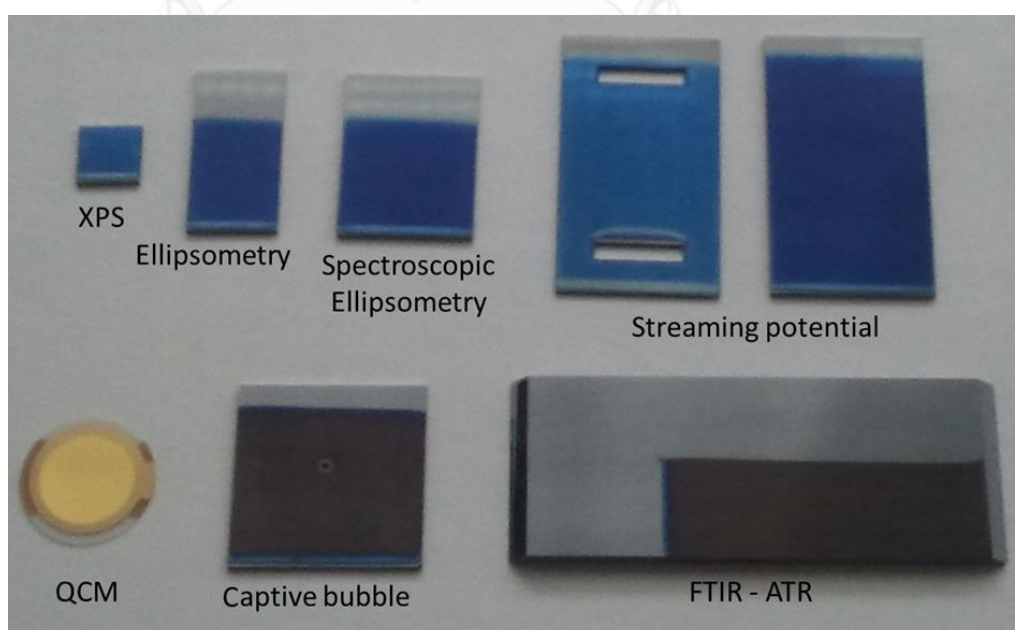


Figure 5-2 Example of SF film on different substrates for all surface characterization

The desired film thickness (70 nm) was achieved by adjusting the dip coating speed (45.7 mm/min). In order to ensure the uniformity of the SF film, any air flow in the dip coating setup was carefully avoided. After the evaporation of HFIP, the coated substrate was smoothly immersed in methanol (99.99%, Acros, Geel, Belgium) for 10 s using the same dip coating device. Subsequently, the sample was placed in a methanol bath for another 1 h to complete  $\beta$ -sheet formation of the SF structure. Example of SF films on different substrates was shown in Figure 5-2.

### **5.3.2 *Microwave plasma experimental setup***

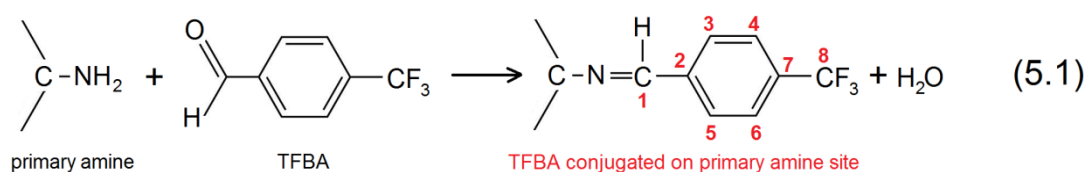
Plasma treatment was carried out in a computer controlled MicroSys apparatus by Roth&Rau, Wüstenbrand, Germany. The cylindrical vacuum chamber, made of stainless steel, has a diameter of 350 mm and a height of 350 mm. The base pressure obtained with a turbomolecular pump is  $<10^{-7}$  mbar. On the top of the chamber, a 2.46 GHz electron cyclotron resonance (ECR) plasma source RR160 by Roth&Rau with a diameter of 160 mm and a maximum power of 800 W is mounted. Oxygen (99.99 %, Air Liquide, Düsseldorf, Germany) was introduced into the active volume of the plasma source via a gas flow control system. Samples were introduced by a load lock system and placed on a grounded aluminum holder near the center of the chamber. The distance between the sample and the excitation volume of the plasma source is about 200 mm.

### 5.3.3 Characterization of untreated and plasma-treated Thai silk fibroin films

#### 5.3.3.1 X ray photoelectron spectroscopy (XPS)

XPS was carried out using both an research grade spectrometer (Axis Ultra, Kratos Analytical, Manchester, UK) with a monochromatic Al K $\alpha$  X-ray source (operated at 300 W and 15 kV) and general spectrometer using for routine measurement (Amicus, Kratos Analytical, Manchester, UK) with a non-monochromatic Mg K $\alpha$  X-ray source (operated at 240 W and 8 kV). The photo-emitted electrons were collected perpendicular to the sample surface. In this case the information depth is about 8 nm. Spectra were referenced to the C<sub>1s</sub> peak of aliphatic carbon at a binding energy of 285.0 eV. For the spectra obtained from non-monochromatic X-ray source (Amicus), a satellite subtraction procedure was applied. Quantitative elemental compositions were determined from peak areas using relative sensitivity factors and the spectrometer transmission function. C<sub>1s</sub> spectra were deconvoluted by CasaXPS (Casa Software Ltd., UK). The fit procedure was allowed to vary the component binding energies, the component intensities and a common value for the full width at half maximum (FWHM) for all peaks.

In order to measure free amine, the surface was reacted with the vapor of TFBA (4-trifluoromethyl-benzaldehyde) for 30 min as shown in equation (5.1) before XPS measurement of C<sub>1s</sub> and F<sub>1s</sub>.



The percentage of primary amine molecule per total carbon atoms could be calculated by evaluating  $F_{1s}$  and  $C_{1s}$  atomic contents. For one primary amine molecule, there will be three fluorine atoms and eight carbon atoms. The percentage of primary amine in carbon functionalities could be derived by the following formula (5.2).

$$\% \text{ primary amine} = \frac{F_{1s}/3}{C_{1s} - \frac{8}{3} * F_{1s}} * 100\% \quad (5.2)$$

where  $F_{1s}$  is fluorine atomic content of sample

and  $C_{1s}$  is carbon atomic content of sample

### 5.3.3.2 Fourier transform infrared attenuated total reflection spectroscopy (FTIR-ATR)

Infrared spectra were obtained with an Equinox 55 FTIR spectrometer (Bruker, Ettlingen, Germany) equipped with a mercury cadmium telluride (MCT) detector and an attenuated total reflection accessory according to the single-beam-sample-reference concept (OPTISPEC, Zürich, Switzerland) [127]. SF films were prepared by dip coating on trapezoidal shaped internal reflection elements (IRE, silicon, 52x20x2 mm<sup>3</sup>, incident angle 45°).

Sample spectra ( $I_s$ ) and background spectra ( $I_r$ ) were acquired from a coated and uncoated lane of the IRE respectively. For each single channel spectrum, 200 scans at a spectral resolution of 2 cm<sup>-1</sup> were co-added. Subsequently, the result spectrum  $-\log(I_s/I_r^{-1})$  was calculated. For the SF film thickness of about 70 nm, the thin-film case of ATR spectroscopy applies [128]. In this case, the film thickness limits the sampling depth, i.e., there is no variation of the sampling depth with wavelength. Consequently, absorbance units are given instead of ATR units.



Fourier self-deconvolution (deconvolution factor 10000 and noise reduction factor 0.5) along with peak fitting of the amide I region 1595 – 1705  $\text{cm}^{-1}$  according to the procedure by Hu *et al* was conducted to evaluate the secondary structure of SF (Opus 2.06, Bruker) [129]. The analysis was based on the following peak assignment: tyrosine side chain (1605–1615  $\text{cm}^{-1}$ ),  $\beta$ -sheet (1616–1637  $\text{cm}^{-1}$  and 1697–1703  $\text{cm}^{-1}$ ), random coil (1638–1655  $\text{cm}^{-1}$ ),  $\alpha$ -helix (1656–1662  $\text{cm}^{-1}$ ), and  $\beta$ -turn (1663–1696  $\text{cm}^{-1}$ ) [129].

### 5.3.3.3 Electrokinetic measurements

The electrokinetic measurements reveal the surface charge at the solid/liquid interface. The substrate surface charge plays a critical role in many adsorption processes such as protein adsorption, the first biological cell-substrate interaction step before any cell interaction steps [50, 52, 53].

The key principle of this technique is based on the fact that the streaming flow of liquid through the narrow channel induces the accumulation of counter ions on the charged surface. The measurements of streaming current and pressure drop across the channel together with the known dimension of the channel and liquid properties allow the calculation of zeta potential based on Smoluchowski equation as illustrated in equation (5.1) [130].

$$\zeta = -\frac{\eta}{\epsilon_0 \epsilon_r} \frac{I_{str}}{\Delta p} \frac{L}{bh} \quad (5.2)$$

where  $\zeta$  is zeta potential,  $\eta$  is the dynamic viscosity,  $\epsilon_0$  is the permittivity of vacuum,  $\epsilon_r$  is the dielectric constant of the liquid,  $I_{str}$  is streaming current,  $\Delta p$  is pressure drop across the channel,  $L$  is the channel-plate length,  $b$  is the channel-

plate width, and  $h$  is the distance between 2 plates which formed channel width.

The swollen SF surface is not considered as an electrokinetically ideal surface (i.e., in the absence of roughness, porosity and swelling of the samples or a patch-like distribution of chemical properties). Therefore, the result calculated by using Smoluchowski equation is considered as an apparent zeta potential for SF surface.

Streaming current measurements were performed across a rectangular streaming channel (length 20 mm, width 10 mm, height 30  $\mu\text{m}$ ) formed by two SF coated silicon carriers using IPF in-house developed electrokinetic set up [131]. Aqueous KCl solution of  $10^{-4}$ ,  $10^{-3}$ , and  $10^{-2}$   $\text{mol.l}^{-1}$  were used as background electrolyte. The pH was varied in the range from 9.5 to 2.5 with the addition of 0.1  $\text{mol.l}^{-1}$  HCl and KOH solutions. The measurements were started at an alkaline pH-value. After each titration step, the system was equilibrated for about 45 minutes. The surface isoelectric point could be observed at the pH which apparent zeta potential equal zero.

#### 5.3.3.4 Ellipsometry

Ellipsometry is used to determine the optical properties and thickness of individual material. Ellipsometric measurements were performed using a variable angle spectroscopic ellipsometer M-2000V (J.A. Woollam Co., Inc., USA). It is a Diode Array Rotating Compensator Ellipsometer (DARCE™) equipped with a computer-controlled goniometer and a horizontally mounted sample stage. The light source is a 50 W mercury lamp. For a given angle of incidence, the instrument measures 400 wavelengths simultaneously covering the spectral range from 370–1000 nm. Accurate measurements over

the full phase difference ( $\Delta$ ) and amplitude ratio ( $\Psi$ ) range were acquired ( $\Delta = 0^\circ\text{--}360^\circ$ ;  $\Psi = 0^\circ\text{--}90^\circ$ ).

In case of dry samples, values from three angles of incidence:  $65^\circ$ ,  $70^\circ$ , and  $75^\circ$  were acquired. To investigate swollen layers, a liquid media cell (angle of incidence  $68^\circ$ ) was used.

To calculate the thickness and the optical properties of SF film, fit procedures based on Cauchy multilayer models were applied. All measurements were conducted at room temperature ( $20^\circ\text{C}$ ).

#### **5.3.3.5 Liquid-fluid contact angle measurements using captive air bubbles**

In general, the water contact angle is characterized with the sessile dropping technique. To have an accurate measurement, the surface properties must not be changed during the measurement process [132]. In the case of silk fibroin, the surface is hydrating and swelling after the sessile dropping of liquid on the surface. The static water contact angle is changing during the whole measurement process.

The captive air bubble technique could be used to measure the wettability of swollen surface. In this technique, the air bubble is injected onto the swollen surface. The expanding air bubble is driving the dewetting process and providing the receding water contact angle, while contracting air bubble represents the wetting process and provides the advancing water contact angle. Inverse advancing and receding water contact angles were measured using an IPF in-house developed set-up [133]. The experiments were performed using captive air bubbles in conjunction with axisymmetric drop shape analysis (ADSA) to study the wettability of the hydrated SF surfaces in contact with distilled water. Axisymmetric drop shape analysis

allows the simultaneous determination of liquid-fluid interfacial tensions and contact angles from the shape of sessile drops or captive bubbles [133, 134].

SF coated silicon precuts  $20 \times 20 \text{ mm}^2$  with a central 0.8 mm diameter hole were fixed in a sample holder and immersed upside down in a glass chamber containing distilled water. A captive air bubble was created through the hole using a motorized syringe. Increasing or decreasing the air bubble volume by pushing or pulling the syringe plunger forces the three phase contact line at the solid-air-liquid interface to recede (dewetting mode) or advance (wetting mode) with a velocity of about  $0.6 \text{ mm} \cdot \text{min}^{-1}$ . The bubble was imaged continuously using a CCD camera and a microscope. Accurate profile data were acquired by image analysis. Contact angles were calculated considering the local gravity, the densities of the liquid and fluid phases, as well as several arbitrary but accurate coordinate points selected from the experimental bubble profile. Finally, receding and advancing water contact angles were obtained as the difference of the measured contact angle value of the air bubble to  $180^\circ$ .

#### **5.3.3.6 Atomic force microscopy and nano-indentation**

The SF surface topography was evaluated using an atomic force microscope (AFM, NanoWizard II, JPK Instruments, Berlin, Germany) in a contact mode. All plasma-treated SF were rinsed with DI and dried before all AFM measurements in air and PBS environments. The surface topographical parameters were extracted from the recorded images by AFM data processing software (JPK Instruments). The surface parameters were averaged from a minimum of 5 areas ( $10 \times 10 \text{ } \mu\text{m}^2$ ) on each sample and expressed as the mean  $\pm$  standard deviation.

Mechanical properties of SF layers on silicon carriers were determined by nano-indentation experiments using the same AFM instrument. For this purpose, colloidal force probes were prepared by attaching glass beads (diameter 20  $\mu\text{m}$ , Kisker Biotech, Germany) to the apex of tipless cantilever having a nominal spring constant of  $0.08 \text{ N.m}^{-1}$  (PNP-TR-TL-Au, Nanoworld, Switzerland) using a two-component epoxy glue as described by Krieg *et al* [135]. Cantilevers were calibrated using the equi-partition theorem [136]. Measurements were performed in phosphate buffered saline (PBS) at room temperature (20  $^{\circ}\text{C}$ ). Force-distance curves were acquired using 500 pN contact force and  $2 \mu\text{m.s}^{-1}$  approach/retract velocity. Young's Modulus was extracted from approach force distance curves using the Hertz model. At least 25 individual measurements in a  $25 \times 25 \mu\text{m}^2$  area were averaged and expressed as the mean  $\pm$  standard deviation.

#### **5.3.3.7 Fibronectin adsorption with quartz crystal microbalance (QCM)**

Human fibronectin (FN; Roche, Switzerland) was prepared in Dulbecco's phosphate buffered saline, pH 7.4 (PBS; Biochrom AG, Germany) with the concentration of  $30 \mu\text{g.ml}^{-1}$ . The adsorption studies were performed with a quartz crystal microbalance with dissipation monitoring (QCM-D, Q-Sense, Sweden). Frequency changes and dissipation data were acquired and further analyzed by the instrument software (QSOFT and QTOOLS). PBS was injected into the QCM-D chamber. After stable frequency ( $\Delta f$ ) and dissipation (d) signals were reached, PBS was exchanged with fibronectin solution. Subsequently, adsorption amount were taken after the stabilization of  $\Delta f$  and d. After that, the chamber was rinsed with PBS for 2 min every hour during 5 h of desorption measurement. The Sauerbrey equation [137] was used to

calculate the adsorbed mass per area ( $\text{ng}\cdot\text{cm}^{-2}$ ) from the measured 3<sup>rd</sup> overtone frequency shift ( $\Delta f$  at 15 MHz). Even though the surface is non-rigid and hydrated, the Sauerbrey equation could still be used for the comparison of different surfaces [138, 139].

#### **5.3.4 *In vitro* cell cultures**

Mouse fibroblast (L929) and human mesenchymal stem cell (hMSC) were used as *in vitro* culture model. For that purpose, SF coated glass carriers (untreated and plasma treated) were placed into 12-well suspension cell-culture plates and sterilized in 70 vol% ethanol for 30 min. Then the films were extensively rinsed with PBS. The cell culture was incubated at 37°C in 5% CO<sub>2</sub> condition. L929 medium was Roswell Park Memorial Institute 1640 Medium (PAN-Biotech GmbH, Germany), while hMSC medium was Dulbecco's Modified Eagle Medium (Life Technology corp., USA). Both media were supplemented with 10 vol% of fetal bovine serum (Biochrom AG) and 100 U.ml<sup>-1</sup> penicillin/streptomycin (Sigma-Aldrich, USA). Cells were seeded onto the SF samples at 300 cells.mm<sup>-2</sup> for L929 and 150 cells.mm<sup>-2</sup> for hMSC.

##### **5.3.4.1 Optical microscopy**

The images of cultured cells on SF surfaces at 2 h, 6 h, and 1 d were captured using an optical microscope (Olympus IX 50, Olympus GmbH, Germany), with Hoffman modulation contrast objective HMC10 LWDLCA 0.25 n<sub>a</sub>, digital camera AxioCam HR and image analysis software AxioVision 4.7 (Carl Zeiss MicroImaging GmbH, Germany).

### 5.3.4.2 Immunofluorescence microscopy

For immunofluorescence analysis, L929 and hMSC cultured for 1 d on untreated and plasma treated SF surfaces were rinsed with PBS and fixed in 4% w/v paraformaldehyde (Sigma-Aldrich) in PBS for 15 min. All experiments were conducted at room temperature (20 °C). Samples were permeabilized with 0.5% w/v TritonX-100 (Sigma-Aldrich) in PBS for 10 min.

Cell nuclei were stained with 2  $\mu\text{g}\cdot\text{ml}^{-1}$  of Hoechst 33342 (Life Technologies) in PBS for 10 min. Samples were then blocked by three consecutive incubations in 10% w/v goat serum albumin (GSA, 60  $\text{mg}\cdot\text{ml}^{-1}$ , Dianova GmbH, Germany) in PBS for 10 min, followed by 60 min incubation with a monoclonal mouse anti-human/mouse paxillin antibody (1:100, BD Transduction Laboratories, Germany), or a polyclonal rabbit anti-human/mouse fibronectin antibody (1:200, Santa Cruz Biotechnology, Inc., USA.) in a 1% w/v GSA in PBS solution.

Samples were rinsed three times for 10 min with 1% w/v GSA in PBS and incubated with Alexa Fluor<sup>®</sup> 488 goat anti-mouse IgG or Alexa Fluor<sup>®</sup> 488 goat anti-rabbit IgG (1:200, Life Technologies) and Alexa Fluor<sup>®</sup> 633 phalloidin (1:50, Life Technologies) in a 1% w/v GSA solution in PBS for 45 min in the dark, in order to visualize antibody binding and F-actin filaments of the cellular cytoskeleton.

Samples were rinsed with PBS, mounted on object slides, and viewed by confocal laser scanning microscopy with a Leica TCS SP5, objective HCX PL APO Lbd. Bl 63x/1.40-0.60 oil, UV-diode (405 nm), argon laser (488 nm) and helium-neon laser (633 nm) (Leica Microsystems GmbH, Germany). Image processing was performed with Fiji open-source imaging processing software.

### 5.3.5 *Statistical Analysis*

All statistical calculations were performed using MINITAB release 14.12.0 software (Minitab, USA). Statistically significant levels were confirmed by the paired t-test at  $p < 0.05$  ( $n = 3$ ).





## 5.4 Comprehensive characterization of well-defined planar silk fibroin surface

### 5.4.1 *Results and Discussion*

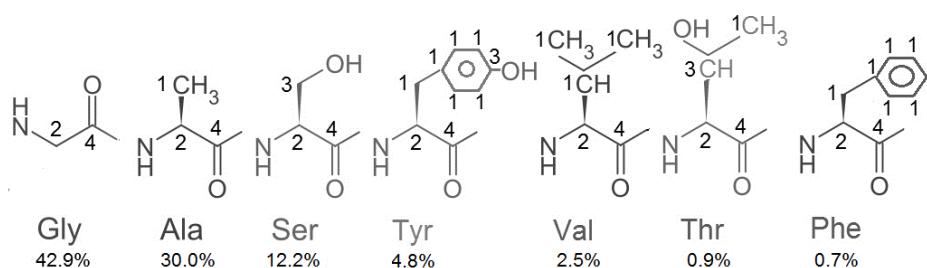
#### 5.4.1.1 Surface chemistry

The discussion of this section was divided into two parts: the first part was the calculation of SF theoretical surface chemistry and the second part was XPS results of the well-defined thin film compared with previous literature data.

XPS was used to check whether the prepared surface has similar chemistry to the theoretical value of silk fibroin. The amino acid composition of silk fibroin is used to calculate the theoretical atomic composition and carbon functionalities. Based on amino acid composition reported by Asakura *et al.* [140], silk fibroin amino acids could be classified into two groups: the crystalline domain amino acids and the amino acids which can be found only in the header, amorphous linkers, and c-terminus as illustrated in Figure 5-3.

From Figure 5-3, there are only 4 elements in silk fibroin amino acids: C, O, N, and S. The derived atomic composition is shown in Table 5-1. For comparison with other reports, the atomic composition is simplified only for 3 elements (C, O, and N) and summarized in the simplified column of Table 5-1. Sulfur content is minuscule and simple XPS could not detect such a small amount.

**Crystalline domain amino acids (also found in other domains)**



**Amino acids found only in header, linkers and c-terminus (not in crystalline domains)**

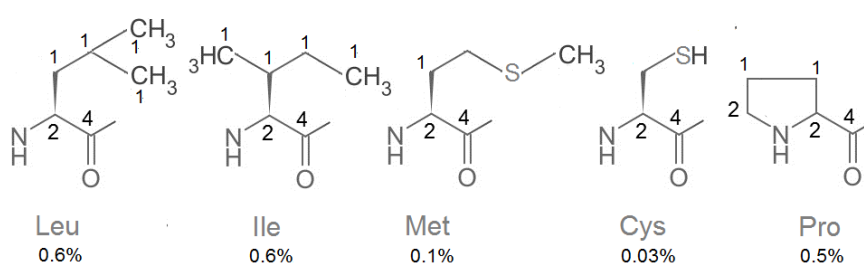
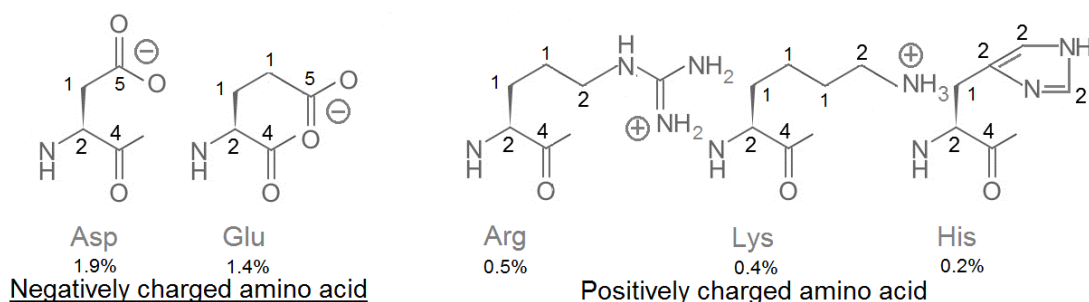


Figure 5-3 Molecular structure of amino acids and its relative abundance in silk fibroin according to Asakura et al [140].

The numbers at the carbon atoms indicate different chemical environments for XPS C1s peak deconvolution i.e. 1:C-C/C-H, 2: C-N, 3: C-O, 4: N-C=O, 5: HO-C=O, 6: arginine, and 7: C-SH

Table 5-1 Percent theoretical atomic composition of silk fibroin derived from the amino acid composition reported by Asakura *et al* [140]

Element	% theoretical atomic composition	
	Full version	Simplified version
C	57.65%	57.7%
O	23.23%	23.2%
N	19.10%	19.1%
S	0.02%	Nil

The theoretical carbon functionality content was calculated based on each amino acid carbon functionality. From Figure 5-3, there are seven carbon functionalities which marked with different number i.e. 1: C-C/C-H, 2: C-N, 3: C-O, 4: N-C=O, 5: HO-C=O, 6: arginine, and 7: C-SH. However, C-N (2) and C-O (3) functionalities could not be differentiated by XPS because of their overlapped binding energies. Moreover, the amount of arginine (6) and thiol (7) were too small to detect by XPS. In addition, the XPS resolution of binding energy is approximately at 1.5 eV so peak deconvolution would be more accurate if the peak separation is at least 1.5 eV. For all reasons set out above, these seven functionalities need to be simplified before these functionalities could be used as a reference peak in XPS deconvolution. The C-C/C-H (1) was maintained as a separate functionality with the center of binding energy at 285 eV. C-N (2) and C-O (3) were combined with the new center of binding energy at 286.5 eV, and N-C=O (4) and HO-C=O (5) were also combined with the binding energy at 288 eV. After simplification, there were 3 peaks for XPS deconvolution i.e. C-C/C-H, C-N/C-O, and N-C=O/HO-C=O as summarized in Table 5-2. The amount of 27.7% of C-C/C-H, 38.8% of C-N/C-O, and 33.5% of N-C=O/HO-C=O was used as the theoretical composition of SF functionality for comparison purpose with other SF surfaces.

Table 5-2 Silk fibroin theoretical carbon functionality composition derived from the amino acid composition reported by Asakura *et al* [140]

Number in Figure 5-3	carbon functionality	Binding energy (eV)	Amount	Simplified Peak <sup>20</sup>	Binding energy (eV)	Amount
1	C-C/C-H	284.6-285.0	27.66%	1	285	27.7%
2	C-N	285.5-286.5	32.87%	2+3	286.5	38.8%
3	C-O	286.4-287.0	5.78%	-	-	-
4	N-C=O	287.4-288.4	32.39%	4+5	288	33.5%
5	HO-C=O	289.2-289.3	1.07%	-	-	-
6	Arginine	289.0-289.5	0.16%	excluded	-	-
7	C-SH	285.2 -285.5	0.07%	excluded	-	-

Table 5-3 summarizes the XPS atomic composition and carbon functionalities composition ( $C_{1s}$  components) of SF obtained from this work, compared to other literature data and the theoretical values of atomic/carbon functionalities composition which were described previously. From the results of this work, the differences of XPS data between the research grade XPS (first data of the pair) and general XPS using for routine measurement (last data of the pair), were not large, i.e. C atom: 62.3% vs. 61.2%, N atoms: 18.6% vs. 18.6%, O atoms: 19.1% vs. 20.2%, C-H functionality: 29.0% vs. 28.7%, C-N/C-O functionalities: 39.0% vs. 38.3%, and N-C=O/O-C=O functionalities: 32.0% vs. 33.0% (Table 5-3, surface 2 vs. 3). In this table, the XPS data of Japanese SF was also presented in order to additionally compare SF from two silkworm races. Regarding the silkworm race (Thai vs. Japanese), the XPS data were quite similar between 2 races, i.e. C atom: 61.2% vs. 62.9%, N atoms: 18.6% vs. 19.2%, O atoms: 20.2% vs. 17.9%, C-C/C-H functionality: 28.7% vs. 29.5%, C-N/C-O functionalities: 38.3% vs. 38.3%, and N-C=O/O-C=O functionalities: 33.0% vs. 32.2% (Table 5-3, surface 3 vs. 4). In addition, Thai SF film was casted from hexafluoroisopropanol (HFIP) SF solution, while Japanese SF film was casted

<sup>20</sup> for comparison purpose with others XPS spectra

from aqueous SF solution. The difference of solvent used to prepare SF solution did not affect on aliphatic hydrocarbon contamination. C-H functionality of both surfaces was similar.

Table 5-3 A summary of XPS atomic composition and carbon functionalities (C<sub>1s</sub> components) results of SF surface from this work compared with previous literatures (theoretical values were % atomic composition and XPS C<sub>1s</sub> components based on the amino acid composition according to Askaura et. al. [140] as shown in Table 5-1 and Table 5-2, respectively)

Surface	Atomic composition				XPS C <sub>1s</sub> components			Reference
	C	N	O	other	1 C-C C-H	2+3 C-N C-O	4+5 N-C=O O-C=O	
1 Theoretical SF	57.7%	19.1%	23.2%	Nil <sup>21</sup>	26.5%	39.5%	34.0%	[140]
2 Thai silk fibroin film <sup>22</sup>	62.3%	18.6%	19.1%	-	29.0%	39.0%	32.0%	this work
3 Thai silk fibroin film <sup>23</sup>	61.2%	18.6%	20.2%	-	28.7%	38.3%	33.0%	this work
4 Japanese silk fibroin	62.9%	19.2%	17.9%	-	29.5%	38.3%	32.2%	this work
5 silk fibroin film	64.3%	13.7%	22.0%	-	72.7%	4.8%	22.5%	[141]
6 degummed silk fabric	60.6%	10.9%	28.5%	-	-	-	-	[142]
7 degummed silk fiber	-	-	-	-	50.0%	26.0%	24.0%	[143]
8 silk fibroin film	68.7%	11.6%	19.4%	0.3 <sup>24</sup>	-	-	-	[144]
9 silk fibroin film	71.9%	13.7%	14.4%	-	-	-	-	[145]
10 degummed silk fiber	70.0%	13.0%	17.0%	-	-	-	-	[146]
11 spun silk fiber	67.3%	6.4%	19.9%	7.0% <sup>25</sup>	61.8%	22.6%	15.5%	[147]
12 silk fibroin film	-	-	-	-	59.3%	17.8%	22.9%	[148]
13 silk fibroin nanofiber	75.5%	8.5%	16.0%	-	-	-	-	[149]

In comparison to the theoretical value and other literature data, the XPS data of SF surface from this work (Table 5-3, surface 2 – 4) were rather

<sup>21</sup> Sulfur content should be around 0.02% if it could be detected by XPS.

<sup>22</sup> From research grade XPS, Axis Ultra spectrometer XPS

<sup>23</sup> From general XPS using for routine measurement, Amicus spectrometer XPS (18 different measurements)

<sup>24</sup> S

<sup>25</sup> Si

close to the theoretical value (Table 5-3, surface 1) in terms of atomic and carbon functionality compositions. The carbon atom contents of SF surface from this work were ranged from 61.2% and 63.2% which were slightly higher than the theoretical value of 57.7%. This phenomenon indicates the small amount of carbon contamination. The literature data of C atom contents were varied from 60.6% - 75% [141, 142, 144-147, 149], mostly indicated higher carbon contamination. The type of carbon contamination was aliphatic hydrocarbon; this could be observed in XPS C1s component of C-C/C-H. In this work, aliphatic hydrocarbon (C-H) were ranged from 28.7% - 30.5%, slightly higher than the theoretical value of 26.5%. The literature data indicated much higher aliphatic hydrocarbon contamination from 50.0% to 72.7% [141, 142, 147, 148], compared to the theoretical value. The contamination from aliphatic hydrocarbon is a common phenomenon in XPS measurement [150].

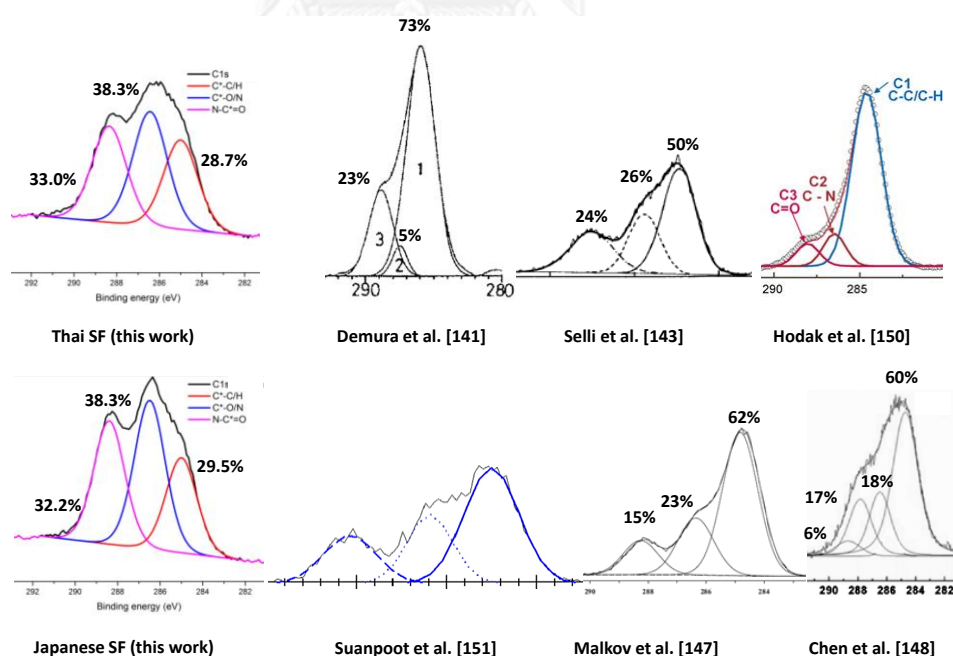


Figure 5-4 XPS C 1s spectra from this work (Thai and Japanese silk fibroin) compared with those reported in the literature

(Note: C-C/C-H peak (285 ev) is the peak which appear on the far right.)

[141, 143, 147, 148, 151, 152]

The XPS spectra from this work compared to those reported in the literature are illustrated in Figure 5-4. This figure shows the previously discussed phenomenon of high aliphatic contamination in other reports as indicated by the excess of C-C/C-H (Binding energy of 285 eV).

#### **5.4.1.2 Surface charge**

Silk fibroin is known to be a negatively charged surface from its amino acid composition. Majority of silk fibroin amino acid are uncharged. However, there were small portion of charged amino acid (4.4%). In that charged amino acids, the negatively charged ones (3.3%) is higher than the positive ones (1.1%) [140]. Figure 5-5 shows the streaming current vs. pressure gradient, and apparent zeta potential of SF in the different ionic strength of the streaming flow (0.1 mM KCl, 1 mM KCl, and 10 mM KCl). The results confirmed that silk was negatively charged surface. The higher ionic strength solution dampened the zeta potential. The zeta potential was closer to the zero value if the ionic strength of streaming solution was increased, i.e., the absolute value of zeta potential was lower under 10 mM KCl than 0.1 mM KCl of streaming flow solution. However, the IEP of SF surfaces was around pH4 and was not affected by the ionic strength of streaming flow solution (0.1 – 10 mM of KCl).

CHULALONGKORN UNIVERSITY

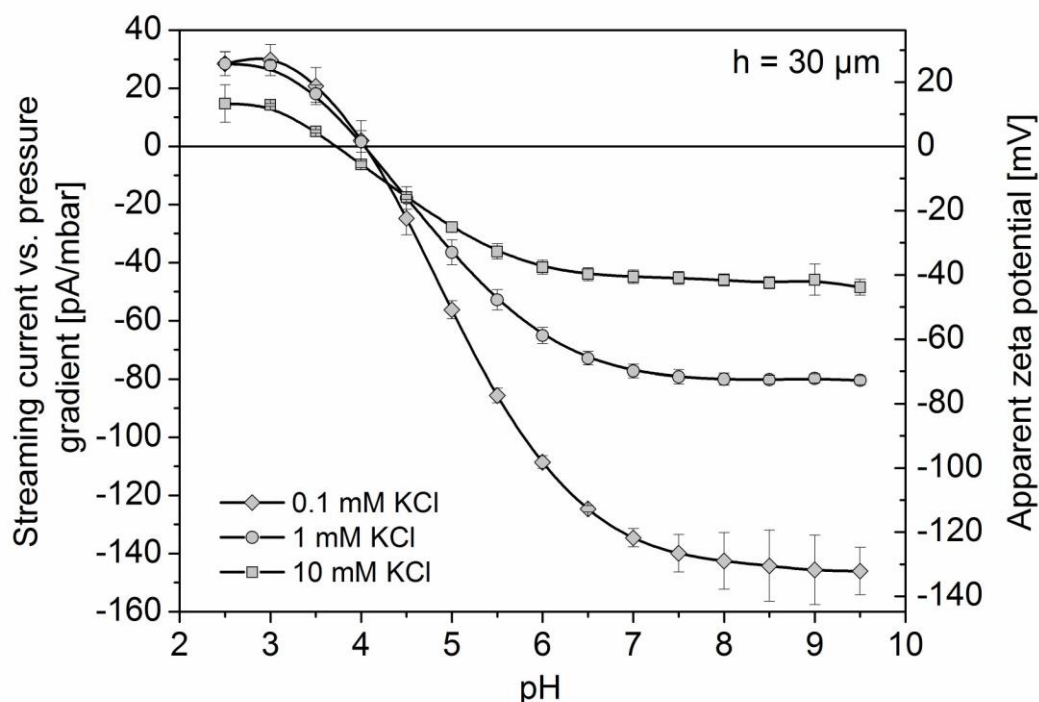


Figure 5-5 Streaming current vs. pressure gradient and apparent zeta potential versus pH value of the silk fibroin surface for 0.1, 1 and 10 mM KCl solution.

#### 5.4.1.3 Thickness, refractive index, and swelling ratio of SF

Ellipsometry was used to determine the thickness, optical property (i.e. refractive index), and swelling ratio of silk fibroin film. The thickness data was used to ensure that the thin film was prepared with the desirable thickness of 70 nm. The refractive index data was mainly used for the quick determination of crystalline content in dry SF. The swelling ratio information indicates the hydration process of SF under various conditions such as liquid ionic strength or liquid temperature. The hydration process is a first step prior to other cell-substrate interaction processes [50, 51].

The effects of methanol annealing on SF thickness and refractive index were studied with the ellipsometry. SF thickness change was slightly decreased about 1 – 2 nm after methanol annealing regardless of annealing time. The refractive index of the amorphous SF film (before annealing with



methanol) was found as  $1.531 \pm 0.001$  and increased upon 60 min of methanol annealing to  $1.563 \pm 0.001$ . The observed change of the optical properties is considered significant and attributed to the formation of the semi-crystalline structure. This effect is well known for other semi-crystalline polymers like polypropylene where a 40% increase of the crystallized volume fraction lead to an increase of the refractive index by 0.02 [153].

The swelling ratio of SF in liquid could be calculated from the thickness of SF film measured in both dry condition and wet condition (with the liquid cell). The swelling ratio of SF could be affected by many parameters such as film thickness, crystalline content, liquid ionic strength, liquid temperature etc.

Figure 5-6 shows silk fibroin swelling ratio and the refractive index in DI water as a function of dry film thickness. In order to understand the effects of dry film thickness on swelling ratio and refractive index, SF films were prepared with the different dry thickness (8 – 120 nm) by adjusting dip coater speed. From Figure 5-6, it could conclude that silk fibroin is swelling. For very thin films (dry thickness < 70 nm), the swelling ratio and refractive index were a function of film thickness. The swelling ratio was at minimal value (1.15) with the thinnest film (8 nm). This was also in line for what Wallet *et al* [154] reported that that the swelling ratio of SF was minimal (about 1) for the thickness of 5 nm. In the case of film thickness higher than 70 nm, the swelling ratio was almost in the same range (1.7 – 1.8) as well as the refractive index. This was the reason to use SF film at the thickness of 70 nm thickness for all experiments in this study.

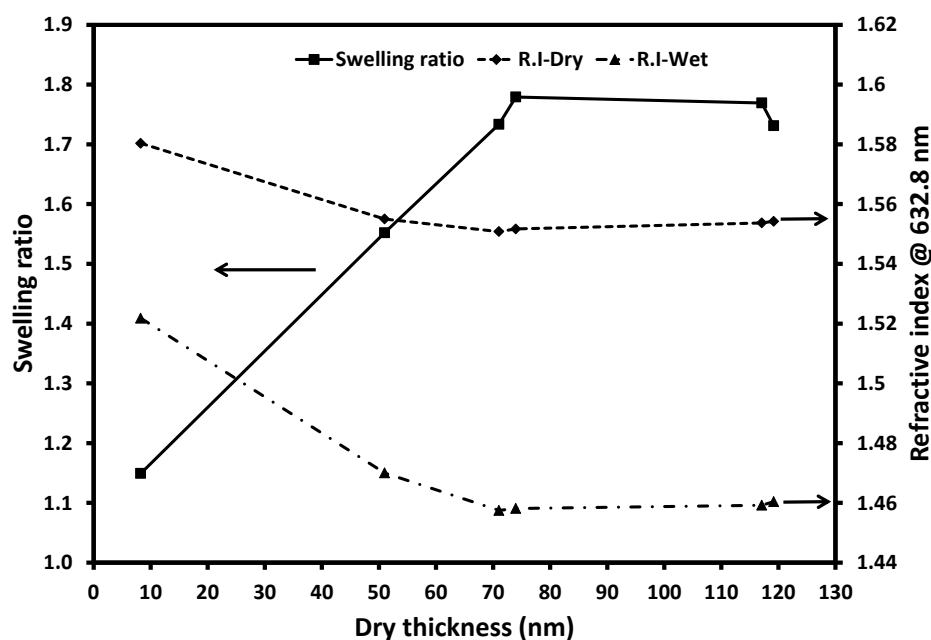


Figure 5-6 Swelling ratio in DI water and refractive index in dry and wet conditions as a function of dry film thickness

The annealing time of SF in methanol might induce different crystalline content in SF structure. In order to find the proper methanol annealing periods, silk fibroin samples annealed with methanol for different period (1h, 1d, and 4d) were assessed with ellipsometry to determine the swelling ratio in DI water and the refractive index in dry and wet conditions as shown in Figure 5-7. From Figure 5-7, the results suggested that different annealing time did not change swelling ratio in DI water and the refractive index of silk fibroin both in air and in DI conditions. The refractive index could be used to indicate the degree of crystallinity of semi-crystalline polymer. Since the refractive index is evaluated by the change of light velocity from one medium (air or DI) to another medium (silk fibroin), the light also travels with different velocity through different molecular sections (crystalline and amorphous) [153]. The refractive index data indicated that there was no change of crystalline content in silk fibroin film with different methanol annealing time (1h, 1d, and 4d). This finding was contrary to the previous

report by Hu *et al* which indicated higher crystallinity of longer methanol annealed sample, i.e. 4d methanol-annealed SF had higher crystalline content than 1d methanol-annealed SF [129]. These conflicting results might be from different film thickness. The film in this study was in nanometer range while the film studied by Hu *et al* was in micrometer range. As a result, the short methanol annealing time (1h) was used in our standard film preparation.

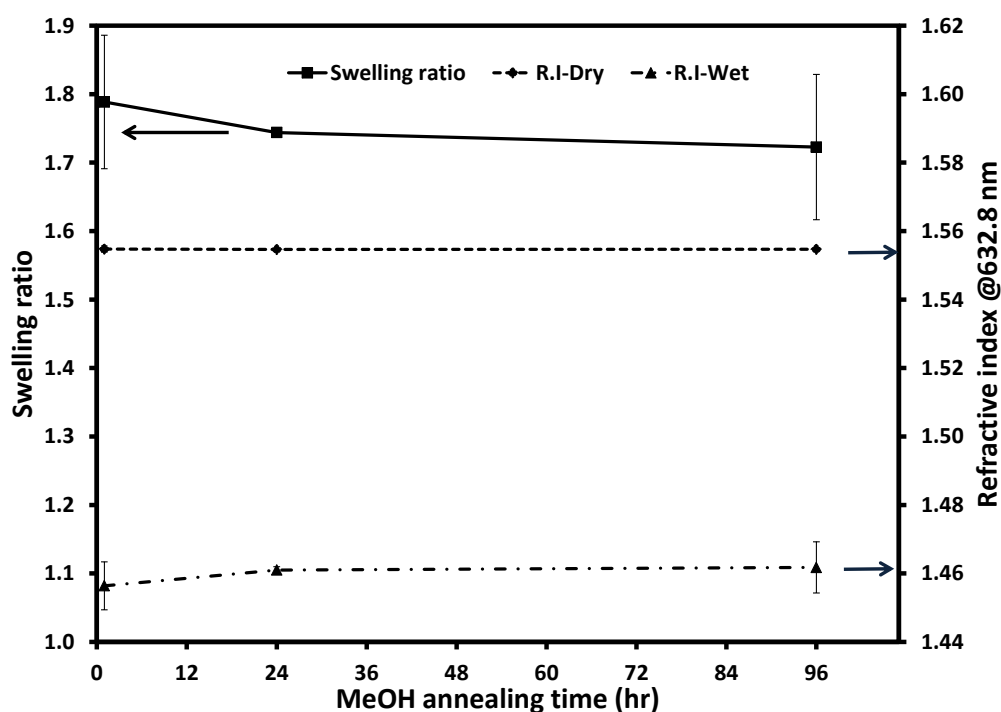


Figure 5-7 Swelling ratio in DI water and refractive index in dry and wet conditions of silk fibroin which had annealed with methanol for different period

The next three experiments focused on the hydration process of the prepared SF film (70 nm thickness, with 1 h of methanol annealing time) in various liquid conditions such as liquid ionic strength and liquid temperature. The understanding of SF hydration behavior could be beneficial to the study of cell-substrate interaction.

Figure 5-8 shows silk fibroin thickness change in different media which have different ionic strength (DI and phosphate buffer solution (PBS1X)) using measurement mode of insitu thickness monitoring at the same spot. The ions in PBS definitely enhanced the swelling of SF compared with the swelling in DI, an almost ion-free condition. The swollen layer in PBS was thicker than in DI. This effect is reversible as could be observed that when PBS in liquid cell was replaced with DI, the thickness was gradually decreased back close to the initial thickness in DI. This slightly higher thickness might be from the trace PBS remained in the swollen silk fibroin.

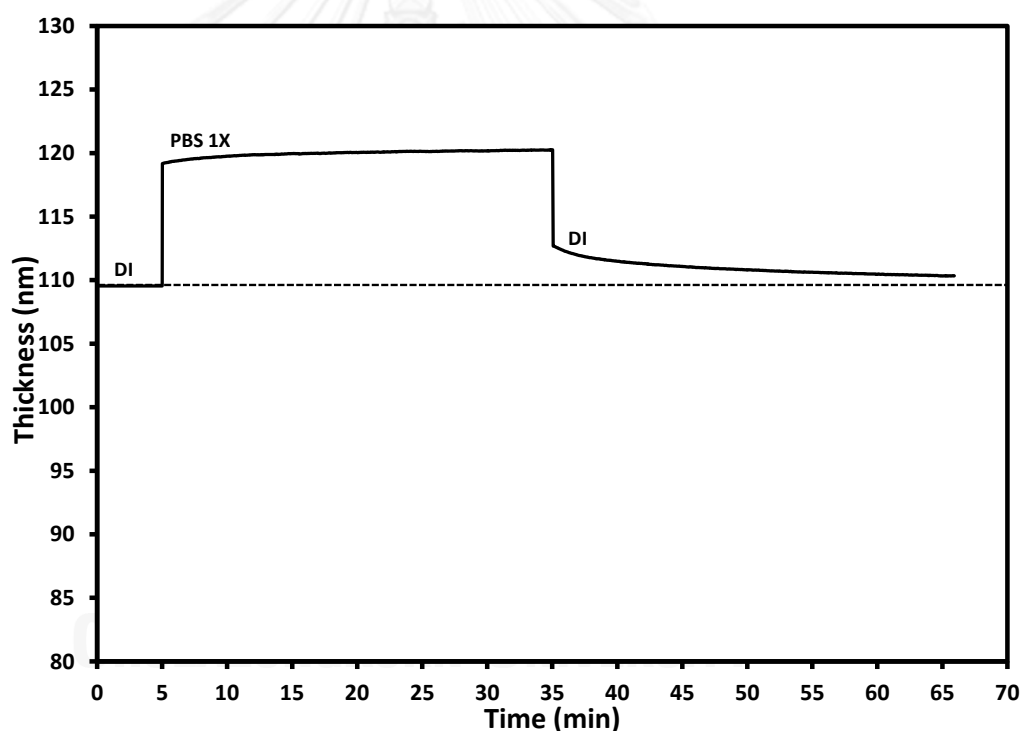


Figure 5-8 Silk fibroin film thickness change in different media which has different ionic strength (deionized water (DI) and phosphate buffer solution (PBS)) using measurement mode of in-situ thickness monitoring at the same spot (dry film thickness of 70 nm)

The previous result suggested that the presence of ions promoted the swelling of SF. However, the effect of ionic strength on SF swelling needed to

be further investigated. The PBS was then prepared with different ionic strength (0.1X, 0.25X, 0.5X, 1X, 5X, and 10X) to study this effect.

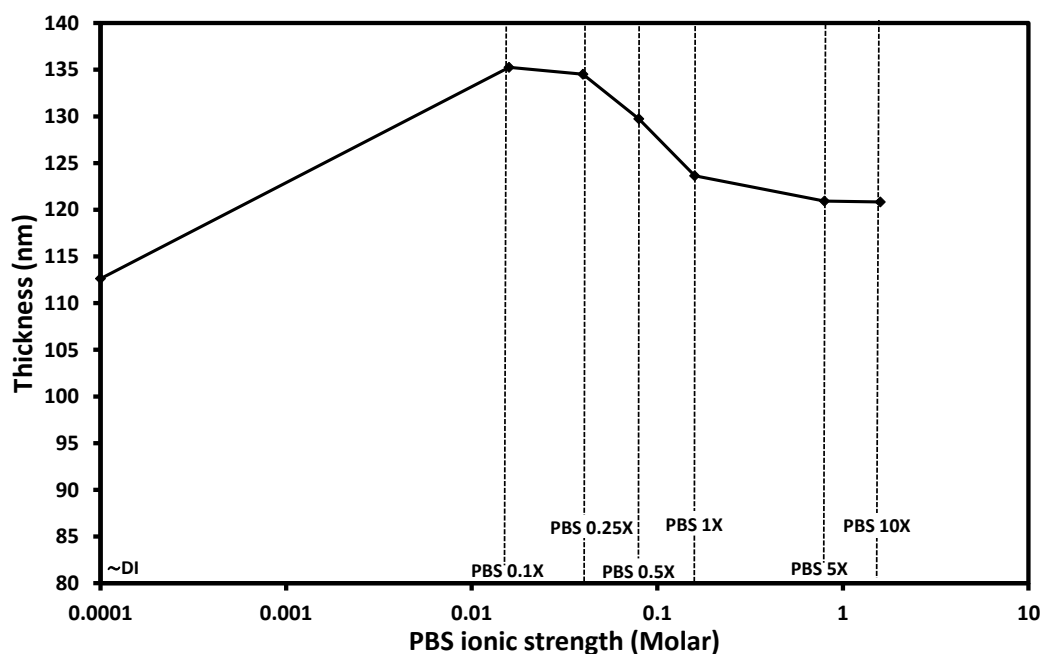


Figure 5-9 Silk fibroin film thickness change in deionized water (DI) and phosphate buffer solution (PBS) with different strength (0.1X – 10X) using measurement mode of in-situ thickness monitoring at the same spot (dry film thickness of 70 nm)

Figure 5-9 shows silk fibroin thickness change in deionized water (DI) and phosphate buffer solutions (PBS) with different strength (0.1X – 10X) using measurement mode of in-situ thickness monitoring at the same spot. The swelling of silk fibroin was highest in PBS which had the lowest ionic strength (0.1X). The swelling of silk fibroin was gradually lower when the concentration (strength) of PBS was continuously increased. At the lowest concentration, the electrostatic repulsion force might be at maximum between silk fibroin and ions in PBS solution. When the PBS concentration was increased, the charge on silk fibroin was dampening by the opposite ions in PBS resulting to the collapse of swollen layer. This phenomena also was reported in different system (polystyrene-poly(acrylic acid) brushes; PS-PAAc ) by Currie *et al* [155].

They reported that PS-PAAc brushes thickness in sodium chloride solution had been steadily increased from ionic strength of 0.0001M and reached the maximum thickness at the ionic strength of 0.1M. When the ionic strength was further increased beyond 0.1M, the thickness was decreased [155].

Another parameter that affected the swelling of materials was liquid temperature, as it was normally found in thermally responsive materials. It should then be worthwhile to confirm whether SF is a thermally responsive material or not because there has not been any report on this property. In the experiment, SF thickness was monitored in the liquid cell of which temperature was controlled by a heating/cooling device.

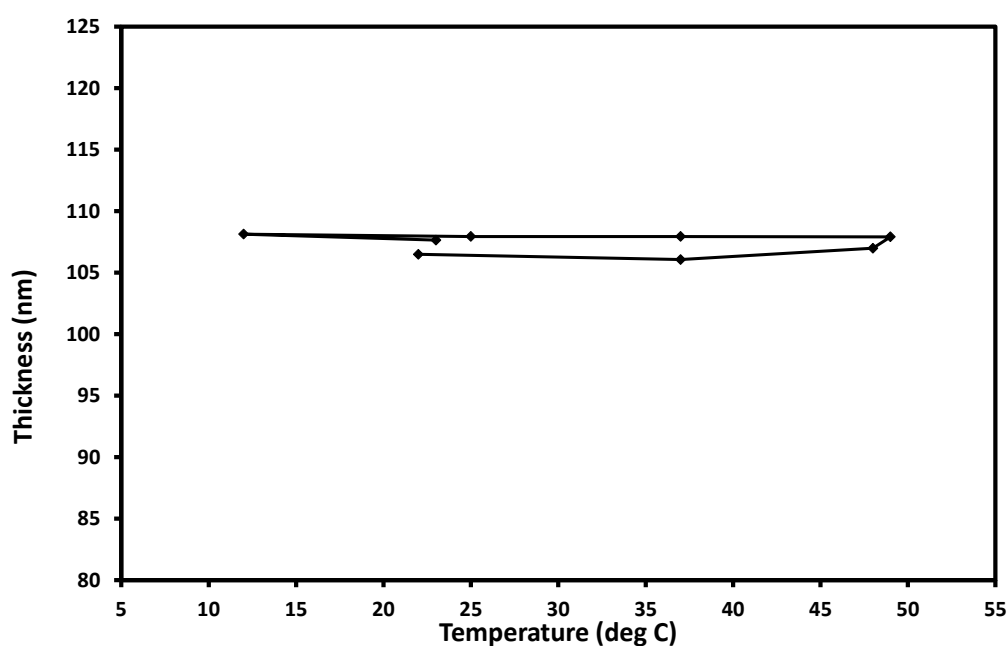


Figure 5-10 Silk fibroin film thickness in phosphate buffer solution at various temperature from 12 to 49 degree Celsius (dry film thickness of 70 nm)

Figure 5-10 shows silk fibroin thickness in phosphate buffer solution (PBS1x) with the variation of temperature from 12 to 49 degree Celsius. It clearly indicated that SF swelling was not temperature dependent.

#### 5.4.1.4 Wetting behavior

The swollen SF makes the measurement of surface de-wetting impossible in the conventional sessile dropping technique because the surface still adsorbed water; the receding water contact angle is extremely low. The captive air bubble technique injects air bubble on the swollen surface of silk fibroin to establish three phase contact point (air-water-silk fibroin). The expanding air bubble volume facilitates the de-wetting process on silk fibroin surface. The advancing air bubble contact angle is used to calculate the receding water contact angle. On the other hand, the collapsing air bubble volume assimilates the wetting process. The receding air bubble contact angle is used to calculate the advancing water contact angle.

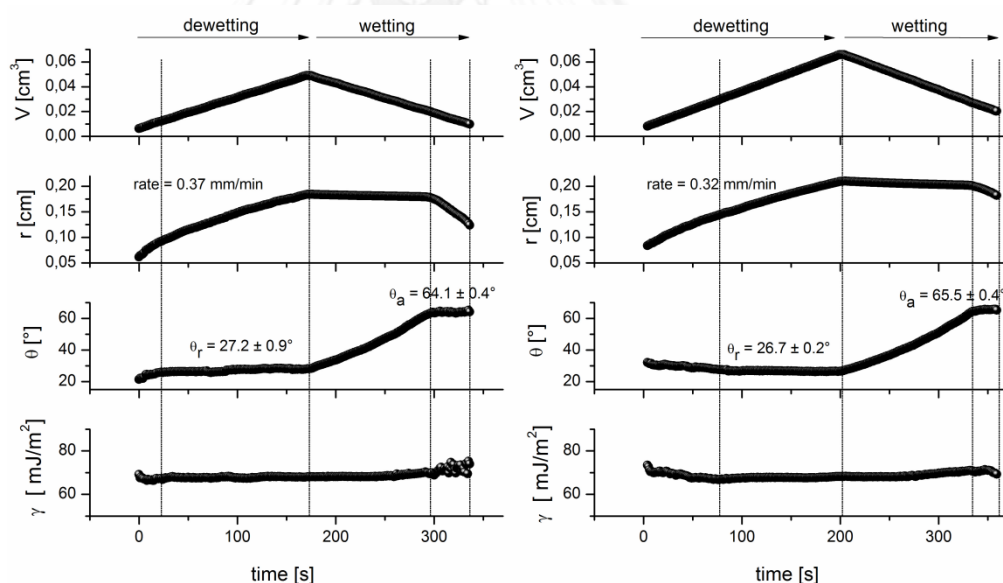


Figure 5-11 Representative data sets of two water contact angle measurements on swollen SF surfaces using the captive bubble technique and ADSA ( $V$ : volume of the bubble;  $r$ : contact radius;  $\theta$ : water contact angle;  $\gamma$ : liquid surface tension; liquid: MilliQ water).

Figure 5-11 shows two data sets from the measurement of the receding water contact angle ( $\theta_r$ ) and advancing water contact angle ( $\theta_a$ ) on swollen SF surface in contact with DI using the captive air bubbles technique

in conjunction with axisymmetric drop shape analysis (ADSA). The calculated data include surface tension, advancing and receding water contact, contact radius, and bubble volume.

In the de-wetting process, air was injected continuously to expand the size of bubble as observed in the increased bubble volume and contact radius (top two panel), while the receding water contact angle, measured during de-wetting process, was nearly constant (the third panel from top). To study the wetting process, air was gradually sucked out of the bubble as noticed by the decreased volume (top panel). However, the contact radius (second panel from top) was unchanged initially, indicated that the solid/air/liquid interface was sticking. The contact interface line sticking was strong on swollen surface. This situation made the measurement of advancing water contact angle difficult. When the contact radius started to retract and the contact angle remained constant, this phenomenon signified the advancing water contact angle (third panel from the top). The hysteresis of water contact angle is defined as the difference between the advancing and receding water contact angle ( $\Delta\theta = \theta_a - \theta_r$ ). The advancing water contact angles were  $64.1 \pm 0.4^\circ$  (left panel) and  $65.5 \pm 0.4^\circ$  (right panel), while the receding water contact angles were  $27.2 \pm 0.9^\circ$  (left panel) and  $26.7 \pm 0.2^\circ$  (right panel) on swollen SF.

Table 5-4 summarizes water contact angle on silk fibroin surface which annealed with methanol from previously reported literatures in comparison to this work. The water contact angles reported in some previous literatures were measured using static water contact angle technique. This technique might provide the result with high variation (20 degree in the report by Seib *et al* [156]) because the technique is not suitable for the case of surface properties changing during the measurement (i.e. swelling in the case of SF)



[132]. The dynamic water contact angle using sessile drooping could provide the better results with lower variation (2 degree) as in the report by Motta *et al* [157]. However, the receding water contact angle could not be measured. There is no report of receding water contact angle as no researchers used the captive air bubble technique. It is clear that the captive air bubble technique is the right method to measure wettability of swollen surface since it could provide the important data of contact angle hysteresis, an information for indicating the surface heterogeneity (chemical or morphological).

Table 5-4 Summary of water contact angle on silk fibroin surface which annealed with methanol from different literature in comparison to this work

Surface	Solvent used for preparation	Water contact angles			Reference
		static	advancing	receding	
silk fibroin film	HFIP	–	66.1±1.7°	26.7±2.8°	this work <sup>26</sup>
silk fibroin film	H <sub>2</sub> O	80°	–	–	[145]
silk fibroin film	HFIP	–	78±2°	not measurable	[157]
silk fibroin film	H <sub>2</sub> O	–	67±2°	not measurable	[157]
silk fibroin film	H <sub>2</sub> O	80±20°	–	–	[156]
silk fibroin film	H <sub>2</sub> O	70±1°	–	–	[148]
degummed Thai silk fabric	n/a	70±5°	–	–	[158]

#### 5.4.1.5 The degree of crystallinity

FTIR-ATR was used in order to determine the degree of crystallinity by evaluating the secondary structure of SF protein at the amide I region 1595 – 1705 cm<sup>-1</sup> [129]. The  $\beta$ -sheet content represents the crystalline structure in SF molecules.

<sup>26</sup> average from 7 individual measurements

Figure 5-12 illustrates the effect of methanol annealing time on FTIR spectra at amide I region ( $1600 - 1705 \text{ cm}^{-1}$ ). Methanol clearly induced the  $\beta$ -sheet structure in silk fibroin as observed by the peak shift from  $1640 - 1660 \text{ cm}^{-1}$  ( $\alpha$ -helix and random coils) to  $1615 - 1640 \text{ cm}^{-1}$  ( $\beta$ -sheet) region [129] for all annealing time (30 min, 1h, 1d, and 4d). The shape of FTIR absorbance curve at amide I was similar for all methanol-annealed silk fibroin. Apparently, the annealing time longer than 30 minutes did not further change the shape of FTIR curve.

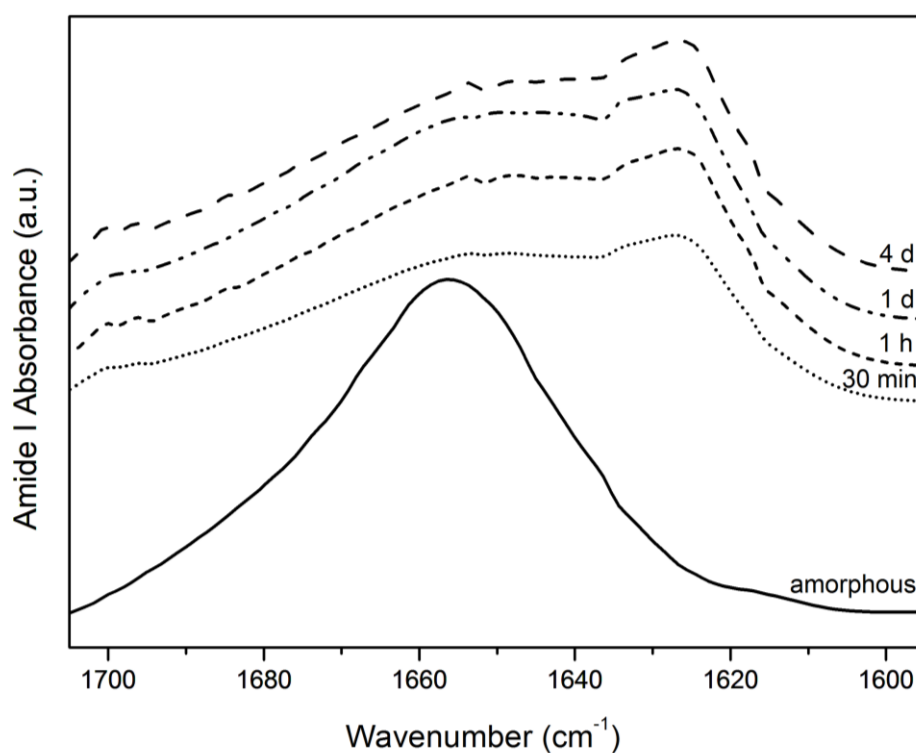


Figure 5-12 Changes in the FTIR spectra of SF samples upon methanol treatment at amide I ( $1600 - 1705 \text{ cm}^{-1}$ )

Fourier self deconvolution (FSD) was applied to modify FITR spectrum for peak fitting according to the procedure by Hu *et al* with following peak assignment: tyrosine side chain ( $1605-1615 \text{ cm}^{-1}$ ),  $\beta$ -sheet ( $1616-1637 \text{ cm}^{-1}$  and  $1697-1703 \text{ cm}^{-1}$ ), random coil ( $1638-1655 \text{ cm}^{-1}$ ),  $\alpha$ -helix ( $1656-1662 \text{ cm}^{-1}$ )

, and  $\beta$ -turn ( $1663\text{--}1696\text{ cm}^{-1}$ ) [129]. The peak deconvolution results of SF before  $\beta$ -sheet induction with methanol and SF after  $\beta$ -sheet induction with methanol for 1 h are illustrated in Figure 5-13.

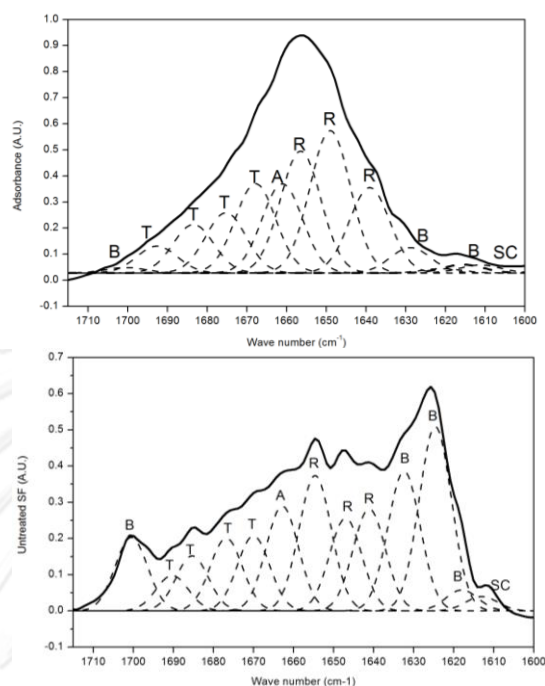


Figure 5-13 Fourier self deconvolution along with peak fitting of SF before  $\beta$ -sheet induction with methanol (top graph) and SF after  $\beta$ -sheet induction with methanol for 1 h (bottom graph) where B:  $\beta$ -sheet, T:  $\beta$ -turn, A:  $\alpha$ -helix, R: random coil, and SC: tyrosine side chain

From Figure 5-13, it is clear that there were differences in SF protein secondary structure of SF before and after  $\beta$ -sheet induction with methanol. The  $\alpha$ -helix (A) and random coil (R) structures were more dominant than the  $\beta$ -sheet (B) structure in the case of untreated SF before  $\beta$ -sheet induction with methanol (top graph). On the contrary, the  $\beta$ -sheet (B) structure was much higher than  $\alpha$ -helix (A) and random coil (R) in the untreated SF after  $\beta$ -sheet induction with methanol (bottom graph).

The deconvolution results of SF protein secondary structure ( $\beta$ -sheet,  $\beta$ -turn,  $\alpha$ -helix, random coil, and tyrosine side chain) for all silk fibroin samples annealed with methanol for different period are summarized in Table 5-5. The  $\beta$ -sheet contents in all methanol-annealed SFs (35.6% - 39.2%) were much higher than the SF without methanol annealing (9%). The

crystalline content in methanol-annealed SF in this work was in the same range as reported by Hu *et al.* for the silk fibroin annealed in methanol for 1 – 2 days [129]. The longer incubation time of 4 days did not significantly increase the crystalline content (~55%) as previously reported by Hu *et al.* [129].

Table 5-5 Percentage of protein secondary structure based on different Fourier self deconvolution factor (deconvolution factor 10000 and noise reduction factor 0.5)

Annealing time	% protein secondary structure				
	$\beta$ -sheet	$\beta$ -turn	$\alpha$ -helix	Random coil	Tyrosine side chain
No annealing	9.0	31.4	11.8	46.3	1.4
1h	36.0	19.5	9.9	32.4	2.2
1d	35.6	20.0	10.3	32.0	2.0
4d	39.2	20.4	9.5	30.0	0.9

#### 5.4.1.6 Surface topography and stiffness

AFM was used to confirm whether the prepared SF surface was smooth. The surface topography of SF was evaluated in both air and phosphate buffer solution (PBS) as shown in Figure 5-14. The AFM images indicated that SF surface prepared from our standard procedure had a smooth texture. The RMS of SF in air was very small ( $0.5 \pm 0.1$  nm) when compared to conventional tissue culture plate ( $3.43 \pm 0.54$ ) [159]. In PBS, the same SF surface was swollen, the RMS was slightly increased to  $0.9 \pm 0.2$  nm.

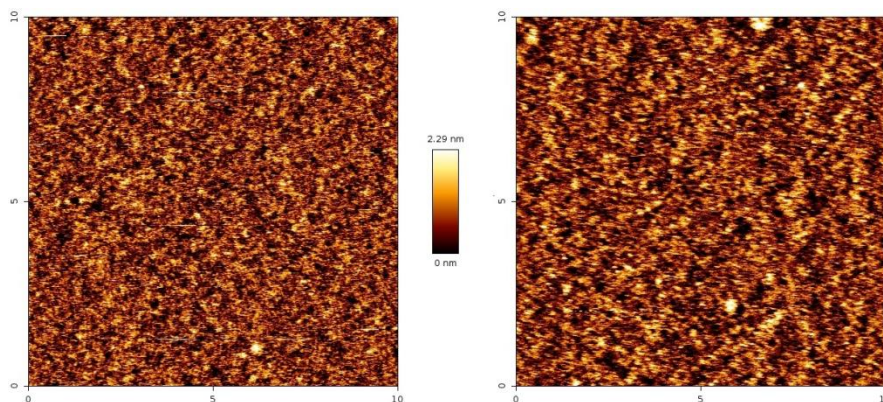


Figure 5-14 AFM images of silk fibroin with the scan area of  $10 \times 10 \mu\text{m}^2$  in air (left) and phosphate buffer solution (PBS) (right)

AFM based nano indentation was employed to determine the stiffness of swollen SF surface. This was to ensure that the prepared SF had a comparable mechanical property with the literature data. Figure 5-15 shows the elastic modulus of the swollen SF surface in PBS. An elastic modulus of approximately 70 kPa was found. From the previous study by Jetbumpenkul [4], the compressive modulus of swollen SF scaffold was 35 kPa.

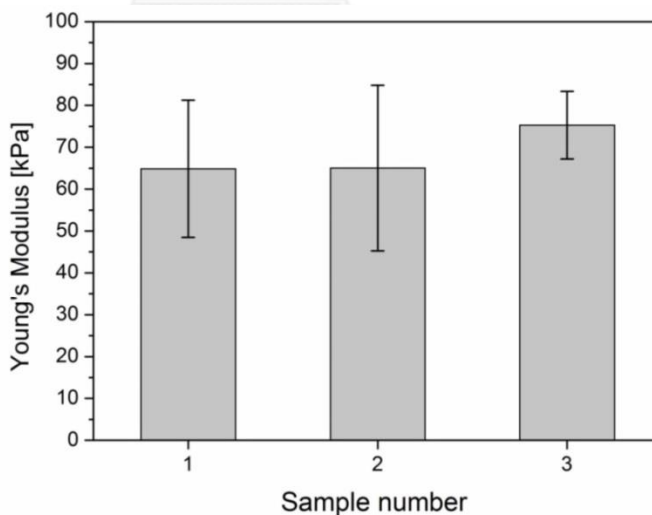


Figure 5-15 Young's modulus of silk fibroin surface in phosphate buffer solution (no. of sample =3, no. of scans per sample = 50)

### 5.4.2 *Conclusions*

The standard procedure was developed to ensure the preparation of a well-defined thin film which represented SF properties and met the requirements of all advanced characterization techniques. This standard thin film was well-defined in terms of surface chemistry as confirmed by XPS, surface charge as determined by electrokinetic measurement, thickness as measured by ellipsometry, degree of crystallinity as analyzed by FTIR-ATR, smooth surface topography as evaluated by AFM, and stiffness as measured by AFM based nano indentation. In addition, the characterizations of SF surface were performed in order to select the suitable analytical techniques and understand the properties before surface modification. Ellipsometry indicated that SF was a swollen material. The swelling degree depended on liquid ionic strength, but neither on film thickness (if thickness is higher than >70 nm) nor liquid temperature. The surface wettability of swollen SF needed to be measured by captive air bubble technique. The preparation procedure of a well-defined SF thin film, the suitable characterization techniques, and the understanding of SF properties provide a good framework for the study of plasma surface modification presented in Chapter 5, section 5.5 and section 5.6.

## 5.5 Finding of plasma operating conditions for surface functionalization

After gaining the knowledge to prepare a well-defined thin film, select the right characterization techniques, and understand the properties of untreated SF sufficiently, the study in this section was then geared to find plasma operating conditions for surface functionalization. The aim of surface functionalization was to change properties of SF surfaces (i.e. surface charge, surface wettability, etc.). These changed SF surface properties would later be evaluated for its effects on cell-substrate interaction. Different plasma gases were intended to induce different functional groups on SF surface. Oxygen and Argon/Oxygen plasma gases were intended to induce negatively charged groups on SF surface. Argon plasma gas was intended to generate free radicals on SF surface; the radicals would react with nitrogen and oxygen during air exposure. Ammonia plasma gas was intended to induce positively charged moieties on SF surface.

The process of finding right plasma operating conditions for surface functionalization was started from the conditions which generate low amounts of plasma active species (i.e. high flow of plasma gas to increase pressure for reducing electron mean free path and low power to generate stable plasma). The plasma treatment time was varied in order to induce desirable amount of functional groups on SF surface. This concept would minimize unwanted etching from high energetic species.

The success of plasma surface functionalization was judged primarily by the difference in XPS spectra before and after plasma treatment. In addition, the plasma-treated surface would be rinsed to ensure that these induced functional groups could stay on the surface in liquid environment

(i.e. no dissolvable low-molecular weight layer in formed). The surface charge would also be evaluated by the electrokinetic measurements as another indicator for successful surface functionalization because XPS could not indicate all functional groups if binding energy of the plasma-induced functional groups were in the same range of SF original functional groups. Moreover, the plasma surface functionalization needed to be more dominant than plasma etching (i.e. the thickness loss should be less than 20 nm after the plasma treatment). The effects of each plasma gas on surface chemistry and surface charge of SF were presented and discussed in the next section.

### **5.5.1 Results and Discussion**

#### **5.5.1.1 Surface chemistry of oxygen plasma-treated SF**

The oxygen plasma treatment was intended to generate negatively charged surface by functionalizing oxygenated moieties such as hydroxyl (C-O), ether (C=O), and carboxylic (O-C=O) on silk fibroin surface. The first parameter set of plasma conditions was started from high oxygen flow of 40 sccm<sup>27</sup> (pressure =  $7.2 \times 10^{-3}$  mbar), plasma power of 250 W with duty cycle of 1 millisecond (ms) of power on and 1ms of power off, 125 W of effective power. Figure 5-16 shows XPS of O<sub>2</sub> plasma-treated samples before and after rinsing with DI compared to the untreated one.

---

<sup>27</sup> 49 sccm was the maximum O<sub>2</sub> flow



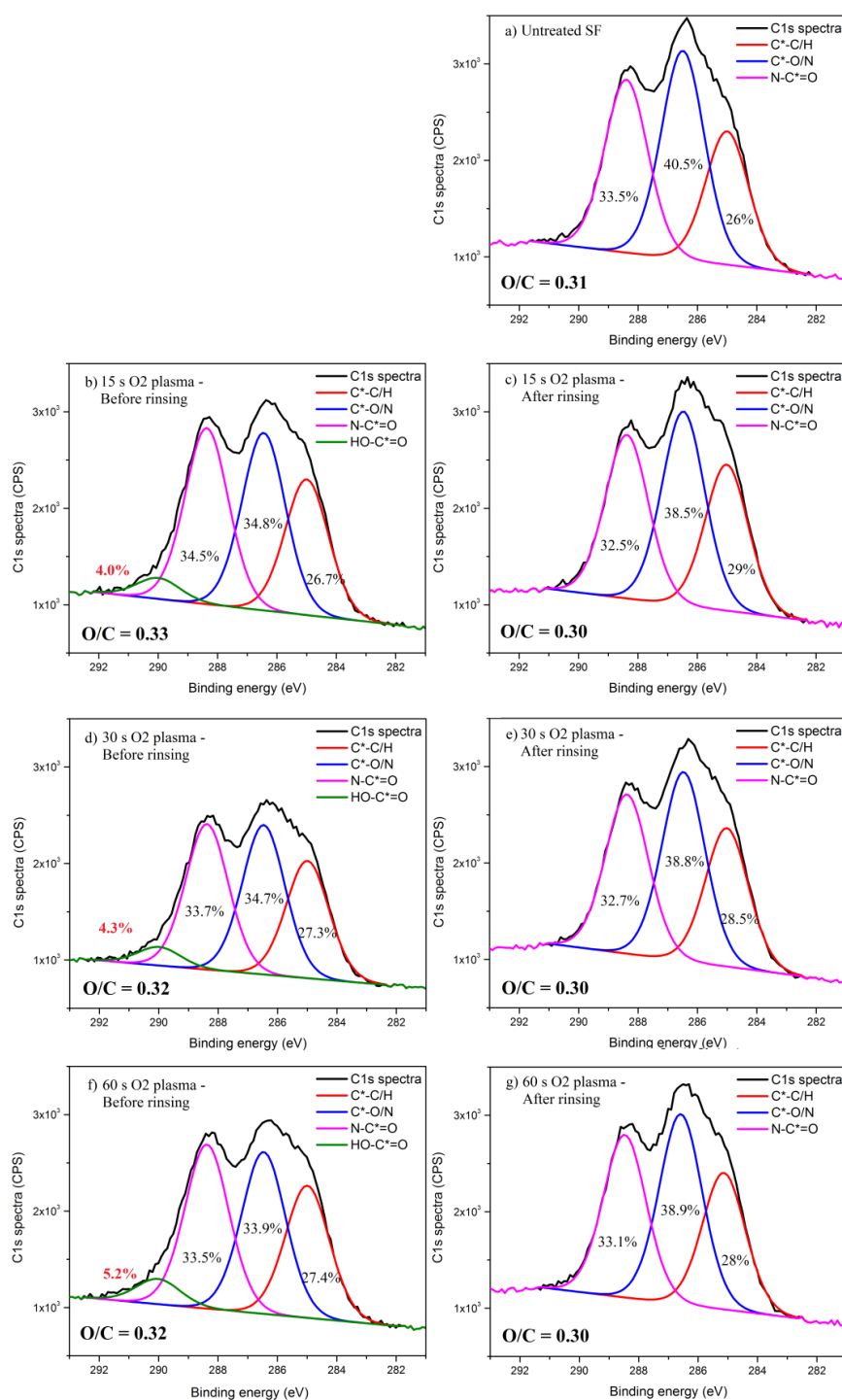


Figure 5-16 XPS spectra together with oxygen to carbon atomic ratios (O/C) of O<sub>2</sub> plasma-treated SF before and after rinsing with DI (O<sub>2</sub> flow 40 sccm, pressure =  $7.2 \times 10^{-3}$  mbar, power 250 W, duty cycle (on/off) 1/1 ms)

The C<sub>1s</sub> peak deconvolution revealed upto four components: aliphatic carbon (C–C/C–H) at 285.0 eV, the chemical shifts of 1.5 eV, 3.3 eV, and 4.6

eV with respect to C–C/C–H [150, 160]. The shift of 1.5 eV represented the combination of (C–N) and (C–O) bonds due to small separation of their binding energy compared to XPS resolution [160]. The shift of 3.3 eV represented amide bond (N–C=O) [160], while the shift of 4.6 eV represented carboxylic bond (O–C=O) [150]. The result of untreated SF (Figure 5-16a) showed 3 components: C–C/C–H, C–O/N, and N–C=O. After O<sub>2</sub> plasma treatment and before rinsing with DI, the XPS data indicated the extra peak of carboxylic group and the increase of O/C atomic ratio (Figure 5-16b, 5-16d, & 5-16f), compared to the case of untreated SF. The O/C atomic ratio was increased from 0.31 (untreated SF: Figure 5-16a) to 0.32 (60 s O<sub>2</sub> plasma - before rinsing: Figure 5-16f). The result indicated that O<sub>2</sub> plasma increased oxygen content as observed from the higher O/C atomic ratio. The carboxylic group (HO–C=O), oxygenated functionality, was increased with increasing treatment time. The 60 s O<sub>2</sub> plasma-treated SF showed 5.2% carboxylic, compared to none on the untreated surface.

However, after rinsing with DI, all XPS spectra of O<sub>2</sub> plasma-treated surfaces were very similar to that of untreated surface (Figure 5-16c, 5-16e, & 5-16g). This implied that all plasma-treated SF had lost their oxygen contents gained from O<sub>2</sub> plasma treatment. The O/C atomic ratio of the rinsed O<sub>2</sub> plasma-treated SF (0.30: Figure 5-16c, 5-16e, & 5-16g) was lower than the values of untreated SF (0.31: Figure 5-16a). The lower value of O/C atomic ratio of the rinsed O<sub>2</sub> plasma-treated SF could be from the contamination from the aliphatic hydrocarbon during rinsing and drying the samples. The similar XPS spectra between of O<sub>2</sub> plasma-treated SF (after rinsing) and untreated SF indicated unsuccessful functionalization on silk fibroin surface by oxygen plasma (i.e. a formation of a dissolvable and low molecular weight layer).

### 5.5.1.1.1 The effects of sample shield installation on surface functionalization by oxygen plasma.

The unsuccessful surface functionalization might be caused by the direct bombardment of high energy ions, so the sample shield, made of silicon wafer, was installed to protect SF from these high energy ions as illustrated in Figure 5-17. The ions would lose their kinetic energy when they hit the top of the shield. Nevertheless, active species from O<sub>2</sub> plasma still could access to functionalize the surface by entering the side opening of the shield.

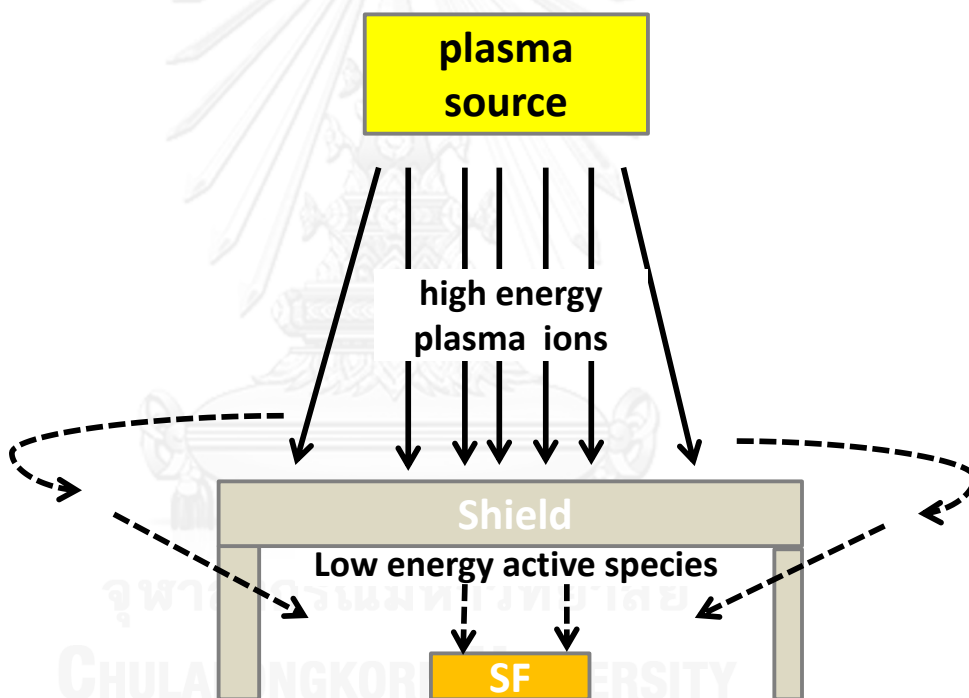


Figure 5-17 An installation of the sample shield for protecting SF high energy plasma ions

Figure 5-18 shows the XPS comparison between untreated SF and 30 s O<sub>2</sub> plasma-treated SF with sample shield after rinsing with DI. The plasma conditions were the same as in previous section (i.e. oxygen flow of 40 sccm and plasma power of 250 W with duty cycle of (1 ms power on/1ms power off)). It was clear that the installation of sample shield could not improve the

SF surface functionalization as indicated by the similar XPS spectra between two surfaces.

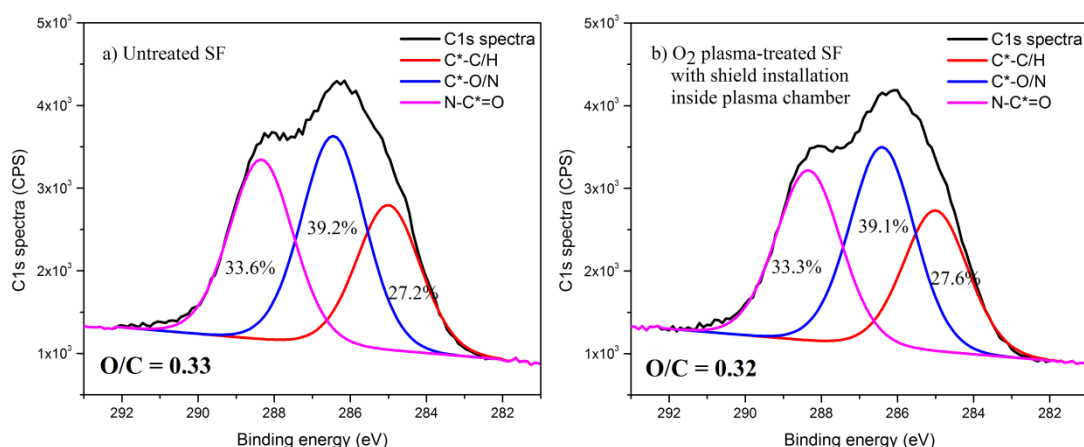


Figure 5-18 XPS spectra together with oxygen to carbon atomic ratios (O/C) of untreated SF and O<sub>2</sub> plasma-treated SF with shielding to prevent direct ion bombardment on the surface (sample was rinsed before XPS measurement)

#### 5.5.1.1.2 The trial of extremely low energy conditions for improving the surface functionalization effect by oxygen plasma

The high energy plasma ions were suspected as a cause of the failed surface functionalization by oxygen plasma. To reduce the energy of plasma ions, operating pressure was maximized (i.e. oxygen flow was increased to the maximum value) while plasma power was minimized.

The first trial of these conditions was that operating pressure was maximized ( $1.0 \times 10^{-2}$  mbar) by increasing oxygen flow to the maximum at 49 sccm and the plasma power was lowered to the region where plasma started to be unstable at 65 W. Figure 5-19 revealed the XPS spectra of O<sub>2</sub> plasma-treated SF with the above plasma treatment conditions after rinsing with DI, compared with the untreated SF. At these low power conditions combined with shorter treatment time, there still were no functionalization of intended

oxygen moieties on SF surface. The only significant increase was aliphatic hydrocarbon (C-C/C-H) content as shown in Figure 5-19 especially for shorter O<sub>2</sub> plasma treatment time of 3s and 10s (Figure 5-19b and Figure 5-19c). This content was increased from the value of 25.4% (untreated SF: Figure 5-19a) to 48.0% (3 s O<sub>2</sub> plasma-treated SF: Figure 5-19b) and 43.4% (10 s O<sub>2</sub> plasma-treated SF: Figure 5-19c). The amount of aliphatic hydrocarbon (C-C/C-H) was reduced with longer oxygen plasma treatment time and reached the saturation point at around 34.7% - 36.7% for the treatment time of 30 s or longer (Figure 5-19d & 5-19e). However, there was no sign of carboxylic peak (the fourth peak with +4.6 eV in binding energy) in any O<sub>2</sub> plasma-treated SF after rinsing with DI.



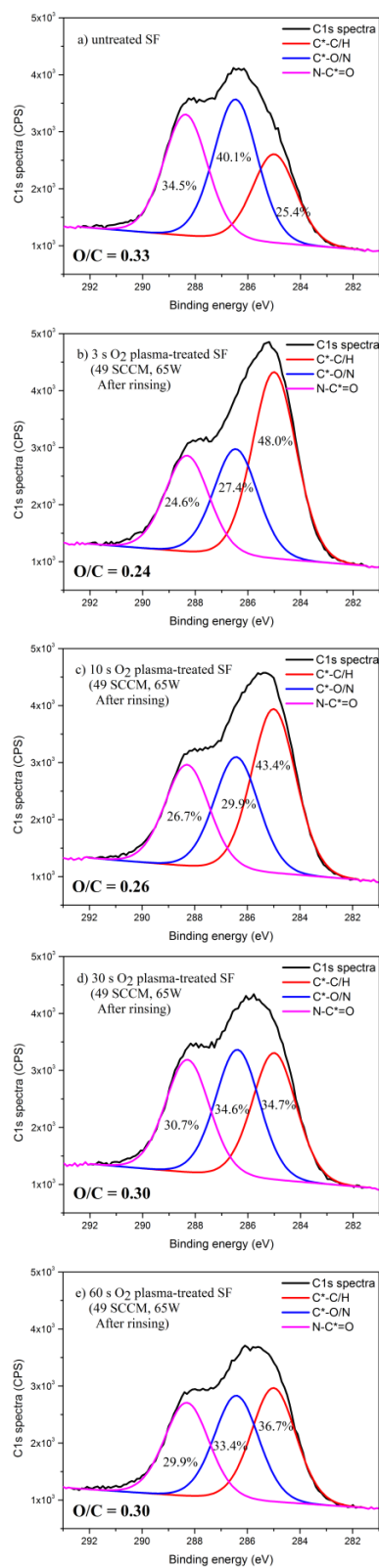


Figure 5-19 XPS spectra together with oxygen to carbon atomic ratios (O/C) of untreated and O<sub>2</sub> plasma-treated SF (after rinsing with DI), the plasma conditions were at highest O<sub>2</sub> flow (49 sccm), pressure =  $1.0 \times 10^{-2}$  mbar and low continuous power (65W)

For the second trial, the plasma power was lowered further to 10 W right after successful ignition plasma with the power of 65 W (1 milli-second after ignition). The XPS results are shown in Figure 5-20.

Before rinsing with DI, the oxygen/carbon atomic ratio was increased from 0.33 (untreated SF: Figure 5-20a) to 0.37 (all O<sub>2</sub> plasma-treated SF before rinsing: Figure 5-20b, 5-20d, 5-20f, & 5-20h). The third peak (N-C=O with 288.3 of binding energy) was also noticeably increased from 34.2% (untreated SF: Figure 5-20a) to the value of 37% (60 s/120 s O<sub>2</sub> plasma-treated SF before rinsing: Figure 5-20f, & 5-20h). The increase of third peak could be from ether peak (C=O) due to its closed binding energy to amide (N-C=O) [160]. Moreover, the increased amount of third peak was in line with the increase of O/C atomic ratio. The fourth peak (O-C=O with 289.6 eV of binding energy) was slightly detectable with the content of 2.0 – 2.7% (all O<sub>2</sub> plasma-treated SF before rinsing: Figure 5-20b, 5-20d, 5-20f, & 5-20h). The longer treatment seems to increase the content of ether (C=O) and carboxylic (O-C=O), but not to O/C atomic ratio.

After rinsing with DI, all O<sub>2</sub> plasma-treated SF lost their oxygen contents gained from O<sub>2</sub> plasma treatment. The O/C atomic ratios of the rinsed O<sub>2</sub> plasma-treated SF (0.31/0.32: Figure 5-20c, 5-12e, 5-20g, & 5-20i) was lower than the value of untreated SF (0.33: Figure 5-20a). The third peak (amide/ether) of all plasma-treated SF was lower than untreated SF. The fourth peak (carboxylic) disappeared from all plasma-treated SF after rinsing with DI.

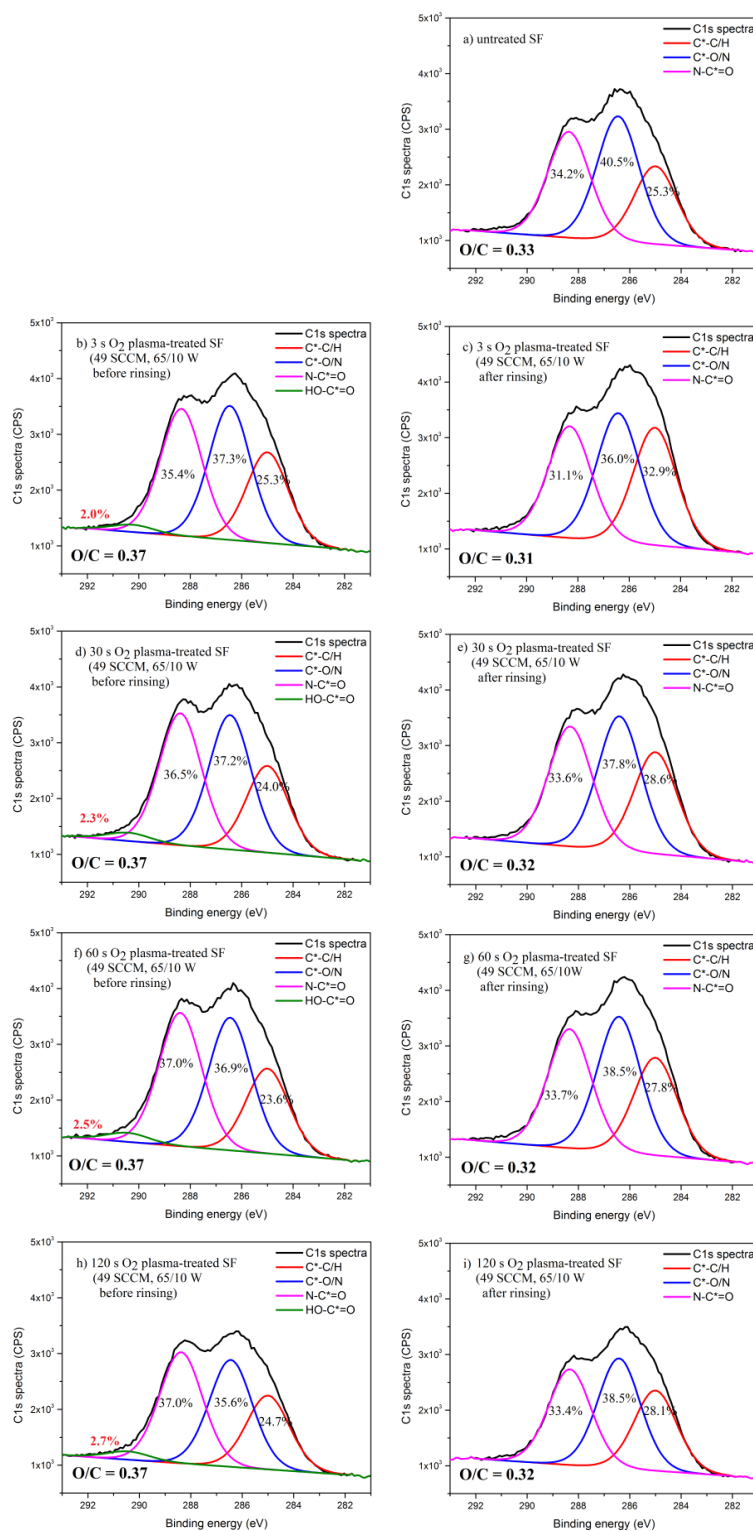


Figure 5-20 XPS spectra together with oxygen to carbon atomic ratios (O/C) of untreated and O<sub>2</sub> plasma-treated SF, the plasma conditions were at highest O<sub>2</sub> flow (49 sccm), maximum pressure ( $1.0 \times 10^{-2}$  mbar), and extremely low power (10W)



From all efforts which had been done to find O<sub>2</sub> plasma operating conditions for SF surface functionalization, the results indicated that there was no surface functionalization after plasma treatment and DI rinsing. This finding has not been reported in any previous literature. It could be either that microwave plasma is too destructive to functionalize SF surface or Thai SF surface is too sensitive for any type of stable plasma functionalization.

#### ***5.5.1.1.3 The effect of silk races (Thai vs. Japanese silk) on the possibility of surface functionalization by oxygen plasma***

The unsuccessful surface functionalization on Thai SF surface might be from the lower molecular weight of Thai SF compared with the most studied Japanese SF (based on unpublished data). To prove this assumption, the same oxygen plasma treatments were conducted on both Thai and Japanese silk fibroin.

Figure 5-21 show XPS spectra of both Thai (a) and Japanese (b) untreated SF, 30s of O<sub>2</sub> plasma treatment before rinsing (Thai SF: c and Japanese SF: d), and 30s of O<sub>2</sub> plasma treatment after rinsing with DI (Thai SF: e and Japanese SF: f). The plasma conditions were the same for both types of SF (i.e. O<sub>2</sub> flow of 40 sccm, plasma power of 250 W with duty cycle (1 ms/1ms of power on/off). The same phenomenon also happened on Japanese silk fibroin. The XPS spectra of O<sub>2</sub> plasma-treated Japanese SF after rinsing with DI (Figure 5-21f) were similar to the untreated Japanese SF (Figure 5-21b). The results indicated that there was no surface functionalization on both Thai and Japanese SF surface by O<sub>2</sub> plasma.

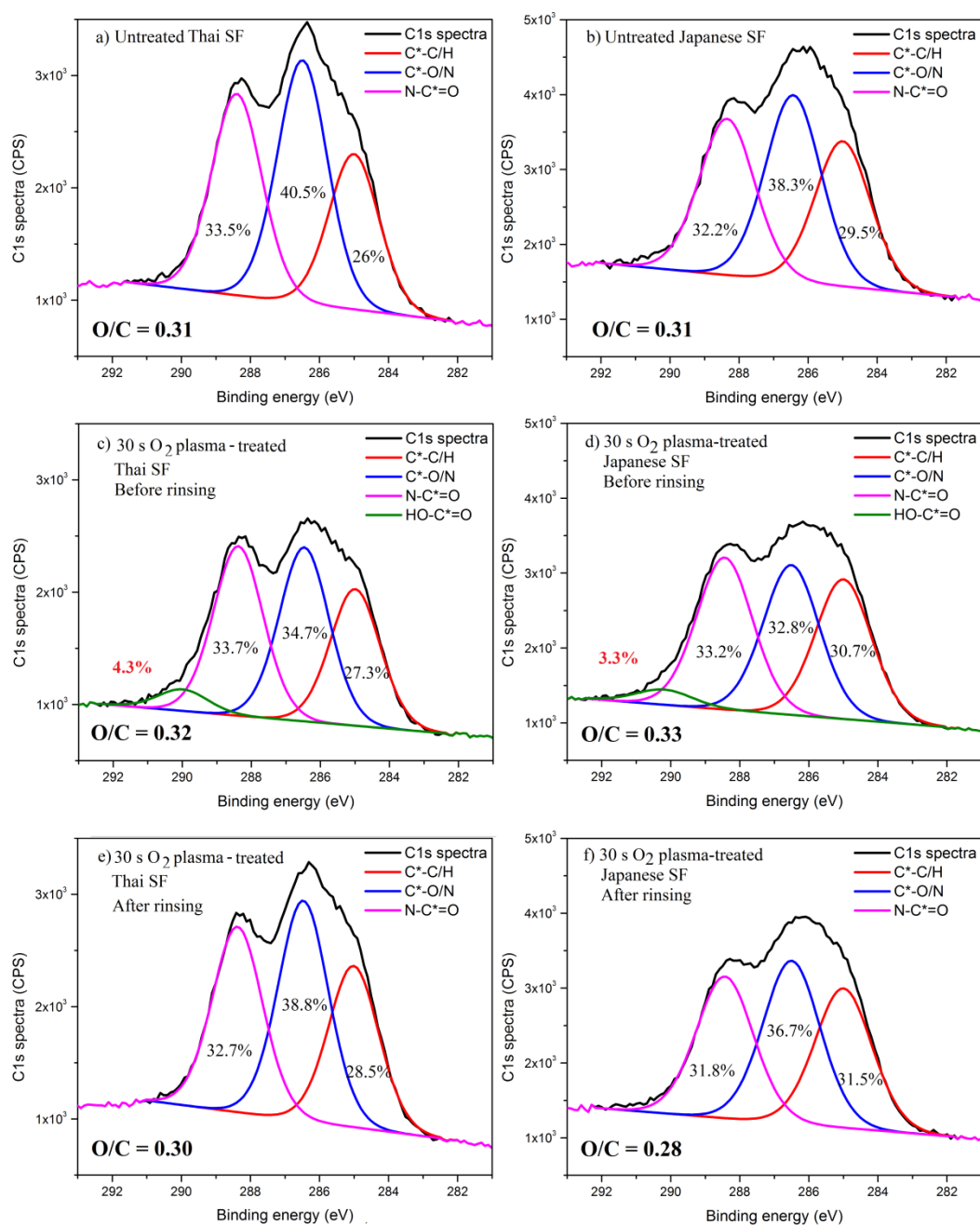


Figure 5-21 XPS spectra together with oxygen to carbon atomic ratios (O/C) of both Thai silk fibroin (a, c, e) and Japanese silk fibroin (b, d, f): untreated (a & b), O<sub>2</sub> plasma-treated SF before rinsing with DI (c & d), and O<sub>2</sub> plasma-treated SF after rinsing with DI (e & f) (O<sub>2</sub> flow 40 sccm, pressure  $7.2 \times 10^{-3}$  mbar, power 250 W, duty cycle (on/off) 1/1 ms)

### 5.5.1.2 Surface chemistry of argon plasma-treated SF

Argon plasma was chosen as an alternative for surface functionalization instead of oxygen plasma. Narayanamoorthy *et al* reported that argon plasma has less effect of etching on SF, compared with O<sub>2</sub> plasma [161]. The surface functionalization would happen after argon plasma generated the free radicals which would be reactive with air after plasma chamber was vented. This is a common effect for many polymeric materials after Ar plasma exposure [36, 37].

Figure 5-21 illustrated XPS spectra of Ar plasma-treated SF after rinsing with DI compared with untreated SF. For argon plasma conditions, the flow of 40 sccm (pressure =  $6.9 \times 10^{-3}$  mbar) was used and two plasma power conditions were tried. The first condition (left panel of Figure 5-21) was continuous plasma power of 120 W, while the second condition (bottom three right panel of Figure 5-21) was cyclical plasma power condition of 500 W with duty cycle (1 ms power on/9ms power off), or 50 W effective power. The treatment time was varied from 15s, 30s, and 60s for both power conditions.

It could be noticed that the obvious change obtained from argon plasma treatment for both power conditions, compared to untreated surface, was the increase of aliphatic hydrocarbon content (C-C/C-H). After rinsing with DI, the C-C/C-H content was increased from the value of 26% on the untreated SF (Figure 5-21a) to the value of 29% - 33.7% on Ar-plasma treated SF (Figure 5-21b - 5-21f). There were no signs of any increase of oxygenated moieties, i.e. the second peak (C-O) and the third peak (C=O) on plasma-treated SF were lower than that of untreated SF. There was no fourth peak (O-C=O) detected from plasma-treated SF. However, the atomic ratio of

oxygen/carbon of Ar-plasma treated SF ( $O/C = 0.31 - 0.33$ ) was slightly increased when compared with the value of untreated SF ( $O/C=0.31$ ). This small increment could not be a solid indication for a functionalization with oxygenated species on SF. It seemed that the longer plasma treatment did not induce any noticeable effects on XPS spectra of Ar plasma-treated SF samples. It could conclude from the XPS results that argon plasma could not introduce oxygenated moieties on SF surface.



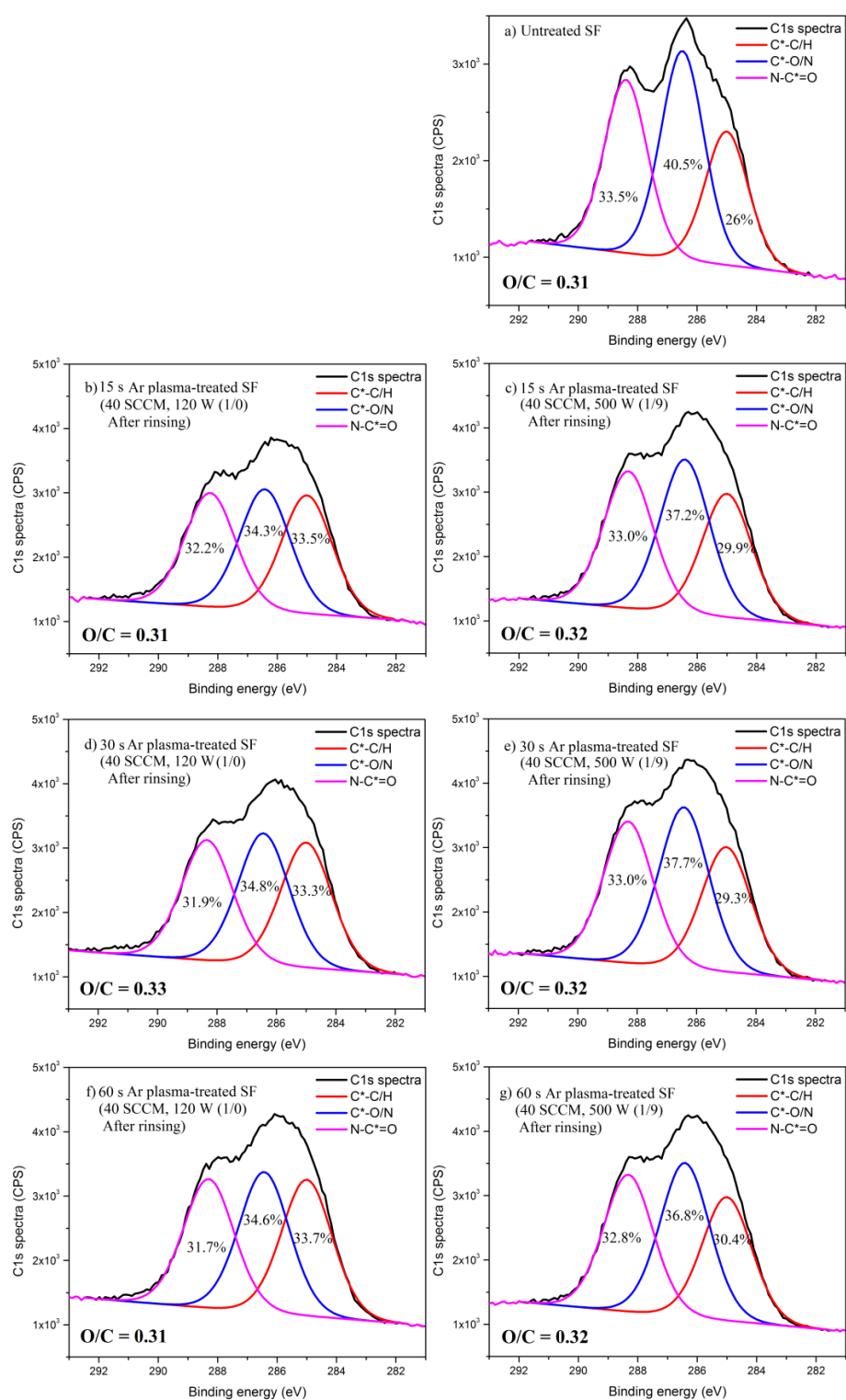


Figure 5-22 XPS spectra together with oxygen to carbon atomic ratios (O/C) of untreated and Ar plasma-treated SF, plasma conditions were argon flow 40 sccm (pressure =  $6.9 \times 10^{-3}$  mbar), left panel: power 120 W, duty cycle (on/off) 1/0 ms and right bottom-three panels: power 500 W, duty cycle (on/off) 1/9 ms (Note: all plasma-treated samples were rinsed with DI before XPS measurement)

### 5.5.1.3 Surface chemistry of argon/oxygen plasma-treated SF

The rationale of using argon and oxygen as a mixed plasma gas was to generate oxygen species in a lower concentration compared to pure oxygen plasma. Argon plasma induced free radicals on SF surface, while oxygen plasma provided reactive oxygen species for functionalization on SF surface. The combination between plasma gases could be either argon rich or oxygen rich.

The first experiment was conducted with argon rich plasma gas (Ar=36 sccm, O<sub>2</sub>=4 sccm, pressure =  $7.2 \times 10^{-3}$  mbar) to minimize effect from the highly reactive oxygen. The intent was to have small amount of oxygen species which were ready to react on the surface inside plasma chamber. This reaction was suspected to be more effective than exposing argon plasma-treated SF to air outside plasma chamber. The plasma was generated with power condition of 500 W with duty cycle (1 ms power on/9ms power off), or 50 W effective power. The treatment time was varied from 15s, 30s, and 60s for both power conditions.

Figure 5-23 showed XPS spectra of Ar/O<sub>2</sub> plasma-treated SF after rinsing with DI, compared with untreated SF. It was clearly seen that the same situation as argon plasma happened again. Ar/O<sub>2</sub> plasma could not functionalize SF with oxygenated functional group, but created the surface with higher aliphatic hydrocarbon (C-C/C-H) content. It seemed that longer duration of Ar/O<sub>2</sub> plasma treatment generated higher level of aliphatic content on the surface. The content of C-C/C-H on SF was increased steadily from 25.3% (untreated SF: Figure 5-23a) to 34.2%. (60 s Ar/O<sub>2</sub> plasma-treated SF: Figure 5-23d). The oxygen/carbon atomic ratios of all plasma-treated samples (0.31 – 0.33) were not higher than that of untreated SF (0.33).

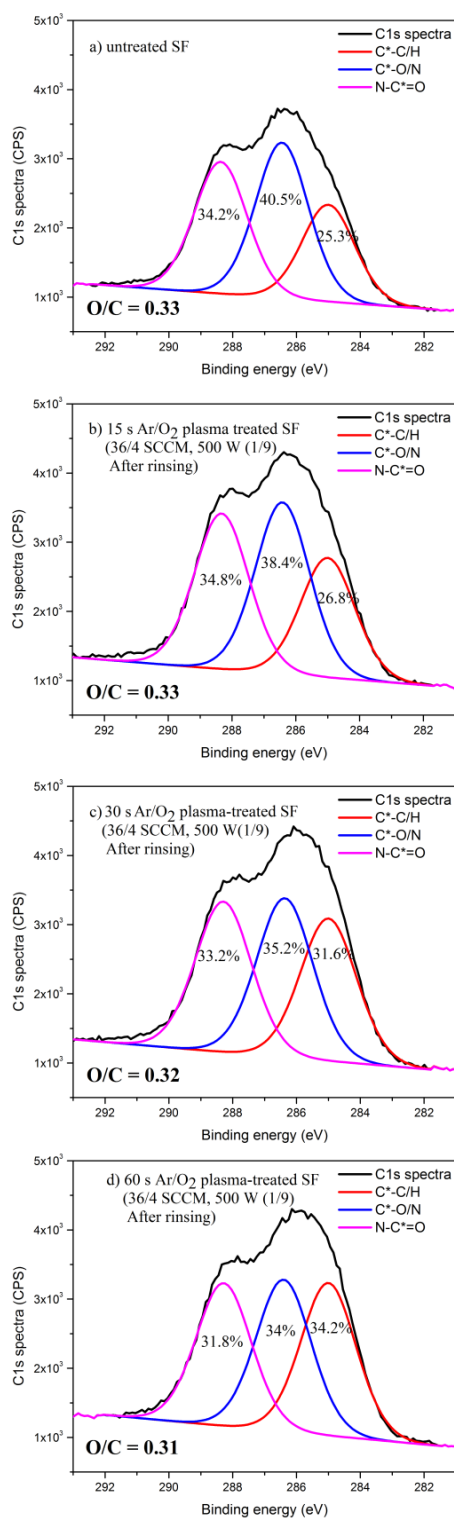


Figure 5-23 XPS spectra together with oxygen to carbon atomic ratio (O/C) of Ar/O<sub>2</sub> plasma-treated SF (Ar flow 36 sccm, O<sub>2</sub> flow 4 sccm, pressure =  $7.2 \times 10^{-3}$  mbar, power 500 W, duty cycle (on/off) 1/9 ms (Note: all plasma-treated samples were rinsed with DI before XPS measurement))

The second experiment of Ar/O<sub>2</sub> plasma was performed with oxygen rich plasma gas (O<sub>2</sub>=49 sccm, Ar=30 sccm, pressure =  $3.3 \times 10^{-2}$  mbar). The higher pressure generated from higher flow of O<sub>2</sub> and Ar, allowed lower power to generate plasma. The plasma power could be lowered to 10 W. For this experiment, the intent was to have much higher oxygen amount for surface reaction while the argon gas was intended to minimize the effect of etching.

Figure 5-24 revealed XPS spectra of Ar/O<sub>2</sub> plasma-treated SF before and after rinsing with DI, compared with untreated SF. In these extremely low plasma power conditions, there was no surface functionalization observed after the samples were rinsed with DI. The oxygen/carbon atomic ratio of all plasma-treated samples (0.28 – 0.33: Figure 5-24b – 5-24i) were not higher than untreated SF O/C ratio (0.33: Figure 5-24a). The XPS spectra of Ar/O<sub>2</sub> plasma-treated SF after rinsing with DI had higher aliphatic hydrocarbon content (26.2% – 34.4%) than the untreated SF (25.3%). It seemed that the treatment for 5 – 240 s did not cause any noticeable effect on XPS spectra of Ar/O<sub>2</sub> plasma-treated SF.

After rinsing with DI, the XPS spectra together with O/C atomic ratio of all Ar/O<sub>2</sub> plasma-treated SF (except 15 s Ar/O<sub>2</sub> plasma-treated SF) were almost identical with the untreated SF except slightly higher aliphatic contents.



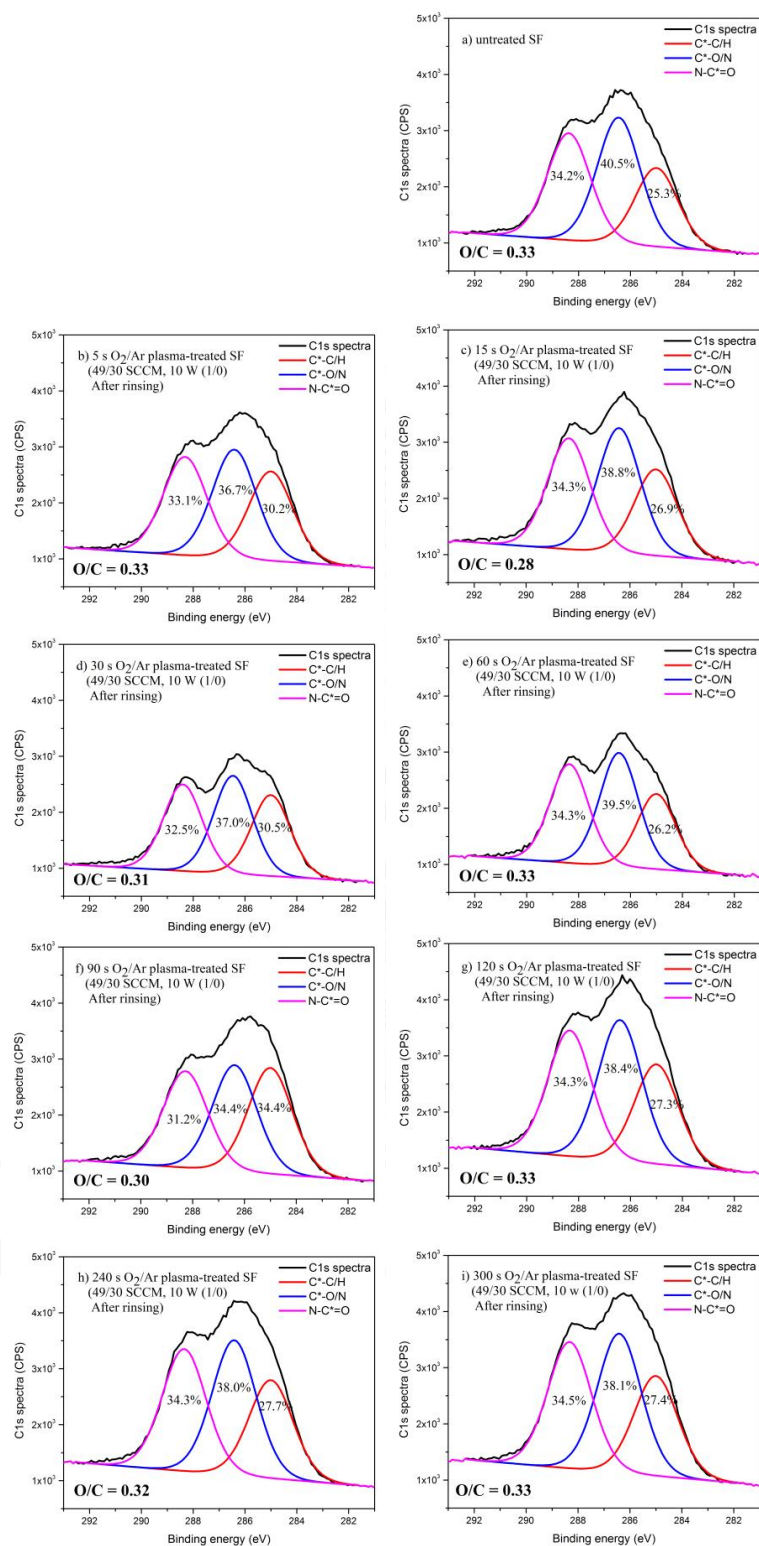


Figure 5-24 XPS spectra together with oxygen to carbon atomic ratios (O/C) of Ar/O<sub>2</sub> plasma-treated SF (Ar flow 30 sccm, O<sub>2</sub> flow 49 sccm, pressure =  $3.3 \times 10^{-2}$  mbar, power 10 W, duty cycle (on/off) 1/0 ms (Note: all plasma-treated samples were rinsed with DI before XPS measurement)

#### 5.5.1.4 Surface chemistry of ammonia plasma-treated SF

The ammonia plasma treatment was intended to generate positively charged surface by introducing amine moieties on silk fibroin surface. The atomic nitrogen to carbon ratio (N/C) was mainly used for indicating a successful surface functionalization since the binding energy between the intended primary amine ( $C^*-NH_2$ ) and amide ( $C^*-N-C=O$ ) are at the same position.

Figure 5-25 shows XPS of  $NH_3$  plasma-treated SF with sample shield installation (as previously described in section 5.5.1.1.1) before and after rinsing with DI, compared to the untreated one. The plasma conditions were ammonia flow of 20 sccm (pressure =  $8.0 \times 10^{-3}$  mbar) and plasma power of 200 W with duty cycle of (1 ms power on/1ms power off), 100 W effective power. The treatment time was varied from 240s, 300s, and 600s.

Before sample rinsing, the N/C atomic ratios of all  $NH_3$  plasma-treated SF (0.33: Figure 5-25b, 5-25d, & 5-25f) were higher than that of untreated SF (0.31: Figure 5-25a). It seemed that the longer plasma treatment than 240s (300s & 600s) did not further increase N/C atomic ratio of  $NH_3$  plasma-treated SF. Regarding XPS spectra of  $NH_3$  plasma-treated SF before rinsing with DI, the spectra were similar to the spectra of untreated SF but the aliphatic hydrocarbon contents were higher in all  $NH_3$  plasma-treated SF (26.9% - 30.7%: Figure 5-25b, 5-25d, & 5-25f) than the untreated SF (26%: Figure 5-25a).

After rinsing with DI, N/C ratios of all  $NH_3$  plasma-treated SF (0.25 - 0.28: Figure 5-25c, 5-25e, & 5-25g) was lower than the untreated sample (0.33: Figure 5-25a). Considering XPS spectra of  $NH_3$  plasma-treated SF before rinsing with DI, the spectra were not similar to the spectra of untreated SF. The aliphatic hydrocarbon contents (C-C/C-H) were much higher in all  $NH_3$  plasma-

treated SF after rinsing (32.3% - 40.2%: Figure 5-25c, 5-25e, & 5-25g) than the untreated SF (26%: Figure 5-25a). It seemed that DI rinsing washed away significant amount of nitrogenated species induced by plasma and left the surface with the remaining aliphatic hydrocarbon (C-C/C-H).

The XPS results of  $\text{NH}_3$  plasma-treated SF after rinsing with DI could not indicate that surface functionalization did happen or not on SF. The N/C atomic ratios of all  $\text{NH}_3$  plasma-treated SF after rinsing with DI, indicated that there was no increase of nitrogen content in the plasma-treated SF, compared with the untreated SF. It was worth to conduct the electrokinetic measurement on the surface of  $\text{NH}_3$  plasma-treated SF of which XPS spectrum was so different from the spectra of untreated SF (i.e. 300s  $\text{NH}_3$  plasma-treated SF after rinsing: Figure 5-25e). The result of electrokinetic measurement would give information whether  $\text{NH}_3$  plasma could functionalize SF surface or not, as discussed in the next section.

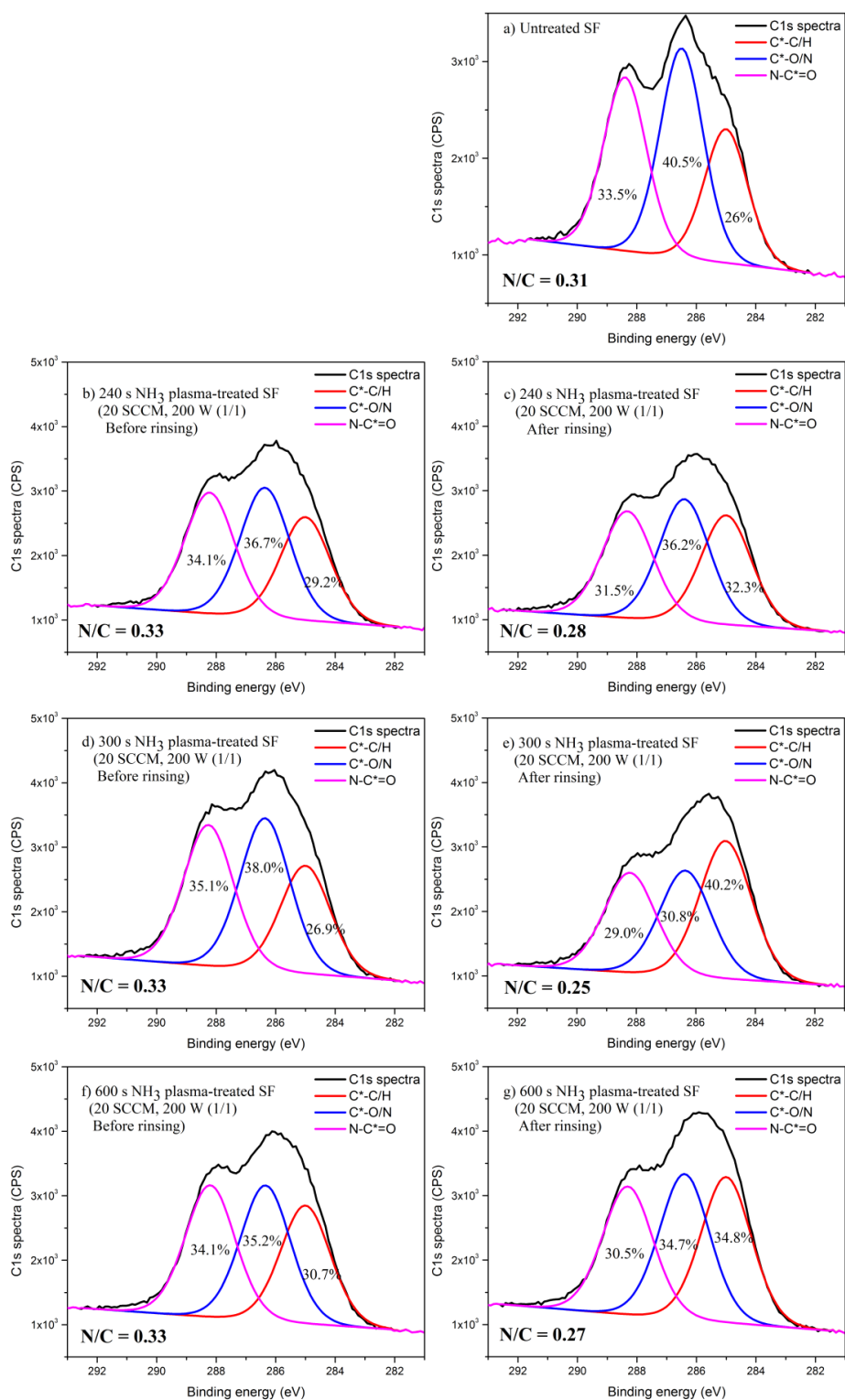


Figure 5-25 XPS spectra together with nitrogen to carbon atomic ratio (N/C) of NH<sub>3</sub> plasma-treated SF (NH<sub>3</sub> flow 20 sccm, pressure =  $8.0 \times 10^{-3}$  mbar, power 200 W, duty cycle (on/off) 1/1 ms with the installation of sample shield to prevent direct bombardment from the high energy plasma ions

### 5.5.1.5 Surface charge

Figure 5-26 summarizes the isoelectric point (IEP) of silk fibroin surface before and after plasma treatment with various plasma gases ( $O_2$ ,  $Ar/O_2$ , and  $NH_3$ ). All plasma-treated SFs were rinsed with DI prior to the electrokinetic measurements. The measurements were conducted with one concentration of background electrolyte (1 mM of KCl). It is obvious that  $O_2$  and  $Ar/O_2$  plasma failed to shift silk fibroin IEP (point of zero zeta potential) toward negatively charge direction. The IEP of both  $O_2$  and  $Ar/O_2$  plasma-treated surfaces still be closed to the IEP of untreated SF (IEP=4). On the other hand,  $NH_3$  plasma could shift the IEP of silk fibroin surface toward positive direction (IEP=4.5).

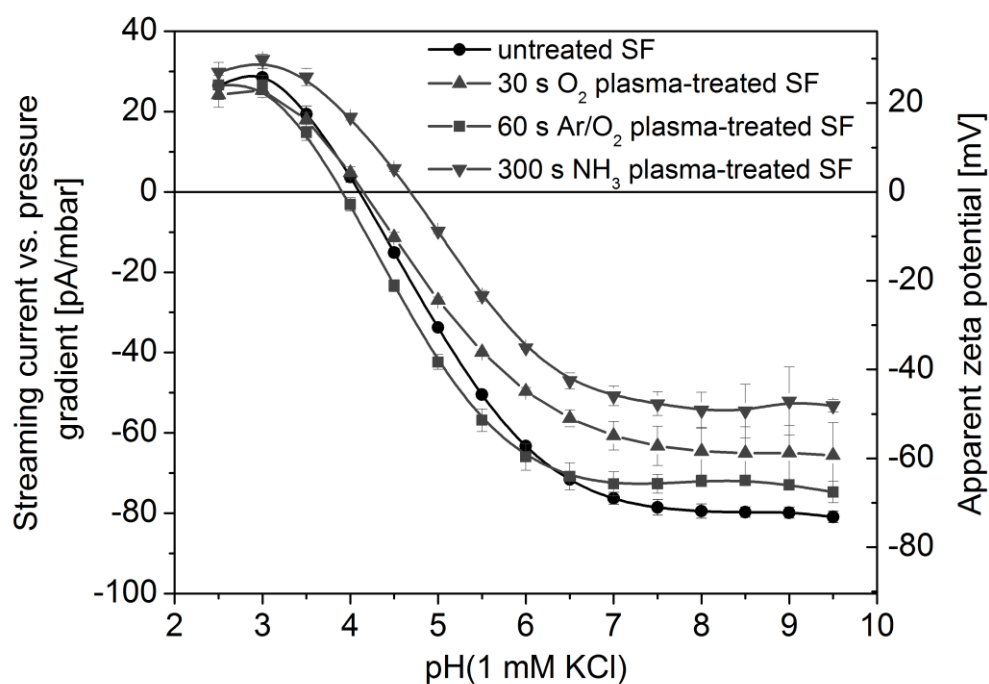


Figure 5-26 Streaming current to pressure gradient and apparent zeta potential of silk fibroin surface before and after plasma treatment with various plasma gases ( $O_2$ ,  $Ar/O_2$ , and  $NH_3$ )

The results from the electrokinetic measurement showed that  $NH_3$  plasma induced positively charged moieties on SF as the IEP was shifted from

pH4 to pH4.5. As mentioned earlier, primary amine moieties could not be detected from XPS by peak deconvolution since its binding energy overlaps with amide, so the labeling with TFBA (4-trifluoromethyl-benzaldehyde) was employed to determine the free amine since TFBA only reacts to the primary amine.

Table 5-6 summarizes the primary amine content by TFBA labeling. The labelling experiments were conducted on the untreated SF and various NH<sub>3</sub> plasma-treated SF surfaces. In the case of NH<sub>3</sub> plasma-treated SF where IEP was shifted to 4.5 (20 sccm, 200 W (1/1), shield), the TFBA test was conducted on the plasma-treated surface before and after rinsing with DI (Table 5-6b, 5-6c). Low power conditions of NH<sub>3</sub> plasma were also conducted on SF surfaces and the plasma-treated SF were rinsed with DI and tested with TFBA to evaluate primary amine content. These plasma conditions were the highest ammonia flow of 36 sccm (pressure =  $1.5 \times 10^{-2}$  mbar) and no sample shield installation. With the continuous power (1/0) of 40W, the treatment time was varied from 30s to 600s (Table 5-6d – 5-6h). In addition, the plasma power was also varied (10W, 40W, and 80W) with the fixed treatment time of 600s (Table 5-6h – 5-6j).

From Table 5-6, it was evident that TFBA method was very specific to primary amine as there was no primary amine detected on the untreated SF (Table 5-6a). The primary amine could only be detected in protein if there is a presence of amino acids which has primary amine side chain such as arginine. The arginine content in silk fibroin was as low as 0.5% of total amino acids (Figure 5-3 in section 5.4.1.1) and the primary amine moiety was 0.16% of carbon moieties (Table 5-2 in section 5.4.1.1). The low primary amine content of SF was far below XPS detecting limit and could not be detected by TFBA labeling.

Table 5-6 Summary of primary amine of NH<sub>3</sub> plasma-treated SF and untreated SF by TFBA (4-trifluoromethyl-benzaldehyde) labelling together with nitrogen to carbon atomic ratio (N/C)

Description	N/C	% primary amine in C 1S
a) untreated SF	0.32	0.0%
b) 300s NH <sub>3</sub> plasma-treated SF (20 sccm, 200 W(1/1), shield, before rinsing)	0.34	1.67%
c) 300s NH <sub>3</sub> plasma-treated SF (20 sccm, 200 W(1/1), shield, after rinsing)	0.25	0.12%
d) 30s NH <sub>3</sub> plasma-treated SF (36 sccm, <b>40 W(1/0)</b> , no shield, after rinsing)	0.18	0.08%
e) 60s NH <sub>3</sub> plasma-treated SF ( <b>36 sccm</b> , 40 W(1/0), no shield, after rinsing)	0.22	0.10%
f) 120s NH <sub>3</sub> plasma-treated SF ( <b>36 sccm</b> , 40 W(1/0), no shield, after rinsing)	0.23	0.10%
g) 300s NH <sub>3</sub> plasma-treated SF ( <b>36 sccm</b> , 40 W(1/0), no shield, after rinsing)	0.24	0.15%
h) 600s NH <sub>3</sub> plasma-treated SF ( <b>36 sccm</b> , 40 W(1/0), no shield, after rinsing)	0.21	0.14%
i) 600s NH <sub>3</sub> plasma-treated SF ( <b>36 sccm</b> , <b>10 W(1/0)</b> , no shield, after rinsing)	0.24	0.15%
j) 600s NH <sub>3</sub> plasma-treated SF ( <b>36 sccm</b> , <b>80 W(1/0)</b> , no shield, after rinsing)	0.23	0.11%

The primary amine amount which shifted IEP from pH4 to pH4.5 was 0.12% of carbon moieties (Table 5-6c). The plasma conditions were 20 sccm of NH<sub>3</sub> flow, 200 W (1/1) of power, 300s of treatment time, and with shield installation. The other low power conditions of NH<sub>3</sub> plasma could generate slightly higher amount of primary amine than the high power. The highest amount of primary was 0.15% of total carbon bonds (C 1s) with plasma conditions of 36 sccm of NH<sub>3</sub> flow, without sample shield installation with either 300s of NH<sub>3</sub> plasma generated by continuous power of 40 W (Table 5-6g) or 600s of NH<sub>3</sub> plasma generated by power of 10 W (Table 5-6i).

In summary, NH<sub>3</sub> plasma could be used to introduce primary amine on silk fibroin surface as observed by the change of IEP of SF toward positive direction. However, the effect was rather small and not expected to modulate protein adsorption and subsequent cell-substrate interaction.

### 5.5.2 *Conclusions*

The finding of plasma operating conditions was not successful for surface functionalization especially in the case of oxygen, argon, and argon/oxygen plasma. Even the surface functionalization existed on the plasma-treated surface before rinsing with DI. However, DI rinsing swept away all plasma-induced functional groups from SF surface as evidenced from the XPS results. The plasma operating conditions were adjusted in the direction of lowering ion energy. The plasma gas flow rate was increased to the maximum value which flowmeter could measure. Moreover, argon was added to further increase of pressure to reduce active species energy. The sample shield was installed to prevent direct bombardment on the silk fibroin surface. The very short treatment time (<1 – 3 sec) of plasma was also explored. None of these efforts could bring a successful (stable) functionalization of oxygenated species on silk fibroin surface. The electrokinetic measurement also confirmed that O<sub>2</sub> and Ar/O<sub>2</sub> plasma could not introduce a charged moieties on SF as noticed from the similar IEP compared to untreated SF

For the case of ammonia gas, NH<sub>3</sub> plasma could functionalize SF as observed from the shift of IEP from pH4 of the untreated SF to pH 4.5. The labelling with TFBA confirmed that free amine was still remained on NH<sub>3</sub> plasma-treated surface even the rinsing with DI washed most free amine away from SF. However, the effect was small compared to other polymer treated with NH<sub>3</sub> plasma [57].

Even though the surface functionalization was not successful, the finding of the similarity of XPS spectra between O<sub>2</sub> plasma-treated SF and untreated SF led into an interesting aspect of plasma etching. UV radiation, a common side effect from plasma etching [21], could be used to alter surface



stiffness through crosslinking process. The plasma etching could provide a rather similar surface chemistry if oxygen plasma is employed and the treatment conditions are optimized to achieve the perfect oxidation reaction [21]. Other properties related to surface chemistry such as surface charge, surface wettability, etc., would be minimally affected. Moreover, plasma treatment affects only few nanometers depth from the surface [22]. That means the bulk properties should be similar to the untreated surface. This could be a promising platform for studying the effects of surface stiffness on cell-substrate interaction that was explored and discussed in section 5.6.



## 5.6 Oxygen plasma etching of silk fibroin alters surface stiffness: A cell-substrate interaction study

In this section, the use of oxygen plasma treatment was investigated as a tool to increase surface stiffness of SF as evaluated by atomic force microscopy (AFM) nano-indentation. Other SF properties, including surface chemistry, degree of crystallization, surface charge, swelling ratio together with optical properties, surface wettability, and protein adsorption were characterized in order to demonstrate that these properties were minimally affected by oxygen plasma etching. Then, the effects of surface stiffness on cell-substrate interaction were studied with two different cell types: L929 mouse fibroblasts and human mesenchymal stem cells (hMSCs) based on their residing on different microenvironment, of which differs in matrix stiffness. *In vitro* studies focused on cell adhesion behaviors by evaluating stress fiber and focal adhesion formation.

### 5.6.1 *Results and Discussion*

#### 5.6.1.1 Surface chemistry

The XPS results of untreated and O<sub>2</sub> plasma-treated SF surfaces before and after rinsing with deionized water (DI) were discussed in the previous section of 5.5.1.1.1 (Figure 5-16). In brief, all XPS spectra of O<sub>2</sub> plasma-treated surfaces after rinsing with DI (Figure 5-16c, 5-16, & 5-16g) were very similar to that of untreated surface (Figure 5-16a). This indicated that the surface functionalization was not a major effect from O<sub>2</sub> plasma as previously mentioned in section 5.5.1.1.1.

### 5.6.1.2 Degree of crystallinity of untreated and O<sub>2</sub> plasma-treated SF

FTIR absorbance at the amide I region (1600–1715 cm<sup>-1</sup>) was used to determine the degree of crystallinity of SF. Figure 5-27a showed FTIR spectra of the untreated SF before  $\beta$ -sheet induction with methanol, the untreated SF after  $\beta$ -sheet induction, and 30 s O<sub>2</sub> plasma-treated SF after rinsing with DI. Methanol clearly induced the  $\beta$ -sheet structure in SF structure as observed by the peak shift from 1655 cm<sup>-1</sup> ( $\alpha$ -helix/random coils) to 1625 cm<sup>-1</sup> ( $\beta$ -sheet). Once the amount of  $\beta$ -sheet structure of SF was induced by methanol, 30 s O<sub>2</sub> plasma treatment did not alter the secondary structure of bulk SF proteins as witnessed by similar FTIR spectra between the untreated SF (after MeOH) and 30 s O<sub>2</sub> plasma-treated SF.

To determine the portion of each protein secondary structure, Fourier self-deconvolution was employed along with peak fitting as shown in Figure 5-27b for untreated before  $\beta$ -sheet induction with methanol, 5-27c for untreated after  $\beta$ -sheet induction with methanol, and 5-27d for 30 s O<sub>2</sub> plasma-treated SF. The peaks are assigned and labeled with B for  $\beta$ -sheet, T for  $\beta$ -turn, A for  $\alpha$ -helix, R for random coil, and SC for tyrosine side chain, as mentioned in experimental section. The analysis showed that the induction with methanol markedly increased the amount of crystalline contents ( $\beta$ -sheet from 8.8% to 36.0%), while other components were reduced ( $\beta$ -turn from 31.3% to 19.5%,  $\alpha$ -helix from 11.9% to 9.9%, and random coil from 46.4% to 32.4%). On the other hand, there were slight differences between untreated SF after  $\beta$ -sheet induction and 30 s of O<sub>2</sub> plasma-treated SF. The differences were still within the error of curve fitting area. It could conclude that O<sub>2</sub> plasma did not affect the degree of crystallization in the bulk of SF.

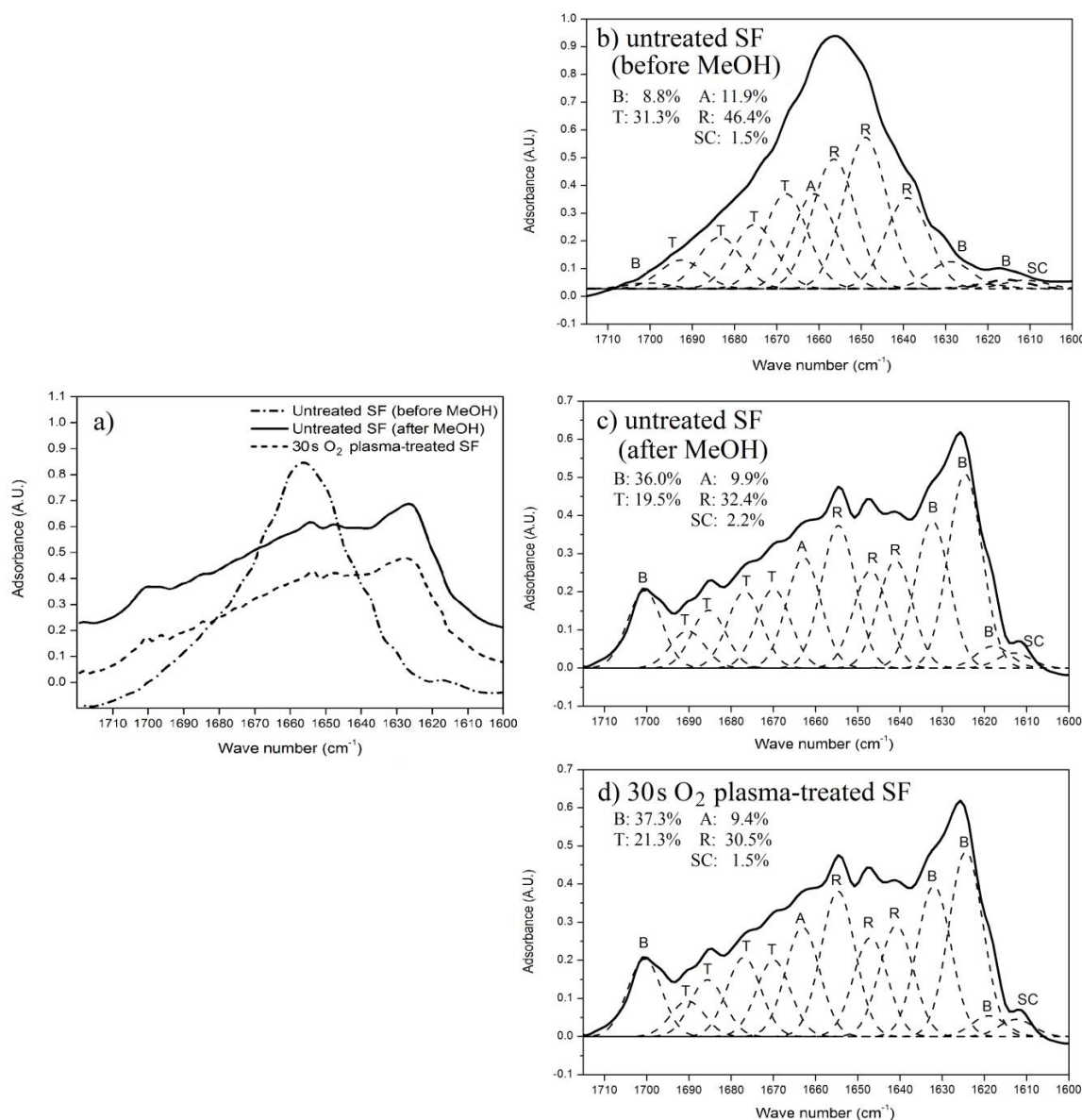


Figure 5-27 a) FTIR spectra of untreated SF before/after  $\beta$ -sheet induction with methanol and 30 s O<sub>2</sub> plasma-treated SF at amide I (1600 – 1715 cm<sup>-1</sup>) and Fourier self deconvolution along with peak fitting of b) the untreated SF before  $\beta$ -sheet induction with methanol, c) the untreated SF after  $\beta$ -sheet induction with methanol, and d) 30 s O<sub>2</sub> plasma-treated SF where B:  $\beta$ -sheet, T:  $\beta$ -turn, A:  $\alpha$ -helix, R: random coil, and SC: tyrosine side chain

### 5.6.1.3 Surface charge

Apparent zeta potential graphs of untreated and O<sub>2</sub> plasma-treated SF surfaces were shown in Figure 5-28. It suggested that both surfaces were negatively charged with approximately same isoelectric point (IEP = 4). The

results suggested that O<sub>2</sub> plasma treatment did not induce any additional charged moieties on SF surface.

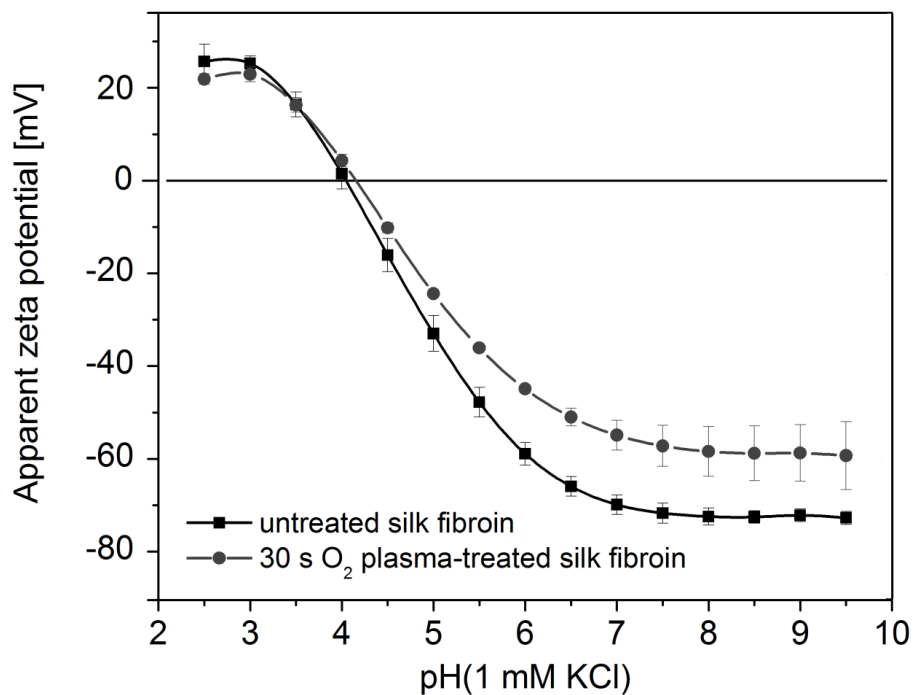


Figure 5-28 Apparent zeta potential versus pH value of both untreated and 30 s O<sub>2</sub> plasma-treated SF surfaces for 1 mM KCl solution

#### 5.6.1.4 Surface wettability

Table 5-7 summarizes the water contact angle of both untreated and O<sub>2</sub> plasma-treated SF using captive air bubbles in conjunction with axisymmetric drop shape analysis (ADSA). The data suggested that O<sub>2</sub> plasma did not increase surface wettability as both advancing and receding water contact angles remained the same as untreated surface.

Table 5-7 Advancing and receding water contact angles on untreated and O<sub>2</sub> plasma treated SF surfaces using captive air bubbles in conjunction with axisymmetric drop shape analysis (ADSA)

Samples	Advancing water contact angle [°]	Receding water contact angle [°]
Untreated SF	58.2±0.5	18.7±0.6
15s O <sub>2</sub> plasma treated SF	58.1±1.0	19.0±0.7
30s O <sub>2</sub> plasma treated SF	54.0±1.9	22.0±0.3

### 5.6.1.5 Surface topography

Figure 5-29 shows the surface topography of both untreated and O<sub>2</sub> plasma-treated SF in both air and wet environments (PBS). The results revealed that the SF surface was rougher after O<sub>2</sub> plasma treatment. From the AFM image in both air and PBS environments, it could be noticed that the shorter treatment induced a lot of rough features. These features were disappeared from the surfaces when longer plasma treatment time was applied. In air environment, the RMS roughness of O<sub>2</sub> plasma-treated SF was increased from the untreated SF value of 0.53±0.04 to 1.85±0.49 nm after 15 s treatment time, and then was reduced to 0.98±0.16 nm after 45 s treatment time. In PBS condition where the roughness should be magnified by swelling, the RMS was increased from 0.94±0.25 to 3.10±0.17 nm after 5 s treatment time, and then was reduced to 1.84±0.87 nm after 45 s treatment time. It was noted that the plasma-induced roughness was very small and the RMS of all O<sub>2</sub> plasma-treated SF surfaces was still lower than that of tissue culture plate (3 – 4 nm) [159].

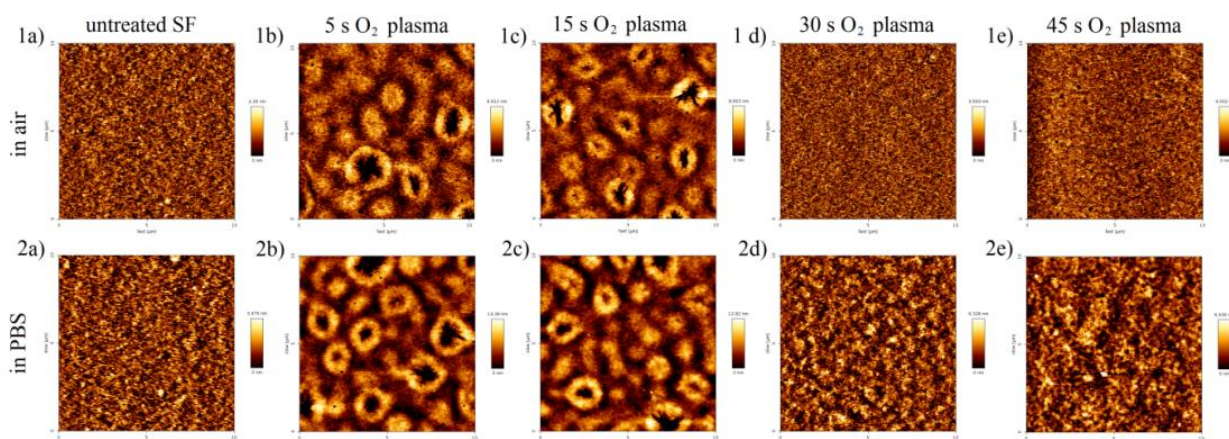


Figure 5-29 AFM surface topography of : a) untreated SF, b) 5 s O<sub>2</sub> plasma-treated SF, c) 15 s O<sub>2</sub> plasma-treated SF, d) 30 s O<sub>2</sub> plasma-treated SF, and e) 45 s O<sub>2</sub> plasma-treated SF in 1) air and 2) in PBS.

The RMS roughness values are shown as below:

- 1a)  $0.53 \pm 0.04$  nm, 1b)  $1.67 \pm 0.33$  nm, 1c)  $1.85 \pm 0.49$  nm, 1d)  $1.17 \pm 0.34$  nm, 1e)  $0.98 \pm 0.16$  nm  
 2a)  $0.94 \pm 0.25$  nm, 2b)  $3.10 \pm 0.17$  nm, 2c)  $2.85 \pm 0.49$  nm, 2d)  $1.88 \pm 0.58$  nm, 2e)  $1.84 \pm 0.87$  nm

#### 5.6.1.6 Swelling, refractive index, and surface stiffness

Table 5-8 summarizes the following properties of SF: thickness, swelling ratio, refractive index from spectroscopic ellipsometry and elastic modulus from AFM nano-indentation. The ellipsometric results showed that thickness loss of SF film was obviously observed after O<sub>2</sub> plasma treatment. The thickness decreased as increasing the treatment time recorded in Table 5-8. The results of thickness reduction by O<sub>2</sub> plasma together with the similar XPS spectra of O<sub>2</sub> plasma-treated SF indicated that plasma etching was more dominant than plasma surface functionalization.

The result of swelling ability of SF in PBS, measured with a liquid cell, showed that both untreated and O<sub>2</sub> plasma-treated surfaces had very similar swelling ratio approximately at 1.6. The results indicated that O<sub>2</sub> plasma did not alter the bulk swelling properties of SF.

The refractive index was evaluated by ellipsometry. If the material contains different substances with different refractive index such as a semi-crystalline polymer, the bulk refractive index could be estimated on volumetric average refractive index [153].

Table 5-8 Summary of thickness, swelling ratio, refractive index and modulus of untreated and O<sub>2</sub> plasma treated SF surfaces

Samples	Thickness [nm]	Swelling ratio	Dry R.I. <sup>28</sup>	Wet R.I. <sup>29</sup>	Modulus <sup>30</sup> [kPa]
Untreated SF	72.7±2.5	1.65±0.02	1.55±0.001	1.47±0.002	62±18 <sup>a</sup>
5s O <sub>2</sub> plasma treated SF	69.1±2.3	1.60±0.02	1.55±0.001	1.47±0.002	461±151 <sup>b</sup>
15s O <sub>2</sub> plasma treated SF	66.5±3.1	1.59±0.02	1.55±0.001	1.47±0.002	494±165 <sup>b</sup>
30s O <sub>2</sub> plasma treated SF	61.23±6.0	1.57±0.02	1.55±0.001	1.47±0.002	506±150 <sup>b</sup>
45s O <sub>2</sub> plasma treated SF	55.15±7.0	1.57±0.02	1.55±0.001	1.47±0.002	438±144 <sup>b</sup>

In addition, the refractive index change could indicate the change in degree of crystallinity in the case of semi-crystalline polymer [153]. SF is considered a semi-crystalline natural polymer which has both crystalline ( $\beta$ -sheet) and amorphous ( $\alpha$ -helix and random coil) structures. So the refractive index of SF could be related to the degree of crystallinity. From Table 5.8, the refractive index (at the wavelength of 632.8 nm) of SF in both air and PBS environment was not changed by O<sub>2</sub> plasma. These results supported the FTIR data that there was no significant change of crystalline content. AFM nano-indentation revealed the pronounced change of the surface stiffness of SF. After a short period of O<sub>2</sub> plasma treatment (5s), the modulus of SF surface was increased sharply from 62±18 to 461±151 kPa. The longer

<sup>28</sup> R.I. is Refractive Index @ 632.8 nm

<sup>29</sup> R.I. is Refractive Index @ 632.8 nm

<sup>30</sup> Each letter represents the significant difference ( $p < 0.05$ ) for all samples (the results with the same alphabet indicate that they are not significantly different).



treatment time did not further increase the modulus of SF surface. The increase of modulus, i.e. the surface stiffness, could be caused by crosslinking from UV radiation. This phenomenon is a common side effect which could happen from plasma etching process [21].

In summary, we have proved the concept of using O<sub>2</sub> plasma etching to modify the surface stiffness of SF, while there was no difference in XPS spectra, degree of crystallinity, surface charge, surface wettability and swelling ratio. Next, the effects of SF surface stiffness on cell-substrate interaction were present.

#### **5.6.1.7 Adsorption of Fibronectin**

The results of fibronectin (FN) adsorption on untreated and O<sub>2</sub> plasma-treated SF surfaces, monitored by quartz crystal microbalance (QCM), were shown in Figure 5-30. FN was chosen as a protein model because it is a major component of extracellular matrix which contains cell binding domain to facilitate cell adhesion process [88, 90, 91]. With the FN solution of 30 µg.ml<sup>-1</sup>, all surfaces adsorbed almost the same amount of FN (680–760 ng.cm<sup>-2</sup>) before they were rinsed with PBS. These adsorbed amounts were much higher than the saturation surface density or monolayer coverage (250 ng.cm<sup>-2</sup>) [47, 162]. The rougher O<sub>2</sub> plasma-treated SF did not have higher adsorbed FN amount, compared to the relatively smooth untreated SF, even the higher adsorption on a rougher surface was expected due to the increased surface area. The same situation was also reported by Hovgaard. FN adsorptions on both smooth (RMS=1.01±0.10 nm) and rough (RMS=4.93±0.14) tantalum oxide were 960±50 and 973±36 ng.cm<sup>-2</sup> respectively, from the FN solution of 10 µg.ml<sup>-1</sup> [163].

The PBS rinsing after adsorption was conducted to understand the relationship of surface properties to the FN anchorage strength on the surface. After rinsing with PBS, the adsorbed amount of FN on all surfaces was dropped to 350–560  $\text{ng}\cdot\text{cm}^{-2}$ , indicating the loss of adsorbed FN. All surfaces retained almost same amount of FN after PBS rinsing ( $P < 0.05$ ).

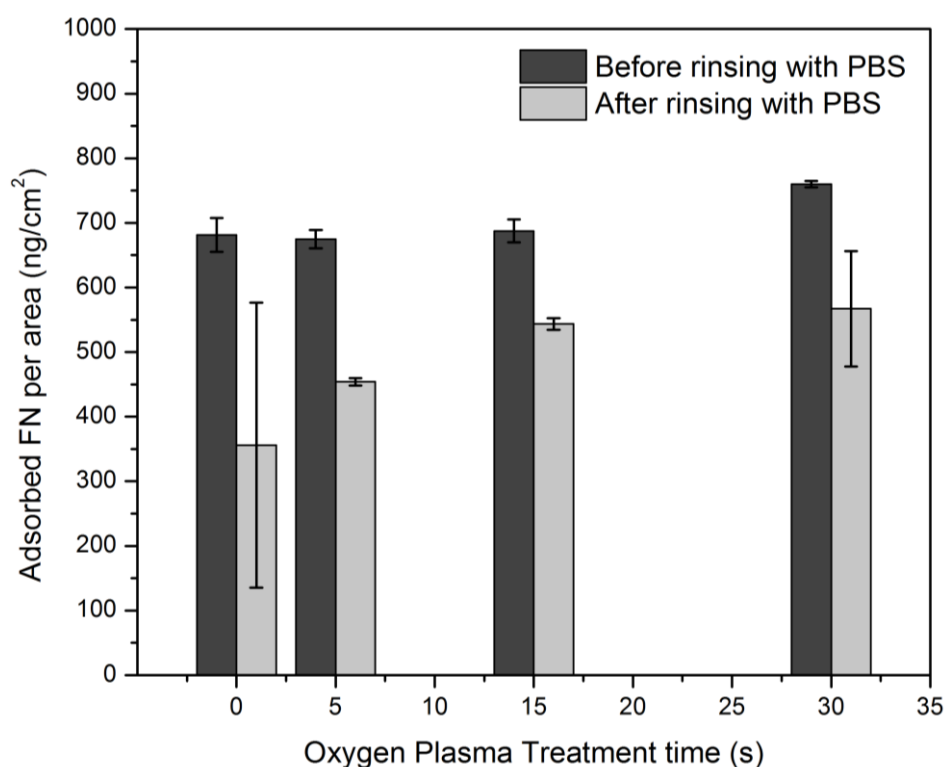


Figure 5-30 Adsorbed fibronectin on the surfaces of untreated and  $\text{O}_2$  plasma-treated SF by QCM-D (the adsorbed mass was estimated by Sauerbrey equation after the stabilization of QCM frequency change ( $\Delta f$ ) and dissipation (D)) (\* represents significant difference between the untreated SF and  $\text{O}_2$  plasma-treated SF before and after rinsing with PBS)

#### 5.6.1.8 L929 and hMSC adhesion

For cell culture, only untreated SF, 5 s, and 30 s  $\text{O}_2$  plasma-treated SF surfaces were selected for the study. The untreated SF and  $\text{O}_2$  plasma-treated (5 s/30 s) SF were paired in order to evaluate the effect of surface stiffness ( $62 \pm 18$  vs.  $461 \pm 151/506 \pm 150$  kPa). In addition, the 5 s and 30 s  $\text{O}_2$  plasma-treated SFs were used to study the side effect of slightly change of

surface roughness (RMS =  $1.67 \pm 0.33$  vs.  $1.17 \pm 0.34$  nm) while both surfaces had similar stiffness.

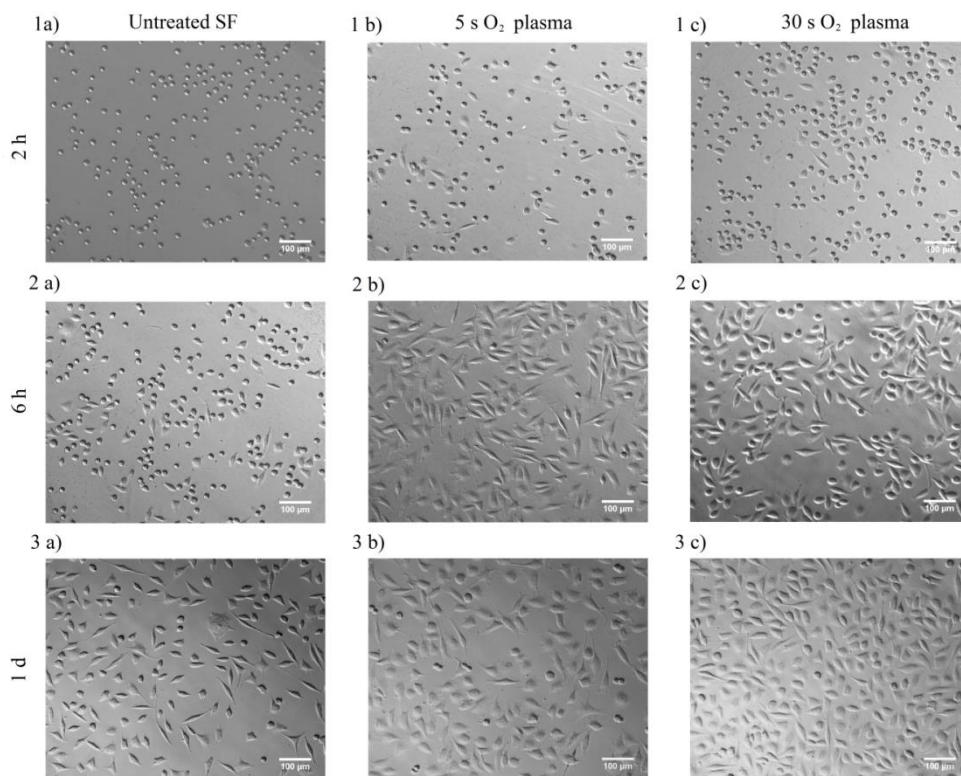


Figure 5-31 L929 mouse fibroblast cultured on the surface of : a) untreated SF, b) 5 s  $O_2$  plasma-treated SF, and c) 30 s  $O_2$  plasma-treated SF after various cultivation time: 1) 2 h, 2) 6 h, and 3) 1 d (scale bar = 100 micron)

Figure 5-31 shows L929 adhesion behavior on untreated and  $O_2$  plasma-treated SF. At 2 h of culture, some L929 started to spread on  $O_2$  plasma-treated SF while there was no sign of spreading on the untreated SF. Later on, at 6 h of culture, L929 fully spread on  $O_2$  plasma-treated SF. Most L929 on the untreated SF were still in round shape. At 1 d of culture, there were still a few of L929 in round shape on the untreated SF. It appeared that L929 preferred to spread on the stiffer surface (5 s/30 s  $O_2$  plasma-treated SF) than the softer surface (untreated SF). However, there was no difference in cell spreading on 5 s and 30 s  $O_2$  plasma-treated SF surfaces.

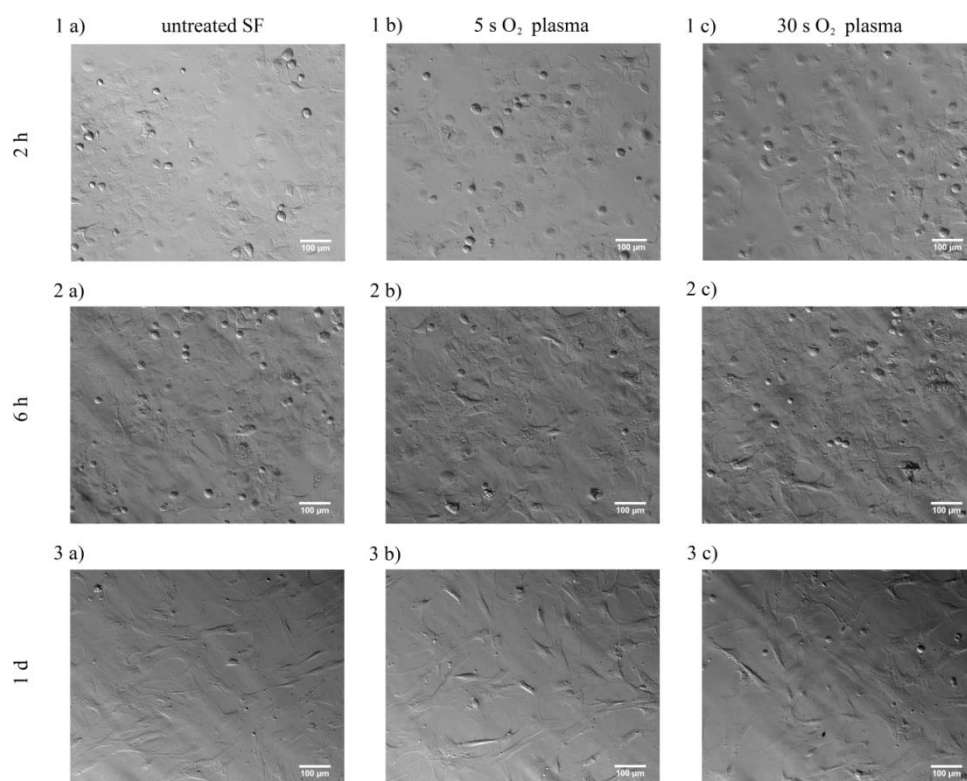


Figure 5-32 Human mesenchymal stem cell (hMSC) cultured on the surface of : a) untreated SF, b) 5 s O<sub>2</sub> plasma-treated SF, and c) 30 s O<sub>2</sub> plasma-treated SF after various cultivation time: 1) 2 h, 2) 6 h, and 3) 1 d (scale bar = 100 micron)

Figure 5-32 shows hMSC adhesion on untreated and O<sub>2</sub> plasma-treated SF. At different culture periods (2 h, 6 h, and 1 d), no difference in cell spreading among all surfaces could be noticed. hMSC showed no preference on either soft or stiff surface, as well as on either smooth or rough surface.

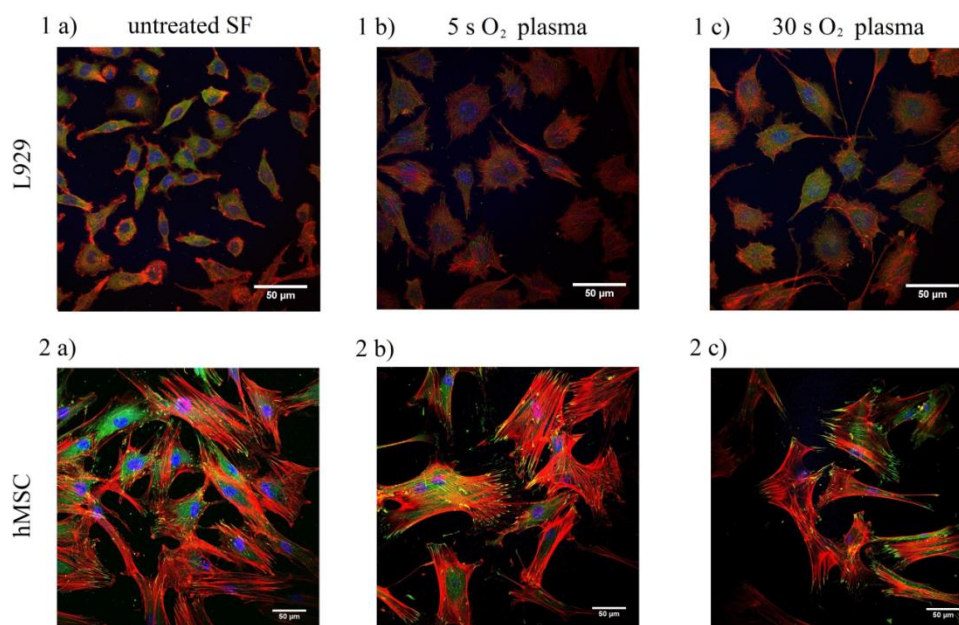


Figure 5-33 Immunocytochemical staining of adhered cells: 1) L929 mouse fibroblast and 2) Human mesenchymal stem cell (hMSC) on the surface of: a) untreated SF, b) 5 s  $O_2$  plasma-treated SF, and c) 30 s  $O_2$  plasma-treated SF after 1 day of cultivation. Paxillin, one of focal adhesive proteins, is shown in green, F-actin stressed fibers are in red (Phalloidin), and the nuclei are in blue (Hoechst33342) (scale bar = 50 micron)

Figure 5-33 illustrates the details of cytoplasmic elements which are involved in cell adhesion: the cell cytoskeleton (F-actin) shown in red and the adaptor protein in focal adhesion (paxillin) shown in green, together with nucleus in blue. The cells shown in Figure 5.35-1a), 1b), & 1c) are L929 while the cells shown in Figure 5.35-2a), 2b), & 2c) are hMSC. For L929, the stress fiber and paxillin localization were evident on  $O_2$  plasma-treated SF, indicating strong attachment on the stiffer surface. In contrary, the stress fiber and paxillin localization could not be easily found on the softer untreated SF. This observation corresponded to previous reports that L929 and other fibroblasts prefer stiffer surface as summarized in Table 5-9. For the soft polyacrylamide gel, fibroblast preferred the stiffest gel of the investigated modulus e.g. 1.09 kPa (0.62–1.09 kPa range), 20 kPa (0.2–20 kPa range), and 18 kPa (0.180 – 18 kPa range) [98, 99, 101]. For a harder system such as PDMS

and poly(HEMA), fibroblast preferred substrate, of which the modulus was in the range of 300–500 kPa [102-104, 106].

In the case of hMSC, cells were spread and attached well on all SF surfaces. The paxillin was localized at the tip of clearly-developed stress fiber, illustrating the well-developed focal adhesion [95, 164, 165]. The fact that SF surface stiffness (62–500 kPa) is higher than all of mesenchymal tissues stiffness (2–40 kPa) [96] might be the reason of no adhesion difference of hMSC on any SF surface. Furthermore, the hMSC adhesion pattern on all SF surfaces resembled to that on stiff glass substrate (69 GPa) [166], reported by Engler *et al.* [56].



Table 5-9 An example of different substrate stiffness which is suitable for different cell adhesion in terms of cell spreading area or growth

Cell	Substrate	Modulus [kPa]	Suitable Modulus[kPa]	Ref
L929 fibroblasts	hyaluronic acid/ PEG di-acrylate	2.5 – 28	28	[107]
hMSC	polyacrylamide-collagen	1 – 15	1:chondrogenic 15:smooth muscle	[100]
MSC	polyacrylamide	1 – 34	1:neurogenic 11:myogenic 34:osteogenic	[56]
NIH 3T3 fibroblasts	polyacrylamide	0.62 – 1.09	1.09	[98]
NIH 3T3 fibroblasts	polyacrylamide	0.2 – 20	20	[99]
NIH 3T3 fibroblasts	polyacrylamide	0.180 – 18	18	[101]
NIH 3T3 fibroblasts	poly(dimethylsiloxane)	40 – 1,800	300	[103]
NIH 3T3 fibroblasts	poly(dimethylsiloxane)	1.5 – 150	>90	[104]
NIH 3T3 fibroblasts Sal/N fibrosarcomas	poly(dimethylsiloxane)	500 – 2,000	500 500 – 2,000	[102]
RMS13 fibroblasts	poly(HEMA)	152 – 1,777	241	[106]

### 5.6.2 *Conclusion*

The oxygen plasma etching has been introduced as a tool to manipulate the surface stiffness of SF for cell-substrate interaction study. This technique mainly affects the surface stiffness while there were almost no change in XPS spectra, surface charge, surface wettability, degree of crystallinity, swelling ratio, and FN adsorption. The RMS roughness of SF was slightly increased after the plasma treatment. The effects of surface stiffness on the adhesion behavior of two different cell types, L929 and hMSC, showed that L929 preferred the stiffer SF surface (500 kPa) than softer one (62 kPa), while hMSC did not show any preference on surface stiffness in the range from 62 to 500 kPa.



## CHAPTER

### 6. CONCLUSIONS AND RECOMMENDATIONS

#### 6.1 Conclusions

This study investigated the effects of plasma treatment on the physical and biological properties of Thai silk fibroin (SF). Following conclusions are the important findings from this work.

The preliminary study using AC50 Hz power supply suggested that nitrogen glow discharge could improve the biocompatibility of SF surface as observed by the early cell adhesion tests and F-actin cytoskeleton staining of L929 mouse fibroblast. L929 took 3 h to reach 100% cell adhesion on 90 s N<sub>2</sub> plasma-treated SF, which was earlier than on other Thai SF surfaces (10 s N<sub>2</sub> plasma-treated SF and untreated SF). L929 F-actin was more evident on 90 s N<sub>2</sub> plasma-treated surface than the others. The characterization results of plasma-treated SF and untreated SF indicated that the bulk chemistry and surface topography were minimally affected by plasma treatment as evaluated by FTIR-ATR and AFM, respectively. The major changes of plasma-treated SF properties were the improved surface wettability and surface chemistry, as measured by a contact angle meter and XPS, respectively. The XPS data indicated that hydrophilic functional groups were induced on plasma-treated SF. The success from this preliminary study that N<sub>2</sub> plasma could improve SF biocompatibility, led into an in-depth investigation, conducted at Leibniz Institute of Polymer Research Dresden.

One of the important learnings from an in-depth investigation was that SF needed to be prepared in a well-defined way (surface chemistry, surface charge, film thickness, degree of crystallinity, surface topography, and mechanical property)

before any plasma surface modification. The consistent surface preparation enabled a precise analysis of the plasma effects on SF properties. The characterization techniques should be chosen according to SF properties, for example, the characterization of surface wettability by captive air bubble technique would be appropriate to SF due to the swollen nature of SF.

The major revelation from the experiment to find plasma operating conditions for treating SF surface was that plasma generated from these gases ( $O_2$ , Ar, and Ar/ $O_2$ ) could induce oxygenated species on SF surface, but the change of surface chemistry was not stable. After rinsing with DI, XPS spectra of plasma-treated SF were either similar to untreated SF or had lower content of oxygenated species. The streaming potential data indicated that the IEP of SF was not affected by either  $O_2$  or Ar/ $O_2$  plasma. On the other hand,  $NH_3$  plasma could shift the IEP of SF toward positive direction (from pH 4 to pH 4.5) even the N/C atomic ratio of  $NH_3$  plasma-treated SF was lower than that of untreated SF, as suggested by XPS. The TFBA labelling revealed that some of free amine, induced by  $NH_3$  plasma, still remained on SF surface after rinsing with DI.

In the case of  $O_2$  plasma treatment, the similarity of XPS spectra between  $O_2$  plasma-treated SF and untreated SF implied that plasma surface etching was more dominant than plasma surface functionalization on SF. The continuous thickness loss during plasma treatment also suggested the dominant  $O_2$  plasma etching effects on SF. The increased elastic modulus of  $O_2$  plasma-treated SF was the most significant plasma-treated effect, while other related properties (e.g. XPS spectra, degree of crystallinity, surface charge, swelling degree, surface wettability, and FN adsorption) were minimally affected from plasma treatment. These findings could enable the use of plasma etching of SF to alter surface stiffness for cell-substrate interaction study. *In vitro* results suggested that L929 mouse fibroblasts preferred to attach and spread on the stiffer  $O_2$  plasma-treated SF (Young modulus of 500 kPa) rather than

softer untreated SF (62 kPa). On the other hand, human mesenchymal stem cells (hMSCs) did not show any preference on any surfaces. They could spread well for all SF surfaces.

In conclusion, plasma etching was more dominant than plasma functionalization on SF surface. The prominent effect from oxygen plasma treatment was the increased surface stiffness of SF. The difference in surface stiffness could impact the behavior of cell adhesion and spreading, depending on cell types.

## **6.2 Recommendations**

In general, researchers know the unique properties of silk fibroin by heart that it is biodegradable, biocompatible, and mechanically strong. Most researches still focus on improving silk fibroin properties with other bioactive molecules for the use as either tissue engineering scaffolds or drug delivery systems. Following are the recommendations which could be explored in biomedical research to fully capitalize all potentials from this unique material, “silk fibroin”.

As found in this study that silk fibroin could be etched easily with plasma and the etching pattern could be generated in a low micron dimension (20 – 30  $\mu\text{m}$ ), this finding could enable researchers to generate any pattern on SF surface for various applications. The plasma etching might be used to generate the micro-vascular pattern on SF or to generate a pattern on SF substrate in biosensor applications.

The new applications of implantable devices might be developed from the fact that the amorphous or low degree of crystallization version of silk fibroin could be dissolved easily and harmlessly in the body. Following examples might illustrate for what could be explored from this unique SF property. Silk fibroin could be used as a major part of biosensor body which makes the devices strong

enough for handling during implantation processes [167, 168]. The flexibility of silk fibroin could enable sensing elements conformed to the curvilinear of tissue. And after the implantation process was finished, the major part of sensors could be designed to resorb in order to minimize the foreign body reaction. This advantage could not be found in the conventional silicon-substrate base biosensor. Kim *et al.* used the resorbable silk fibroin as a platform for holding 30 gold electrodes array for brain/computer interface application. After exposing the device to brain, the device was rinsed with saline to remove silk fibroin, then the device was conformed to the brain contour texture without any remaining SF [167].

The optical transparency of silk fibroin might be explored for new biophotonic sensor applications [169, 170]. Following reports showed what had been done in this research area. The silk fibroin surfaces were modified with either chemicals [169] or surface patterning [170] to generate a light sensitive surface for detection the change of pH [169] or glucose concentration [170].

## REFERENCES

- [1] Langer R. Biomaterials and Biomedical Engineering. Chemical Engineering Science. 1995;50:4109 - 21
- [2] Murphy MB, Mikos AG. Polymer Scaffold Fabrication. In: R.P. Lanza RL, J.P. Vacanti, editor. Principles of Tissue Engineering. 3rd Edition ed: Elsevier Inc; 2007. p. 309-21.
- [3] O'Brien FJ. Biomaterials & scaffolds for tissue engineering. Material Today 2011;14:88 - 95.
- [4] Jetbumpenkul P, Amornsudthiwat P, Kanokpanont S, Damrongsakkul S. Balanced electrostatic blending approach - An alternative to chemical crosslinking of Thai silk fibroin/gelatin scaffold. Int J Biol Macromol. 2012;50:7-13.
- [5] Ratanavaraporn J, Damrongsakkul S, Kanokpanont S, Yamamoto M, Tabata Y. Osteogenic differentiation of bone-marrow-derived stem cells cultured with mixed gelatin and chitooligosaccharide scaffolds. J Biomater Sci Polym Ed. 2011;22:1083-98.
- [6] Tungtasana H, Damrongsakkul S, Shuangshoti S, Kanokpanont S, Kaplan DL, Bunaprasert T. Tissue response and biodegradation of composite scaffolds prepared from Thai silk fibroin, gelatin and hydroxyapatite. J Mater Sci Mater Med. 2010;21:3151-62.
- [7] Vachiraroj N, Ratanavaraporn J, Damrongsakkul S, Pichyangkura R, Banaprasert T, Kanokpanont S. A comparison of Thai silk fibroin-based and chitosan-based materials on in vitro biocompatibility for bone substitutes. Int J Biol Macromol. 2009;45:470-7.
- [8] Vorrapakdee R, Kanokpanont S, Ratanavaraporn J, Waikakul S, Charoenlap C, Damrongsakkul S. Modification of human cancellous bone using Thai silk fibroin and gelatin for enhanced osteoconductive potential. J Mater Sci Mater Med. 2013;24:735-44.
- [9] Wongputtaraksa T, Ratanavaraporn J, Pichyangkura R, Damrongsakkul S. Surface modification of Thai silk fibroin scaffolds with gelatin and chitooligosaccharide

- for enhanced osteogenic differentiation of bone marrow-derived mesenchymal stem cells. *J Biomed Mater Res B*. 2012;100:2307-15.
- [10] Okhawilai M, Rangkupan R, Kanokpanont S, Damrongsakkul S. Preparation of Thai silk fibroin/gelatin electrospun fiber mats for controlled release applications. *Int J Biol Macromol*. 2010;46:544-50.
- [11] Somvipart S, Kanokpanont S, Rangkupan R, Ratanavaraporn J, Damrongsakkul S. Development of electrospun beaded fibers from Thai silk fibroin and gelatin for controlled release application. *Int J Biol Macromol*. 2013;55:176-84.
- [12] Kanokpanont S, Damrongsakkul S, Ratanavaraporn J, Aramwit P. An innovative bi-layered wound dressing made of silk and gelatin for accelerated wound healing. *Int J Pharm*. 2012;436:141-53.
- [13] Kanokpanont S, Damrongsakkul S, Ratanavaraporn J, Aramwit P. Physico-chemical properties and efficacy of silk fibroin fabric coated with different waxes as wound dressing. *Int J Biol Macromol*. 2013;55:88-97.
- [14] Ratanavaraporn J, Rangkupan R, Jeeratawatchai H, Kanokpanont S, Damrongsakkul S. Influences of physical and chemical crosslinking techniques on electrospun type A and B gelatin fiber mats. *Int J Biol Macromol*. 2010;47:431-8.
- [15] Zeiger E, Gollapudi B, Spencer P. Genetic toxicity and carcinogenicity studies of glutaraldehyde—a review. *Mutation Research/Reviews in Mutation Research*. 2005;589:136-51.
- [16] Speit G, Neuss S, Schütz P, Fröhler-Keller M, Schmid O. The genotoxic potential of glutaraldehyde in mammalian cells in vitro in comparison with formaldehyde. *Mutation Research/Genetic Toxicology and Environmental Mutagenesis*. 2008;649:146-54.
- [17] Shen H, Hu X, Bei J, Wang S. The immobilization of basic fibroblast growth factor on plasma-treated poly(lactide-co-glycolide). *Biomaterials* 2008;29:2388-99.
- [18] Finke B, Luethen F, Schroeder K, Mueller PD, Bergemann C, Frant M, et al. The effect of positively charged plasma polymerization on initial osteoblastic focal adhesion on titanium surfaces. *Biomaterials* 2007;28:4521-34.

- [19] Shen H, Hu X, Yang F, Bei J, Wang S. Combining oxygen plasma treatment with anchorage of cationized gelatin for enhancing cell affinity of poly(lactide-co-glycolide). *Biomaterials*. 2007;28:4219-30.
- [20] Yang Z, Wang J, Luo R, Maitz MF, Jing F, Sun H, et al. The covalent immobilization of heparin to pulsed-plasma polymeric allylamine films on 316L stainless steel and the resulting effects on hemocompatibility. *Biomaterials*. 2010;31:2072-83.
- [21] Roth JR. Plasma Etching. *Industrial Plasma Engineering*. London, UK.: Institute of Physics Publishing; 1995. p. 540-613.
- [22] König U, Nitschke M, Pilz M, Simon F, Arnhold C, Werner C. Stability and ageing of plasma treated poly(tetrafluoroethylene) surfaces. *Colloids Surf B Biointerfaces*. 2002;25:313-24.
- [23] Baek HS, Park YH, Ki CS, Park J-C, Rah DK. Enhanced chondrogenic responses of articular chondrocytes onto porous silk fibroin scaffolds treated with microwave-induced argon plasma. *Surface & Coatings Technology*. 2008;202:5794-7.
- [24] Jin SC, Baek HS, Woo YI, Lee MH, Kim J-S, Park J-C. Beneficial Effects of Microwave-Induced Argon Plasma Treatment on Cellular Behaviors of Articular Chondrocytes Onto Nanofibrous Silk Fibroin Mesh. *Macromolecular Research*. 2009;17:703-8.
- [25] Valdes TI, Ciridon W, Ratner BD, Bryers JD. Surface modification of a perfluorinated ionomer using a glow discharge deposition method to control protein adsorption. *Biomaterials*. 2008;29:1356-66.
- [26] Mwale F, Wang HT, Nelea V, Luo L, Antoniou J, Wertheimer MR. The effect of glow discharge plasma surface modification of polymers on the osteogenic differentiation of committed human mesenchymal stem cells. *Biomaterials*. 2006;27:2258-64.
- [27] Rhodes NP, Wilson DJ, Williams RL. The effect of gas plasma modification on platelet and contact phase activation processes. *Biomaterials*. 2007;28:4561-70.
- [28] Meichsner J, Nitschke M, Rochotzki R, Zeuner M. Fundamental investigations in plasma modification of polymers. *Surf Coat Technol*. 1995;74-75:227-31.

- [29] Meichsner J, Zeuner M, Krames B, Nitschke M, Rochotzki R, Barucki K. Plasma diagnostics for surface modification of polymers. *Surface and Coatings Technology*. 1998;98:1565-71.
- [30] Pavlica S, Piscioneri A, Peinemann F, Keller M, Milosevic J, Staudte A, et al. Rat embryonic liver cell expansion and differentiation on NH<sub>3</sub> plasma-grafted PEEK-WC-PU membranes. *Biomaterials* 2009;30:6514-21.
- [31] Chen R, Bayon Y, Hunt JA. Preliminary study on the effects of ageing cold oxygen plasma treated PET/PP with respect to protein adsorption. *Colloids and Surfaces B: Biointerfaces*. 2012;96:62- 8.
- [32] Bax DV, McKenzie DR, Bilek MMM, Weiss AS. Directed cell attachment by tropoelastin on masked plasma immersion ion implantation treated PTFE. *Biomaterials*. 2011;32:6710-8.
- [33] Bax DV, McKenzie DR, Weiss AS, Bilek MMM. The linker-free covalent attachment of collagen to plasma immersion ion implantation treated polytetrafluoroethylene and subsequent cell-binding activity. *Biomaterials* 2010;31:2526-34.
- [34] Wang H, Kwok DTK, Wang W, Wu Z, Tong L, Zhang Y, et al. Osteoblast behavior on polytetrafluoroethylene modified by long pulse, high frequency oxygen plasma immersion ion implantation. *Biomaterials*. 2010;31:413-9.
- [35] Qu X, Cui W, Yang F, Min C, Shen H, Bei J, et al. The effect of oxygen plasma pretreatment and incubation in modified simulated body fluids on the formation of bone-like apatite on poly(lactide-co-glycolide) (70/30). *Biomaterials*. 2007; 28:9-18.
- [36] Ding Z, Chen J, Gao S, Chang J, Zhang J, Kang ET. Immobilization of chitosan onto poly-L-lactic acid film surface by plasma graft polymerization to control the morphology of fibroblast and liver cells. *Biomaterials*. 2004;25:1059-67.
- [37] Wu Y-C, Lee T-M, Lin J-C, Shaw S-Y, Yang C-Y. Argon-Plasma-Treated Chitosan: Surface Characterization and Initial Attachment of Osteoblasts. *Journal of Biomaterials Science*. 2010;21:563-79.



- [38] Alves CM, Yang Y, Carnes DL, Ong JL, Sylvia VL, Dean DD, et al. Modulating bone cells response onto starch-based biomaterials by surface plasma treatment and protein adsorption. *Biomaterials*. 2007;28:307-15.
- [39] Vasilev K, Poh Z, Kant K, Chan J, Michelmore A, Losic D. Tailoring the surface functionalities of titania nanotube arrays. *Biomaterials*. 2010;31:532-40.
- [40] Zelzer M, Majania R, Bradley JW, Rose FRAJ, Davies MC, Alexander MR. Investigation of cell-surface interactions using chemical gradient formed from plasma polymers. *Biomaterials*. 2008;29:172-84.
- [41] Andersen TE, Palarasah Y, Skjødt M-O, Ogaki R, Benter M, Alei M, et al. Decreased material-activation of the complement system using low-energy plasma polymerized poly(vinyl pyrrolidone) coatings. *Biomaterials*. 2011;32:4481-8.
- [42] Prasertsung I, Kanokpanont S, Mongkolnavin R, Wong CS, Panpranot J, Damrongsakkul S. Plasma Enhancement of In Vitro Attachment of Rat Bone-Marrow-Derived Stem Cell on Cross-Linked Gelatin Films. *Journal of Biomaterials Science*. 2012;23:1485-504.
- [43] Prasertsung I, Mongkolnavin R, Damrongsakkul S, Wong CS. Surface modification of dehydrothermal crosslinked gelatin film using a 50 Hz oxygen glow discharge. *Surface & Coatings Technology*. 2010;205:S133-8.
- [44] Prasertsung I, Mongkolnavin R, Kanokpanont S, Damrongsakkul S. The effects of pulsed inductively coupled plasma (PICP) on physical properties and biocompatibility of crosslinked gelatin films. *International Journal of Biological Macromolecules*. 2010;46:72-8.
- [45] Mitchell SA, Davidson MR, Bradley RH. Improved cellular adhesion to acetone plasma modified polystyrene surfaces. *Journal of Colloid and Interface Science*. 2005;281:122-9.
- [46] Mitchell SA, Davidson MR, Emmison N, Bradley RH. Isopropyl alcohol plasma modification of polystyrene surfaces to influence cell attachment behaviour. *Surface Science*. 2004;561:110-20.
- [47] Pompe T, Keller K, Mothes G, Nitschke M, Teese M, Zimmermann R, et al. Surface modification of poly(hydroxybutyrate) films to control cell-matrix adhesion. *Biomaterials*. 2007;28:28-37.

- [48] Pu FR, Williams RL, Markkula TK, Hunt JA. Effects of plasma treated PET and PTFE on expression of adhesion molecules by human endothelial cells in vitro. *Biomaterials*. 2002;23:2411-28.
- [49] Nitschke M, Ricciardi S, Gramm S, Zschoche S, Herklotz M, Rivolo P, et al. Surface modification of cell culture carriers: Routes to anhydride functionalization of polystyrene. *Colloids and Surfaces B: Biointerfaces*. 2012;90:41- 7.
- [50] Meyer U, Büchter A, Wiesmann HP, Joos H, Jones DB. Basic reactions of osteoblasts on structured material surfaces. *European Cells and Materials*. 2005;9:39-49.
- [51] Vogler EA. Protein adsorption in three dimensions. *Biomaterials*. 2012;33:1201-37.
- [52] Anselme K. Osteoblast adhesion on biomaterials. *Biomaterials*. 2000;21:667-81.
- [53] Rabe M, Verdes D, Seeger S. Understanding protein adsorption phenomena at solid surfaces. *Advances in Colloid and Interface Science*. 2011:87-106.
- [54] Lehmann K, Herklotz M, Espig M, Paumer T, Nitschke M, Werner C, et al. A new approach to biofunctionalisation and micropatterning of multi-well plates. *Biomaterials*. 2010;31:8802-9.
- [55] Chiquet M, Gelman L, Lutz R, Maier S. From mechanotransduction to extracellular matrix gene expression in fibroblasts. *Biochimica et Biophysica Acta - Molecular Cell Research*. 2009;1793:911-20.
- [56] Engler AJ, Sen S, Sweeney HL, Discher DE. Matrix Elasticity Directs Stem Cell Lineage Specification. *Cell*. 2006;126:677-89.
- [57] Meyer-Plath AA, Schröder K, Finke B, Ohl A. Current trends in biomaterial surface functionalization—nitrogen-containing plasma assisted processes with enhanced selectivity. *Vacuum*. 2003;71:391-406.
- [58] Goldston RJ, Rutherford PH. Chapter 1 : Introduction to plasmas. *Introduction to Plasma Physics*. London: Institute of Physics Publishing; 1995.
- [59] Roth JR. Chapter 1 : Introduction. *Industrial Plasma Engineering Volume 1: Principles*. London: Institutes of Physics Publishing; 1995.
- [60] Roth JR. Chapter 2 : The Kinetic Theory of Gases. *Industrial Plasma Engineering Volume 1: Principles*. London: Institute of Physics Publishing; 1995.

- [61] Roth JR. Chapter 3 : Motion of Charges in Electric and. Industrial Plasma Engineering Volumel1: Principles. London: Institute of Phycis Publishing; 1995.
- [62] Roth JR. Chapter 4 : Characteristics of Plasma. Industrial Plasma Engineering Volume 1: Principles. London: Institute of Physics Publishing; 1995.
- [63] Roth JR. Chapter 8 : Dark Electrical Discharges in Gases. Industrial Plasma Engineering Volume 1: Principles. London: Institute of Physics Publishing; 1995.
- [64] Roth JR. Chapter 9 : DC Electrical Glow Discharges in Gases. Industrial Plasma Engineering Volume 1: Principles London Institute of Physics Publishing; 1995.
- [65] Roth JR. Chapter 11 : Inductive RF Electrical Discharges in Gases. Industrial Plasma Engineering Volume 1: Principles. London: Institute of Physics Publishing. p. 1995.
- [66] Roth JR. Chapter 12 : Capacitive RF Electrical Discharges in Gases. Industrial Plasma Engineering Volume 1: Principles. London Institute of Physics Publishing; 1995.
- [67] Roth JR. Chapter 13 : Microwave Electrical Discharges in Gases. Industrial Plasma Engineering Volume 1: Principles. London Institute of Physics Publishing; 1995.
- [68] Roth JR. Chapter 17 : Plasma Reactors for Plasma Processing. Industrial Plasma Engineering Volume 2: Applications. London: Institute of Physics Publishing; 1995.
- [69] Roth JR. Chapter 21 : Plasma Treatment of Surfaces. Industrial Plasma Engineering Volume 2: Applications. London: Institute of Physics Publishing; 1995.
- [70] Roth JR. Chapter 22 : Surface Modification by Implantation and Diffusion. Industrial Plasma Engineering Volume 2: Applications London Institute of Physics Publishing; 1995.
- [71] Roth JR. Chapter 23 : Thin-Film Deposition by Evaporative Condensation and Sputtering. Industrial Plasma Engineering Volume 2: Applications. London Institute of Physics Publishing; 1995.
- [72] Roth JR. Chapter 24 : Plasma Chemical Vapor Deposition (PCVD). Industrial Plasma Engineering Volume 2: Applications London Institute of Physics Publishing; 1995.

- [73] Roth JR. Chapter 25 : Plasma Etching. Industrial Plasma Engineering Volume 2: Applications London: Institute of Physics Publishing; 1995.
- [74] Roth JR. Chapter 20 : Diagnostics for Plasma Processing. Industrial Plasma Engineering Volume 2: Applications London: Institute of Physics Publishing; 1995.
- [75] Vainker S. Chinese Silk: A Cultural History. New York: British Museum Press; 2004.
- [76] Vepari C, Kaplan DL. Silk as a biomaterial. *Prog Polym Sci.* 2007;32:991-1007.
- [77] Ho M-p, Wang H, Lee J-H, Ho C-k, Lau K-t, Leng J, et al. Critical factors on manufacturing processes of natural fibre composites. *Composites Part B: Engineering.*
- [78] Zhou CZ, Confalonieri F, Jacquet M, Perasso R, Li ZG, Janin J. Silk Fibroin: Structural Implications of a Remarkable Amino Acid Sequence. *PROTEINS: Structure, Function, and Genetics.* 2001;44:119-22.
- [79] Tanaka K, Inoue S, Mizuno S. Hydrophobic interaction of P25, containing Asn-linked oligosaccharide chains, with the H-L complex of silk fibroin produced by *Bombyx mori*. *Insect Biochemistry and Molecular Biology.* 1999;29:269-76.
- [80] Dickerson RE, Geis I. The structure and action of proteins: Harper & Row; 1969.
- [81] Spatz JP, Geiger B. Molecular Engineering of Cellular Environments: Cell Adhesion to Nano-Digital Surfaces. *Methods in Cell Biology.* San Diego: Academic Press; 2007. p. 89-111.
- [82] Dubash AD, Menold MM, Samson T, Boulter E, Garcia-Mata R, Doughman R, et al. Chapter 1 Focal Adhesions: New Angles on an Old Structure. *International Review of Cell and Molecular Biology.* San Diego: Academic Press; 2009. p. 1-65.
- [83] Nori A, Yim EKF, Chen S, Leong KW. 38- Cell-Substrate Interactions. *Principles of Regenerative Medicine.* San Diego: Academic Press; 2008. p. 666-85.
- [84] Keselowsky BG, Collard DM, AJ. Gi. Surface chemistry modulates fibronectin conformation and directs integrin binding and specificity to control cell adhesion. *Journal of Biomedical Materials Research.* 2003;66A:247-59.
- [85] Garland A, Shen L, Zhu X. Mobile precursor mediated protein adsorption on solid surfaces. *Progress in Surface Science.* 2012;87:1-22.

- [86] Browne MM, Lubarsky GV, Davidson MR, Bradley RH. Protein adsorption onto polystyrene surfaces studied by XPS and AFM. *Surface Science*. 2004;155-67.
- [87] Costa P, Parsons M. New Insights into the Dynamics of Cell Adhesions. *International Review of Cell and Molecular Biology*. 2010;283:57-91.
- [88] Dubash AD, Menold MM, Samson T, Boulter E, Garcia-Mata R, Doughman R, et al. Focal Adhesions: New Angles on an Old Structure. *International Review of Cell and Molecular Biology*. 2009;277:1-65.
- [89] Petit V, Thiery J-P. Focal adhesions: structure and dynamics. *Biology of the Cell*. 2000;92:477-94.
- [90] Gomperts BD, Kramer IM, Tatham PER. Chapter 13 – Signal Transduction to and from Adhesion Molecules. *Signal Transduction (Second Edition)*. 2 ed: Academic Press; 2009.
- [91] Keselowsky BG, Bridges AW, Burns KL, Tate CC, Babensee JE, LaPlaca MC, et al. Role of plasma fibronectin in the foreign body response to biomaterials. *Biomaterials* 28. 2007;28:3626-31.
- [92] Faucheux N, Schweiss R, Lutzow K, Werner C, Groth T. Self-assembled monolayers with different terminating groups as model substrates for cell adhesion studies. *Biomaterials*. 2004 25:2721-30.
- [93] Curran JM, Chen R, Hunt JA. Controlling the phenotype and function of mesenchymal stem cells in vitro by adhesion to silane-modified clean glass surfaces. *Biomaterials*. 2005;26:7057-67.
- [94] Keselowsky BG, Collard DM, Garcia AJ. Surface chemistry modulates focal adhesion composition and signaling through changes in integrin binding. *Biomaterials*. 2004;25:5947-54.
- [95] Discher DE, Janmey P, Wang Y-l. Tissue Cells Feel and Respond to the Stiffness of Their Substrate. *Science*. 2005;310:1139-43.
- [96] Buxboim A, Rajagopal K, Brown AEX, Discher DE. How deeply cells feel: Methods for thin gels. *Journal of Physics Condensed Matter*. 2010;22.
- [97] Almo SC, Bresnick AR, Zhang X. Chapter 10 - Mechanistic Features of Cell-Surface Adhesion Receptors. In: Bradshaw RA, Dennis EA, editors. *Handbook of Cell Signaling (Second Edition)*. San Diego: Academic Press; 2010. p. 63-9.

- [98] Lo CM, Wang HB, Dembo M, Wang YL. Cell movement is guided by the rigidity of the substrate. *Biophys J*. 2000;79:144-52.
- [99] Solon J, Levental I, Sengupta K, Georges PC, Janmey PA. Fibroblast adaptation and stiffness matching to soft elastic substrates. *Biophys J*. 2007;93:4453-61.
- [100] Park JS, Chu JS, Tsou AD, Diop R, Tang Z, Wang A, et al. The effect of matrix stiffness on the differentiation of mesenchymal stem cells in response to TGF- $\beta$ . *Biomaterials*. 2011;32:3921-30.
- [101] Yeung T, Georges PC, Flanagan LA, Marg B, Ortiz M, Funaki M, et al. Effects of substrate stiffness on cell morphology, cytoskeletal structure, and adhesion. *Cell Motil Cytoskeleton*. 2005;60:24-34.
- [102] Tzvetkova-Chevolleau T, Stéphanou A, Fuard D, Ohayon J, Schiavone P, Tracqui P. The motility of normal and cancer cells in response to the combined influence of the substrate rigidity and anisotropic microstructure. *Biomaterials*. 2008;29:1541-51.
- [103] Seo JH, Sakai K, Yui N. Adsorption state of fibronectin on poly(dimethylsiloxane) surfaces with varied stiffness can dominate adhesion density of fibroblasts. *Acta Biomater*. 2013;9:5493-501.
- [104] Ghibaudo M, Saez A, Trichet L, Xayaphoummine A, Browaeys J, Silberzan P, et al. Traction forces and rigidity sensing regulate cell functions. *Soft Matter*. 2008;4:1836-43.
- [105] Bartalena G, Loosli Y, Zambelli T, Snedeker JG. Biomaterial surface modifications can dominate cell-substrate mechanics: The impact of PDMS plasma treatment on a quantitative assay of cell stiffness. *Soft Matter*. 2012;8:673-81.
- [106] Guiseppi-Elie A, Dong C, Dinu CZ. Crosslink density of a biomimetic poly(HEMA)-based hydrogel influences growth and proliferation of attachment dependent RMS 13 cells. *J Mater Chem*. 2012;22:19529-39.
- [107] Ouasti S, Donno R, Cellesi F, Sherratt MJ, Terenghi G, Tirelli N. Network connectivity, mechanical properties and cell adhesion for hyaluronic acid/PEG hydrogels. *Biomaterials*. 2011;32:6456-70.

- [108] Schneider A, Francius G, Obeid R, Schwinté P, Hemmerlé J, Frisch B, et al. Polyelectrolyte multilayers with a tunable young's modulus: Influence of film stiffness on cell adhesion. *Langmuir*. 2006;22:1193-200.
- [109] Thompson MT, Berg MC, Tobias IS, Rubner MF, Van Vliet KJ. Tuning compliance of nanoscale polyelectrolyte multilayers to modulate cell adhesion. *Biomaterials*. 2005;26:6836-45.
- [110] Kawai H, Shibata Y, Miyazaki T. Glow discharge plasma pretreatment enhances osteoclast differentiation and survival on titanium plates. *Biomaterials*. 2004;25:1805-11.
- [111] Kim YJ, Kang I-K, Huh MW, Yoon S-C. Surface characterization and in vitro blood compatibility of poly(ethylene terephthalate) immobilized with insulin and/or heparin using plasma glow discharge. *Biomaterials*. 2000;21:121-30.
- [112] Nitschke M, König U, Lappan U, Minko S, Simon F, Zschoche S, et al. Low Pressure Plasma-Based Approaches to Fluorocarbon Polymer Surface Modification. *Journal of Applied Polymer Science*. 2006;103:100-9.
- [113] Wan Y, Tu C, Yang J, Bei J, Wang S. Influences of ammonia plasma treatment on modifying depth and degradation of poly(L-lactide) scaffolds. *Biomaterials*. 2006;27:2699-704.
- [114] Kim U-J, Park J, Joo Kim H, Wada M, Kaplan DL. Three-dimensional aqueous-derived biomaterial scaffolds from silk fibroin. *Biomaterials*. 2005;26:2775-85.
- [115] Ishida M, Asakura T, Yokoi M, Saito H. Solvent- and mechanical-treatment-induced conformational transition of silk fibroins studies by high-resolution solid-state carbon-13 NMR spectroscopy. *Macromolecules*. 1990;23:88-94.
- [116] Mosmann T. Rapid colorimetric assay for cellular growth and survival: Application to proliferation and cytotoxicity assays. *Journal of Immunological Methods*. 1983;65:55-63.
- [117] Barak LS, Yocum RR, Nothnagel EA, Webb WW. Fluorescence staining of the actin cytoskeleton in living cells with 7-nitrobenz-2-oxa-1,3-diazole-phalloidin. *Proceedings of the National Academy of Sciences*. 1980;77:980-4.

- [118] Miyanaga S, Kaneko T, Ishida H, Hatakeyama R. Synthesis evaluation of nitrogen atom encapsulated fullerenes by optical emission spectra in nitrogen plasmas. *Thin Solid Films*. 2010;518:3509-12.
- [119] Kramida A, Ralchenko Y, Reader J, Team NA. NIST Atomic Spectra Database (ver.5.0). December 19, 2012 ed. Gaithersburg, MD.: National Institute of Standards and Technology; 2012.
- [120] Jedlicka SS, Rickus JL, Zemlyanov DY. Surface Analysis by X-ray Photoelectron Spectroscopy of Sol-Gel Silica Modified with Covalently Bound Peptides. *J Phys Chem B*. 2007;111:11850-7.
- [121] Vandencastele N, Reniers F. Plasma-modified polymer surfaces: Characterization using XPS. *J Electron Spectrosc Relat Phenom*. 2010;178-179:394-408.
- [122] Gu J, Yang X, Zhu H. Surface sulfonation of silk fibroin film by plasma treatment and in vitro antithrombogenicity study. *Materials Science and Engineering: C*. 2002;20:199-202.
- [123] Jewett S, Zemlyanov D, Ivanisevic A. Adsorption of Mixed Peptide/Thiol Adlayers on InAs: Assessment of Different Functionalization Strategies Using X-ray Photoelectron Spectroscopy. *J Phys Chem C*. 2011;115:14244-52.
- [124] Lee H-U, Jeong Y-S, Jeong S-Y, Park S-Y, Bae J-S, Kim H-G, et al. Role of reactive gas in atmospheric plasma for cell attachment and proliferation on biocompatible poly  $\epsilon$ -caprolactone film. *Appl Surf Sci*. 2008;254:5700-5.
- [125] Pleul D, Simon F. X-Ray Photoelectron Spectroscopy. In: Stamm M, editor. *Polymer Surfaces and Interfaces*: Springer Berlin Heidelberg; 2008. p. 71-89.
- [126] Gogoi D, Choudhury AJ, Chutia J, Pal AR, Dass NN, Devi D, et al. Enhancement of hydrophobicity and tensile strength of muga silk fiber by radiofrequency Ar plasma discharge. *Applied Surface Science*. 2011;258:126-35.
- [127] Müller M, Rieser T, Lunkwitz K, Meier-Haack J. Polyelectrolyte complex layers: a promising concept for anti-fouling coatings verified by in-situ ATR-FTIR spectroscopy. *Macromol Rapid Commun*. 1999;20:607-11.
- [128] Harrick NJ. *Internal reflection spectroscopy*. New York: Interscience Publishers; 1967.



- [129] Hu X, Kaplan D, Cebe P. Determining beta-sheet crystallinity in fibrous proteins by thermal analysis and infrared spectroscopy. *Macromolecules*. 2006;39:6161-70.
- [130] Lyklema H. Electrokinetics and related phenomena. In: Lyklema JJ, de Keizer A, Bijsterbosch BH, Flerer GJ, Cohen Stuart MA, editors. *Fundamentals of Interface and Colloid Science*: Academic Press; 1995. p. 1-135.
- [131] Zimmermann R, Osaki T, Schweiss R, Werner C. Electrokinetic microslit experiments to analyse the charge formation at solid/liquid interfaces. *Microfluid Nanofluid*. 2006;2:367-79.
- [132] Marmur A. Soft contact: measurement and interpretation of contact angles. *Soft Matter*. 2006;2:12-7.
- [133] Grundke K, Werner C, Poschel K, Jacobasch HJ. Characterization of adsorbed protein layers by low-rate dynamic liquid-fluid contact angle measurements using axisymmetric drop shape analysis (part II). *Colloids Surf Physicochem Eng Aspects*. 1999;156:19-31.
- [134] Kwok DY, Li A, Lam CNC, Leung A, Neumann AW. Low-rate dynamic contact angles on noninert poly(propene-alt-N-(n-alkyl)maleimide) copolymers by an automated axisymmetric drop shape analysis (ADSA-P). *Langmuir*. 1998;14:2221-4.
- [135] Krieg M, Arboleda-Estudillo Y, Puech PH, Kafer J, Graner F, Muller DJ, et al. Tensile forces govern germ-layer organization in zebrafish. *Nat Cell Biol*. 2008;10:429-U122.
- [136] Hutter JL, Bechhoefer J. Calibration of atomic-force microscope tips. *Rev Sci Instrum*. 1993;64:1868-73.
- [137] Sauerbrey G. Verwendung von Schwingquarzen zur Wägung dünner Schichten und zur Mikrowägung. *Z Physik*. 1959;155:206-22.
- [138] Voinova MV, Jonson M, Kasemo B. 'Missing mass' effect in biosensor's QCM applications. *Biosens Bioelectron*. 2002;17:835-41.
- [139] Höök F, Kasemo B, Nylander T, Fant C, Sott K, Elwing H. Variations in Coupled Water, Viscoelastic Properties, and Film Thickness of a Mefp-1 Protein Film during Adsorption and Cross-Linking: A Quartz Crystal Microbalance with

- Dissipation Monitoring, Ellipsometry, and Surface Plasmon Resonance Study. *Anal Chem.* 2001;73:5796-804.
- [140] Asakura T, Watanabe Y, Uchida A, Minagawa H. NMR of silk fibroin 2 C-13 NMR study of the chain dynamics and solutin structure of Bomby mori silk fibroin. *Macromolecules.* 1984;17:1075-81.
- [141] Demura M, Takekawa T, Asakura T, Nishikawa A. Characterization of low-temperature-plasma treated silk fibroin fabrics by ESCA and the use of the fabrics as an enzyme-immobilization support. *Biomaterials.* 1992;13:276-80.
- [142] Zhang J. The surface characterization of mulberry silk grafted with acrylamide by plasma copolymerization. *J Appl Polym Sci.* 1997;64:1713-7.
- [143] Selli E, Riccardi C, Massfra MR, Marcandalli B. Surface modifications of silk by cold SF6 plasma treatment. *Macromol Chem Phys.* 2001;202:1672-8.
- [144] Gu JW, Yang XL, Zhu HS. Surface sulfonation of silk fibroin film by plasma treatment and in vitro antithrombogenicity study. *Mater Sci Eng C Biomimetic Supramol Syst.* 2002;20:199-202.
- [145] Iriyama Y. Preparation of silk film and its plasma treatment for better dyeability. *J Photopolym Sci Technol.* 2003;16:75-80.
- [146] Shen L, Dai JJ. Improvement of hydrophobic properties of silk and cotton by hexafluoropropene plasma treatment. *Appl Surf Sci.* 2007;253:5051-5.
- [147] Malkov GS, Fisher ER. Pulsed Plasma Enhanced Chemical Vapor Deposition of Poly(allyl alcohol) onto Natural Fibers. *Plasma Process Polym.* 2010;7:695-707.
- [148] Chen GL, Zhou MY, Zhang ZX, Lv GH, Massey S, Smith W, et al. Acrylic Acid Polymer Coatings on Silk Fibers by Room-temperature APGD Plasma Jets. *Plasma Process Polym.* 2011;8:701-8.
- [149] Wang SD, Zhang YZ, Wang HW, Dong ZH. Preparation, characterization and biocompatibility of electrospinning heparin-modified silk fibroin nanofibers. *Int J Biol Macromol.* 2011;48:345-53.
- [150] Jedlicka SS, Rickus JL, Zemlyanov DY. Surface Analysis by X-ray Photoelectron Spectroscopy of Sol-Gel Silica Modified with Covalently Bound Peptides. *The Journal of Physical Chemistry B.* 2007;111:11850-7.

- [151] Hodak SK, Supasai T, Paosawatyanong B, Kamlangkla K, Pavarajarn V. Enhancement of the hydrophobicity of silk fabrics by SF(6) plasma. *Appl Surf Sci.* 2008;254:4744-9.
- [152] Suanpoot P, Kueseng K, Ortmann S, Kaufmann R, Umongno C, Nimmanpipug P, et al. Surface analysis of hydrophobicity of Thai silk treated by SF6 plasma. *Surf Coat Tech.* 2008;202:5543-9.
- [153] Samuels RJ. Application of refractive index measurements to polymer analysis. *J Appl Polym Sci.* 1981;26:1383-412.
- [154] Wallet B, Kharlampieva E, Campbell-Proszowska K, Kozlovskaya V, Malak S, Ankner JF, et al. Silk Layering As Studied with Neutron Reflectivity. *Langmuir.* 2012;28:11481-9.
- [155] Currie EPK, Sieval AB, Fler GJ, Stuart MAC. Polyacrylic Acid Brushes: Surface Pressure and Salt-Induced Swelling. *Langmuir.* 2000;16:8324-33.
- [156] Seib FP, Maitz MF, Hu XA, Werner C, Kaplan DL. Impact of processing parameters on the haemocompatibility of Bombyx mori silk films. *Biomaterials.* 2012;33:1017-23.
- [157] Motta A, Maniglio D, Migliaresi C, Kim H-J, Wan X, Hu X, et al. Silk Fibroin Processing and Thrombogenic Responses. *J Biomater Sci Polym Ed.* 2009;20:1875-97.
- [158] Chaivan P, Pasaja N, Boonyawan D, Suanpoot P, Vilaithong T. Low-temperature plasma treatment for hydrophobicity improvement of silk. *Surf Coat Tech.* 2005;193:356-60.
- [159] Mitchell SA, Poulsson AHC, Davidson MR, Bradley RH. Orientation and confinement of cells on chemically patterned polystyrene surfaces. *Colloids Surf B Biointerfaces.* 2005;46:108-16.
- [160] Beamson G, Briggs D. High resolution XPS of organic polymers: The Scienta ESCA 300 database. Chichester: John Wiley & Sons Ltd.; 1992.
- [161] Narayanamoorthy J, Tsioris K, Omenetto FG, Hopwood J. Plasma etching of silk fibroin: Experiments and models. *Plasma Processes and Polymers.* 2013;10:451-8.

- [162] Renner L, Pompe T, Salchert K, Werner C. Fibronectin Displacement at Polymer Surfaces. *Langmuir*. 2005;21:4571-7.
- [163] Hovgaard MB, Rechendorff K, Chevallier J, Foss M, Besenbacher F. Fibronectin Adsorption on Tantalum: The Influence of Nanoroughness. *The Journal of Physical Chemistry B*. 2008;112:8241-9.
- [164] Sastry SK, Burridge K. Focal adhesions: A nexus for intracellular signaling and cytoskeletal dynamics. *Exp Cell Res*. 2000;261:25-36.
- [165] Nicolas A, Geiger B, Safran SA. Cell mechanosensitivity controls the anisotropy of focal adhesions. *Proc Natl Acad Sci U S A*. 2004;101:12520-5.
- [166] Constantinides G, Kalcioglu ZI, McFarland M, Smith JF, Van Vliet KJ. Probing mechanical properties of fully hydrated gels and biological tissues. *J Biomech*. 2008;41:3285-9.
- [167] Kim DH, Viventi J, Amsden JJ, Xiao J, Vigeland L, Kim YS, et al. Dissolvable films of silk fibroin for ultrathin conformal bio-integrated electronics. *Nature materials*. 2010;9:511-7.
- [168] Kim D-H, Kim Y-S, Amsden J, Panilaitis B, Kaplan DL, Omenetto FG, et al. Silicon electronics on silk as a path to bioresorbable, implantable devices. *Appl Phys Lett*. 2009;95:-.
- [169] Tsioris K, Tilburey GE, Murphy AR, Domachuk P, Kaplan DL, Omenetto FG. Functionalized-silk-based active optofluidic devices. *Adv Funct Mater*. 2010;20:1083-9.
- [170] Amsden JJ, Perry H, Boriskina SV, Gopinath A, Kaplan DL, Negro LD, et al. Spectral analysis of induced color change on periodically nanopatterned silk films. *Opt Express*. 2009;17:21271-9.

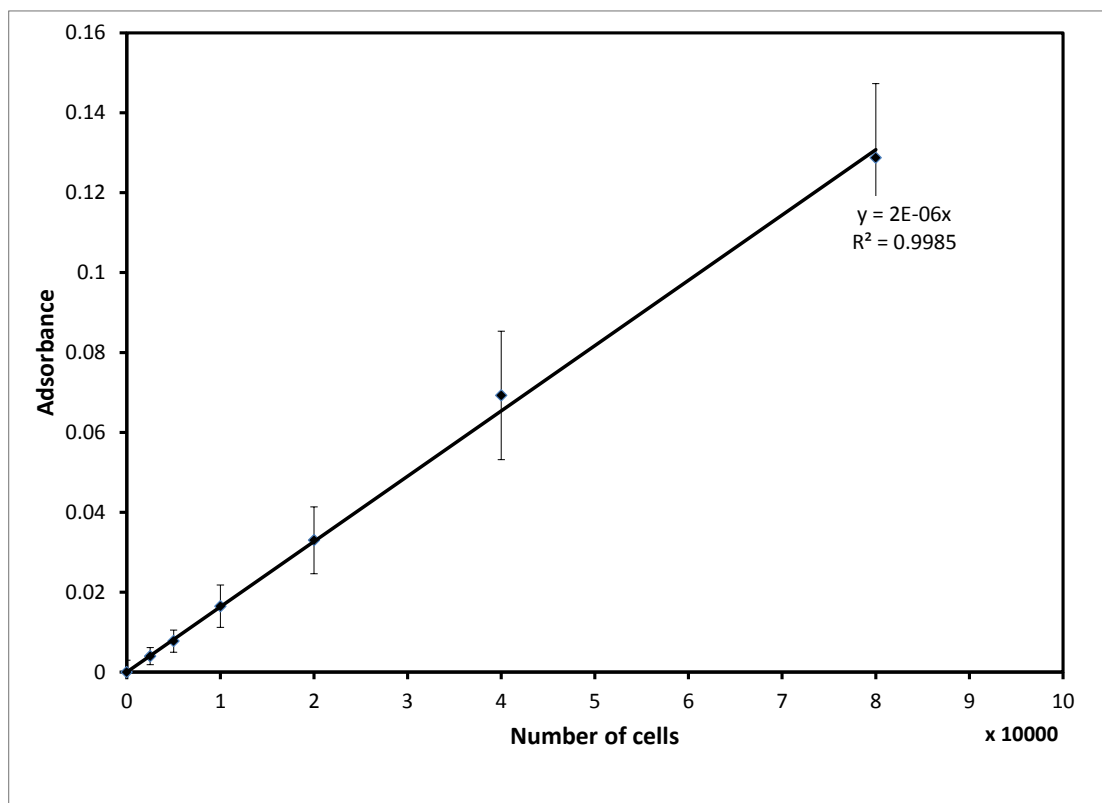


APPENDIX

จุฬาลงกรณ์มหาวิทยาลัย  
CHULALONGKORN UNIVERSITY

## APPENDIX A: MTT standard curve

Standard curve for MTT assay



จุฬาลงกรณ์มหาวิทยาลัย  
CHULALONGKORN UNIVERSITY

## VITA

Mr. Phakdee Amornsudthiwat was born in Bangkok, Thailand on November 23, 1973. He graduated at the high school level in 1991 from Suankularb College. In 1995, he received his Bachelor Degrees of Engineering (2nd class honor) with a major of Chemical Engineering from Faculty of Engineering, Chulalongkorn University.

After graduation, he went to work with Siam Cement Group and Dow Chemical joint venture companies (SCG-Dow) for 15 years. He held numerous positions in both technical and administrative areas i.e., Commissioning and Start-up Coordinator – Map Ta Phut, Thailand, Manufacturing Representative for new Polyethylene Project in Thailand – Houston, Texas, Lead Production Engineer (Polyethylene Plant), Site Human Resource Services Leader, Polyethylene Project Engineer - (Overseas assignment in Texas, Louisiana, & Alberta), Polystyrene Plant Engineer, etc.

After 15 years of working, he decided to pursue his personal passion which he could not do at the early of his career due to family issue. He just simply wants to be a university lecturer or researcher. Because he loves to do the research and grooms students for the real world.

จุฬาลงกรณ์มหาวิทยาลัย  
CHULALONGKORN UNIVERSITY